TECHNISCHE UNIVERSITÄT MÜNCHEN

Physik-Department

Lehrstuhl für Experimentalphysik IV (E13)

Structure and kinetic of stimuli-responsive thin hydrogel films

Weinan Wang

Vollständiger Abdruck der von der Fakultät für Physik der Technischen Universität München zur Erlangung des akademischen Grades eines

Doktors der Naturwissenschaften (Dr. rer. nat.)

genehmigten Dissertation.

Vorsitzender: Univ.-Prof. Dr. Roland Netz

Prüfer der Dissertation:

1. Univ.-Prof. Dr. Peter Müller-Buschbaum
2. Univ.-Prof. Dr. Thorsten Hugel

Die Dissertation wurde am 08.02.2010 bei der Technischen Universität München eingereicht und durch die Fakultät für Physik am 11.02.2010 angenommen.

Contents

Chapter 1

Introduction

Hydrogels are cross-linked polymer networks which can contain large amounts of water but do not dissolve in water [HAS02, DJL03, DD91, DD99]. In the last three decades, intelligent hydrogels, which can change physical or chemical properties in response to environmental stimuli, like temperature, pH, light, chemical stimuli, and others, have attracted increased interest [TT78, TT82]. Thermoresponsive aqueous polymer systems are known to exhibit large, reversible conformational changes in response to small thermal stimuli [SM96]. It can be used as actuators [OY87, SS96], artificial muscles [OY93, LZ00], solute separators [FH91, PYS98], drug delivery systems [RKVR88, BCS96, SPS95, GP02], thermoresponsive surfaces [KA04, LL00, KD07], light modulation systems [AR02, ASA00], optical switching devices [MS07], and molecular recognition agents [KR04, MT02].

Poly(*N*-isopropylacrylamide) (PNIPAM) is probably among the most studied thermosensitive polymers [WFM90, SHG92, TKC93, TEI94]. PNIPAM in water exhibits a phase transition at a lower critical solution temperature (LCST), which has been investigated by a variety of experimental techniques in the dilute and concentrated regimes. The LCST of PNIPAM in water is approximately at 32°C and thus slightly less than body temperature, which makes PNIPAM a representative of environmental-sensitive polymers studied for biomedical applications [HDL03].

Although PNIPAM has been well studied, compared to the large body of work on water based PNIPAM solutions and the achieved understanding of the system, the knowledge on thin PNIPAM films is still limited. This is surprising as many advanced applications of responsive hydrogels are based on thin films and make use of the switching of the film properties at LCST. For example, below the LCST a PNIPAM coated surface shows a

hydrophilic behavior, however, when heated above the LCST the behavior changes to hydrophobic [JDM02]. This effect on substrates offers the ability to control important interfacial phenomena such as wetting [XY01, LP99], fluid flows [KDE99], adhesion [CME00] and the reversible adsorption of biomolecules as a function of temperature [GD02]. Thus having thermoresponsive surfaces, which undergo a strong change in wetting and adhesive properties triggered by a change in temperature, are much desired. In particular, regarding the response time, bulk hydrogels are slow, promoting micro-gels [PR00, MMJ95, KM08, SS08] and thin films [TS05, SMJ03, SMJ04] to be considered as better systems with shorter response times. The volume change appears much faster if the hydrogel dimensions are in the sub-micrometer range. Thus, thin films allow for advanced applications such as miniaturized sensor systems and nano-switches [TPA06, GM07, GM08, KD09]. Figure 1.1 shows how a nano-switch system based on a thermoresponsive hydrogel thin film works in water vapor. When the temperature is lower than the LCST, the film swells in the water vapor and is in contact with the electrode. Thus, the switch is in "on" state. When the temperature is higher than the LCST, the film deswells and is disengagement with the electrode. Thus, the switch is in "off" state.

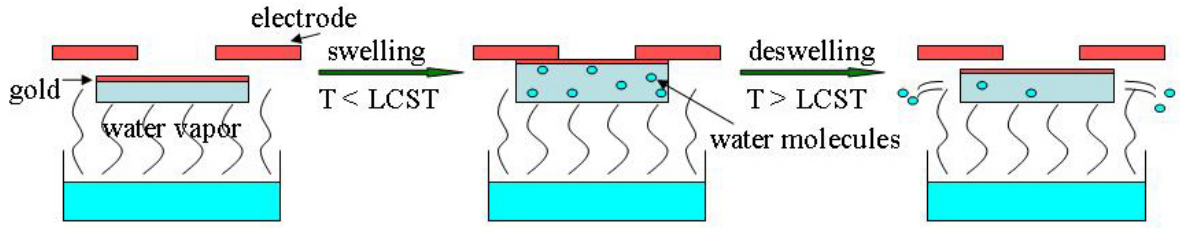

Figure 1.1: Sketch of a nano-switch system based on a thermoresponsive hydrogel thin film.

On the other hand, most of these responding systems are based on changes of the polymer chain conformation, which can cause problems in applications related to the swelling induced strain. Thus, a polymer material based on PNIPAM in thin film geometry which allows for water incorporation and at the same time can keep the film volume fixed is also interested.

Moreover, because pure PNIPAM homopolymer films miss the possibility of internal crosslinks to build up a gel, the addition of hydrophobic chain ends is necessary. On the other hand, the swelling and the switching behavior of the hydrogel thin film is strongly influ-

enced by the level of hydrophobe incorporation, the chemical structure of the hydrophobic group and the position of the hydrophobic group in the chain [KP01, CZ05].

Therefore, in the present work, several different PNIPAM based copolymers are selected and compared. They have different chemical structures of hydrophobic group (n-butyltrithiocarbonate and polystyrene), or different hydrophobic group length (volume fraction of hydrophobic group varied from 1% to 72.6%), or different hydrophobic group positions in the chain (diblock and triblock copolymers). Thin films with different thicknesses prepared from their 1,4-dioxane solutions by spin-coating are investigated in detail. In particular, the answer to the following questions is addressed: What is the internal structures in these films and how they influence the swelling and switching behavior? What is the role of the hydrophobic group in the film swelling and switching? Does an additional gold top layer (normally used as an electrode of a nanoswitch) on the thin film influence the swelling and the switching behavior? And the most important for applications: What is the swelling and switching mechanism of these response systems?

Besides of these, PNIPAM based thin films swelling in the water fluid and undergoing gold deposition on top of them are investigated. This is important as microfluidic devices are applied in many applications like microanalytics or high throughput devices and reactors [DE97, WBH99, IRF01]. The combination of them and hydrogel thin films will open new applications like miniaturized sensor systems and nano-switches in flow.

Finally, the investigation focused on a small length scale structure (from a few angstroms to a few tens of angstroms) like the correlation length, ξ, during the switching process completes this work. This is helpful for further understanding of the switching mechanism of the hydrogel thin films.

Chapter 2

Theoretical Background

2.1 Block Copolymer Thin Films

2.1.1 Microphase Separation

A block copolymer is defined as two different polymeric species coupled together by a chemical link [SG97]. Such material possesses peculiar properties and the combination of distinct polymers can give materials with defined physical properties. Because the polymer chains are tethered to each other, macroscopic phase separation cannot occur and structural organization occurs in domains. Because all domains have a uniform size, they can be arranged in a regular manner producing ordered mesoscopic lattices. Such kind of phase separation in block copolymer systems is called *microphase separation*. A theoretical prediction and experimental investigation of microphase separation in block copolymer can be found in literature [SG97]. Figure 2.1 shows a typical phase diagram of block copolymers and different classes of microphase-separated structures in block copolymers. The type of the structures is dependent on the ratio between the degrees of polymerization of the A and B spieces. For $N_A \ll N_B$ spherical structures of A in matrix B are formed. For larger values N_A, but still $N_A < N_B$, the A-domains have a cylinderical shape. Layered lattices form under essentially symmetrical conditions, i.e. $N_A \approx N_B$. Then, for $N_A > N_B$, the phases are inverted, and the block A now constitutes the matrix. Under special conditions, continuous and periodic structures, known as bicontinuous gyroid structures can also be formed and interpenetrate each other, but only in a narrow range of values N_A/N_B, between the regimes of the cylinderical and lamellar structures. Although little is known about how general special types like the bicontinuous gyroid structures are, spherical, cylindrical and lamellae-like domains are generally ob-

served in all block copolymers consisting of two species. Besides the diblock copolymers, triblocks and multiblocks, comprising an arbitrary number of A- and B- chains, exhibit qualitatively similar phase behaviors.

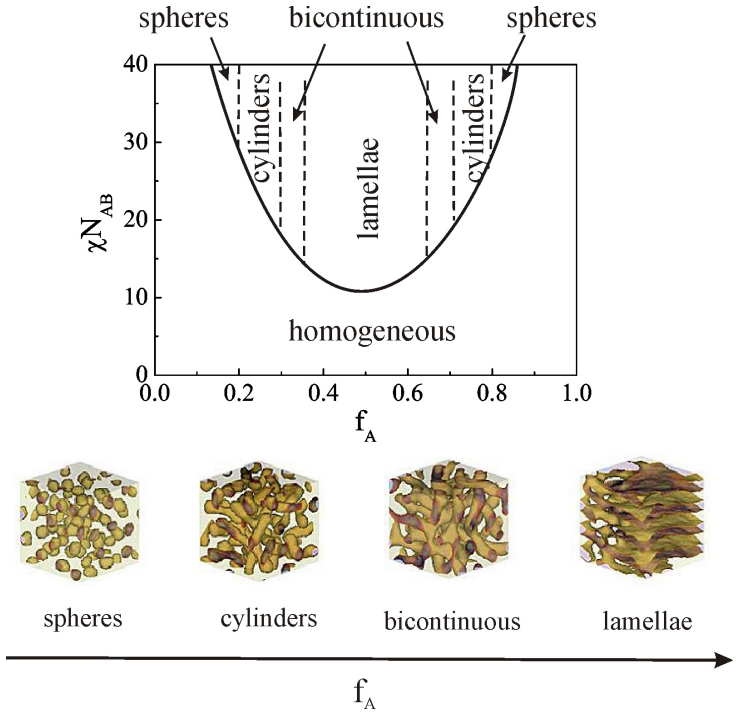

Figure 2.1: phase diagram of a diblock copolymer in a schematic representation: f_A = volume fraction of A block, χ = Flory interaction parameter, N = diblock degree of polymerization, $N_{AB} = N_A + N_B$. Known equilibrium mesophases are spheres, cylinders, bicontinuous, and lamellae, as well as the disordered (homogeneous) state at small interblock segregation strength (χN_{AB}). Images are taken from [MBP07b]

In binary polymer mixtures, homogeneous phases are found under favorable conditions. They either arise if the forces between unlike monomers are attractive or, generally, if the molar masses are sufficiently low. Block copolymers behave similarly and can also have a homogeneous phase. For a symmetric mixture ($N_A = N_B$) the two-phase region begins at $(\chi N_A)_c = 2$ [SG97], whereas for the case of a symmetric diblock copolymer, the transition between the homogeneous phase and the microphase-separated state takes place at a higher χ, namely for $(\chi N_A)_c \approx 10.5$. Moreover, different from the phase diagram of the binary mixtures [SG97], a schematic phase diagram of the block copolymer (figure 2.1) contains variables like volume fraction of the A-blocks ($f_A = N_A/(N_A + N_B)$), and the product χN_{AB}, where N_{AB} describes the total degree of polymerization ($N_{AB} = N_A + N_B$). Another difference from the binodal phase diagram is that in a binary blend there

are two components but in a diblock copolymer there is only one component. Therefore, the line corresponds to the phase transition between two microphases and contains no information about the internal compositions. The transition from a homogeneous melt to a heterogeneous melt of ordered microphase-separated domains is called *order-disorder transition* (ODT). It occurs at a critical value of $(\chi N)_c$. In case of a symmetric monodisperse diblock copolymer, the ODT occurs at $(\chi N)_c \approx 10.5$.

2.1.2 Surface Induced Ordering

When a block copolymer melt is placed between one solid wall and one free interface, like a thin film on top of a solid substrate, preferential block segregation occurs at both interfaces. It was reported that surface fields (propagating from both air and substrate interfaces) induce ordering at the surface, even above the *order-disorder transition* [ASH89, MA92]. Therefore, this films can show phase-separated microdomain structures right after the preparation without any further equilibrating (annealing) process [MBP05]. However, this effect become less significant as the film thickness increases, as anticipated as the bulk phase behaviour becomes dominant. This is due to that the entropy of the chain conformation at the interfaces and preferential affinity of the different blocks in the copolymer melt towards the interfaces determine the internal and external morphology of the thin film. As a result, the thickness of the film is strongly influencing the film morphology [MTL97, FMJ00].

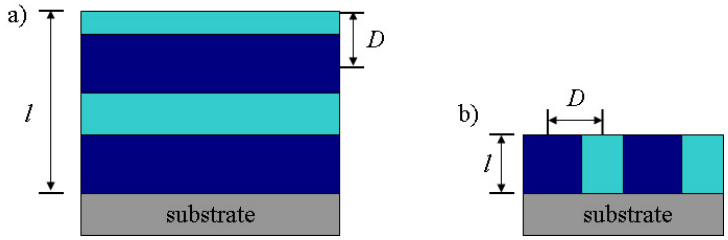

Figure 2.2: Schematic drawing of a section view of a block copolymer thin film on top of a solid substrate having surface induced lamellar structures: (a) parallel lamellar structures formation at $l > D$; (b) perpendicular lamellar structures formation at $l \approx D$.

In general, the surface induced ordering is analogous to that in lamellar phases [KA02, HHP00, KH-C01]. As shown in figure 2.2a, parallel morphologies are prominent in case of preferential affinity of one block toward the substrate surface when the equilibrium bulk period fullfills $l > D$, where l is the film thickness and D is the bulk period. Holes and

islands formation depends additionally on the wetting properties of both blocks. If the major component wets the surface, islands and holes can form, and if the minor component wets the interfaces, a flat surface can form [SN95]. With decreasing film thickness the confinement gives rise to an interplay between the intrinsic length scales of the bulk structures, i.e., the bulk period D and the geometry of the film. At $l \approx D$, as shown in figure 2.2b, perpendicular orientation of the microdomains with respect to the substrate surface is predicted theoretically [HHP00] and observed experimentally [MTL97, KA02, MBP05]. When the substrate surface is neutral to both blocks perpendicular orientation of cylinders occurs at all thicknesses [HHP00]. A transition from cylindrical morphology to non-cylindrical morphology can also occur if the film thickness is $l \ll D$ and surface prefers one block strongly. This polymer-surface interaction increases the total area of contact with substrate surface of one block, which yields a cylinder to lamellae or cylinder to cartenoid lamellae transition [HHP00, KA02].

2.1.3 Dewetting of Polymer Thin Films

A homogeneous film of polymer may be prepared from a solution on a non-wetting surface with spin-coating. Such films are metastable. The thermodynamic stability may be disturbed and the homogeneous film ruptures, holes grow laterally and build a cellular pattern, which breaks again until a stable droplet formation is reached [MBP98, MBP99, MBP02]. This phenomenon of film rupture is called dewetting. Wetting is a phenomenon refering to the spontaneous spreading of a liquid on a solid or liquid surface to form a homogeneous film. Dewetting of a film means the spontaneous withdrawal of liquid film from its hostile surface. The parameter that distinguishes wetting and dewetting probability of a liquid on a surface is called spreading coefficient S. S is given by

$$S = \gamma_{sv} - (\gamma_{lv} - \gamma_{ls}) \tag{2.1}$$

where γ_{sv} is the sum of the interfacial energy of the substrate, γ_{ls} is the sum of the interfacial energy between the substrate and the liquid and γ_{lv} is the interfacial energy of the liquid-vapor interface. Therefore, S is a measure of the free-energy change associated with the spreading of a macroscopically thick liquid (polymer solution) on a surface in the presence of vapor environment. In thick films, when $S > 0$, the spreading of the liquid (polymer solution) and if $S < 0$, dewetting occurs. If the film thickness is thin or ultra-thin (nanometers or tens of nanometers), the destability of the film or dewetting

is strongly inuenced by the long-range intermolecular van der Waals forces. A typical dewetted structure of polymer film on silicon wafer is shown in figure 2.3. The polymer is polystyrene and two different nonwetting surfaces (type A and type B) are applied [RG92]. Figure 2.3a shows a droplet-like structure and figure 2.3b shows a polygon-like structure due to the different nonwetting surfaces. The detail of the theory and experiments of polymer film dewetting can be found elsewhere [BWF92].

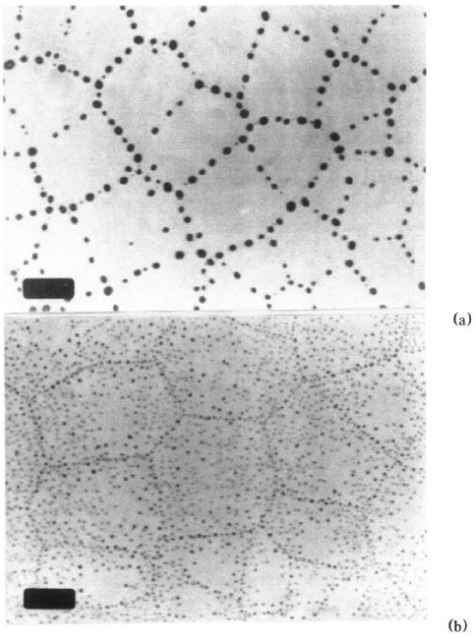

Figure 2.3: Micrographs of the final stage of dewetting of 45-nm-thick polystyrene films on silicon wafers of (a) type A and (b) type B. The length of the bar is 100 μm. The images are taken from [RG92].

2.1.4 Metal Deposition on Polymer Thin Films

Sputtering is one of the promising methods used for deposition of metals on polymer thin films. It was known that polymers and metals are very dissimilar materials, and that interaction between these materials is weak. Metals, especially noble ones, do not wet polymer surfaces but form 3D clusters on untreated polymer surfaces. As shown in figure 2.4, after the noble metal atoms adsorb on the polymer they will remain and diffuse on the polymer surface for a certain time, and then desorbs into the vacuum or will be trapped somewhere on or beneath the polymer surface. Only metal atoms remaining on the film surface contribute to the condensation coefficient. The condensation coefficient, C, is defined as the ratio of the number of adsorbed metal atoms to the total number of metal atoms arriving at the surface. Metal nucleation is a preferred process, when

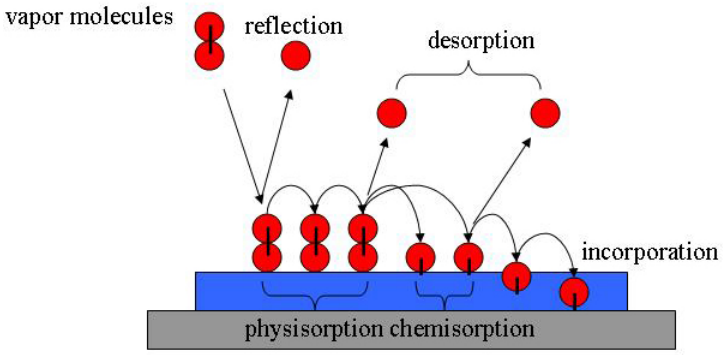

Figure 2.4: Schematic drawing of metal adsorption on polymer film by sputtering.

metal atoms are trapped at some defect sites, and random nucleation where nuclei are formed by metal atom encounters. The probability to find a preferred site is related to the density of these sites (impurities, terminal groups, etc.), the mean distance between these sites and the diffusion length of the adatoms on the polymer surface. Due to dissimilar nature of polymer and metal, sticking coefficient of simultaneously arriving metal atoms become quite low. However, such metal sticking coefficient could be enhanced by applying higher metal deposition rates. This would enable the formed clusters to act as trapping centers to attract other arriving atoms and eventually metal sticking coefficient could be increased. The details of the theory and experiments of metal deposition on polymer thin film can be found elsewhere [HA03, KG09].

2.2 PNIPAM Based Hydrogels

2.2.1 Introduction

Hydrogels are water-based cross-linked polymer networks that can incorporate large amounts of water but do not dissolve in water [HAS02, DJL03, DD91, DD99]. Depending on the type of cross-links, physical and chemical gels are distinguished. Physical gels are held together by polymer chain entanglement and/or by attractive forces present between the network polymers [HAS02, DD91, AK00], whereas in chemical gels the polymers are covalently cross-linked [HAS02, AK00]. In the case of physical gels, attractive forces can be due to a variety of interactions, typically electrostatic or hydrophobic in nature. Environmentally stable physical gel networks are synthesized by mixing appropriate polymeric components together in the proper ratio. Although these networks have structural integrity they can be easily dissolved by exposure to chemical species, i.e. organic sol-

vent, acid/base or salt, that weaken the interactions between the polymers holding the network together. In contrast to physical gels, chemical gels contain a network structure which is inherently more stable than physical gels under a variety of conditions and is for all purposes a permanent structure. Both gels have found numerous uses such as contact lenses [MTT00, OA04], membranes [OAA97], and drug delivery platforms [HAS02, KA02, KSW92, QY01].

Hydrogels, whether stabilized by physical or chemical interactions, can be classified as responsive or non-responsive. Non-responsive hydrogels are water swollen materials that are able to retain their integrity upon exposure to various stimuli unless a stimulus is able to completely break up the polymeric network [HAS02, DJL03]. Responsive hydrogels are a more interesting class of material, which can be designed to expand and contract in response to various external stimuli such as temperature, pH, liquid composition, and electric stimulation [TT78, TT82]. In general, the responsivity of a hydrogel arises from competing solvation mechanisms, where under one condition the network polymer chains are fully solvent swollen but upon introduction of an external stimulus the favorable polymer-solvent interactions are disrupted and polymer-polymer interactions begin to dominate, causing the polymer network to aggregate and deswell therefore expelling its entrained solvent [WC95, WC97, WC98a, WC98b]. In all classes of responsive hydrogels, thermoresponsive aqueous polymer systems, which are known to exhibit large, reversible conformational changes in response to small thermal stimuli, attract increasing attentation due to its widely applications in actuators [OY87, SS96], artificial muscles [OY93, LZ00], solute separators [FH91, PYS98], drug delivery systems [RKVR88, BCS96, SPS95, GP02], thermoresponsive surfaces [KA04, LL00, KD07], light modulation systems [AR02, ASA00], optical switching devices [MS07], and molecular recognition agents [KR04, MT02].

Poly(*N*-isopropylacrylamide) (PNIPAM) is probably among the most studied thermosensitive polymers because it exhibits a phase transition at a *lower critical solution temperature* (LCST) around 32 °C [WFM90, SHG92, TKC93, TEI94]. This temperature is slightly less than body temperature, which makes PNIPAM a representative of environmental-sensitive polymers studied for biomedical applications [HDL03]. However, compared to the large body of work on water-based PNIPAM solutions, thin PNIPAM films are less frequently investigated. Thus, PNIPAM based hydrogel thin films are especially interesting. For all investigations presented in this dissertation responsive, physical crosslinked

hydrogel thin films mainly composed of *N*-isopropylacrylamide (NIPAM) were used. The chemical structure of PNIPAM can be seen in figure 2.5.

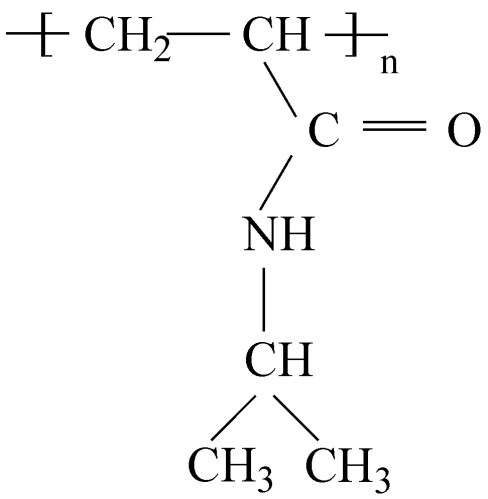

Figure 2.5: The chemical structure for poly(*N*-isopropylacrylamide) (PNIPAM).

2.2.2 Basic Characteristics

As stated above, hydrogels are crosslinked (whether physically or chemically), polymeric materials that are highly water swollen. PNIPAM is one of the intensively studied thermoresponsive hydrogels. The linear and network structures of PNIPAM possesses the ability to respond to changes in temperature by undergoing reversible swelling/deswelling transitions. This temperature-driven change in the conformation of single PNIPAM chains and the macroscopic phase seperation reflect rather subtle changes in polymer/water interactions, primarily the release of water molecules from a polymer hydration layer into bulk water. Several models have been described to account for the coil-to-globule collapse of PNIPAM in water and the complex water/PNIPAM phase diagram [MA91, WC95, OY05]. At low temperatures, intermolecular hydrogen bonds between water and polar groups of PNIPAM solubilize the polymer. Above LCST the hydrogen bonds break, and hydrophobic associations between the collapsed polymer chains take place.

2.2.3 Volume Phase Transition

Numerous experimental and theoretical studies [TLD75, TT78, TT80, HY84, WC95] have examined polymer gels exhibiting temperature-induced volume-change transitions.

Tanaka [TT78] stated that the collapse of gels upon changing temperature can be explained in terms of mean-field theory based on the extention of Flory´s formula for the free energy of gels. The theory predicts the existence of a critical endpoint when the segment length of the polymer is a certain value. Kutoba et al. [KK90] first seriously studied the coil-to-globule transition of a single PNIPAM chain in water. Later on, Grosberg et al. [GAY93] predicted a two-stage kinetics of a single-chain collapse process, namely, a fast crumpling process of unknotted polymer chain followed by a slow knotting process of the collapsed polymer chain. Wu and Zhou [WC95] suggested that there are four-stage coil-to-globule transition process for a single PNIPAM chain in water: (1) the chain contracting; (2) the chain crumping; (3) the chain knotting or rearranging; and (4) the chain collapsing into a compact globule with a uniform density.

Recently, Okada and Tanaka [OY05] explained the phase diagram of PNIPAM: In gen-

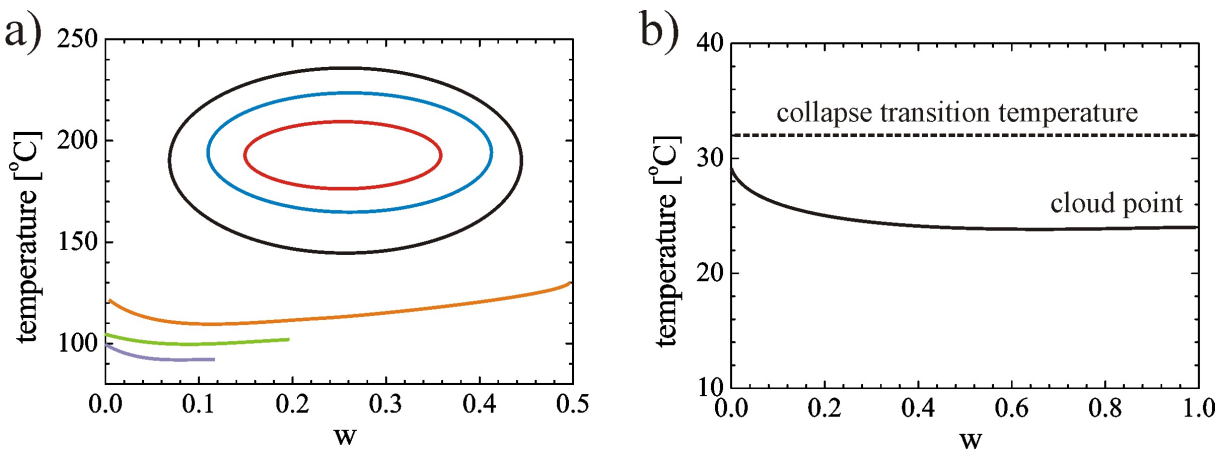

Figure 2.6: Schematic drawing of phase diagrams of PEO and PNIPAM. w is the weight fraction of polymer in water. (a) Phase diagram of PEO taken from [KR81]: red line, $M = 2.18 \times 10^3$ kg/mol; blue line, $M = 2.27 \times 10^3$ kg/mol; black line, $M = 2.29 \times 10^3$ kg/mol; orange line, $M = 8 \times 10^3$ kg/mol; green line, $M = 14.4 \times 10^3$ kg/mol; violet line, $M = 1020 \times 10^3$ kg/mol; (b) Phase diagram of PNIPAM taken from [KT08]: It schematically shows collapse transition temperature (broken line), cloud-point line (solid line).

eral, phase diagrams of water-soluble polymers often exhibit peculiar phase separation. For instance, aqueous poly(ethylene oxide) (referred to as PEO) solutions show closed-loop phase separation region (miscibility loop) at intermediate temperatures as shown in figure 2.6a [MGN53, SS76]. The phase boundary is highly sensitive to the molecular weight of polymers and also to the external pressure. The miscibility loop expands with the polymer molecular weight, and its LCST approaches an inverted *theta temperature* in the limit of infinite molecular weight [SS76]. *Theta temperature* is the temperature at

which the coiled polymer molecules in the dilute solutions expand to their full contour lengths and become rod-shaped. Also known as *flory temperature*. These peculiar phase behavior was first theoretically shown to be caused by the hydrogen bonding between ether groups [MA90]. Later, it was shown by molecular dynamics simulation [TK96] that a PEO chain takes a loose helical conformation in aqueous solution, whose pitch ($\cong$1.7 nm) just fits the size of a water molecule for adsorption by hydrogen bonds through the two hydrogen atoms on a water molecule. There is a competition in forming polymer-water hydrogen bonds and water-water hydrogen bonds. The hydrogen-bond networks in water are, however, not so strong in the temperature region of loop-shaped phase separation that indirect interaction between the neighboring water molecules on a chain via water hydrogen-bond network is expected to be weak. The water molecules are therefore randomly and independently adsorbed into the pockets of the helices.

In contrast to PEO, other water-soluble polymers such as PNIPAM show very flat LCST behavior whose cloud-point lines and spinodal lines are horizontal up to 20 wt% of polymer concentration as shown in figure 2.6b and almost independent of the molecular weight [HM68, FS89]. Here, a concept of 'cloud-point' and 'spinodal' is applied: When a temperature is near to the 'cloud-point', the unmixing starts and the nucleation and growth occurs, where the system is still stable with regard to small concentration fluctuations. Further away from the 'cloud-point' this restricted 'metastability' gets lost and spinodal decomposition sets in, which causes a stable two-phase region. The spinodal decomposition in the present case is named as the collapse transition temperature in figure 2.6b. The phase separation region takes a shape like the bottom part of a square, in what follows called as the miscibility square. Obviously, the miscibility square cannot be explained by random adsorption of water molecules onto a polymer chain. However, by introducing positive correlation between the neighboring hydrogen bonds along the polymer chain, i.e., if adsorption of a water molecule onto a site next to the already adsorbed one is preferential, phase separation may take place in a narrow temperature region. For PNIPAM, it is the case because the hydrogen-bonding site (amido group) is blocked by a large hydrophobic group (isopropyl group). The well-solvated random coil parts sharply turn into collapsed globules on approaching the phase separation temperature [FS89], so that hydrogen bonding is easier at the boundary between an absorbed water sequence and a collapsed coil. Such a steric hindrance by hydrophobic isopropyl side groups is the main origin of the strong correlation between the neighboring water molecules. This formation of sequential hydrogen bonds along the polymer chain, or cooperative hydration, in fact

leads to the miscibility square behavior of aqueous polymer solutions by the so-called domino effect.

2.2.4 Influence of Hydrophobic Groups

Slight changes in the chemical composition of PNIPAM have important consequences on the water/PNIPAM phase diagram. The LCST of PNIPAM can be raised or lowered via introduction of hydrophilic or hydrophobic comonomers, respectively [TLD75]. The hydrophobic groups drive the self-assembly of the polymers, leading to the formation of polymeric micelles that exist as isolated entities in dilute cold aqueous solutions. Upon heating, dehydration of the PNIPAM chains triggers changes in the size and shape of the micelles, often leading to macroscopic aggregation. In figure 2.7, an example of the LCST dependent on the level of hydrophobe incorporation is shown. The polymer is poly(styrene-*block*-*N*-isopropylacrylamide), denoted P(S-*b*-NIPAM). With increasing weight percentage of PS, the LCST is shifted to a lower temperature and the transition is significantly broadened.

Moreover, the phase transition temperature depends not only on the level of hydrophobe incorporation and on its chemical structure but also on its position on the chain [KP01, CZ05]. This effect can be traced to differences in the structure of the micelles formed by the various hydrophobically modified (HM) PNIPAMs in cold water. Randomly modified HM-PNIPAMs adopt a loose micellar conformation in which the hydrophobic groups are partly exposed to water; the cloud point of their solutions is depressed significantly compared to that of PNIPAM solutions [KP01]. As shown in figure 2.8, polymers which carry a hydrophobic group at one chain end tend to form core-shell structures in which the hydrophobic core is insulated from the water by a brushlike corona of PNIPAM chains [CJE97, WFM92]; PNIPAM carrying a hydrophobic group at each chain end form another type of micelle in water-based solution: the micelles are described as flowerlike associates consisting of loops of hydrated polymer chains having both end groups entrapped in the micellar core [AV]. In general, the introduction of hydrophobic end groups affects the phase behavior of PNIPAM solutions 2-fold: The miscibility of the polymer in water becomes poorer as a result of direct interactions between water and the hydrophobic end groups. In addition, the mixing entropy of the polymer chains is reduced due to the increase of their apparent molecular weight via micelle formation. Both factors favor phase separation, and the LCST tends to decrease. However, association of the end chains does

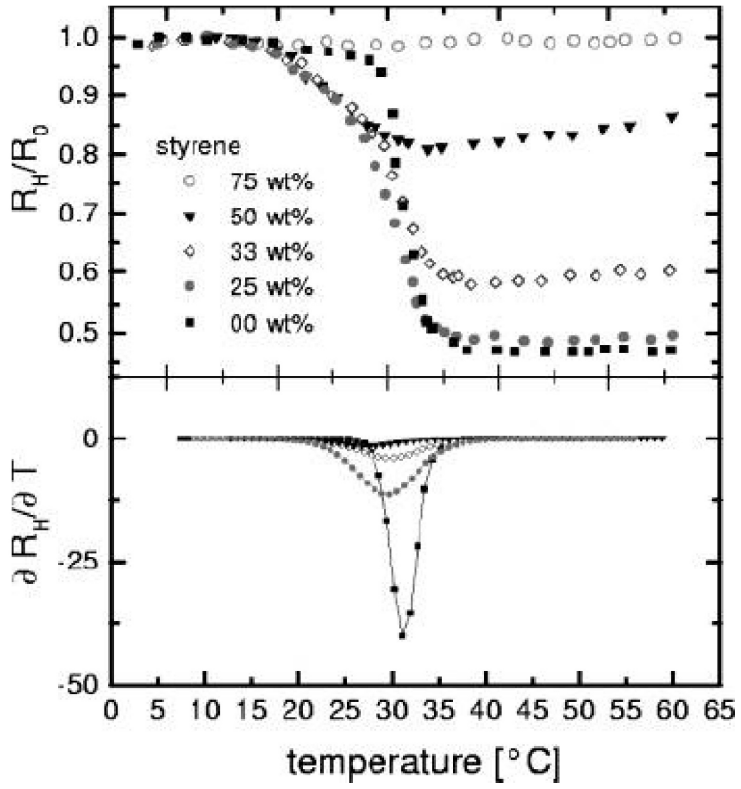

Figure 2.7: Swelling curves of microgels with different styrene to NIPAM ratio. Increasing the styrene content leads to a decrease in swelling capacity and to a lower transition temperature. R_H is the hydrodynamic radius of microgel particles at different temperatures, and R_0 is the maximum hydrodynamic radius. The image is taken from [HT04].

not affect the hydration of the main chains, except for segments near the micellar core, because they remain exposed to water even when association takes place. Therefore, the telechelic PNIPAM/water system is an interesting example of the coexistence, without competition, of two phenomena: end-chain association and hydration [KP06]. With increasing molecular weight the effect of end groups of PNIPAM homopolymers decreases [FS06]. Such a miscibility improvement or shrinkage of the phase-separated region is a natural tendency, since for a fixed polymer concentration, the concentration of hydrophobic groups becomes smaller with increasing molecular weight.

However, Kujawa et al. [KP06] stated, for a given polymer sample, the cloud point temperature, T_{cp}, detected by light scattering, differs significantly from T_M, the temperature corresponding to the maximum of the endotherm measured by microcalorimetry. It was observed [KP06] that end-chain association does not affect the coil-to-globule transition to the same extent as the cloud point because release of the bound water molecules upon

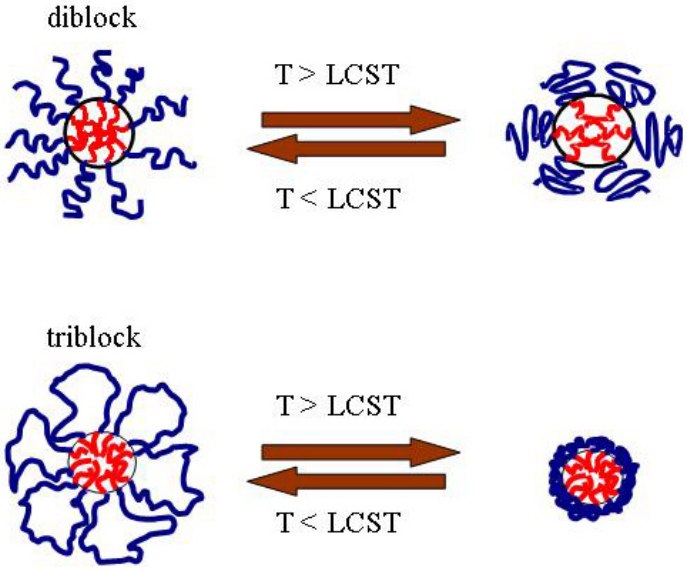

Figure 2.8: Schematic drawing of structures of diblock copolymer P(S-*b*-NIPAM) and triblock copolymer P(S-*b*-NIPAM-*b*-S) below and above the LCST in water taken from [AJ09].

heating takes place independently of association, in the ideal limit. Therefore, T_M is expected to remain independent of polymer molecular weight. Since the sharp chain collapse seen in dilute aqueous PNIPAM solutions is mainly due to a cooperative dehydration [OY05], i.e., bound waters are dissociated into the bulk not independently but in groups, the molecular-weight dependence of T_M is also expected to be weak. It was reported that [KP06] the enthalpy of the transition increases with increasing molar mass of telechelic HM-PNIPAM and is independent of solution concentration. It is lower than the value registered for the phase separation of PNIPAM under the same conditions [KP01]. The heat evolved upon phase separation is attributed to the release of water molecules bound to the polymer chain into bulk water. As the heat evolved during the phase transition of telechelic HM-PNIPAMs is smaller compared to PNIPAM, one has to conclude that fewer water/polymer H-bonds are broken, per NIPAM unit, during their heat-induced phase transition. This tendency may be taken as an indication that near the core of the micelles the PNIPAM chains are crowded to such an extent that the monomer density is sufficiently high to prevent formation of water/polymer hydrogen bonds. The temperature of the transition is not expected to change much as a result of the presence of such regions inaccessible to water molecules, given that T_M depends only weakly upon the polymer molecular weight.

In summary, linking hydrophobic termini to a hydrophilic polymer chain results in a decrease of the cloud point temperature of this polymer. The cloud point depression is a direct consequence of the association of telechelic polymers into micelles and networks, which leads to an effective molecular weight higher than that of the corresponding PNIPAM homopolymer. Thus, the mixing entropy of telechelic polymers is lower than that of the homopolymer, and they tend to demix. However, The T_M value is almost the same for all polymers, independently of their molecular weight, and it is always higher than T_{cp}.

2.2.5 Swelling and Shrinking Kinetics

The swelling phenomena of hydrogels and its kinetics have been long investigated. Tanaka, Hocker, and Benedel (THB) derived an equation of motion of the fiber network in a gel in order to establish a theory on the light scattering from a viscoelastic gel [TT73]. Tanaka and Fillmore (TF) applied the THB equation of motion to the swelling kinetics of a spherical polyacrylamide gel [TT79], wherein the shear modulus was considered to be negligible in comparison with the osmotic compressive modulus. Their calculation predicted that the relaxation time τ is proportional to the gel linear size squared. This power law relation has been confirmed experimentally [TT79, TT85] with the power in the range 1.75-2. In the case of a spherical gel, the THB equation of motion is reduced to the form [TT73, LLD86]

$$\frac{\partial \mathbf{u}}{\partial t} = D\frac{\partial}{\partial r}\left[\frac{1}{r^2}\frac{\partial}{\partial r}(r^2 u)\right] \tag{2.2}$$

where $\boldsymbol{u}$=$\boldsymbol{u}(r,t)$ is the displacement vector of the network at time t of a point in the gel from its final location r when swelling reaches the equilibrium; D is defined by

$$D = (K + 4\mu/3)/f \tag{2.3}$$

where K and μ are the bulk and shear modulus of the polymer network alone, respectively, and f is the friction coefficient between the network and fluid medium. TF theory solved the THB equation with the following three assumptions: i) the initial condition that before the gel is transferred into the fluid the network is under uniform radial stress π_0, where π_0 is interpreted as the osmotic pressure of the gel by TF; ii) the boundary condition that the stress vanishes at the surface of the gel; and iii) the modulus μ may be neglected compared with K since μ is, through experiment, found to be smaller than K by a factor

of 40. The solution obtained by TF is expressed by

$$u = -6\Delta \sum_{n=1}^{\infty} \frac{(-1)^n}{n\pi} \left[\frac{X_n \cos X_n - \sin X_n}{X_n^2} \right] \exp(-\frac{n^2 t}{\tau}) \tag{2.4}$$

where $X_n \equiv n\pi(r/R_\infty)$, R_∞ is the radius of the fully swollen gel;

$$\tau \equiv (R_\infty/\pi)^2/D,\ \Delta \equiv \pi_0 R_\infty/3K \tag{2.5}$$

The last quantity Δ is the total increase in the radius of the gel in the entire process of swelling. The radius, $R(t)$ of the gel at any time t is given by

$$R(t) = R_\infty - \frac{6\Delta}{\pi^2} \sum_{n=1}^{\infty} \frac{1}{n^2} \exp(-\frac{n^2 t}{\tau}) \tag{2.6}$$

By including a non-negligible shear modulus, Peters and Candau [PA88] developed a general model to characterize the swelling kinetics of spherical, cylindrical, and disklike polymer gels. Later, Li and Tanaka [LY90] proposed a two-process mechanism after realizing that neither gel swelling nor shrinking can be considered to be a pure diffusion process. They think that the TF kinetics theory is insufficient for nonspherical gels. This insufficiency is due to the existence of the shear modulus of the network. The nature of the shear modulus is to keep the system in shape, i.e., minimize the nonisotropic deformation. Since during a shear relaxation process there is no friction between gel network and solvent, the system can instantly adjust its shape to minimize the total shear energy.

In general, the total energy of a gel can be separated into a bulk energy and a shear energy [LLD86]. The bulk energy of the system is related to the volume change, which is controlled by diffusion. The shear energy, on the other hand, can be minimized instantly by readjusting the shape of the gel. The shear energy of a gel of arbitrary shape is [LLD86]

$$F_{sh} = \mu \int_v \left[\left(u_{xx} - \frac{T}{3} \right)^2 + \left(u_{yy} - \frac{T}{3} \right)^2 + \left(u_{zz} - \frac{T}{3} \right)^2 \right] dV \tag{2.7}$$

where $T=(u_{xx}+u_{yy}+u_{zz})$ is the trace of the strain tensor u_{ik}. Without losing any generality, the coordinate system is chosen to be the one in which u_{ik} is diagonalized. At any instance, this energy is minimized. As long as the shear modulus μ is not zero, the change of the total shear energy in response to any small change in shape that maintains constant volume element within the gel should be zero,

$$\delta F_{sh} = 0 \tag{2.8}$$

This equation plus the TF diffusion equation should be able to determine the kinetics of the gel swelling and shrinking processes. Every tiny diffusion process determined by TF equation should be coupled to (or corrected by) a small shear process governed by eq. 2.8.

For the case of disklike gels, Li and Tanaka predicted that the shear modulus μ is related to the net osmotic modulus (M_{os}) and the osmotic bulk modulus K by [LY90]

$$R = \frac{\mu}{M_{os}} = \frac{\mu}{K + \frac{4}{3}\mu} \tag{2.9}$$

According to Li and Tanaka, the swelling or shrinking follows

$$\frac{W_\infty - W}{W_\infty} = \sum_{n=1}^{\infty} B_n \exp(-t/\tau_n) \tag{2.10}$$

where W and W_∞ are the solvent uptake at time t and infinit time (i.e., at equilibrium), respectively; $[(W_\infty\text{-}W)/W_\infty]$, the relative swelling capacity at time t; B_n, a function of R; and τ_n, the relaxation time related to the n-th mode. When $t \gg 1$ or $\tau_1 \gg \tau_n$ ($n \geq 2$) or $B_1 \gg B_n$ ($n \geq 2$), all high-order terms ($n \geq 2$) in eq 2.10 can be dropped. In this case, the swelling and shrinking follows a first-order kinetics, i.e.,

$$\ln\left(\frac{W_\infty - W}{W_\infty}\right) = \ln B_1 - t/\tau_1 \tag{2.11}$$

where B_1 is related to R by

$$B_1 = \frac{2(3-4R)}{\alpha_1^2 - (4R-1)(3-4R)} \tag{2.12}$$

and τ_1 is related to the collective diffusion coefficient D_c by

$$D_c = \frac{3Z_\infty^2}{\tau_1 \alpha_1^2} \tag{2.13}$$

with α_1 being a function of R, i.e.,

$$R = \frac{1}{4}\left[1 + \frac{\alpha_1 J_0(\alpha_1)}{J_1(\alpha_1)}\right] \tag{2.14}$$

and Z_∞ being the disk thickness in the final swelling equilibrium state, where J_0 and J_1 are the zeroth- and first-order Bessel functions. The t-dependence of $[(W_\infty\text{-}W)/W_\infty]$ can lead first to B_1 and τ_1, and then to R and D_c on the basis of eqs 2.11-2.14. The theoretical relation within B_n, τ_1 and R for sphere-like, cylinder-like and disk-like gels can be found in figure 2.9.

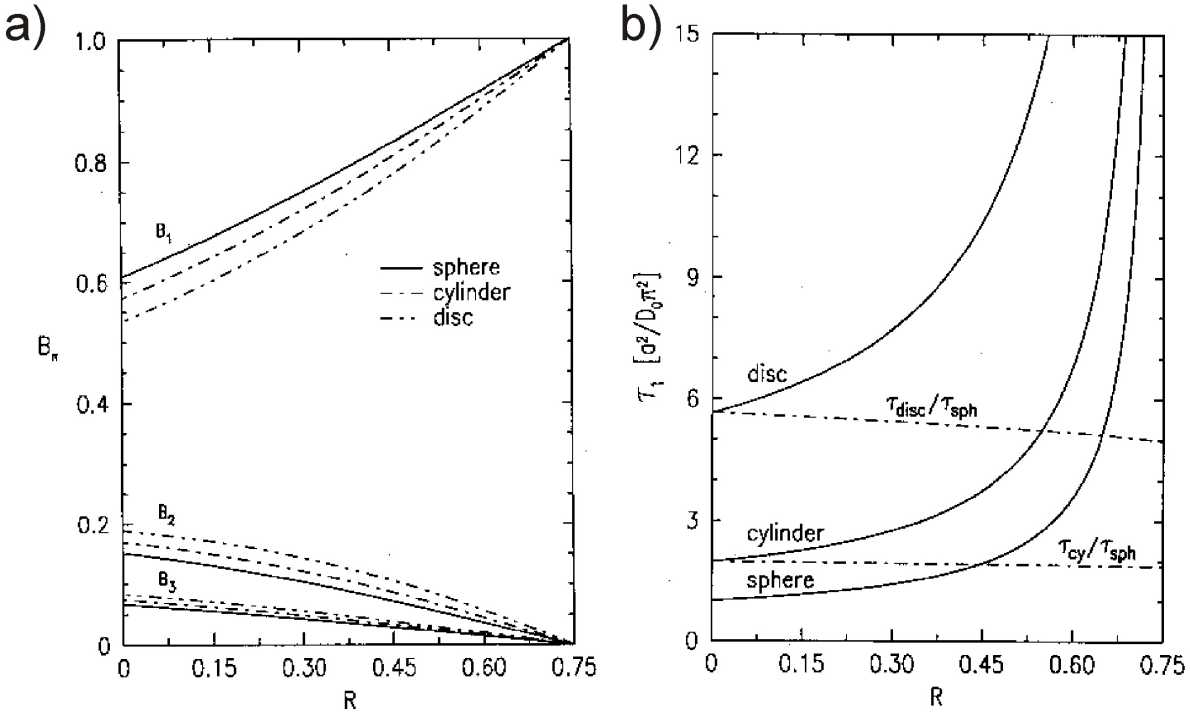

Figure 2.9: (a) Theoretically predicted first three coefficients B_n as a function of R. (b) theoretical calculation of the dependence of the relaxtion time τ_1 for spherical, long cylinderical, and disk gel on R. The images are taken from [LY90].

2.3 X-ray Scattering

The structures in the polymer film and on the polymer surface were investigated by X-ray scattering technique in reflection geometry. The specular and off-specular scattering of X-rays provide the lateral and vertical nanostructure length scales and their spatial distribution. In this section the X-ray scattering process is explained following the textbook as *X-ray Scattering from Soft-Matter Thin Films* [TM99].

2.3.1 Basic Principle

Figure 2.10 shows schematically the scattering process in the plane perpendicular to the sample surface. An X-ray beam with incident wave vector $\mathbf{k}_i$ impinges a film surface and is scattered. X-rays can be understood as electromagnetic plane waves and are expressed by its electric field vector

$$\mathbf{E}(\mathbf{r}) = \mathbf{E}_0 \exp(i\mathbf{k}_i \cdot \mathbf{r}) \tag{2.15}$$

If the scattered wave is the same as the incident wave and no energy is transferred in the scattering process, it is called *elastic scattering*. The momentum transfer in the elastic

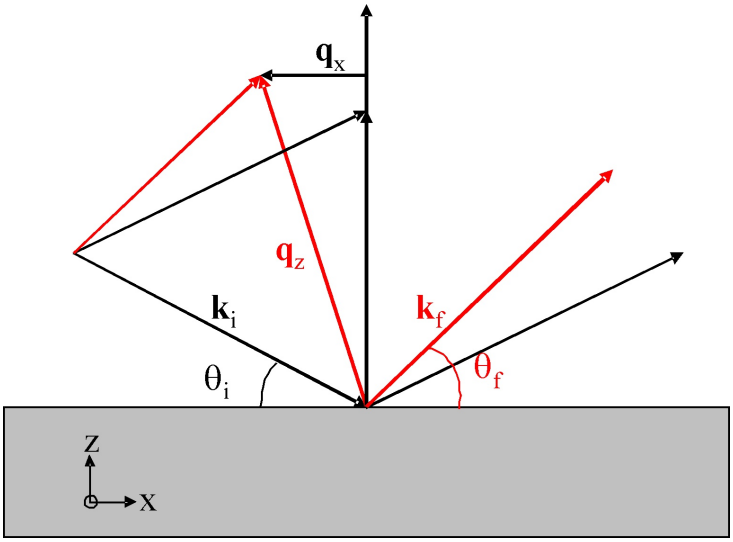

Figure 2.10: Basic Principle of X-ray off-specular scattering. An X-ray beam with incident wave vector $\boldsymbol{k}_i$ impinges a film surface at an incident angle θ_i. One part of the wave is scattered with wave vector $\boldsymbol{k}_f$ at the angle θ_f. The angles are measured towards the surface.

scattering event is given by

$$\begin{aligned} \mathbf{q}_z &= \mathbf{k}_f - \mathbf{k}_i \\ &= (2\pi/\lambda \sin\theta_f) + (2\pi/\lambda \sin\theta_i) \\ &= 2\pi/\lambda(\sin\theta_f + \sin\theta_i) \end{aligned} \tag{2.16}$$

for θ_f=θ_i

$$q_z = 4\pi/\lambda \sin\theta_i \tag{2.17}$$

$\boldsymbol{q}_z$ is the wave vector transfer or scattering vector perpendicular to the direction of the scattered wave given by the incoming and out going wave vector $\boldsymbol{k}_i$ and $\boldsymbol{k}_f$, respectively. The wave vector is given by the wave number $k = 2\pi/\lambda$ describing the wave propagating along $\mathbf{x}$ direction over 2π with wavelength λ. The incident wave is a sine wave given by the real form of electric field vector $\boldsymbol{E}$. For equivalence of the incoming and outgoing scattering angle $\theta_f = \theta_i$ the reflected beam from the surface is called *specular*, and its intensity *specular reflectivity*. If $\theta_f \neq \theta_i$ but still in the plane of incidence, the wave vector transfer is split into a component along $\mathbf{z}$ and along $\mathbf{x}$. The wave vector $\boldsymbol{k}_f$ then describes the scattered wave *off-specular in-plane* of the scattering plane, the plane perpendicular to the sample surface.

$$\begin{aligned} \mathbf{q}_x &= \mathbf{k}_f + \mathbf{k}_i \\ &= (2\pi/\lambda \cos\theta_f) - (2\pi/\lambda \cos\theta_i) \\ &= 2\pi/\lambda(\cos\theta_f - \cos\theta_i) \end{aligned} \tag{2.18}$$

for $\theta_f = \theta_i$, $q_x = 0$.

2.3.2 Refractive Index and Snell´s Law

If the material at which the wave is refracted is of the same optical density as the material of the incoming wave, the incoming and the refracted wave vector are equal, i.e. $\mathbf{k}_i = \mathbf{k}_f$. As shown in figure 2.11, when it is not the case, the refracted wave vector is different from the incoming wave vector by n, which is called *refractive index*.

$$\begin{aligned} n &= |\mathbf{k}_i/\mathbf{k}_r| \\ &= \frac{a_i k \cos\theta_i + a_f k \cos\theta_f}{a_r k \cos\theta_r} \\ &= \frac{(a_i + a_f) k \cos\theta_i}{a_r k \cos\theta_r} \end{aligned} \tag{2.19}$$

with the amplitude of the wave vector $a_i + a_f = a_r$

$$n = \frac{\cos\theta_i}{\cos\theta_r} \tag{2.20}$$

which is *Snell´s law*. Usually the refractive index is smaller than 1 as the phase velocity of a refracted beam in a medium is higher as in vacuum. Thus n can be expressed as deviation from 1

$$n = \frac{\cos\theta_i}{\cos\theta_r} = 1 - \delta + i\beta \tag{2.21}$$

with the dispersion term of δ and the absorption term of β.

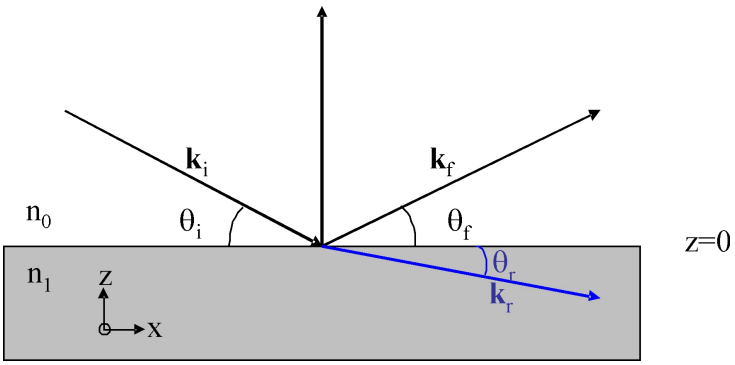

Figure 2.11: An X-ray beam with incident wave vector $\boldsymbol{k}_i$ impinges a film surface at an incident angle θ_i. One part of the wave is reflected with wave vector $\boldsymbol{k}_f$ at the angle θ_f and the other part is refracted with wave vector $\boldsymbol{k}_r$ at the angle θ_r. The angles are measured towards the surface.

If there is no refraction, i.e. $\theta_r = 0$, the remaining angle θ_i is the *critical angle of total reflection* θ_c.

$$\cos\theta_c = 1 - \delta \approx \sqrt{2\delta} \tag{2.22}$$

This critical angle θ_c is a material specific property according to the equation 2.22. When the incident angle $\theta_i \leq \theta_c$ the X-ray does not penetrate far into the medium. All incoming radiation is reflected with small loss due to absorption from the surface. This phenomenon is called *total external reflection.*

2.3.3 Reflectivity

The reflected intensity R is defined as the product of the amplitude reflectivity $\boldsymbol{r}$ with its conjugate complex $\cdot\mathbf{r}^*$ expressed by the ratio of incident and outgoing amplitude a_i/a_f

$$R = |a_i/a_f|^2 = \mathbf{r} \cdot \mathbf{r}^* \tag{2.23}$$

The incident, outgoing and refracted waves $E_i = a_i \exp(i\boldsymbol{k}_i \cdot \boldsymbol{r})$, $E_f = a_f \exp(i\boldsymbol{k}_f \cdot \boldsymbol{r})$ and $E_r = a_r \exp(i\boldsymbol{k}_r \cdot \boldsymbol{r})$ show for the amplitude at $z = 0$

$$\begin{aligned} a_i + a_f &= a_r \\ a_i \mathbf{k}_i + a_f \mathbf{k}_f &= a_r \mathbf{k}_r \end{aligned} \tag{2.24}$$

Thus the reflection and transmission coefficients at the surface $z = 0$ can be expressed as

$$r = \frac{a_f}{a_i} = \frac{k_i - k_r}{k_i + k_r} \tag{2.25}$$

and

$$t = \frac{a_r}{a_i} = \frac{2k_i}{k_i + k_r} \tag{2.26}$$

Equation 2.25 and 2.26 are applicable only for a single surface. Moreover, the practical field of application is mostly multilayers, either real separated layers or single layers having varying refractive index with thickness of the medium. For example, in microphase separated ordered block copolymer film, vertical or lateral layers of different refractive indexes are present. Therefore, one needs to take into account scattering from all interfaces. Let us consider a multilayer system containing N interfaces at the positions z_j as shown in figure 2.12. The amplitude of the transmitted and reflected waves are T_j and R_j, respectively and corresponding wave vectors are $k_{i,j}$ and $k_{f,j}$ inside the layer j. Considering the amplitude of the incident wave normalized to ($T_1 = 1$) and the tangential components of the electric and magnetic field vectors to be continuous at the interface one can express the ratio of the amplitude of the reflected wave and transmitted wave according to the recursive approach of *Parratt* [PLG54] as

$$X_j = \frac{R_j}{T_j} = e^{-2ik_j z_j} \frac{r_{j,j+1} + X_{j+1} e^{2ik_{j+1} z_j}}{1 + r_{j,j+1} X_{j+1} e^{2ik_{j+1} z_j}} \tag{2.27}$$

where

$$r_{j,j+1} = \frac{k_j - k_{j,j+1}}{k_j + k_{j,j+1}} \tag{2.28}$$

is the Fresnel coefficient of interface j with $k_j = k(n_j^2 - \cos^2\theta_i)^{1/2}$ being the z component of the wavevector in layer j. If the penetration depth of the X-rays is smaller than the thickness of the substrate then no reflection occurs from the substrate, i.e., $R_{N+1} \equiv T_{N+1} = 0$ can be set at the start of the recursion. The specularly reflected intensity R then can be obtained using the eq. 2.27 after N iterations:

$$R_{j+1} = \frac{1}{t_{j,j+1}} \{T_j r_{j+1,j} \exp[-i(k_{j+1} + k_j)z_j] + R_j \exp[-i(k_{j+1} - k_j)z_j]\} \tag{2.29}$$

$$T_{j+1} = \frac{1}{t_{j,j+1}} \{T_j \exp[i(k_{j+1} + k_j)z_j] + R_j r_{j+1,j} \exp[i(k_{j+1} + k_j)z_j]\} \tag{2.30}$$

with the Fresnel transmission coefficient $t_{j+1,j} = 1 + r_{j+1,j}$ of interface j. Equation 2.29 can be used to calculate the reflectivity from a multilayer system. The oscillations in the reflectivity profile result from the interference term in the above equation and depend on the thickness of the layer thickness regarding the position and the difference in scattering contrast between the respective interfaces. The oscillations are often called *Kiessig fringes*.

If the system has repeating subunits with equal distance d the reflected intensity superimposes giving rise to Bragg peaks in the reflectivity pattern which obey *Bragg´s law* $n\lambda = 2d\sin\theta$.

2.3.4 Roughness

The roughness of the surface and the interfaces are not considered in the calculation of reflectivity in the equation 2.29. So far, in the previous calculation only sharp interfaces are considered. However, an interface is usually not ideally sharp and the reflectivity is damped by diffuse scattering due to surface roughness expressed as

$$R(q) = R_f(q)e^{-q^2\sigma^2} \tag{2.31}$$

σ is a measure of the width of the interface roughness given as root mean square (rms) roughness. The damping of the diffuse scattering is the Fourier transform of the deviative of the error function

$$f(z) = erf\left(\frac{z}{\sqrt{2\sigma}}\right) \tag{2.32}$$

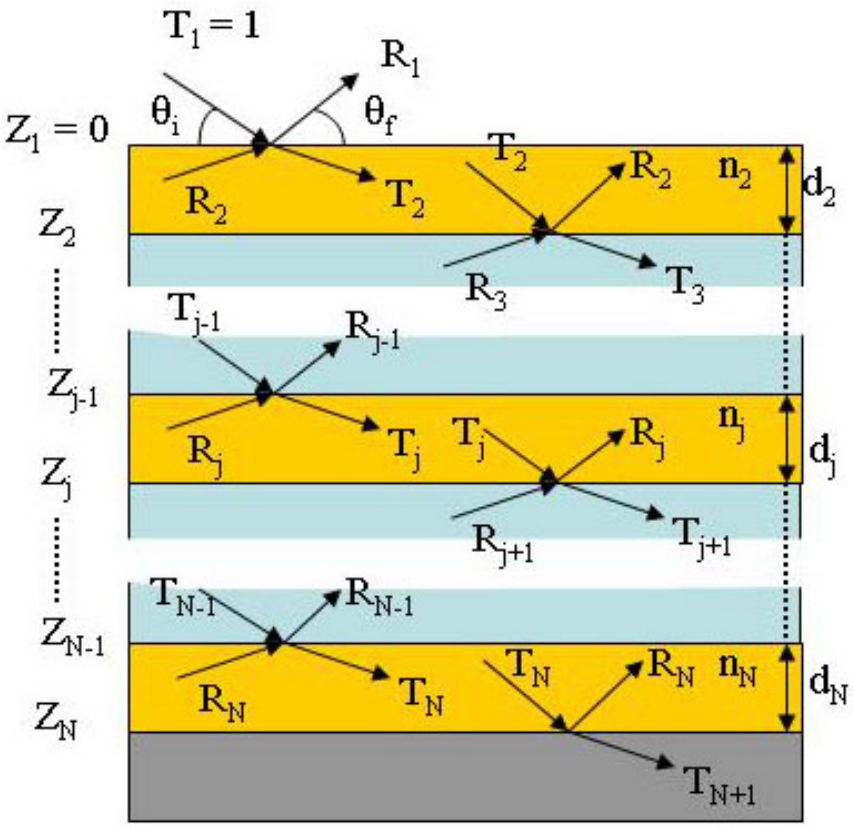

Figure 2.12: Schematically drawn scattering medium consisting of N layers with N interfaces present in between a substrate (layer $N+1$) and vacuum ($N = 0$). The incident angle θ_i is equal to the exit angle θ_f. The incident wave amplitude is normalized to unity.

which is a Gaussian. The error function describes the density distribution at the rough interface. Basically the ideally sharp density profile is convoluted with a Gaussian smoothing function or Debye-Waller factor. Such a rough interface exhibits no correlation between the heights at different points of the surface. The scattering of the uncorrelated surface is confined to the specular direction.

2.3.5 Grazing Incidence Small-angle X-ray Scattering

Grazing incidence small-angle X-ray scattering (GISAXS) is developed from small-angle X-ray scattering (SAXS). SAXS from particles can be used to determine the particle shape or their size distribution. This technique is suited for bulk materials. A small-angle scattering pattern can be fitted with intensities calculated from different model shapes when

the size distribution is known. If the shape is known, a size distribution may be fitted to the intensity. If the particles are dispersed in a solution and known to be monodisperse, all of the same size, then a typical strategy is to measure different concentrations of particles in the solution.

GISAXS is similar to SAXS using a reflection geometry but suited for thin films. In GISAXS, the beam does not transmit through the sample but impinges under a shallow angle ($< 1°$) and the reflected and scattered intensities are recorded with a 2d detector. Thus, big advantages of GISAXS over SAXS are the high sensitivity to the surface structures and the improvement of the resolution limit. Varying the distance between the sample and the detector, structures of 5 nm to 15 μm can be resolved by GISAXS. The scattering data are analyzed in a similar way as done with SAXS. The basic experimental set-up is shown schematically in figure 2.13.

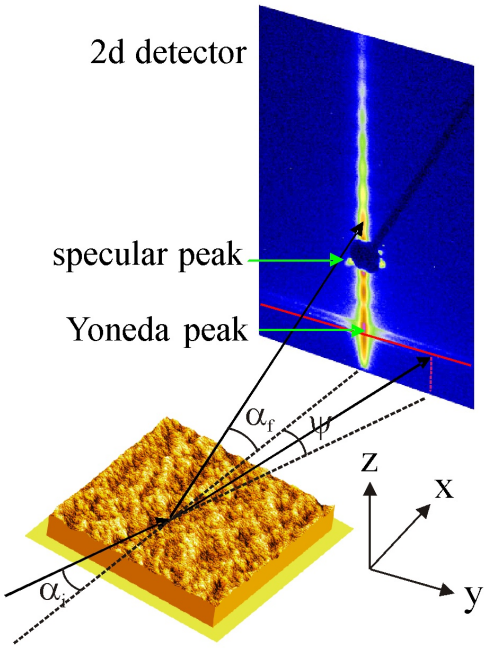

Figure 2.13: The basic experimental set-up of GISAXS. The sample is placed horizontally. The incident, exit and out-of-plane angles are denoted by α_i, α_f and ψ , respectively. The 2d detector represents the q_y-dependence along the horizontal axis and the q_z-dependence along the vertical axis. The scattered intensity distribution on the detector is presented in logarithmic scale. The scattering pattern shows the diffuse scattering with a splitted Yoneda and a specular peak (shielded by a beam-stop).

As shown in figure 2.13, the coordinate system is in a way that the sample surface is the

x, y-plane and the X-ray beam direction defines the x-direction. The z-axis is oriented perpendicular to the sample surface. The components of the scattering vector $\boldsymbol{q}$ are

$$\begin{aligned} q_x &= \frac{2\pi}{\lambda}(\cos\psi\cos\alpha_f - \cos\alpha_i) \\ q_y &= \frac{2\pi}{\lambda}(\sin\psi\cos\alpha_f) \\ q_z &= \frac{2\pi}{\lambda}(\sin\alpha_i + \sin\alpha_f) \end{aligned} \tag{2.33}$$

where α_i and α_f and the incident and exit angles of the X-ray beam in the scattering plane (by conversion). ψ is called out-of-plane angle. The scattering intensity at an out-of-plane angle $\psi \neq 0$ is denoted as out-of-plane scattering and probes the structures parallel to the sample surface. The reflected specular intensity is usually shielded to avoid the possible damage of the detector and to use the full available flux of the synchrotron beamline to record the intensities of the diffuse scattering, because the intensity of specular scattering is several orders of magnitude higher than that of the diffuse scattering. The characteristic diffuse scattering feature named Yoneda peak appears when the incident angle of the X-ray beam is equal to the critical angle of the material, $\alpha_i = \alpha_c$. If the incident angle α_i is larger than the critical angle α_c of the material, the beam penetrates the full depth of thin films. The interference of the scattering wave vectors from all interfaces gives rise to the *resonance diffuse scattering* (RDS). This resonance diffuse scattering appears in the scattering plane on the detector [DJ92, HV94]. The information of the interface correlations can be extracted from the modulations in between the Yoneda and the specular peak. The modulations that appear at an scattering angle $\alpha_f > \alpha_i$, can be compared with the modulation of the X-ray reflectivity measurements and used to determine the layer thicknesses in thin films. Due to the presence of average, lateral structural length correlations, side maxima of scattered intensities appear in the q_x, q_y-plane. Figure 2.14 shows the splitted Yoneda as two intensity side maxima. It was known that the structure factor $S(\mathbf{q})$ and the form factor $P(\mathbf{q})$ give rise to intensity maxima in the scattering pattern on a 2d detector [ST95]. The lateral and vertical structural information corresponding to these structure factors and form factors can be extracted by mainly two types of cuts from a 2d scattering intensity distribution data [MBP03a, MBP06, ST95, ST96]. The cuts parallel to the sample surface are called *horizontal cuts* or *out-of-plane cuts* and the cuts normal to the sample surface are called *vertical cuts* or *detector cuts*. Vertical cuts at position $q_y = 0$ and horizontal cuts at the critical angle α_c are the two most important cuts, which give information of lateral and vertical structures. Figure 2.14 shows these cuts in the usual types of presentation.

2.3.5.1 Out-of-Plane Cuts

As figure 2.14a pictures, out-of-plane cuts depend on the wave vector component q_y only. As a consequence only structures parallel to the sample surface are probed. To become more sensitive to one component of the film forming materials, the cuts are made at an exit angle equal to the critical angle of that component.

For better statistics the intensities are integrated usually over a few neighboring channels. Figure 2.14b shows the logarithmic intensity as a function of the corresponding out-of-plane angle ψ. The scattered intensity is symmetric with respect to the center. Figure 2.14c gives the common double logarithmic presentation in reciprocal space. The strong peak corresponds to a highly ordered surface structure as installed in thin P(S-*b*-NIPAM) diblock copolymer thin films. In the framework of the distorted-wave Born approximation (DWBA) the differential cross-section is given by [ST96]

$$\frac{d\sigma}{d\Omega} = \frac{\Pi\pi^2}{\lambda^4}(1-n^2)\left|T_i\right|^2\left|T_f\right|^2 F(\mathbf{q}) \propto F(\mathbf{q}) \tag{2.34}$$

where Π is the illuminated surface area, λ the wavelength used, n the refractive index, $T_{i,f}$, the Fresnel transmission functions, and $F(\mathbf{q})$ the diffuse scattering factor.

Because the incident and exit angle are fixed, the Fresnel transmission functions act only as overall scaling factors and the diffuse scattering factor is directly probed. The intensity is dominated by the Fourier transform of the height-height correlation function of one 'effective surface' [ST96]. In case either the incident or exit angle is equal to the critical angle of the material (e.g., PS), the transmission functions have a maximum, which is called Yoneda peak. Therefore out-of-plane cuts at these positions increase the scattering contribution of the material (e.g., PS). For N identical and centrosymmetrical objects with a random orientation, the diffuse scattering factor can be approximated by

$$I(\mathbf{q}) \propto NP(\mathbf{q})S(\mathbf{q}) \tag{2.35}$$

that is, to depend on the form factor of the individual objects $P(\boldsymbol{q})$ and the structure factor $S(\boldsymbol{q})$. In the case of highly monodisperse objects the form factor becomes visible. If the objects have a well-defined nearest neighbor distance, irrespective of the monodispersity of the individual objects, the structure factor directly yields the most prominent in-plane length ξ. Since the q_x component of the scattering wave vector is very small in the small-angle regime the real-space length scales of a structure factor type of information can be

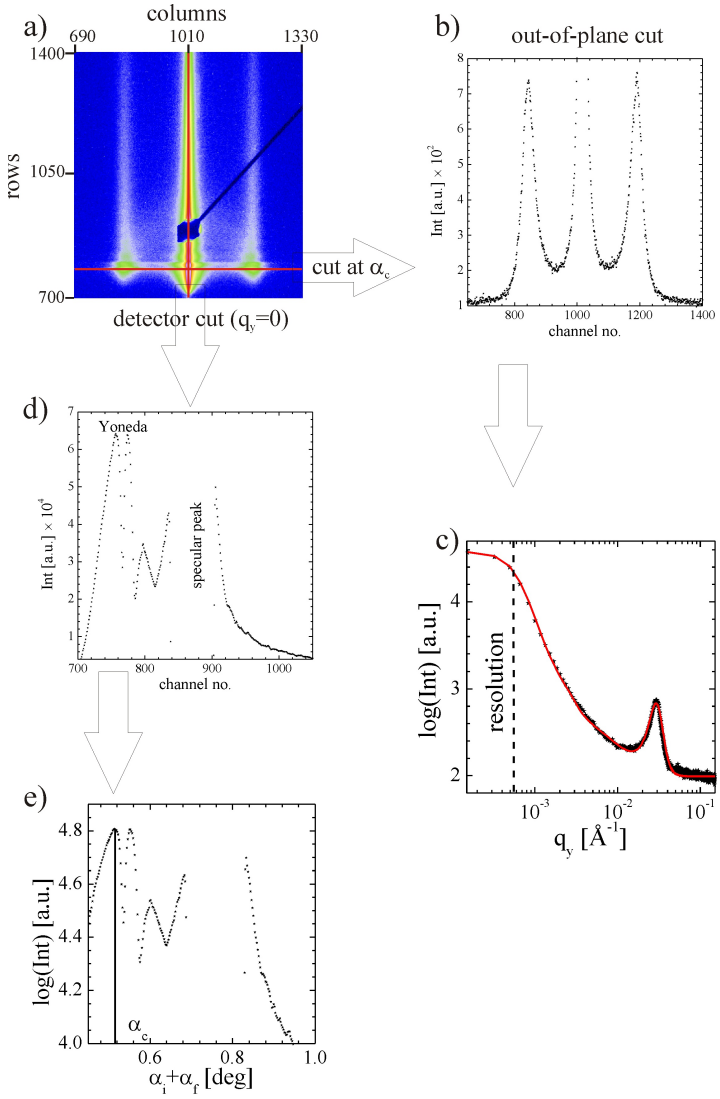

Figure 2.14: Extraction of the lateral and vertical structural information by characteristic cuts from 2d scattering data. (a) scattering 2d pattern on the detector; (b) out-of-plane cut at constant position q_z and (d) detector cut at position q_y=0, respectively, both represented with respect to the positions on the detector by channel numbers; (c) and (e) are the logarithmic presentation style of the out-of-plane and detector cuts. The denoted "resolution" line in (c) represents the maximum lateral length scales resolvable in the used experimental setup.

calculated by $d = 2\pi/q_y$. For a more detailed analysis, a model fit to the data as the solid line shown in figure 2.14c is needed. The model fit takes the form and structure factors as well as the resolution function into account. Form and structure factors are assumed to have a Gaussian distribution. Such model fit is mainly used in this thesis.

2.3.5.2 Detector Cuts

From vertical slices, information dependent on the q_z component of the wave vector results. At $\psi = 0$ (corresponding to q_y=0), this scan is called the detector scan as it would be measurable with a point detector moving in the reflection plane behind the sample. By neglecting the small q_x component in this scan which yields the parabolic path of the detector scan in the q_x,q_y-plane, a detector scan basically probes a structure perpendicular to the sample surface. Figure 2.14d shows data measured at thin P(S-*b*-NIPAM) films in the commonly used detector scan plot, and figure 2.14e shows the logarithmic intensity as a function of the incident and exit angle. As in the two-dimensional maps, the Yoneda and the specular peak are visible. The high frequent modulation next to the Yoneda peak is originated by resonant diffuse scattering (RDS). As the detector scan probes the in-plane wave vector dependence of long-wavelength fluctuations, a determination of the displacementdisplacement correlation function without assumptions about the local layer structure is possible. The correlation between separated interfaces yields a coupling of the correlation functions of the individual interfaces. From the detector scan, direct information about such interface correlation is obtained. In the case of uncorrelated interfaces, all interfaces scatter independently and the diffuse intensities of all individual interfaces superpose. Partially or fully correlated roughness gives rise to scattering with partial coherence and resonant diffuse scattering (RDS) is observed. The partial phase coherence of the waves diffusely scattered from different interfaces concentrates the intensity in narrow sheets. These sheets of resonant diffuse scattering are oriented parallel to the q_x axis with the center fulfilling the one-dimensional Bragg condition $\Delta q_z = 2\pi/d_{corr}$. The modulations of the resonant diffuse scattering are in phase with the fringes of the reflectivity and enable a direct determination of the distance d_{corr} of the correlated interfaces.

2.3.5.3 Off-Detector Cuts

While the detector scan is cut from the two-dimensional intensity distribution at $q_y = 0$ along the vertical direction, off-detector scans are vertical cuts with $q_y \neq 0$ [43]. These off-detector cuts are made in the high-resolution set-up displaying the decay of the RDS with increasing q_y. The q_z range of these cuts is from the start of the Yoneda peak to the start of the specular peak. Thus the specular peak is not visible, but the substructure of the Yoneda peak and the modulations of the RDS are resolved. The decreasing amplitude of the fringes resulting from resonant diffuse scattering with increasing q_y indicates the loss of correlation at smaller in-plane length scales.

2.4 Neutron Scattering and Reflectometry

In contrast to X-rays, which are an electromagnetic radiation, neutrons are elementary particles with a mass of $m = 1.675 \times 10^{27}$ kg, charge is zero, spin is 1/2, the magnetic moment is $\mu_m = -1.913\mu_n$, the nuclear magneton is $\mu_n = 5.051 \times 10^{27}$ JT^{-1}. It has particle as well as wave properties. Due to the pronounced differences in the neutron *scattering length density* (SLD) of different isotopes neutrons often provide better contrast compared to X-rays. On the other hand, X-rays provide better q resolutions. The methods of elastic scattering and reflectometry with neutrons deliver structural information from arrangements of atoms and magnetic moments in condensed material. Those arrangements can be precipitated phases in mixtures of metals, low molecular liquids or polymers. The information one can get is size, number density and correlations between these objects. Similar to X-ray scattering, in scattering experiments the intensity of neutrons is measured as a function of momentum transfer q

$$q = \frac{4\pi}{\lambda} \sin\theta \tag{2.36}$$

while the scattering angle is 2θ and the wavelength of neutrons is λ. q is the difference of the wave mumbers $\boldsymbol{k}$ (absolute value $k = 2\pi/\lambda$) of incoming and scattered neutrons. The momentum transfer is inversely proportional to the length scale of investigation: at q of the order of 1 Å $^{-1}$ one measures inter atomic distances and in the region 10^{-1} Å $^{-1}$-10^{-4} Å $^{-1}$ mesoscopic objects of sizes between 10 Å - 10^4 Å. In this section the neutron scattering process is explained following the textbook as *Neutron scattering* [BT00].

2.4.1 Principle of Neutron Reflectometry

Similar to X-rays as shown in figure 2.11, specular reflection of neutrons on the thin film is defined by the same incoming and outgoing angles. In this case the $\boldsymbol{q}$ vector has a orientation perpendicular to the surface and only heterogeneities in direction perpendicular to the surface e.g. parallel to $\boldsymbol{q}$ are measured. The intensity profile would show total reflection at small angles and then at larger angles strongly decrease with periodic oscillations. From this profile, one can determine thickness and roughness of the film.

The energy of a wave propagating in vacuum is

$$E_0 = \frac{\hbar}{2m} k_0^2 \tag{2.37}$$

with $k_0 = 2\pi/\lambda$. On interation with matter an interaction potential is added, which is described as a Fermi pseudo potential

$$V_F = \frac{\hbar}{2} 2\pi\rho b \tag{2.38}$$

Solving the Schroedinger equation for this interaction gives

$$\frac{\hbar^2}{2m}\frac{d^2\varphi}{dr^2} + (E_0 - V_F)\varphi = 0 \tag{2.39}$$

with $\varphi(r) = \varphi_+(r) + \varphi_-(r)$ for two spin states of the neutron. It follows with

$$k^2 = \frac{2m}{\hbar}(E_0 - V_F) \tag{2.40}$$

$$\frac{d^2\varphi}{dr^2} + k^2\varphi = 0 \tag{2.41}$$

with $k^2 = n^2 k_0^2$ is

$$\frac{2m}{\hbar}(E_0 - V_F) = n^2\frac{2m}{\hbar}E_0 \tag{2.42}$$

$$n^2 = 1 - \frac{V_F}{E_0} = 1 - \frac{4\pi}{k_0^2}\rho b = 1 - \frac{\lambda^2}{\pi}\rho b \tag{2.43}$$

where ρb is the scattering length density with the coherent scattering length ρ and the number density b. Since for most materials, the adsorption cross-section is effectively zero, the imaginary part of refractive index can be neglected and n can be expressed as

$$n \approx 1 - \frac{\lambda^2}{\pi}\rho b = 1 - \delta \tag{2.44}$$

To calculate the reflectivity for a single interface, derivation proceeds precisely as in the case of the Fresnel reflectivity for X-rays, where the following result are found:

$$R = \left|\frac{\mathbf{E}_f}{\mathbf{E}_i}\right| \sim \frac{16\pi^2\rho b}{q^4} \tag{2.45}$$

For a multilayer system, similar results to X-ray reflectivity such as eq. 2.27 and eq. 2.29 are acquired.

The neutron scattering length b is a nuclear property describing the interaction between the neutron and the atomic nucleus. The value of b varies randomly across the periodic table and also between isotopes of the same element. Here neutrons present a big advantage over other radiation such as light or X-rays, with isotopic substitution providing enhanced contrast between two otherwise equivalent species. The large difference in b between ^{1}H and ^{2}H (D) is of particular usefulness to the polymer scientist, as will be discussed in more detail later.

2.4.2 Time-of-flight Mode

Time-of-flight (TOF) spectrometer is a frequently used method of neutron scattering experiments. It determines the energy transfer during neutron scattering by using the particle character - by measurement of the velocity v_f of the scattered neutrons. Figure 2.15 illustrates the generic setup of a classical TOF instrument [RS09].

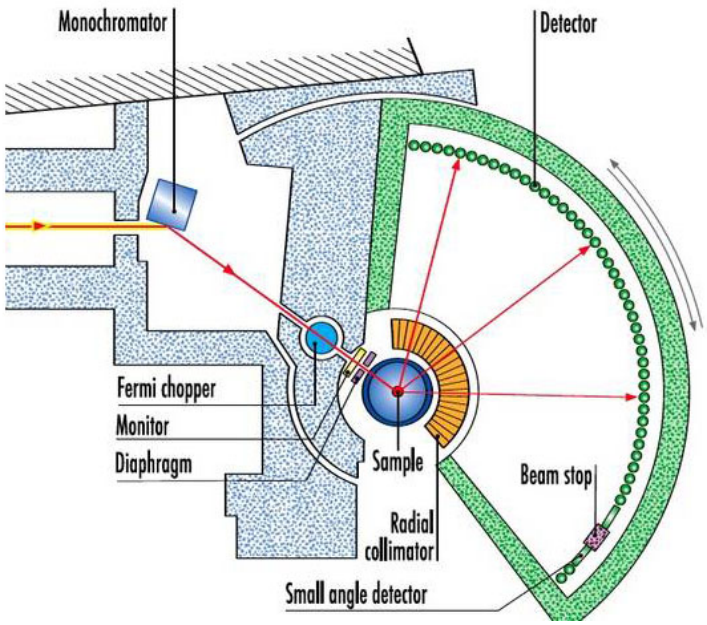

Figure 2.15: Generic setup of a classical TOF instrument. The image is taken from [RS09], and modified to fit the thesis.

When a neutron beam enters from the left, a monochromator filters a limited wavelength band $\lambda + \Delta\lambda$. By doing this typically a bandwidth of $\Delta\lambda/\lambda \approx 10^{-2}$ is achieved. Thus the monochromatized beam enters a so called chopper which opens the beam path periodically for a short moment. Typical frequencies are between 20 and 200 Hz, the ratio of time-open:time-close is around 1:100. The resulting pulse widths are of the order of several (tens) of microseconds. After an as short as possible flight path the neutron bunches hit the sample and are sacttered according to the double differential cross section of the sample material. In this process some neutrons exchange kinetic energy with excitations in the sample, i.e. change their velocities. After scattering into different directions the neutrons transverse the flight space between sample and the detectors. The path length between sample and dector is usually kept the same for all detectors placed at the periphery of the flight space. The dectors most often consists of ^{2}He ($\cong$10 bar) filled counting tubes of $30 \cdots 40$ cm length. Up to 1000 (and more) tubes are used in some installations

to cover as much solid angle as possible.

The elastically scattered neutrons (like those from the direct beam) reach the detectors after the time $t_{cp} + t_0 = d_{chopper-sample}/v_0 + L/v_0$ where $d_{chopper-sample}$ is the chopper to sample distance and L is the sample to detector distance, and those scattered inelastically arrive earlier (energy gain of the neutron) or later (energy loss of the neutron). Each pulse from a counting tube causes via the associated electronics an increment of one cell in the histogrammic memory. The address of this cell is derived from the time diffference between chopper opening and arrival time of the neutron (pulse), i.e. TOF, and the detector number ($\rightarrow$ scattering angle). Thus the distribution of flight times evolves as a histogram of $512 \cdots 2048$ channels with a width of around 10μs each. For each detector (resp. group of detectors) such an histogramm vs. time is obtained. A monitor (Mo) in the direct beam serves to normalize the histograms to the incoming neutron flux.

Since the physics of the systems under investigation is usually expressed in terms of the scattering function $S(\mathbf{q}, \omega)$, a transformation of the raw data representing intensity $I(2\theta$, t) into the ($\mathbf{q}$, ω)-space is necessary. The energy transfer during neutron scattering is

$$\hbar\omega = E_i - E_f \tag{2.46}$$

where E_i, E_f denote the energies of the incoming and scattered neutrons respectively. The variables of the scattering function depend on $\boldsymbol{k}_i$, $\boldsymbol{k}_f$; $\mathbf{q} = \mathbf{k}_i - \mathbf{k}_f$ is the moment transfer and

$$\hbar\omega = (\hbar^2/2m)(k_i^2 - k_f^2) \tag{2.47}$$

With $t = L/v_f$ and $t_0 = L/v_i$ inserted in eq. 2.47 yields

$$\omega(t) = \frac{m}{2\hbar} L^2 \frac{t^2 - t_0^2}{t^2 t_0^2} \tag{2.48}$$

and

$$q = \frac{m}{\hbar} L \sqrt{\frac{t^2 + t_0^2 - 2cos(2\theta)t_0 t}{t_0^2 t^2}} \tag{2.49}$$

The nonlinear mapping from channels to energy given by eq. 2.48 also causes a strongly varing energy-width of TOF-channels, G.

$$I(2\theta, G) \propto \int_{(G-1)\Delta\tau_n}^{G\Delta\tau_n} \frac{k_f}{k_i} 4\pi b^2 S(q, \omega(t)) \frac{d\omega}{dt} dt \tag{2.50}$$

where b is the scattering length, and pulses of neutrons with defined velocity are periodically transmitted by the chopper with the frequency $1/\tau_n$. or sometimes simpler

$$I(2\theta, G) \propto \frac{k_f}{k_i} 4\pi b^2 S(q, \omega(G\Delta\tau_n)) \frac{d\omega}{dt} \Delta\tau_n \tag{2.51}$$

with

$$\frac{k_f}{k_i} = \frac{t_0}{t} \tag{2.52}$$

and

$$\frac{d\omega(t)}{t} = \frac{m}{\hbar} L^2 \frac{1}{t^3} \tag{2.53}$$

the result

$$I(2\theta, G) \propto S(q, \omega(G\Delta\tau_n)) \frac{1}{t^4} \tag{2.54}$$

is obtained. All constant factors are ommited and lumped into a still undetermined proportionality factor. Note the factor t^{-4} between S and I which causes asignificant intensity enhancement for the early arriving time channels, however intimately connected with a corresponding loss of energy resolution. Application of the transforms eq. 2.48 and 2.54 allows a display of the spectra in terms of $S(2\theta, \omega)$. The left data treatment is similar to general neutron reflectivity measurements as described before. The details of time-of-flight mode can be found elsewhere [BT00].

Chapter 3

Experimental Techniques

3.1 Spin Coating

The initial dry hydrogel films with different thicknesses were prepared with spin-coating (2000 rpm, 30 s) from a 1,4-dioxane solution at room temperature onto pre-cleaned Si and glass substrates. The spin coating was carried out by using a Delta 6RC spin coater (SÜSS MicroTec GmbH). The process of spin coating can be descripted as follows: A small quantity of the polymer solution was dispensed onto the center of a substrate and spread out to form a puddle. Then the substrate was rotationally accelerated to high speed. The centripetal acceleration caused most of the solution to be immediately ejected from the substrate, leaving a thin film of polymer which flowed slowly outward from the center of the substrate under the action of centrifugal force. As the film was thinning, the solvent evaporated and the solution viscosity increased, reducing the radial flow. Eventually, the viscosity became so large that relative motion virtually ceases; the spinner was stopped and the spin coating process was completed. Final film thickness and other properties depend on the nature of the polymer solution (solution concentration, viscosity, evaporation rate of the solvent, surface tension, etc.) and the parameters chosen for the spin process (spin speed, spin time, temperature, humidity, etc.). The details of the spin coating of polymer films can be found elsewhere [LCJ88, SDW97].

3.2 Optical Microscopy

The sample surfaces were observed by an optical microscope Zeiss Axiotech 25H with magnifications of 5×, 10×, 50× and 100×. The images were captured by a CCD-camera

(Hitachi KPD-50) without using any filter. There are 500 × 375 pixels^2 for each image. The size of each pixel for magnifications of 5×, 10×, 50× and 100× of the objectives are 2.6 μm, 1.3 μm, 0.26 μm and 0.13 μm, respectively.

3.3 Atomic Force Microscopy (AFM)

The real-space imaging and analysis of sample surface was carried out with a Park autoprobe CP atomic force microscope (Thermomicroscopes - Veeco, California, USA). All the measurements were performed in air at room temperature. The basic principle of AFM is showen in figure 3.1: The AFM consists of a soft cantilever spring mounted with a sharp tip, a system of sensing the cantilever deflection, a mechanical scanning system, a signal processing and feedback system and a display system that converts the measured data to images. When the tip is brought close to the sample surface, the forces between the tip and the sample lead to a deflection of the cantilever. This deflection is measured by focusing a laser spot on the backside of the cantilever and measuring the displacement of the reflected laser on a position-sensitive multi-segment photodiode (PSPD). The corresponding signals are processed by a feedback system which controls the movement of the scanner in x, y and z -direction by a piezoelectric scanner. The sample is mounted onto a piezoelectric translator that moves the sample in the x, y and z directions underneath the tip. By comparing the amplitude, driving voltages, shift of the phase of the cantilever frequency with respect to the reference frequency, the topographical, error and the phase images are built by the computer program with consideration of the scanning parameters.

When a sharp tip in an AFM comes close to a sample surface, the forces F_{ts} exerted on the tip can be divided in three groups: surface forces, F_s, forces due to the sample deformation, F_d, and the elastic force of the cantilever, F_c. An AFM uses the force F_{ts} or some entity (depending on the mode of operation) derived from the force F_{ts} as the signal for imaging.

An elementary constituent of the interaction between a flat, rigid subtrate and a sharp, rigid tip in vacuum is the pair potential between atoms at the tip and the sample. At large distances (1-30 nm) the forces are attractive and are described by a van der Waals pair potential $p(r)$=-C/r^6, where C is the interaction constant determined by the polarizability and dipole moments of the molecules and r is the distance between two atoms. Three different terms contribute to the van der Waals forces: the Keesom interaction (between two free rotating dipoles), the Debye interaction (between a dipole and a single charge)

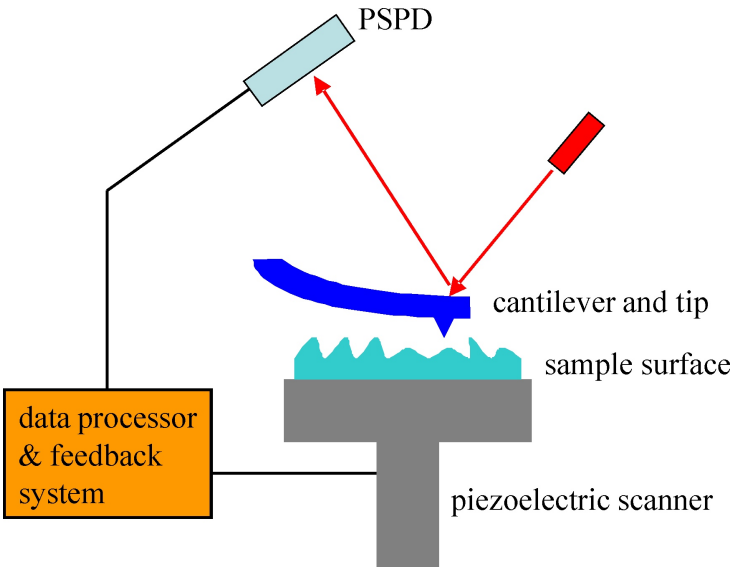

Figure 3.1: The basic principle of AFM: the deflection of the cantilever caused by forces between the tip and the sample measured by focusing a laser spot on the backside of the cantilever and measuring the displacement of the reflected laser on a position-sensitive multi-segment photodiode (PSPD).

and London interaction (between induced dipoles). Usually the London or dispersion term is dominating. For a sphere-surface potential, which is a good approximation for the interaction between the tip and the sample, the attractive part of the interaction energy is

$$W(D) = -\frac{AR}{6D} \tag{3.1}$$

where A is the Hamaker constant, R is the radius of the spherical tip, and D is the distance between the surface plane and the tip. This gives the attractive force:

$$F_a = -\frac{\delta W}{\delta D} = -\frac{AR}{6D^2} \tag{3.2}$$

The van der Waals force depends on the medium between the tip and the sample. If the surrounding media contains ions and dissolved molecules,the interaction potential can be changed in a complicated fashion, depending on the molecular composition, pH and ionic strength of the medium.

Because the soft samples like polymer are often significantly deformed elastically by the tip, the forces due to the deformation of samples F_d also should be considered. Details of F_d can be found elsewhere [IJN92]. Besides, the interaction forces between sample and tip are balanced by the elastic force due to the cantilever bending: F_c=$k\Delta Z_c$, where k is the spring constant of the cantilever and ΔZ_c is the measured cantilever deflection. In

summary, the delection of the cantilever, ΔZ_c, results from a combination of deformation and surface force: F_c=F_d+F_s.

In general, there are three imaging modes which normally can be used, contact mode, non-contact mode and tapping mode. However, to avoid the damage to soft sample because of the indentation of the tip on the polymer surface, only non-contact mode and tapping mode were used.

Non-Contact Mode (NCM): In non-contact mode, the tip of the cantilever does not contact the sample surface. The cantilever is oscillated slightly above its resonance frequency with a small oscillation amplitude (<10 nm). The van der Waals forces, which are strongest from 1 nm to 10 nm above the surface, or any other long range force which extends above the surface acts to decrease the resonance frequency of the cantilever. This decrease in resonance frequency combined with the feedback loop system maintains a constant oscillation amplitude or frequency by adjusting the average tip-to-sample distance. The voltage applied for expansion and retraction of the piezo-scanner is measured and is used to build the *topography* image. In best conditions, the lateral resolution of *non-contact* mode is about 1 nm depending on the curvature of the tip-apex. Because there is no direct contact between the tip and the sample surface, non-contact mode AFM does not suffer from tip or sample degradation effects that are sometimes observed after taking numerous scans with contact AFM. This makes non-contact AFM preferable to contact AFM for measuring soft samples.

Tapping Mode (TM): In tapping mode the cantilever is driven to oscillate periodically up and down below its resonance frequency by a small piezoelectric element mounted in the AFM tip holder. The amplitude of this oscillation is greater than 10 nm, typically 20 to 100 nm. During the scanning, the cantilever touches the surface for a very small fraction of its oscillation period. Due to the interaction of forces acting on the cantilever when the tip comes close to the surface (repulsive forces), the amplitude of this oscillation decreases and the resonance frequency increases, which can be detected and used to built a 3 dimensional image. Because the tip gets contact with the surface in this mode, the elastic constant of the material plays an important role in the change of the amplitude and the phase shift of the frequency [MS02]. The phase shift during the scanning process can be used to image the contrast between the hard and soft matter present on the surface, which is called *phase image*. Phase images are very useful in the investigations of microdomain

structures due to microphase seperation in a copolymer film. The lateral resolution of the tapping mode is approximately 1 nm depending on the curvature of the apex of the tip.

In detail of operation, the samples were placed on the magnetized sample holder by attaching a metal disc underneath the samples. The sample holder was mounted on a piezoelectric 100 μm-scanner. The amplitude of the oscillation of the tip was calibrated with respect to the vertical position of the piezoelectric scanner. The distance calibration of the piezocontroller was performed with a standard gold grating. Scanning was performed in both x- and y-direction. Each scanned micrograph consists of 265 lines, scanned with 0.5 Hz up to 1.0 Hz. The silicon gold coated conical cantilevers have resonant frequencies at about 60 KHz and a spring constant of $\sim$2.1 Nm^{-1}. Several images were measured for each sample at different sample positions. At each individual sample position, scans with different ranges from 0.5 μm $\times$ 0.5 μm up to 2 μm $\times$ 2 μm were performed.

The images obtained initially from the AFM measurement were raw data, which included artifacts, slope and curvatures that can alter the height data of the image. The slope was caused by a non-parallel orientation of the sample surface to the scanning plane. The curvatures were introduced by the bending motion of the piezo-scanner when it scanned the sample. These artifacts were elimated from the images presented in this thesis by flattening. A Wiener filter was used to remove the noise caused by mechanical vibration or electrical noise in the fast scan direction. The software used for image processing is PSI ProScan Image Processing from Park Scientific Instruments.

3.4 X-ray Reflectivity (XRR)

X-ray reflectivity experiments were performed with a laboratory Siemens D5000 diffractometer with a reflectivity extention. The detail of the XRR theory can be found in chapter 2. A knife edge was mounted above the sample surface to reduce background and control the footprint of the X-ray beam on the sample. The X-ray beam with a wavelength of 1.54 Å(Cu Kα) was collimated by a slit system in order to run the experiment with a proper beam divergence. Measurements were performed in air with a scintillation counter. The automatic beam absorber was used to avoid saturation of the detector. The sample was fixed on the sample stage by a vacuum chuck. A large range of the scattering

vector component perpendicular to the sample surface q_z=$2\pi(\sin\alpha_i+\sin\alpha_f)/\lambda$ was covered to allow for the detection of thickness and surface roughness of the thin films. Fitting was performed with the program Parratt32 (version 1.5.2) [BC97] with a model system containing layers of varying refractive index.

3.5 Grazing Incidence Small Angle X-ray Scattering (GISAXS)

Grazing incidence small angle X-ray scattering is a technique for the investigation of film structures. The detail of the GISAXS theory is explained in chapter 2. Compared to AFM, GISAXS can probe not only the surface structures but also the structures inside the film. All GISAXS measurements were carried out at the beamline BW4 of the DORIS III storage ring at HASYLAB (DESY, Hamburg) [RSV06]. The X-ray beam was produced by a wiggler (N=19 periods, K=13.2) and monochromatized by a fixed exit double silicon (111) monochromator. It was focused horizontally and vertically with a fixed cylindrical mirror and a plane mirror with a mirror bender, respectively [RSV06]. The selected wavelength was $\lambda = 1.38$ Å. The beam divergence in and out of the plane of reflection was set by two entrance cross-slits. To operate a microbeam the X-ray beam was moderately focused to the size of (H×B) 40×80 μm^2 by using an assembly of refractive beryllium lenses [MBP06]. The set up is shown schematically in figure 2.13. The sample was placed horizontally on a goniometer. The direct beam was blocked by a diode beam stop in front of the detector to protect the detector from high intensity beam. A second, point-like moveable beam stop was also used to block the specular peak on the detector. The flight path of the incoming and scattered beam was evacuated to avoid scattering from air. The scattered intensity was recorded by a MARCCD detector. The incident angle was set to 0.45°, which is well above the critical angles of PNIPAM (0.148°) and of Si (0.20°). As a result, at the chosen sample-detector distance of 2.11 m, the Yoneda and the specular peaks are well separated on the detector, and additional features in the intensity originating from resonant diffuse scattering can be detected for the regime of film thicknesses [DJ92, HV94]. Because of the simple shape of the two-dimensional GISAXS pattern, structural information is obtained from vertical and horizontal cuts of the 2d intensity distribution with respect to the sample surface [MBP03a]. The vertical cut at q_y = 0, called detector cut, contains the information on the structure perpendicular to the surface. Horizontal cuts at constant q_z allow extracting the information (geometry, size

distribution, and spatial correlation) of lateral structures. The intensity of the horizontal cuts was integrated over a small slice Δq_z in the vertical direction to obtain an improved statistics. In the literature these horizontal cuts are also named GISAXS cuts and out-of plane cuts [MBP03a].

3.6 Neutron Reflectivity (NR)

The neutron reflectivity experiments were performed at the D17 beamline at ILL, Grenoble, France, in time-of-flight (TOF) mode. The detail of neutron scattering and TOF mode is explained in chapter 2. TOF mode, in which neutrons with a broad range of wavelength λ are used simultaneously and registered as a function of their respective times of flight, allowed for the collection of specular and off-specular scattering data. The necessary pulsing of the beam was realized by a double chopper system. The set up is shown in figure 3.2. The largest available sample-detector distance of 3.4 m was operated. The diffracted intensity was recorded on a two-dimensional (2d) detector without the movement of any motors. The absence of motor movements was crucial for achieving a high time resolution as well as for avoiding mechanically induced vibrations which might destabilize swollen films (by activation of long wavelength surface waves). On the detector the counts were registered for each spatial pixel (x, y) as a function of TOF in 1000 channels. After integration of the counts for fixed x and TOF channel along the vertical detector axis y, and the TOF to λ conversion, the scattered intensity is displayed as a function of λ and the exit angle α_f. Finally, the corrected data set $I(\alpha_f, \lambda)$ is transformed to $I(q_x, q_z)$ with the given (constant) angle of incidence α_i=0.5°, where q_z denotes the wave vector component perpendicular to the surface and q_x the one in the surface parallel to the neutron beam. All the reflectivity curves were fitted with the Motofit program [NA06] with a model system containing layers of varying scattering length density, appropriate error weighting and point-by-point resolution smearing. An automated batch fit approach is taken, with all the data sets being analyzed in series. The scattering length densities taken for substrate and different layers agree well with literature values. The special vapor chamber made for the neutron scattering experiments is shown in figure 3.3. The chamber is made of aluminum. Because aluminum is highly transparent to neutrons due to its low neutron mass attenuation coefficient [LM01], there is no influence from the chamber itself to the neutron scattering. The chamber can be thermostated between 0° to 100° by the thermobath. The sample was mounted in the chamber vertically in air at

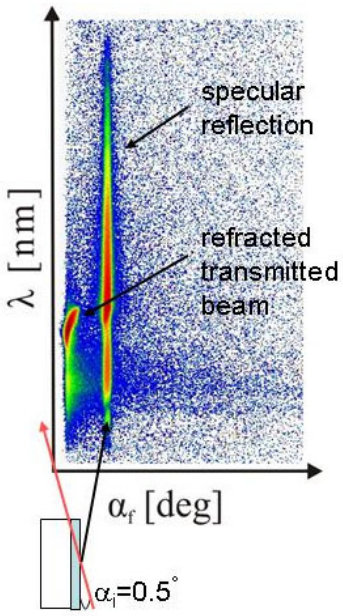

Figure 3.2: The basic experimental setup of neutron reflectivity. The sample is placed vertically. The incident angles is denoted by α_i. The 2d detector represents the exit angle α_f dependence along the horizontal axis and the wavelength λ dependence along the vertical axis. The scattering intensity distribution on the detector is presented in logarithmic scale. The detected scattering pattern shows the diffuse scattering with specular reflection and refracted transmitted beam.

23°. Before the swelling, the chamber was evacuated by a vacuum pump (DIVAC 0.8 T, Leybold AG) to reach a moderate vacuum. Then D_2O was filled in the reservoir of the vapor chamber with a syringe. Due to the moderate vacuum, the vapor of D_2O reached a saturated state in a few minutes and the sample started to swell in the saturated vapor until reaching the equilibrium state. To perform dewelling, the syringe was used to suck the D_2O out of the reservoir and then the chamber was evacuated again to remove the residual D_2O vapor from the chamber. During the neutron scattering measurements, the neutron beam was illuminating the sample through the aluminum foil window on the one side of the chamber and reflected forwards the detector through the aluminum foil window on the other side of the chamber.

3.7 White Light Interferometry

Thickness and optical constants (n and k) were measured with the Filmetrics F20 Thin-Film Measurement System (Filmetrics Inc., San Diego). The spot size of the light beam is adjustable from 500 μm into 1 cm. The characteristic intensity oscillations in the re-

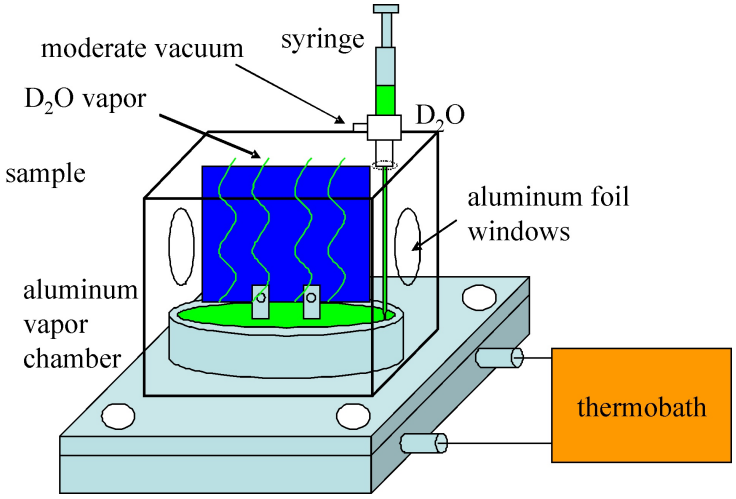

Figure 3.3: Schematic of the vapor chamber.

flectance spectrum were analyzed in a wavelength regime from 340 to 1100 nm. The basic idea behind the technique is to reflect a batch of light with different wavelength from a flat surface or interface and to then measure the intensity of the light reflected in the specular direction (reflected angle equal to incident angle). Based on Fresnel equations, when light makes multiple reflections between two or more parallel surfaces, the multiple beams of light generally interfere with each another, resulting in net transmission and reflection amplitudes that depend on the light-wavelength [HE02]. Therefore the reflection spectrum shows a series of fringes of which the positions and the amplitude are mainly dependent on the film thickness, surface roughness and optical constants (n and k). By fitting with a model system containing layers of varying refractive index/thickness, the thickness/refractive index values can be acquired.

The setup for white light interferometry measurements is shown in figure 3.4. The vapor chamber is made of aluminum. The temperature of the vapor chamber can be adjusted by the thermobath. The sample was placed horizontally in the chamber, and the optic cables of the white light interferometry were mounted vertically on the cap of the chamber. Water was filled in the reservoir of the vapor chamber to creat saturated water vapor atmosphere. During the measurement, the light beam was emitted, passed through a optic cable and finally was focused on the sample by a focus lens with a very large incident angle ($\sim 90°$). The reflected light then passed through another optic cable and was detected by the detector system.

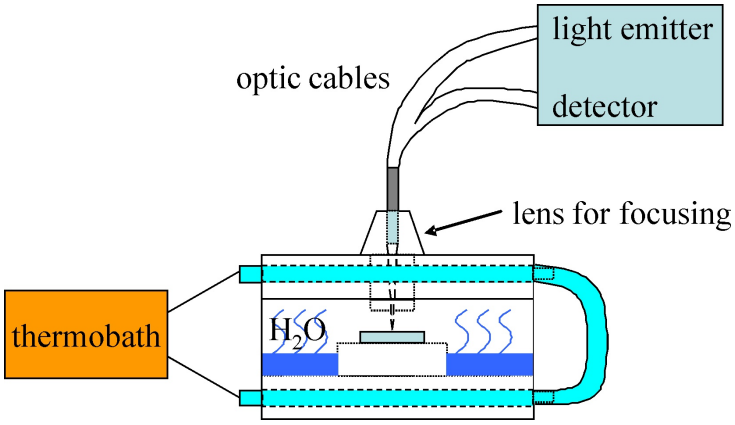

Figure 3.4: Schematic of the setup for white light interferometry measurements.

3.8 FTIR Spectroscopy

The H-D exchange reaction between P(S-*b*-NIPAM) and D_2O was measured with FTIR spectroscopy using a JASCO FTIR-4100 spectrometer. The scan wavelength range is 1000-3900 cm^{-1}. The theory of FTIR is: When a material is irradiated with infrared radiation, absorbed IR radiation usually excites molecules into a higher vibrational state. The wavelength of light absorbed by a particular molecule is a function of the energy difference between the at-rest and excited vibrational states. The wavelengths that are absorbed by the sample are characteristic of its molecular structure. The FTIR spectrometer uses an interferometer to modulate the wavelength from a broadband infrared source. A detector measures the intensity of transmitted or reflected light as a function of the wavelength. The signal obtained from the detector is an interferogram, which must be analyzed with a computer using Fourier transforms to obtain a single-beam infrared spectrum. The FTIR spectra are usually presented as plots of intensity versus wave number (in cm^{-1}). The wave number is the reciprocal of the wavelength. The intensity can be plotted as the percentage of light transmittance or absorbance at each wave number. To identify the material being analyzed, the unknown IR absorption spectrum is compared with standard spectra in computer databases or with a spectrum obtained from a known material. Spectrum matches identify the polymer or other constituent(s) in the sample. Absorption bands in the range of 4000-1500 wavenumbers are typically due to functional groups (e.g., -OH, C=O, N-H, CH_3, etc). The region from 1500-400 wavenumbers is referred to as the fingerprint region. Absorption bands in this region are generally due to intramolecular phenomena and are highly specific to each material. The specificity of these bands allows computerized data searches within reference libraries to identify a

material. In detail of operation, the initial P(S-*b*-NIPAM) film was prepared by solution-casting from a 1,4-dioxane solution on a MIRacle diamond substrate at 23 °C in the air. The film thickness was in the range of 1-3 μm. Next, the P(S-*b*-NIPAM) film was exposed to a saturated D_2O atmosphere at 23 °C for 30 min. Afterward, the P(S-*b*-NIPAM) film was dried in air at 23 °C for 15 min before the FTIR measurement. For comparison, a second dry P(S-*b*-NIPAM) film was prepared and treated in the same way but with H_2O replacing the D_2O used before. The experiments were repeated to ensure reproducibility of the reported results.

Chapter 4

End-capped PNIPAM Thin Film

4.1 Introduction

Poly(N-isopropylacrylamide) (PNIPAM) is one of the most studied thermosensitive polymers which exhibits a phase transition at a lower critical solution temperature (LCST) of ~ 32 °C in water. The LCST of PNIPAM can be changed by introduction of hydrophilic or hydrophobic comonomers, respectively [TLD75]. Moreover, the phase transition temperature depends not only on the level of hydrophobe incorporation and on its chemical structure but also on its position on the chain [KP01, CZ05]. With decreasing molecular weight the effect of end groups of PNIPAM homopolymers increases [FS06]. In water, polymers which carry a hydrophobic group at one chain end tend to form core-shell structures in which the hydrophobic core is insulated from the water by a brush-like corona of PNIPAM chains [CJE97, WFM92]. PNIPAM carrying a hydrophobic group at each chain end form another type of micelle in water based solution. The micelles are described as flowerlike associates consisting of loops of hydrated polymer chains having both end groups entrapped in the micellar core.

Although PNIPAM has been well studied, the knowledge on thin PNIPAM films is still limited. In the case of triblock copolymers with two polystyrene (PS) blocks sandwiching a central PNIPAM block all well-known microphase separation structures were reported [NA07]. Depending on the ratio between PS and PNIPAM, the ABA-type copolymers self-assemble into spherical, cylindrical, lamellar, or double-gyroid morphologies. Swelling of the middle block leads to physically cross-linked gels, where the end-block domains form the physical cross-links. In the triblock copolymer terminology the investigated

end-capped homopolymer investigated in this work can only allow for the spherical morphology due to the chosen short hydrophobic chain ends.

Because pure PNIPAM homopolymer films miss the possibility of internal cross-links to build up a gel, the addition of hydrophobic chain ends (a triblock copolymer in the extreme case) is a simple way to overcome this problem. However, with increasing glassy, hydrophobic block length the ability to swell decreases. In case of the triblock copolymer P(S-*b*-NIPAM-*b*-S) bulk compositions with spherical PS domains and a PNIPAM continuous phase swell very well in water, whereas composition resulting in cylindrical PS domains or in the bicontinous gyroid structure in bulk swell only by a factor of 3 to 5, respectively. Finally, lamellar compositions do not show any swelling. Along this line short hydrophobically end-capped PNIPAM chains might be expected to exhibit the strongest swelling, thereby maintaining the gel character.

So far, several different techniques were reported for the preparation of thin PNIPAM films: Micelle and vesicle adsorption from solution [YY06], plasma polymerization [CX05], solution casting [TS05], layer-by-layer deposition [SMJ03, SMJ04], self-assembled monolayers [MC02], spin-coating [HI04, NA07], dip coating [YYZ07] and surface graft polymerization [IH91, YL03, YH03, YH06]. Grafting PNIPAM to surfaces is a promising strategy for creating responsive surfaces, since the physical properties of PNIPAM are readily controlled by changing the temperature, however, it turned out that the ability to swell is strongly suppressed by the connection of one chain end to the solid surface. Thus spin-coating appears to be an interesting alternative, being on the one hand widely used in many areas of thin polymer film preparation and being on the other hand well suited to control film thickness over a broad range.

Thus, within the present work the spin-coating technique is applied, which is rarely applied to PNIPAM, for the preparation of thin films. Instead of a PNIPAM homopolymer, hydrophobically end-capped PNIPAM is applied to address the question if end-capped PNIPAM undergoes microphase separation and creates an internal structure in thin films. At each chain end a very short hydrophobic end group, *n*-butyltrithiocarbonate, was chosen (denoted nbc-PNIPAM, see figure 4.1). Reversible addition-fragmentation chain transfer (RAFT) polymerization, being an extremely versatile, controlled free radical polymerization technique for the synthesis of well-defined polymer architectures, was applied to obtain nbc-PNIPAM, using a bifunctional bis(trithiocarbonate) as chain transfer agent.

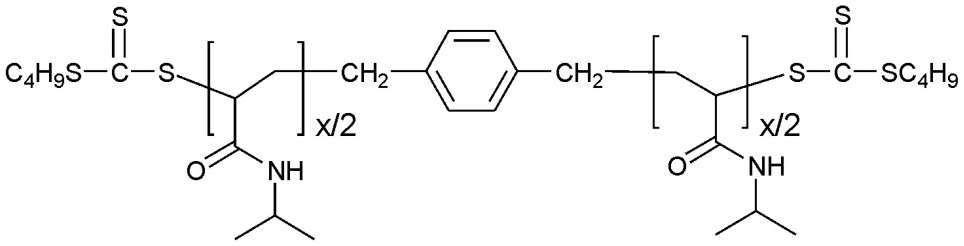

Figure 4.1: The chemical structure for nbc-PNIPAM. X = 168.

The nbc-PNIPAM can be considered as the limiting case of a triblock copolymer with a middle PNIPAM block and extremely short hydrophobic end blocks. In solution the association of telechelic polymers into micelles and networks leads to an effective molecular weight higher than that of the corresponding PNIPAM homopolymer, which yields a depression of LCST. Moreover, the mixing entropy of telechelic polymers is lower than that of the homopolymer, and they tend to demix. Until now, for thin films no one except the author is aware of any investigation focusing on end-group-induced microphase separation. The interaction with the substrate might change the behavior as compared to the bulk.

The structural investigation is based on X-ray reflectivity, microbeam grazing-incidence small-angle X-ray scattering (μGISAXS) and is accompanied by optical methods and atomic force microscopy. Thus, the surface and the inner film structure can be accessed. The LCST for the thin nbc-PNIPAM films was probed in swelling experiments in a saturated water vapor atmosphere.

This chapter has the following structure: The introduction is followed by a sample preparation part. The next sections show the results and discuss the thin film investigation of nbc-PNIPAM.

4.2 Sample Preparation

Materials. The polymer used is *n*-butyltrithiocarbonate end-capped poly(N-isopropylacrylamide), denoted nbc-PNIPAM, with a molecular weight of 39000 g mol^{-1}. The synthesis process and molecular characteristics of the polymer are described in detail elsewhere [WW08]. 1,4-dioxane was received from Acros. Dichloromethane, ammonia solutions

(NH_3, 30-33%), and hydrogen peroxide (H_2O_2, 30%) were ordered from Carl Roth GmbH. Silicon substrates (Si 100, n-type) were purchased from Silchem, and glass substrates were purchased from Carl Roth GmbH, respectively.

Substrate Cleaning and Thin Film Preparation. Silicon with an oxide layer surface and glass were used as substrate materials. For cleaning the precut silicon (Si 100, n-type, Silchem) and glass pieces were placed in dichloromethane in an ultrasonic bath for 5 min and rinsed with Millipore water shortly after. Afterward, the substrates were kept for 2 h in an oxidation bath at 75 °C consisting of 1400 mL Millipore water, 120 mL of H_2O_2, and 120 mL of NH_3 to clean the surface from organic traces. Thereafter, the samples were stored in Millipore water. Directly before spin-coating the substrates were rinsed with Millipore water at least five times to remove possible traces of the oxidation bath. The substrates were dried using compressed nitrogen before coating the SiO_x surface. Because of this protocol at the Si surface a hydrophilic oxide layer of 2 nm is present, which has a small surface roughness below 1 nm [MBP03b]. Dry hydrogel films were prepared by spin-coating (2000 rpm, 30 s) from 1,4-dioxane at room temperature (relative humidity 50%) onto precleaned silicon substrates. The concentration of the nbc-PNIPAM in 1,4-dioxane was varied from 0.3 to 30 mg/mL to achieve different film thicknesses. The solutions used for spin-coating were transparent and do not show any sign of aggregates. Several identical samples were prepared to prove the reproducibility.

4.3 Structural Investigation

a. Dry Hydrogel Film Surface Structures. Thin nbc-PNIPAM films were prepared with spin-coating from a 1,4-dioxane solution. Compared to other solvents, e.g. water, dioxane turned out to be best suited to achieve smooth and homogeneous films in combination with the described substrate cleaning protocol. The concentration of the solution used for spin-coating is varied from 0.3 to 30 mg/mL to obtain a large range of different film thicknesses. The spin-coating parameters (spinning speed, acceleration, and spinning time) are kept fixed. Films were prepared at room temperature and thus from solutions containing nbc-PNIPAM micelles with the hydrophobic chain ends located in the micellar core. No aggregates were present in these solutions.

The resulting dry films do not show large scale heterogeneities. The surface topography of the sample is investigated by optical microscopy in reflection mode. Optical microscopy

yields the overall top view of the film describing the large surface structures. Figure 4.2 shows the optical microscopic image of 46, 66, and 126 nm films taken at 100x zoom. To ensure focusing on the film surface an area with several "holes" is selected for presentation. As shown in figure 4.2, with optical microscopy the surfaces appear smooth and continuous, whereas it was reported that very thick and bulk-like PNIPAM gel film (thicknesses on the order of 60μm) were inhomogeneous on a micrometer scale [ZS96].

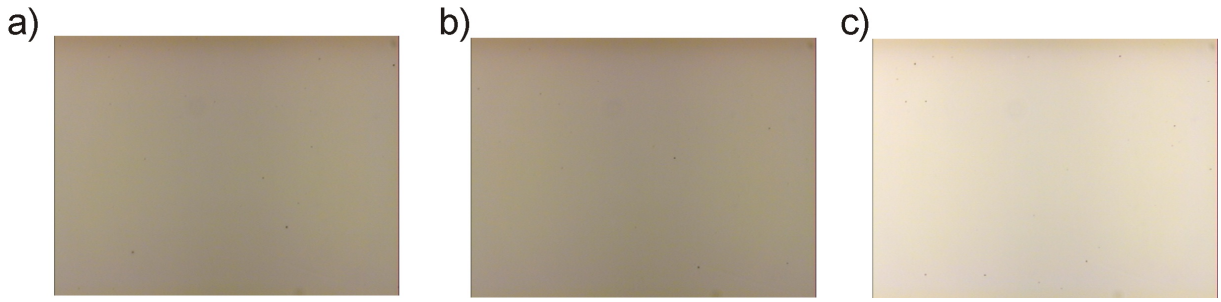

Figure 4.2: The optical micrograph shows a image size of 99 μm $\times$ 74 μm to emphasize on local surface structures for film thickness of (a) 46, (b) 66, and (c) 126 nm.

The optical image cannot give detailed information about the surface structures present on the surface, which have the dimensions of a few nanometers only. AFM in non-contact mode is used to observe the local structures on the surface. With atomic force microscopy (AFM) the absence of largescale heterogeneities is confirmed, and the surface topography is visualized with high resolution. Figure 4.3 shows the example of topography data with a scan size of 1 μm $\times$ 1 μm to emphasize on local surface structures for dry film thickness of 10, 46, and 240 nm. All films have a surface structure on the nanometer scale, which is caused by the micelle structure of the nbc-PNIPAM. For 10 nm film thickness (Figure 4.3a) the presence of the micelles as building blocks for the hydrogel film is best seen. The polymeric structures are worm-like instead of sphere-like as the micelle structure in polmyer solutions because of the spin coating process. Before starting the spin coating, sedimentation starts and the micelles migrate towards the substrate surface. During spin coating the migration is stopped by centrifugal forces and the increase of the viscosity of the polymer solution because of solvent evaporation. This leads to a shape deformation and a non-uniform stacking of micelles. With increasing film thickness the surface structures coarsen laterally but decrease in height (peak-to-valley amplitude) from 0.8 to 0.3 nm. At larger film thickness the attractive surface interaction is weaker for the topmost nbc-PNIPAM micelles, and a larger number of micelles are stacked which allows for an improved space filling with polydisperse spherical soft objects.

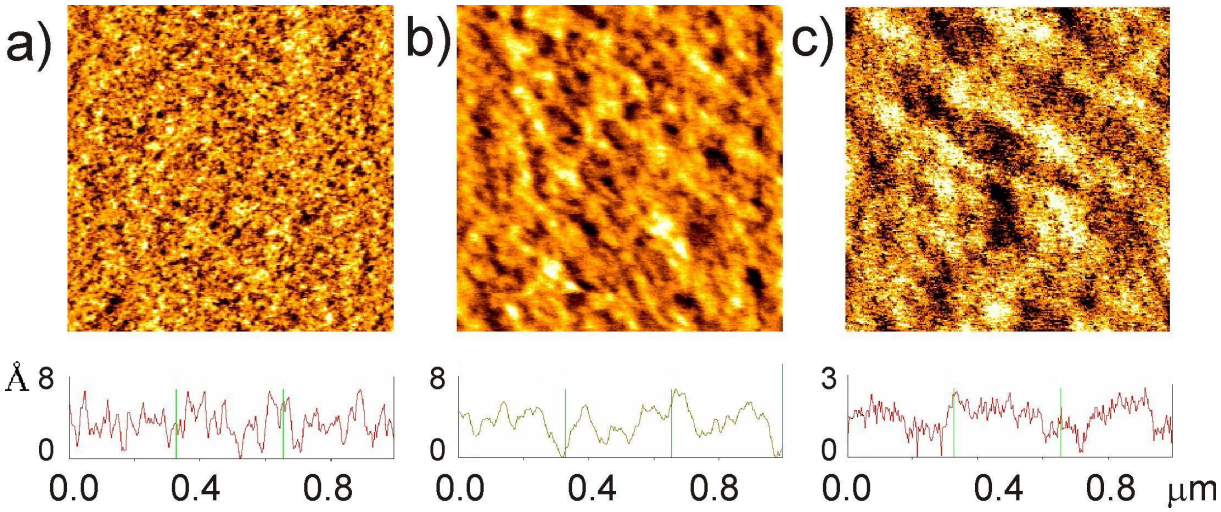

Figure 4.3: AFM micrographs show a scan size of 1 μm $\times$ 1 μm to emphasize on local surface structures for film thickness of (a) 10, (b) 46, and (c) 240 nm. The structure heights increase with the increase in brightness of structures in the images. In the representative line cuts from the AFM data the x-axis (lateral, micrometer) differs strongly from the y-axis (height, angstrom).

b. Density Profile of Dry Hydrogel Films. The density profile along the surface normal is determined with X-ray reflectivity measurements. Figure 4.4a shows the corresponding data for a selection of the dry nbc-PNIPAM films. From the bottom to the top, the film thickness increases from 5 to 241 nm. Despite in case of the thinnest film, all reflectivity curves exhibit well pronounced fringes, which extend to large values of the scattering vector component q_z, confirming the homogeneity and small surface roughness. For the thinnest nbc-PNIPAM film the fringes in the reflectivity curve are strongly damped due to the imperfections of the hydrogel layer. Instead of a continuous layer, the SiO_x surface is covered with polymer patches. This incomplete surface coverage causes a large surface roughness (peak-to-valley amplitude equal to film thickness). With decreasing of film-substrate interface correlation, wavelength fluctuations are damped. The reason is the micelle structure of nbc-PNIPAM in solution and the limited compressibility of the micelles on the SiO_x surface. Because of the applied base surface treatment, the substrate has a hydrophilic oxide surface with a water contact angle of 0° (water can spread on the surface) [MBP06].

Theoretically, a depletion of segments from the surface is present for a neutral or repulsive segment-surface interaction, and an excess of segments is present for an attractive interaction. The magnitude of the excess is dependent upon the strength of the attraction.

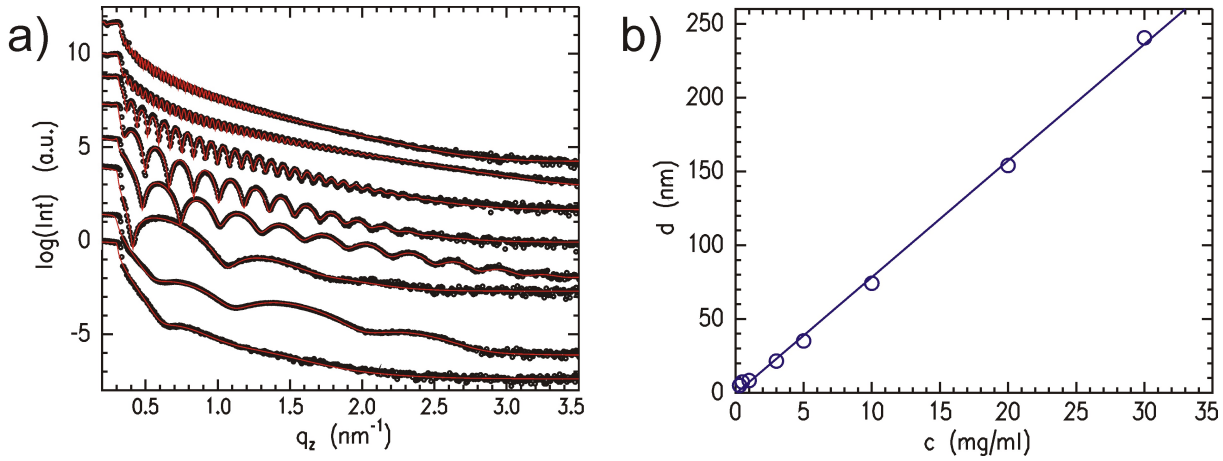

Figure 4.4: (a) Representative X-ray reflectivity data (dots) shown together with model fits (lines) for the thickness regime covered in this investigation. With increasing film thickness (5, 7, 8, 22, 35, 74, 154, and 241 nm from bottom to top) the curves are shifted along the y-axis for presentation. (b) Film thickness d plotted as a function of the nbc-PNIPAM concentration of the dioxane solution used for spin coating. The solid line is a linear fit.

With neutron reflectivity it was shown that a bilayer profile of end-tethered PNIPAM chains is present in D_2O. It indicates that the attraction of the NIPAM segments to the substrate surfaces is very strong, and a high volume fraction of NIPAM segments in the surface layer forms [YH03]. Thus, the interaction of the SiO_x surface is more favorable for the NIPAM segments. In contrast, the second interface, namely the polymer film surface, is in contact with air (room temperature and relative humidity of 50%). This interface is much less hydrophilic and might even favor the interaction with the hydrophobic n-butyltrithiocarbonate end groups. As a consequence, the nbc-PNIPAM micelles are collapsed perpendicular to the substrate surface, and the total height (film thickness of 5 nm) gives the extension along the surface normal. The part of the micelle, which is attracted to the surface via the hydrophobic core, modifies the shape of the micelle from the core-shell structure in solution toward a fried-egg-type structure. A similar behavior was observed with amphiphilic block copolymers adsorbed from solution onto solid substrates [WH99, MBP01]. Because it is energetically unfavorable to compress the micelles stronger, which would be necessary to make a space-filling homogeneous dry hydrogel film, at a solution concentration of 0.3 mg/mL no more a continuous film is obtained. For the given energetic conditions (hydrophilic SiO_x surface) 5 nm is correspondingly the lowest film thickness, which can be prepared from the investigated molecular weight. All films with larger thickness are homogeneous as probed with AFM and X-ray reflectivity.

Unfortunately, the spin-coating process is very complicated and even in the case of simple homopolymers not fully understood. Despite its frequent use in practice, in theory it can only be modeled within a three-step model [LCJ88] including many simplifications. The first step describes the early stages, which may have no influence on the resulting structures. In the second step fluid flow reduces the amount of solvent on the rotating sample until in the third step a resulting structure is frozen in due to solvent evaporation. Thus, in the second and third step the concentration of nbc-PNIPAM is increased, which results in the change of the structure. The bridging of micelles in addition to entanglements at high concentrations favors the gelation in hydrophobically end-capped systems, resulting in physically cross-linked hydrogels. Such physically cross-linked thin hydrogel films are extremely desirable because the ability to swell and to react to temperature changes is supposed to be superior to chemically cross-linked systems.

In figure 4.4b the linear dependence of the resulting dry film thickness on the concentration used for the spin-coating is shown. The thickness values come from a model assumption of the in-plane structures and composition of the film because the average density profile of the film influences the reflectivity data. The fitted curves are the lines shown in figure 4.4a. Thus, although of micellar type, the simple linear spin-coating relation still holds and the spin-coating works as with simple polymer solutions (without micelles) [SLL90, SDW97]. The experimental equation of the spin-coating from the literature [SDW97] is

$$d\ [nm] = A \left(\frac{1950\ min^{-1}}{f} \right)^{0.5} \frac{C}{20\ mg/mL} \left(\frac{M_w}{100\ kg/mol} \right)^{0.25} \tag{4.1}$$

where A is the parameter dependent on experimental conditions, f is the rotation frequency of the coater, C is the polmyer concentration, and M_w is the polymer molecular weight. In the present case, f is set to 2000 min^{-1}, and M_w is 39.0 kg/mol. By fitting, the value of A is obtained, which is 202.5.

Thus, a simple way to control the film thickness for applications of physically cross-linked thin nbc-PNIPAM hydrogel films is the variation of the concentration of the nbc-PNIPAM solution.

c. Long-Ranged Correlations between Interfaces. Whereas with X-ray reflectivity only the structure along the surface normal is detectable, microbeam grazing incidence small-angle X-ray scattering (μGISAXS) is well suited to investigate structures parallel to the surface, so-called lateral structures and long-ranged correlations. In contrast to

AFM, this is not limited to the sample surface, but structures inside the film are probed. Figure 4.5 shows the line cuts from the two-dimensional μGISAXS data measured for a representative set of nbc-PNIPAM films of different thicknesses.

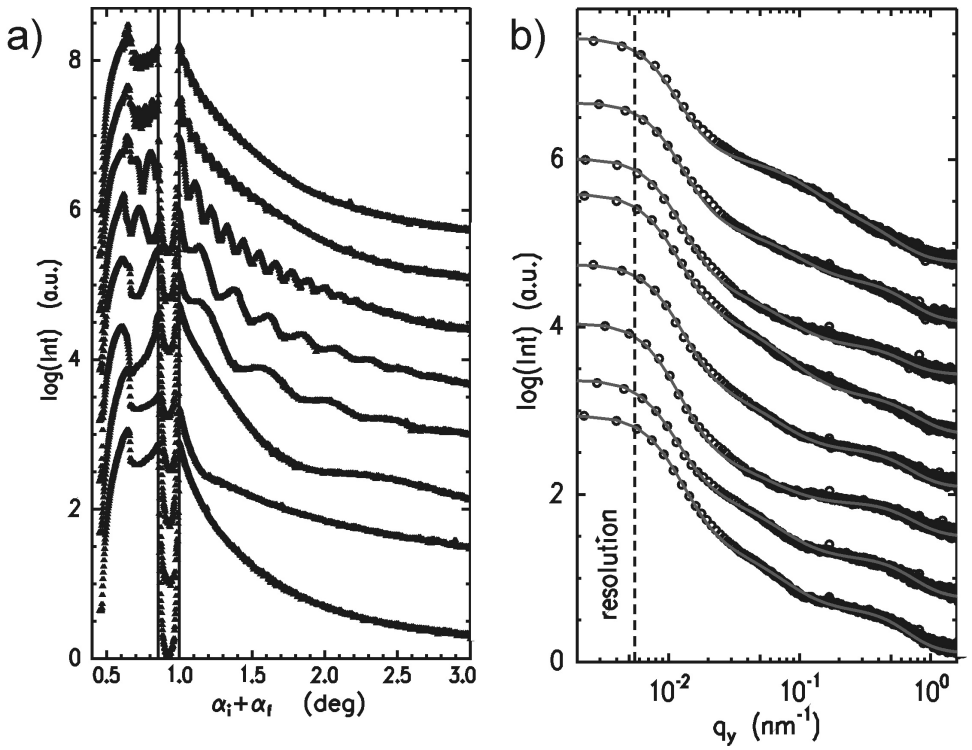

Figure 4.5: Line cuts from the μGISAXS 2d data for a representative selection of different film thicknesses (5, 7, 8, 22, 35, 74, 154, and 241 nm from bottom to top). (a) Detector scans shown as a function of the detector angle $\alpha_i + \alpha_f$ and (b) out-of plane scans shown as a function of the q_y component of the scattering vector. The solid lines are fits to the data as described in the text. The resolution limit is indicated by the dashed line. From bottom to top the film thickness increases and the curves are shifted along the y-axis for clarity.

In figure 4.5a detector scans are shown. To focus on the modulation of the intensities along the vertical direction (at $q_y = 0$), starting near the Yoneda region, a zoom-in line cut of the 2d intensity is selected. The specular peak is blocked by a beam stop to avoid damage to the sensitive detector. In addition to the Yoneda peaks, which are located at the critical angles of the investigated materials (Si and PNIPAM), strong modulations in the intensity are detected. These strong modulations are caused by a partial phase coherence of X-ray waves diffusely scattered from different interfaces, which yields a concentration of intensity in narrow sheets in reciprocal space. The detector scan cuts through these narrow intensity sheets giving rise to a modulation of the intensity. If the film is uncorrelated,

all interfaces scatter independently and the diffuse intensities of all individual interfaces superpose. Thus, the necessary condition for observing the partial phase coherence of diffusely scattered waves is a roughness correlation between the SiO_x surface and the nbc-PNIPAM surface. Analogous to a thin layer of snow on hills, the thin nbc-PNIPAM film replicates the SiO_x surface topography. Thus, a long-ranged correlation between both interfaces is installed and the thickness d of the nbc-PNIPAM film determines the distance between adjacent minima in the intensity modulation in the detector scan

$$\Delta q_z = \frac{2\pi}{d} \tag{4.2}$$

Meanwhile, long-ranged correlation such as roughness replication have been observed in many different types of polymer systems. Most of them were single-layer systems, prepared by spin-coating [MBP98b, MBP98c, MBP00, MBP01], but multilayer systems and films prepared by other preparation techniques were also reported to show correlated (interface) roughness [KJ99].

Because of the conformation of the polymer chains, not all lateral structure sizes of the roughness spectrum of the substrate can be replicated by a polymer film. The quality of roughness replication for different polymeric film can be compared by the critical lateral cut-off length R_c, which is defined as the smallest lateral structure's length that is replicated on top of the surface of the film. This means that the substrate morphology is replicated by the thin polymer film for in-plane length scales larger than the cut-off length. The in-plane cut-off length scale, R_c is determined from the decay of the intensity modulations as a function of y-component of the scattering vector, q_y. The critical cut-off length R_c is calculated by equation 4.3 [MBP01]:

$$R_c = \frac{2\pi}{\Delta q^{corr}} \tag{4.3}$$

where Δq^{corr} is the lateral (along q_y) propagation length of the modulation arisen due to the roughness replication or waveguide effect in reciprocal space in the GISAXS data.

In case of simple homopolymers such as polystyrene, it was shown that the morphology induced during the spin-coating process is dominated by bending elasticity of the freezing polymer solution, resulting in a characteristic cut-off R_c at short wavelengths of the substrate surface roughness spectrum. At the short-wavelength cut-off, a crossover from a conformal to a statistically independent roughness spectrum is observed. For large

wavelengths within the limited experimental resolution, the substrate and the polymer-vacuum interface are correlated [MBP98c]. For thin hydrogel films so far no experimental evidence of roughness correlation is known to the author.

Accessing the so-called off-detector scans, the film thickness dependent increase of the short wavelength cut-off R_c describing the changes in the surface morphology was measured. Figure 4.6 shows these off-detector scans for a selected film thickness of $d = 35$ nm. From the top to the bottom q_y increases in steps of $\Delta q_y = 1.8 \times 10^{-3}\ nm^{-1}$. The curves are shifted against each other for clarity. The amplitude of the fringes resulting from resonant diffuse scattering decreases with increasing q_y. This indicates the loss of correlation at smaller in-plane length scales while at long in-plane length scales the substrate and the polymer-vacuum interface are still correlated. Thus, the behavior of the physically cross-linked thin nbc-PNIPAM hydrogel films is qualitatively identical to the behavior of thin homopolymer films. However, the thickness dependence of the cut-off is different. Within the experimental error, independent of the film thickness a constant cut-off at $R_c = 16.2$ nm is detected. This value is very similar to $2R_H = 15.6$ nm determined for the size of the nbc-PNIPAM objects in dioxane. Thus, one might conclude that the micelle structure installed in solution defines an object size which cannot deform to follow the roughness spectrum of the solid support.

d. Lateral Structures Inside the Dry Hydrogel Films. The adsorption of such micelles or vesicles of polystyrene-*b*-poly(*N*-isopropylacrylamide) (PS-*b*-PNIPAM) diblock copolymers on a gold surface from aqueous solution revealed that the micelles and vesicles were intact with some deformation when they were deposited on the surface [YY06]. However, on strongly interacting surfaces, the micelles are deformed and even micelle or vesicle fusion into layered films can occur.

nbc-PNIPAM films with thicknesses larger than 5 nm are physically cross-linked hydrogels because during spin-coating with increasing concentration of the deposited nbc-PNIPAM solution on the solid support the bridging of micelles in addition to entanglement favors the gelation. Thus, an internal structure comparable to the microphase separation structure in triblock copolymers with hydrophobic end blocks is expected. Figure 4.5b shows out-of plane scans cut from the two-dimensional μGISAXS data. None of the scattering curves exhibit a strong intensity peak such as one will expect for microphase-separated systems. Instead, a weak and broad intensity peak at large q_y values is present, and the

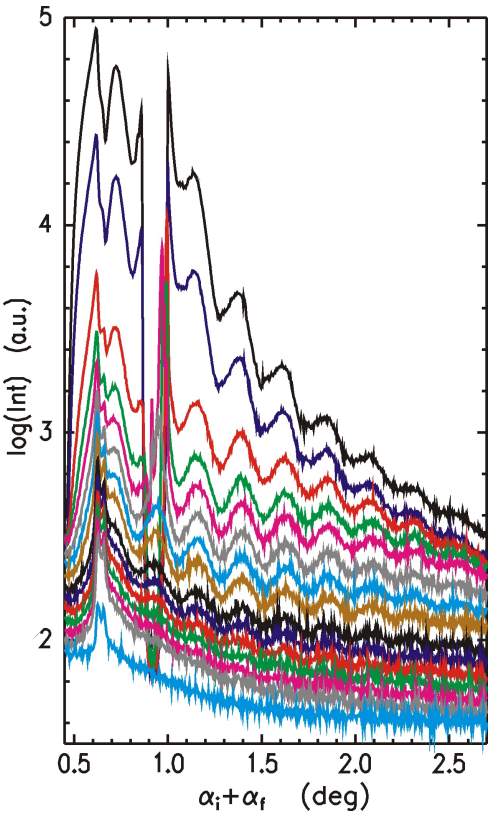

Figure 4.6: Off-detector scans measured at the angle of incidence $\alpha_i = 0.465°$ for a nbc-PNIPAM film with a film thickness of 35 nm at different values of q_y showing the disappearance of interference fringes of the resonant diffuse scattering. The offset in q_y increases from the top to the bottom. For clarity, the curves are shifted against each other.

intensity rises toward smaller q_y values. The rise in intensity is due to the presence of large-scale structures, which are not resolved in the scattering experiment. Such a behavior is very common for many types of polymer thin film systems. Possible origins are contributions of long-ranged surface waves.

Identical to microphase-separated systems, the peak is a structure factor type information, giving a nearest-neighbor distance (e.g., between spheres in a matrix, cylinders in a matrix, or adjacent lamellae in case of a triblock copolymer). Thus, the thin nbc-PNIPAM films exhibit an internal structure, which differs from a well-defined microphase separation. The presence of a weak broad peak, instead of a strong sharp peak, is due to an increased deviation in the nearest-neighbor distances from its mean value, typically expressed with a Gaussian-type distribution with an increased full width at half-maximum. Therefore, in the investigated films the mean distance between adjacent regions of hydrophobic *n*-butyltrithiocarbonate end groups is more broadly distributed than in systems with long

end groups. A reason can be the broad distribution of the micellar size in the solution. The out-of plane cuts are fitted with a simplified model. This model accounts for a structure factor due to the distance between neighboring domains of hydrophobic chain ends in the PNIPAM matrix (denoted structure factor 1). Moreover, it includes a structure factor due to the presence of large heterogeneities (denoted structure factor 2) and takes the experimental resolution into account. Both structure factors are distributed with a Gaussian type. The form factor (spherical shape of the micelles) is omitted due to the polydispersity of the micelles as probed in solution and due to the gelation of the micelles in the thin film. The solid lines in figure 4.5b show the corresponding fits to the out-of plane scans. The resulting mean distance between domains of chain ends is 25 nm. Compared to the micellar size detected in solution, the micelles are indeed bridged and entangled inside the film. The resulting distance corresponding to structure factor 2 decreases from 600 to 400 nm with increasing film thickness. In addition, for films with thicknesses lower than 30 nm, structure factor 1 is more pronounced than structure factor 2 while for thicker films, the situation is opposite. Thus, the heterogeneities are more densely populated in thicker films, or in other words, thicker films are less perfect with respect to the inner structure. The nature of the heterogeneities remains undetermined; however, errors in the positioning of hydrophobic domains, such as merging of two or more domains, are quite likely. A possible reason is the increased concentration, which was used for spin-coating of films with increased thicknesses. At high concentrations, already in solution larger, entangled associates of core-shell type micelles might have formed, which cause large-scale density inhomogeneities embedded in the thin film.

4.4 Swelling Experiments

To address the LCST behavior in thin films as a function of the degree of swelling, the films are exposed to saturated water vapor. For this purpose a temperature-controlled swelling chamber with a water reservoir inside was operated (see chapter 3.7). The thickness of dry films and of swollen films is measured as a function of temperature with optical interference. Starting at room temperature, each sample is allowed to equilibrate after each temperature increase by $\Delta T = 1°C$ for 30 min. Equilibration is concluded from the absence of any changes in the spectra of the optical interference measurements. The reported temperature-dependent changes are reversible. The resulting spectra are fitted including changes in the refractive index due to incorporation of water. The optical constant of PNIPAM is taken as reference for the dry film.

The thicknesses of the dry films agree well with the values determined with X-ray reflectivity. Exposed to saturated water vapor atmosphere, a clear response in terms of swelling is observed at room temperature. Figure 4.7 shows a very strong film thickness dependence of the total swelling. Ultrathin films with a thickness of 10.5 nm, which is twice the minimum thickness installable for the given surface energy of the SiO_x, exhibit a swelling by a factor of 6.5 as compared to the dry film (triangles in figure 4.7) and a factor of 2.9 as compared to the collapsed film at 34 °C (circles in figure 4.7). With increasing film thickness the nbc-PNIPAM films undergo swelling with a decreasing factor. In case of the 200 nm thick film the swollen film thickness increases only by a factor 1.3 as compared to the dry film. With the net volume change in water for PNIPAM hydrogels being around a factor of 8-10 (changes in volume of a factor of 10 have been reported) [HS95], corresponding to a one-dimensional size increase of 2-3, the observed swelling factors for ultrathin films are surprisingly high - even more because one needs to take into account that the solid substrate is not deformable and thus a net swelling can only occur in one direction along the surface normal.

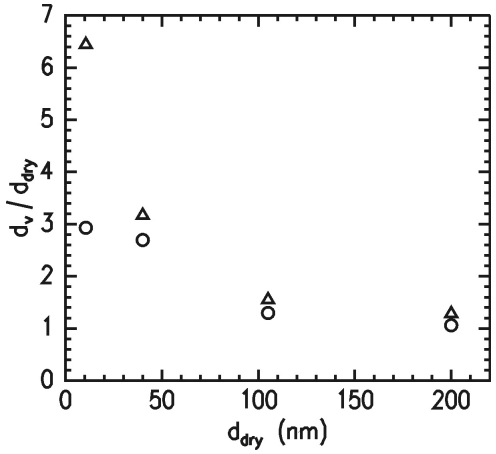

Figure 4.7: Thickness of the nbc-PNIPAM films exposed to saturated water vapor d_v at 21.7 °C (triangles) and 34 °C (circles) normalized by the thickness of the dry films in air d_{dry}.

In literature only a few swelling experiments for thin PNIPAM films are performed, and most of them were related to end-grafted PNIPAM [YQ95, KY98, YH06]. The conformation of end-tethered PNIPAM chains with thicknesses below 4 nm and a low surface density at the interface of silicon with D_2O and d-acetone was investigated with neutron reflection. No conformational change with temperature was detected for the lowest

molecular weight sample (33K), which is comparable to the PNIPAM block used in this investigation. Only a slight change in conformation with temperature was detected for the higher molecular weight sample (220K) [YH03]. In contrast, for larger film thicknesses of 25-150 nm the swollen film thickness decreased by a factor of 2 upon increasing the temperature from 25 to 40 °C [OT98].

For a film thickness range of 5-35 nm Hirata et al. observed a linear increase due to swelling by a factor of 4.6, comparing the dry with the swollen film below the transition temperature [HI04]. However, the experimental conditions were considerably different because a reactive copolymer (co-PNIPAM) was used, and layers were immobilized on a gold surface with a selfassembled monolayer (OH-SAM) by grafting one chain end to the surface. Moreover, swelling was performed in Dulbecco's phosphate buffered saline without calcium and magnesium (Nissui Pharmaceutical, Tokyo).

Block copolymer films with one PNIPAM block, adsorbed sequentially by the layer-by-layer technique, were observed to show only a very weak response to temperature changes. The decrease in thickness of the adsorbed planar film was below 10% and, moreover, irreversible. The strong interdigitation between adjacent layers in the case of polyelectrolyte multilayers leads to an additional restriction of the chain dynamics and swelling [SR02]. So one reason for the strong swelling observed in this investigation might be the collapsed chain conformation, which is forced in the dry film due to the applied spin-coating technique. In combination with the hydrophilic substrate surface, which favors the PNIPAM segments as well as water, the swelling might be increased by a type of entropic spring change in the conformation of the micelles. With increasing film thickness this effect gets weaker because fewer nbc-PNIPAM molecules in the micelles are in a perturbed conformation. At a thickness of 40 nm the factor of 3.2 is reached when comparing the dry with the swollen film below the transition temperature. A further increase of the film thickness results in a weaker swelling.

Figure 4.8 shows the measured LCST behavior. The temperature-dependent changes of the film thickness measured for nbc-PNIPAM films exposed to saturated water vapor decrease with increasing film thickness (see figure 4.8a). In the derivative $\delta d/\delta T$ the transition temperature and the widths of the transition are visible (see figure 4.8b). Within the experimental errors the transition temperature is at 29 °C for the thin films and seems to shift towards lower temperatures for thicker films. In addition, the width of the tran-

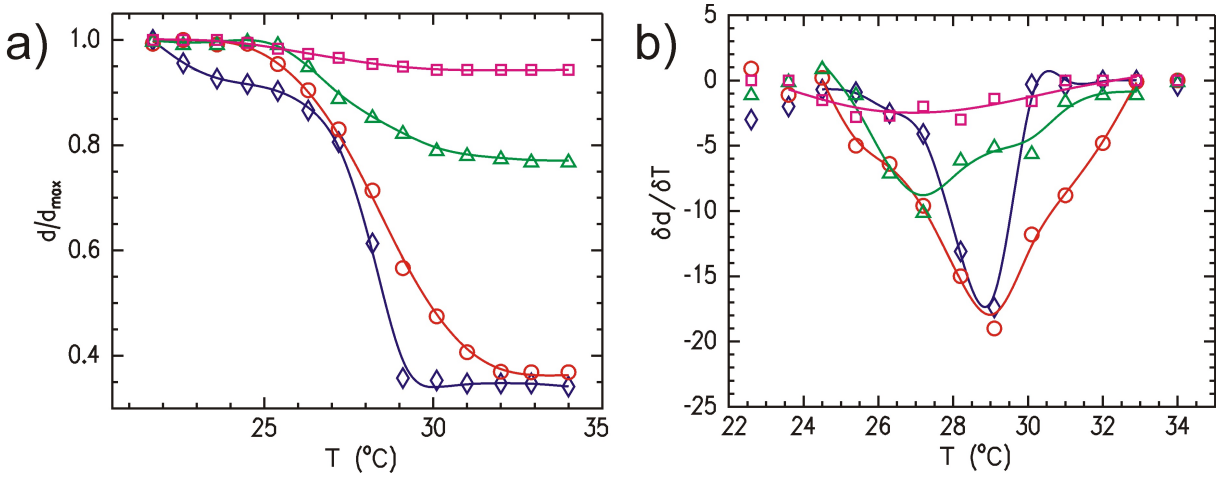

Figure 4.8: (a) Temperature-dependent changes of the film thickness measured for nbc-PNIPAM films exposed to saturated water vapor and (b) first derivative indicating the transition temperature and the width of the transition. The swelling curves are measured for film thickness of 10.5 (rhombs), 40 (circles), 105 (triangles), and 200 nm (squares). The solid lines are guides to the eye.

sition increases with film thickness. The 10.5 nm thick nbc-PNIPAM film exhibits a very sharp transition within a temperature change of $\Delta T = 2$ °C, which is small as compared to bulk samples, and at 200 nm film thickness the observed transition width is equivalent to the bulk behavior.

The introduction of hydrophobic end groups was observed to decrease the LCST temperature in bulk samples. Thus, in solution we have observed already a decrease of the transition temperature down to 30 °C. In thin films the transition temperature is decreased slightly further, which might result from a confinement into a thin film or from the interaction with the interfaces (substrate and water vapor).

Because of the missing or weak response, which was so far observable in thin films on flat solid supports, confined PNIPAM was realized by encapsulation into polyelectrolyte microcapsules. The transition temperature inside the capsules was observed to be reduced as compared to bulk PNIPAM by 2 °C because the capsule wall protects the PNIPAM, but the transition temperature still follows the trend of a lower LCST with higher salt concentration of the solution [PM06].

In addition, the missing decrease in the LCST temperature in case of thin plasma polymerized PNIPAM films strongly underlines the sensitivity of the transition to the molecular

structure [CX05]. However, confinement typically would result in a lower transition temperature in stronger confinement, and thus with increasing film thickness the value should approach the bulk value. As a consequence, it is more likely that the interaction with the interfaces affects the transition temperature.

4.5 Conclusion

Thin nbc-PNIPAM films are successfully prepared on SiO_x surfaces using spin-coating. The very short end groups can be regarded as degraded hydrophobic blocks of an ABA-type block copolymer (A denoting a hydrophobic and B a thermosensitive block). The ABA block copolymers can be swollen by midblock selective solvents, leading to physically cross-linked gels, where the end-block domains form physical cross-links. This concept still works for very short end groups, and correspondingly the prepared nbc-PNIPAM films exhibit an internal structure due to the microphase separation of the hydrophilic and hydrophobic segments. The structure is expected in the analogy to triblock copolymer films and consists of small spherical domains of hydrophobic chain ends randomly distributed in a matrix of PNIPAM with a measured neighboring distance.

In the thin film geometry the thermosensitivity is still present for the investigated nbc-PNIPAM films. Thus, omitting reactive groups, spin-coating results in physically cross-linked hydrogel films on solid supports. These films are not anchored and only attached to the support by the polymer-solid interaction. Therefore, such kind of responsive hydrogel films exhibits a much stronger response to the external stimulus as compared to anchored ones. The transition temperature is only slightly reduced as compared to the bulk. Therefore, the prepared films maintain the interesting features of PNIPAM revealed in the strength of the transition and by the transition temperature which is slightly above room temperature.

Thus, with respect to application, the presented system of end-capped PNIPAM thin films prepared with spin-coating appears to be interesting. In contrast to most other reported thin PNIPAM films, the thickness can be tuned over a wide range (from 5 to 240 nm) and the thermal switching remains possible. This will open novel possibilities in applications ranging from simple switches, solute separation, and drug delivery to tissue culture substrates and controlled adsorption of biopolymers.

Chapter 5

Gold Coated End-capped PNIPAM Thin Film

5.1 Introduction

In chapter 4, PNIPAM end-capped with *n*-butyltrithiocarbonate (nbc-PNIPAM) thin films have been deeply investigated [WW08]. This end-capped PNIPAM can be understood as the extreme of a triblock copolymer by showing an internal structure and a strong swelling even in water vapor [WW08]. Regarding the response time, bulk hydrogels are slow, promoting micro-gels [PR00, MMJ95, KM08, SS08] and thin films [TS05, SMJ03, SMJ04] to be considered as better systems with shorter response times. The volume change appears much faster if the hydrogel dimensions are in the sub-micrometer range. In particular, thin films allow for advanced applications such as thermoresponsive surfaces, miniaturized sensor systems and nano-switches [TPA06, GM07, GM08, KD09]. Whereas thermoresponsive surfaces make use of a change in the wetting properties, triggered by a change in temperature, miniaturized sensor systems and nano-switches are based on the change in hydrogel film thickness, because the surface area is fixed [WW08].

A simplified thin film sensor and nano-switch will consist of the active (sensor) layer and a metal top-layer. The active layer contains PNIPAM. In the present investigation nbc-PNIAPM and a gold top-layer are used. Central aim of this work is to probe the swelling and switching kinetics of such gold coated nbc-PNIPAM films. These films are exposed to water vapor atmosphere to detect the swelling kinetics and capacity, resembling the sensor function. In addition, these films are switched by a temperature jump from a temperature

well below the LCST to a temperature well above the LCST and then back to the temperature below the LCST again. Such a temperature jump operates the film as a nano-switch.

With the use of deuterated water and protonated nbc-PNIPAM there is a good contrast to detect the amount of water absorbed inside the polymer layer by using neutron reflectivity. With neutron reflectivity the density profile along the surface normal is accessed. In-situ measurements allow for monitoring changes in the composition during contact with a surrounding (deuterated) water vapor. These measurements are complemented by atomic force microscopy to observe the surface morphology of the gold layer and by grazing incidence small angle x-ray scattering to detect lateral structures inside the nbc-PNIPAM films. Two different gold layer thicknesses are investigated: A thin gold layer of 0.4 nm nominal total thickness and a thick gold layer being nominally 5 nm thick.

This chapter has the following structure: The introduction is followed by the experimental section describing the sample preparation and the experimental process applied. The next sections show results and discussion of the gold layer deposition, the switching kinetics caused by the temperature jump, followed by the swelling kinetics and cyclic swelling. A conclusion ends the chapter.

5.2 Experimental Section

Materials. The polymer is the same one described in chapter 4, which is *n*-butyltrithiocarbonate end-capped poly(*N*-isopropylacrylamide), denoted nbc-PNIPAM. Deuterated water (D_2O) (purity 99.95 %) was purchased from Deutero GmbH. 1,4-dioxane was received from Acros. Dichloromethane, ammonia solutions (NH_3, 30-33 %), and hydrogen peroxide (H_2O_2, 30 %) were ordered from Carl Roth GmbH. Silicon substrates (Si 100, n-type) were purchased from Silchem.

Sample Preparation. The sample preparation process is also similar to that in chapter 4: The initial nbc-PNIPAM films were prepared with spin-coating (2000 rpm, 30 s) from a 1,4-dioxane solution at room temperature onto pre-cleaned Si substrates. A film thickness of 39 nm was selected by making use of the recently determined film thickness dependence on the concentration of the solution used in the spin-coating process [WW08]. In a second step the top gold layer was added by sputter deposition. For this purpose the

samples were mounted in a sputter deposition chamber [CS08] and the gold deposition was performed at an argon pressure of 4×10^{-3} mbar while the deposition rate was set to 0.43 nm/min. The final, two nominal gold layer thicknesses after deposition were 0.4 and 5 nm, respectively. The gold layers were investigated with AFM and neutron reflectivity measurements.

Temperature Jump Experiment. The initial dry, gold coated nbc-PNIPAM film of the desired gold layer thickness was mounted in a custom-made vapor chamber in air, thermostated to 23 °C and investigated. To prepare a swollen and equilibrated film for the temperature jump experiment, the vapor chamber was evacuated, and the water reservoir of the vapor chamber was filled with D_2O to install a saturated D_2O atmosphere. After reaching equilibrium of swelling water vapor atmosphere (230 min) the film coated with 0.4 nm gold was cycled in 7 swelling and deswelling cycles as described below. To initiate the temperature jump from 23 to 40 °C, the set up was thermostated to 40 °C and investigated with in-situ neutron reflectivity (time = 0). A rate of 3.1 °C/min for increasing the temperature in the set-up was applied. When the film reached the equilibrium state, the set-up was thermostated to 23 °C and investigated. The rate for decreasing the temperature was 1.1 °C/min. For the film coated with 5 nm gold, the experimental process is the same as the film coated with 0.4 nm gold except that before the temperature jump, the film coated with thicker gold layer was not cycled. Instead, it took the temperate jump immediately after reaching the swelling equilibrim state at 23 °C.

Swelling Cycle Protocol. The initial swelling process of the dry, gold coated nbc-PNIPAM film was the same as that described in the temperature jump experiment. The addition of D_2O marks the starting point of the water absorption kinetics (time = 0). Again, equilibrium of swelling was reached after 230 min and the film was fully swollen. The deswelling by removal of D_2O was initiated by pumping the vapor chamber through a vacuum pump (DIVAC 0.8 T, Leybold AG). Thus water release from the thin film occured and the gold coated nbc-PNIPAM film relaxed back in vacuum to a new dry state. This de-swollen film was used in the next swelling cycle as the initial dry film. To address the aging effects of the swelling in water vapor atmosphere, the swelling and deswelling cycles were repeated 7 times. Samples were investigated in-situ during these cycles with neutron reflectivity and ex-situ after individual cycles with the other experimental techniques.

Neutron Reflectivity and Off-specular Scattering The theory and the set-up of this

technique has been described in detail in chapter 2 and 3, respectively. Kinetic changes in the temperature jump experiment and in the swelling and deswelling cycles were probed by performing reflectivity scans every 14 s (10 s data acquisition time and 4 s data read-out time). In case of the 0.4 nm gold layer thickness 24 s were necessary to account for the weaker scattering signal as compared to the 5 nm thick gold layer samples. With static scattering experiments the initial gold coated nbc-PNIPAM films and the resulting de-swollen gold coated nbc-PNIPAM film at the end of each cycle were additionally probed. An increased counting time of 3600 s and a larger angular range with two fixed incident angles were operated.

The scattering length densities of 2.07×10^{-6} Å^{-2} for Si, 3.47×10^{-6} Å^{-2} for Si oxide, 0.88×10^{-6} Å^{-2} for nbc-PNIPAM, 4.2×10^{-6} Å^{-2} for gold and 6.36×10^{-6} Å^{-2} for D_2O were obtained from initial fits. These values agree with textbook ones.

5.3 Gold Layer Deposition

In order to have a basic model system for thin film sensors and nano-switches, the thin nbc-PNIPAM films on silicon supports are capped with a top gold layer via sputter deposition. Two different nominal gold layer thicknesses are selected, a small one (0.4 nm) and a big one (5 nm). The nbc-PNIPAM film thickness is kept fixed (39 nm) for both types of top layers. These initial films are characterized with neutron reflectivity and atomic force microscopy to detect the density profile along the surface normal and the surface morphology of the gold.

In figure 5.1 the neutron reflectivity data are displayed together with model fits using the approach as described in the experimental section. With two fixed incident angles in the static neutron reflectivity experiment a large rage of scattering vectors q_z is covered. In both curves the intensity modulation originating from the total nbc-PNIPAM film thickness is clearly visible. This is due to the high scattering length density (SLD) of the substrate and the gold top layer as compared to the polymer film. In addition, for the thick gold layer a weak long-wavelength modulation results from the thickness of the gold layer itself. For the thin gold layer this is not resolved.

The SLD profiles belonging to the fits shown in figure 5.1 are displayed in figure 5.2. Both profiles show a bilayer on top of the Si substrate. The nbc-PNIPAM layer agrees

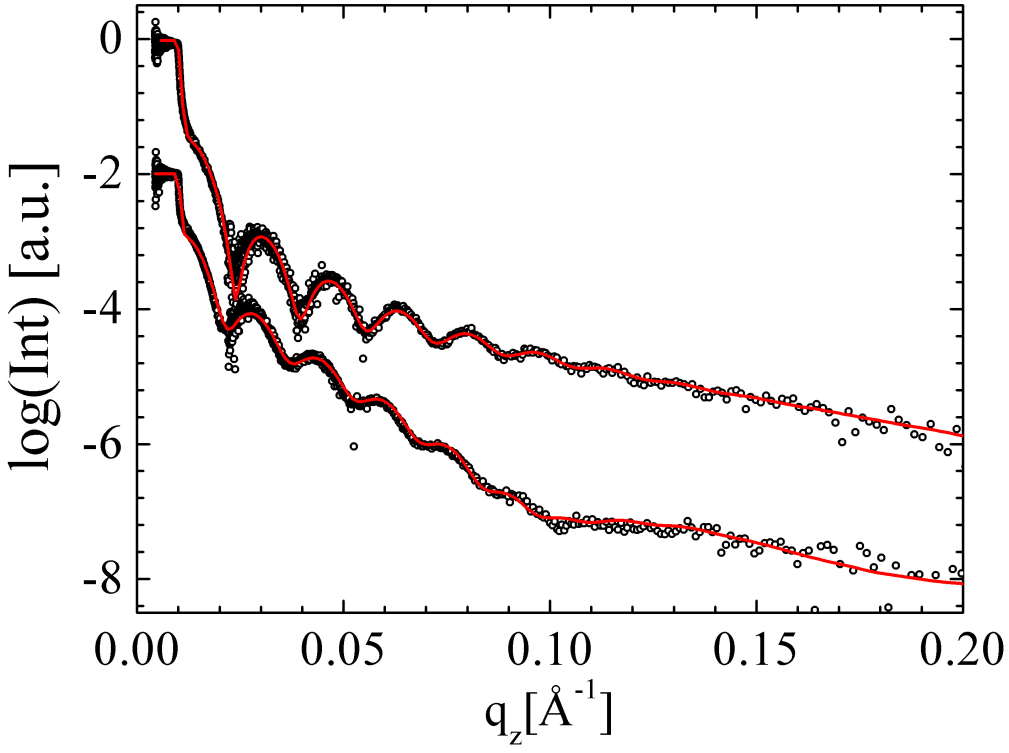

Figure 5.1: Neutron reflectivity data (dots) shown together with model fits (lines) for the 39.2 nm thick nbc-PNIPAM film coated with 0.4 nm nominal thick gold layer (top) and 5 nm nominal thick gold layer (bottom).

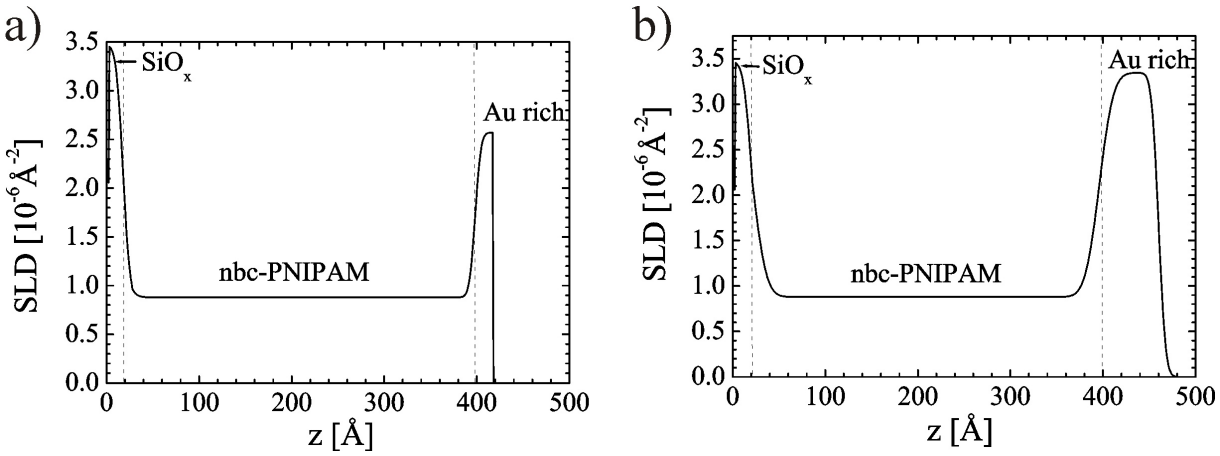

Figure 5.2: Resulting scattering length density (SLD) profiles of the two 39.2 nm thick nbc-PNIPAM films coated with a (a) 0.4 nm nominal thick gold layer and (b) 5 nm nominal thick gold layer.

well with the SLD value expected for this polymer. An internal structure caused by the end-groups is not resolved due to a missing contrast between *n*-butyltrithiocarbonate and

poly(*N*-isopropylacrylamide) in the neutron scattering experiment. As expected from the different sputter deposition times used in the preparation of the gold layers, the gold layers show the desired difference in thickness (nominal values 0.4 versus 5 nm). However, the nominal thicknesses are of course not obtained due to the complex process of gold deposition on the polymer material [KG09]. Moreover, the SLD values of the gold layers are smaller as compared to bulk gold and depend on the thickness. In case of the thin layer a smaller SLD value is present as compared to the thick one. The thin gold layer extends over 1.9 nm and has a low amount of only 21 vol% gold. The thick gold layer spreads over 6.5 nm with 77 vol% gold. Thus both gold layers exhibit an extension along the surface normal which exceeds the nominal value by 1.5 nm. From the profile it is obvious that gold diffuses into the nbc-PNIPAM surface region and that the gold surface is less flat as compared to the pure nbc-PNIPAM film surface (without gold deposition). Figure 5.3 visualizes the corresponding structure of both films. It includes already information from the atomic force microscopy (AFM) measurements about the lateral surface structure of the gold films.

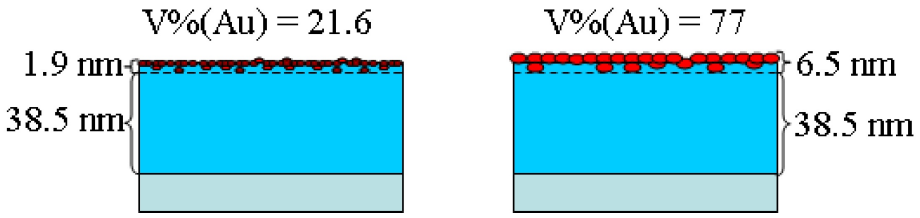

Figure 5.3: Schematic side view of the bilayer films obtained by sputter deposition of gold on nbc-PNIPAM films: (left) 0.4 nm nominal gold layer thickness and (right) 5 nm.

Whereas neutron reflectivity is sensitive to the structural information being projected onto the surface normal, AFM accesses lateral information [MBP05]. As sketched in figure 5.3 and shown by the AFM data presented in figure 5.4, the thin gold film consists of small sized, circular-shaped gold grains, whereas the thick gold film shows larger gold grains. A circular shape of the clusters is expected from the non-wetting behavior of gold on polymer surfaces [MBP05, VBC99]. Consequently, a 3D cluster growth (Volmer-Weber growth) is preferred over a 2D layer-by-layer growth (Frank-Van der Merwe growth) expected for the wetting case. In the thin gold film the gold structures have a mean size of 25 nm and on the thick gold film this value is increased to 55 nm. Such increase of the gold structure with increasing gold layer thickness is in agreement with the typical growth behavior of gold on polymer surfaces [KG09]. For both samples the gold clusters have grown to a

size in which the mean diameter is close to the mean correlation distance between two clusters; i.e., the clusters are in close contact with each other. Therefore both, the thin and the thick gold film, belong to the coarsening stage of gold on polymer as described in the reference [KG09]. In this stage coalescence is no longer dependent on migration, and the clusters grow rapidly in size. The same holds for the distance and the thickness. A detailed investigation of the growth behavior of gold on nbc-PNIPAM is beyond the scope of this thesis. Important is that both gold layers are closed layers with a grain morphology.

5.4 Switching Kinetics

a. Jump from 23 to 40 °C. The equilibrated bilayer films are exposed to saturated (deuterated) water vapor atmosphere in a custom-made vapor chamber. At the initial temperature of 23 °C nbc-PNIPAM is below its LCST and thus the films are swollen with water [AK00, KP01, KP06, KT08, MZ09]. The swelling kinetics and the cycling necessary to reach equilibrated films are described in the next section. Here films are considered to have reached an equilibrium regarding the swelling in water vapor atmosphere. With a temperature jump above the LCST the switching kinetics are determined for both gold layer thicknesses. A jump to 40 °C is chosen because for thin nbc-PNIPAM films the LCST is significantly more spread out in temperature as compared to solutions [WW08]. For 39 nm nbc-PNIPAM films a LCST at 29 °C is determined [WW08].

Due to the use of deuterated water a good contrast is acquired in the neutron reflectivity experiment and one can follow the temperature jump with a high time resolution.

In figure 5.5, a representative 2D detector pattern of the scattered intensity (displayed as a function of wavelength λ and the exit angle α_f) is shown. Because off-specular neutron intensities are significantly lower than the specular ones, a detailed analysis of intensity as a function of lateral scattering vector component q_x is impossible for the kinetic data. The necessary improvement of statistics is achieved by an integration of the off-specular intensities. Thus to keep a very high time resolution (14 s between successive neutron reflectivity curves) of the scattering experiment and to account for the kinetic changes of the films due to the temperature jump, an integration of intensities is performed in reciprocal space rather than in the time domain (by an increase of the counting time). The black boxes in figure 5.5a mark selected regions in the intensity, which are used for the in-

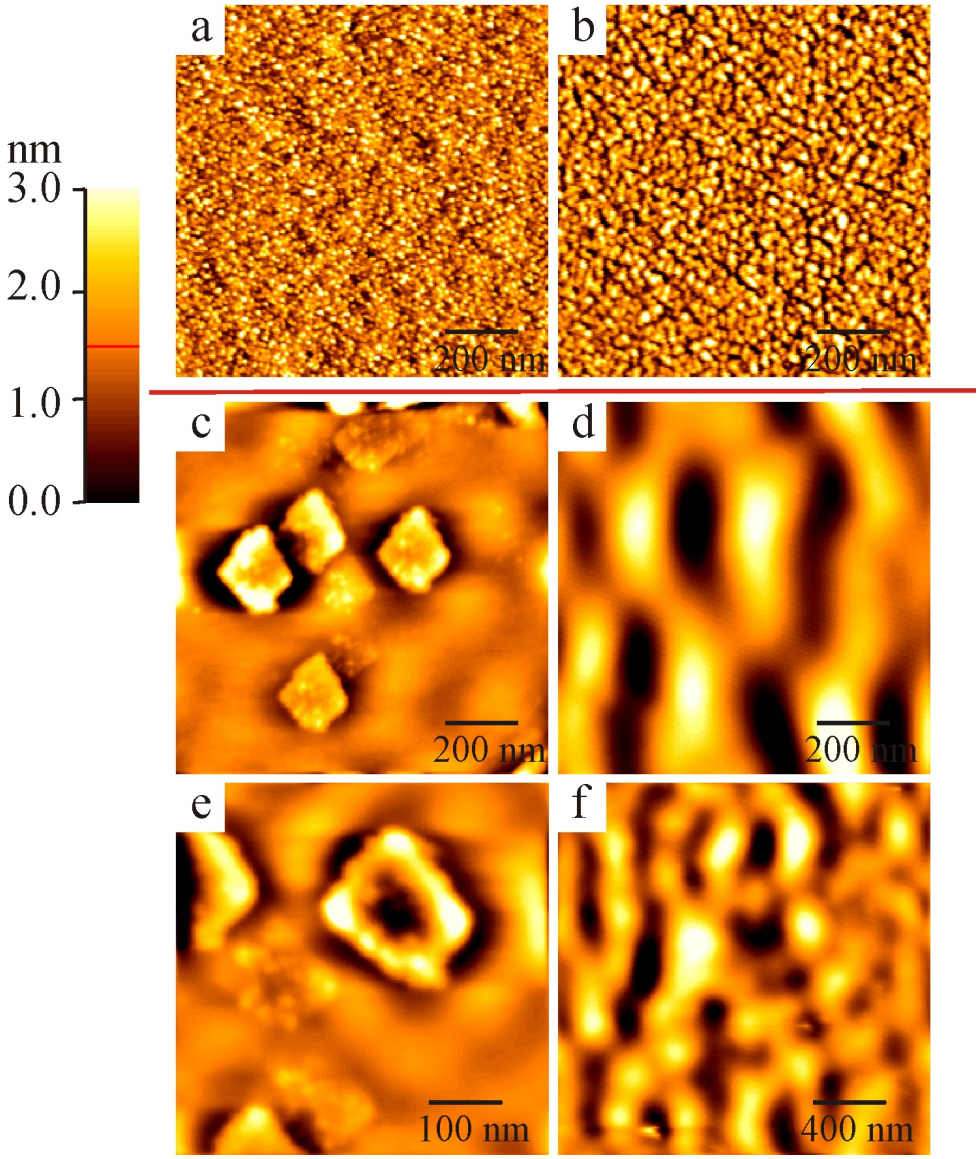

Figure 5.4: Topography AFM images of the bilayer films: (a,c,e) thin and (b,d,f) thick gold layer samples show different morphologies (a,b) before being subjected to water vapor atmosphere and (c,d,e,f) after the temperature jump experiments. The scan size for (a-d) is $1 \times 1\ \mu m^2$, for (e) is $0.5 \times 0.5\ \mu m^2$, and for (f) is $2 \times 2\ \mu m^2$. The structure height increases with the brightness of the structures in the images. The height scale bar range is 0 to 3 nm.

tegration and further analysis: The integration region of off-specular scattered intensities are for the Yoneda peak intensities of deuterated material ($Y1$) and protonated material ($Y2$), respectively. For comparison the specularly reflected intensity (M) is integrated in a minimum of the reflectivity as well to monitor changes in the film thickness.

Figures 5.5b and 5.5c show the time evolution of specular reflectivity (M), and off-specular

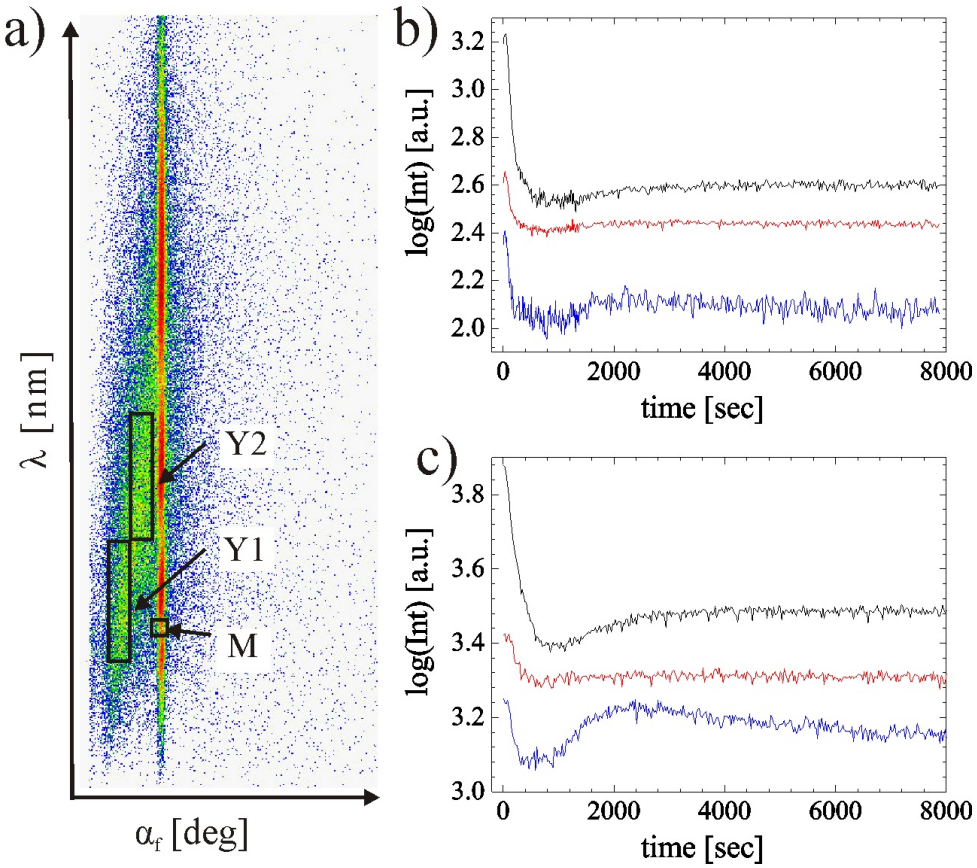

Figure 5.5: (a) Representative 2D detector pattern of the scattered intensity displayed in the wavelength λ to exit angle α_f presentation. The black boxes mark the areas integrated for the analysis of diffuse scattering. Intensities integrated over the areas *M* (top), *Y1* (middle), and *Y2* (bottom) (as explained in the text) are shown as a function of time for the (b) thick and (c) thin gold layer sample.

reflectivities (*Y1*, *Y2*) for the temperature jump. Due to the jump above the LCST deuterated water is repelled from the nbc-PNIPAM films [KT08] and the SLD of the films decreases. This causes a decrease of the reflected intensity and a shift of the position of the total reflection edge towards a larger λ values. Accordingly, the intensity in the region *M* decreases with repelling of D_2O. Due to a loss of contrast the off-specular intensities *Y1* and *Y2* decrease both with time as well. In the swollen state D_2O had selectively diffused into parts of the film causing this contrast which upon extraction of D_2O gets lost. However, figures 5.5b and 5.5c show that the decay is not monotonic and the all over behavior is more complex.

A more detailed analysis of the kinetics of the temperature jump is achieved by fitting the individual neutron reflectivity curves [NA06, PLG54]. In these fits the bilayer sample

is modeled with a main nbc-PNIPAM layer and a second gold-rich top-layer in agreement with the findings from the static samples. Figure 5.6 shows a selection of fitted neutron reflectivity curves for both gold layer film thickness and a two dimensional intensity presentation (mapping) of these specular intensities for both temperature jump experiments.

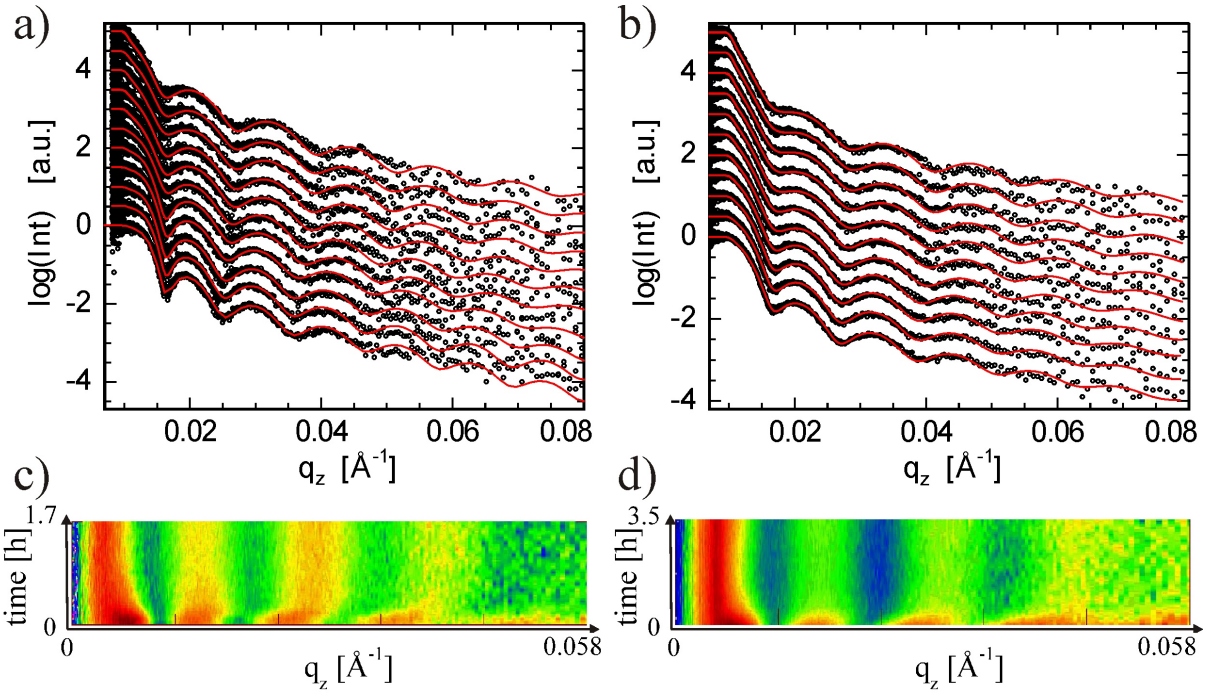

Figure 5.6: Comparison of the kinetics of the temperature jump of the (a,c) thick and (b,d) thin gold layer sample. In (a,b) the measured reflectivities (dots) are shown with the fits to the data (lines). The curves are shifted along the y-axis for clarity of the presentation. (c,d) are mappings of the measured specular neutron reflectivity versus time. The differences in colors show the differences in scattered intensities (red is high intensity, blue is low intensity).

For both films the critical angle of total external reflection shifts towards smaller values of the scattering vector component q_z and the over all reflected intensity decreases. Both observations result from D_2O which is repelled out of the nbc-PNIPAM film [WW09a]. Moreover, the wavelength of the intensity oscillations increases with time which shows that the films both get thinner. From a comparison of figure 5.6c and figure 5.6d it is notable that the sample with the thin gold layer reacts faster to the temperature jump as compared to the thick gold layer. Parameters extracted from the fit to the reflectivity data are shown in figure 5.7 as a function of time. From the changes of the SLD values, the D_2O volume fraction $V\%_{D_2O}$ of the film is calculated using

$$V\%_{D_2O} = \frac{n - n_1}{n_2 - n_1} \tag{5.1}$$

where n denotes the in-situ probed SLD of the film, n_1 the initial SLD of the dry film, and n_2 the SLD of D_2O.

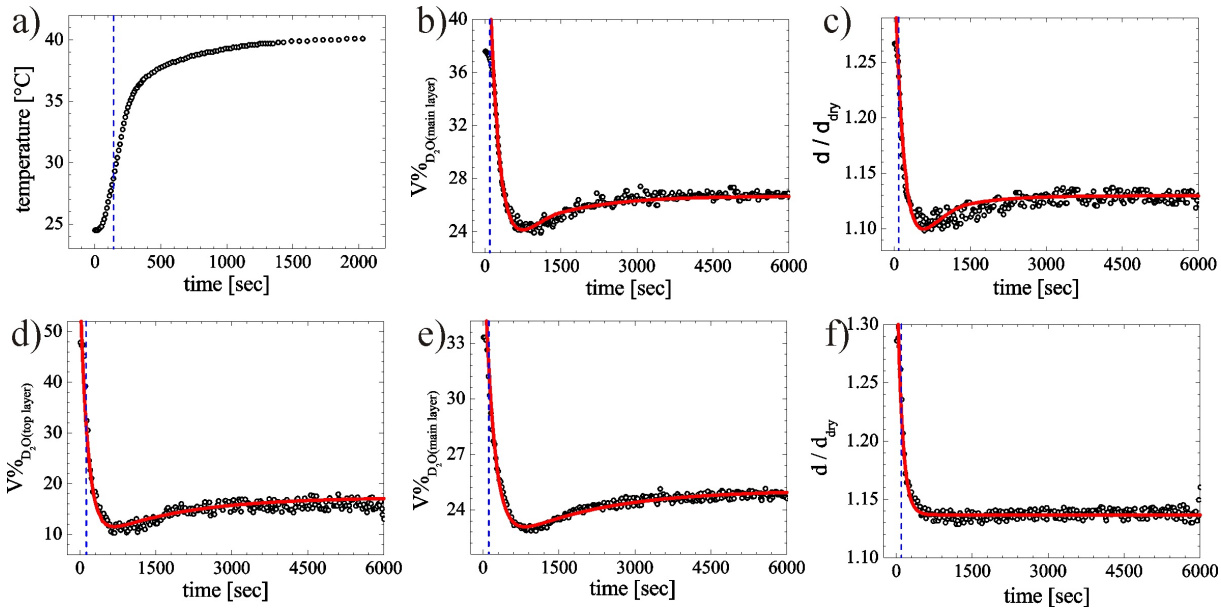

Figure 5.7: Switching kinetics from 23 to 40 °C followed by neutron reflectivity: (a) temperature increases as a function of time in the film. Volume percentage of water (D_2O) in the main layer of the film is shown as a function of time (b) for the thick and (e) the thin gold layer. Time dependent change of the film thickness d normalized by the initial dry film thickness d_{dry} (c) for the thick and (f) the thin gold layer. Volume percentage of water in the top layer of the film is shown as a function of time (d) for the thin gold layer. LCST of the nbc-PNIPAM film is reached at a time marked by the dash line in all images.

The temperature increase in the bilayer sample is shown in figure 5.7a. After 110 s the LCST of 29 °C is reached (marked by the dashed line). The response of the thick gold layer film is presented in figure 5.7b and 5.7c. Because the gold layer contains 77 vol% gold, it remains unchanged during the temperature jump and is not displayed in figure 5.7. The nbc-PNIPAM film (main layer) below the thick gold layer reacts with a decrease of its water content from 38 to 24 vol%. This is accompanied by a decrease in the relative film thickness d/d_{dry} from 1.27 to 1.10. The characteristic time constant for this water release is 280 s. However, surprisingly this decrease is followed by a slight relaxation back to higher water content and larger film thickness (26.7 vol% and 1.13). The time constant of this relaxation is larger with 900 s. Already from the integrated intensities presented in figure 5.5 such a two step process was visible. Therefore, the temperature jump causes the nbc-PNIPAM film to collapse and afterwards slowly rearrange into a

different structure. In the relaxation a small amount of the surrounding water is uptaken again and correspondingly the film relaxes to a larger film thickness as compared to the collapse.

Table 5.1: values of $V\%_{D_2O}(\infty)$, τ_1, B_1, R, and D_c of the nbc-PNIPAM film coated with 5 nm gold.

	part No.	d/d_{dry}	$V\%_{D_2O}(\infty)$	$\tau_1/10^4$ s	B_1	R	$D_c/10^{-14}$ cm^2/s
main layer	1		24.1±0.3	280±2	0.80±0.02	0.38±0.02	5.25±0.08
	2		26.7±0.3	600±5	0.80±0.02	0.38±0.02	2.55±0.02
thickness	1	1.10±0.01		280±2	0.70±0.02	0.35±0.01	3.50±0.05
	2	1.13±0.01		900±5	0.80±0.02	0.38±0.01	1.34±0.02

Table 5.2: values of $V\%_{D_2O}(\infty)$, τ_1, B_1, R, and D_c of the nbc-PNIPAM film coated with 0.4 nm gold.

	part No.	d/d_{dry}	$V\%_{D_2O}(\infty)$	$\tau_1/10^4$ s	B_1	R	$D_c/10^{-14}$ cm^2/s
top layer	1		12.0±0.2	120±2	0.98±0.02	0.71±0.02	0.17±0.02
	2		15.0±0.2	1330±5	0.98±0.02	0.71±0.02	0.020±0.003
main layer	1		23.1±0.5	190±2	0.80±0.02	0.38±0.01	7.61±0.08
	2		25.0±0.5	1800±5	0.80±0.02	0.38±0.01	0.83±0.02
thickness		1.14±0.01		100±2	0.80±0.02	0.38±0.01	12.20±0.10

The solid lines in figure 5.7 are model fits based on the gel swelling and shrinking model by Li and Tanaka [LY90]. In this model swelling and shrinking follows first-order kinetics and is not considered to be a pure diffusion process. The detail of this model would be described in chapter 7. Recently, this model was used to describe the water storage in

PNIPAM based block copolymer films, which resist swelling [WW09a]. Despite the initial stages of the temperature jump experiment reported here, the observed behavior can be explained within this model by assuming a first fast shrinkage process followed by a second (small) slow re-swelling process. The initial stages will be influenced by the passing of the LCST and thus are not expected to match to such a simple model approach. According to this model, the swelling or shrinking of thin hydrogel films follows

$$\ln\left(\frac{V\%_{D_2O}(\infty) - V\%_{D_2O}}{V\%_{D_2O}(\infty)}\right) = \ln B_1 - t/\tau_1 \tag{5.2}$$

where τ_1 is the relaxtion time, B_1 and R are the parameters related to the shear modulus and the osmotic bulk modulus (see chapter 2), and D_c is the collective diffusion coefficient. The fitting results for the first process (marked as 1) and the second process (marked as 2) are listed in table 5.1 and 5.2.

Comparing now the thick gold layer film behavior (top row images in figure 5.7) with the one of the thin gold layer (bottom row images in figure 5.7) some differences are obvious. In contrast to the thick film, for the thin gold film, the gold layer itself (top layer) changes its water content (see figure 5.7d). This is caused by the small gold volume (21.6 vol%) of this layer, which means that most part of the layer is nbc-PNIPAM as well. The full film, main (nbc-PNIPAM) and top (gold and nbc-PNIPAM) part exhibit the same two step characteristics as seen for the sample with a thick gold layer as well. However, the time constants are different. The nbc-PNIPAM film reacts much faster, with a time constant of 190 s, as compared to the sample with a thick gold layer on top. In the sample with a thin gold layer the top part reacts even faster with a time constant of 120 s. The relaxation processes behave oppositely and relaxation takes 1800 and 1330 s for main and top layer of the thin gold layer sample, respectively. Due to the interaction with the gold in the top layer part a large amount of water is incorporated (48 vol%) before the temperature jump. The release is very strong and finally only 15 vol% is left. The nbc-PNIPAM layer behaves quite similar to the one with more gold on top and reduces its amount of water from 34 to 23 vol%. In the change of the relative film thickness d/d_{dry} the values reduce from 1.28 to 1.13 which is as well equal to the observation on the thick gold layer sample. However, the two step process is not visible and the change in relative film thickness appears to be a simple release.

b. Jump from 40 to 23 °C. After films reaching the equilibrium state at 40 °C, the temperature of the vapor chamber is jumped back to 23 °C and re-swelling of the films

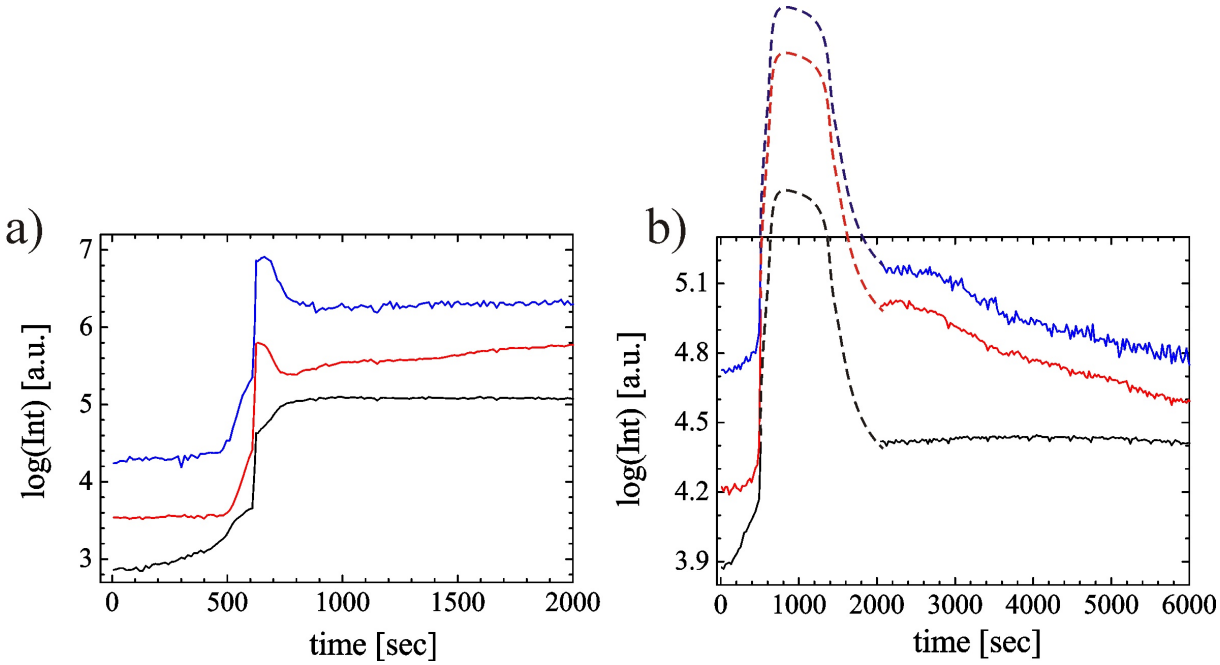

Figure 5.8: Switching kinetics from 40 to 23 °C followed by neutron reflectivity: Intensities integrated over the areas *M* (bottom), *Y1* (middle), and *Y2* (top) are shown as a function of time for the (a) thick and (b) thin gold layer sample.

happens. Figure 5.8 shows the time evolution of specular reflectivity (*M*), and off-specular reflectivities (*Y1*, *Y2*) for the temperature jump back. Due to the jump below the LCST deuterated water is incorporated into the nbc-PNIPAM films and the SLD of the films increases. This causes an increase of the reflected intensity and a shift of the position of the total reflection edge towards smaller λ values. Accordingly, the intensity in the region *M* increases with absorption of D_2O. Due to an increase of contrast the off-specular intensities *Y1* and *Y2* both increase with time as well. This contrast is due to in the swollen state D_2O selectively diffusing into parts of the film.

In figure 5.8a, which is corresponding to the film coated with a thick gold layer, the intensity in the region *M* shows a three-step increase: A slow increase in the first 600 s, followed by a sharp jump close to the LCST and finally a slow increase again until the film reaches an equilibrium state. The intensities in the region *Y1* and *Y2* both show a more complicate behavior: There is a small decay between the sharp increase of the intensity and the equilibrium state. In figure 5.8b, which is corresponding to the film coated with thin gold layer, the situation is even more complex: The intensities in the region *Y1* and *Y2* both show a slow and long decay after the sharp increase of intensity. Unfortunately, there is a gap (marked by the dash lines) in the data shown in figure 5.8b between 520 s

and 2040 s. This gap is caused by the intensity oversaturation of the detector during the measurement. The intensity gets too high and saturates the detector due to a large amount of deuterated water incorporated into the film within a short time close to the LCST. Otherwise, one might expect a similar peak as probed for the thin gold layer sample. However, this peak has to be even higher to cause the oversaturation of the detector (peaks marked by the dash lines).

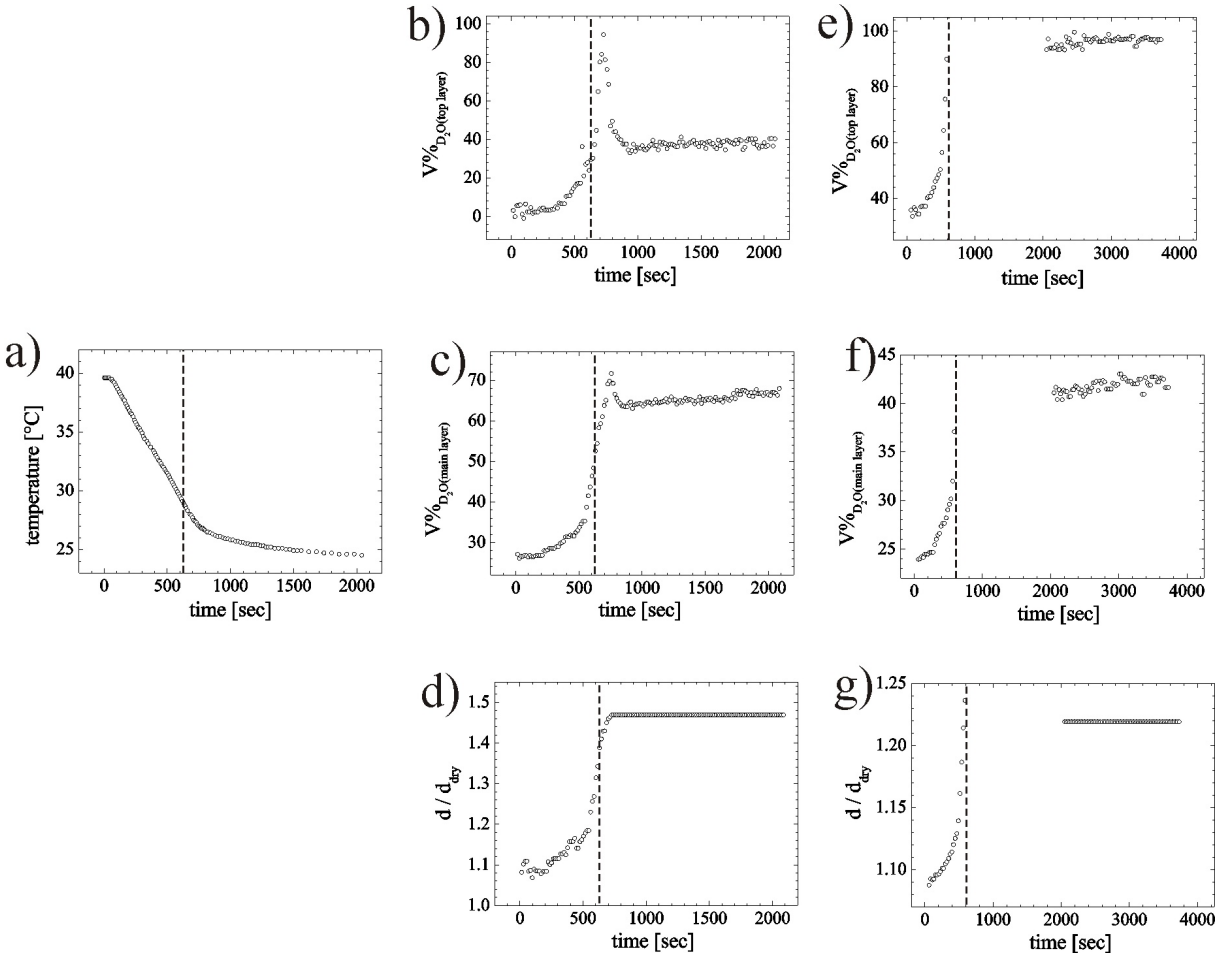

Figure 5.9: Switching kinetics from 40 to 23 °C followed by neutron reflectivity: (a) temperature decreases as a function of time in the film. Volume percentage of water (D_2O) in the top layer of the film is shown as a function of time (b) for the thick and (e) the thin gold layer. Volume percentage of water in the main layer of the film is shown as a function of time (c) for the thick and (f) the thin gold layer. Time dependent change of the film thickness d normalized by the initial dry film thickness d_{dry} (d) for the thick and (g) the thin gold layer. LCST of the nbc-PNIPAM film is reached at a time marked by the dash line in all images.

A more detailed analysis of the kinetics of the temperature jump back is achieved again

by fitting the individual neutron reflectivity curves. The temperature decrease in the bilayer sample is shown in figure 5.9a. After 620 s the LCST of 29 °C is reached (marked by the dashed line). The response of the thick gold layer film is presented in figure 5.9b, 5.9c and 5.9d. The nbc-PNIPAM film (main layer) below the thick gold layer reacts with an increase of its water content from 24 to 72 vol%, and then after a small decay, it reaches an equilibrium state with a water content of 65 vol%. This is accompanied by an increase in the relative film thickness d/d_{dry} from 1.10 to 1.48. The characteristic time constant for this water release is 150 s. Compared to the temperature jump from 23 to 40 °C, the characteristic time constant in this case is smaller which means the thick gold film responses faster during temperature decreasing. It should be addressed that in this case the rate of temperature decreasing is only 1/3 of the rate of temperature increasing. Thus, the response of films is much quicker than the change of temperature, which again confirms that this gold coated nbc-PNIPAM thin film is a fast response system. Another difference is the gold layer itself (top layer), which changes its water content (see figure 5.9b). This is caused by a small amount of water condensation. When the temperature is decreasing, the temperature of the sample decreases faster than the temperature of the vapor surrounding. Thus, the vapor condenses on the film surface and forms a thin water layer (the water content increasing from 0 to 90 vol%). However, when the film reaches an equilibrium state and the temperature becomes constant, most of this water layer evaporates to the surrounding atomosphere again (the water content decreasing from 90 to 35 vol%). The main layer also shows a small decay in the water content between its sharp swelling stage and equilibrium state. This is an opposite to the behavior of films jumping from a low temperature to a high temperature: The temperature jump causes the nbc-PNIPAM film to swell and afterwards slowly rearrange into a different structure. In the process a small amount of the surrounding water is repelled again and correspondingly the film relaxes to another swollen state.

Compared to the thick film, for the thin gold film, the behavior is similar but different in absolute values. The main layer of nbc-PNIPAM film below the gold layer reacts with an increase of its water content from 23 to 42 vol%. Due to the interaction with the gold in the top layer part and also the water condensition effect, the water content increases from 15 to 90 vol%. In the change of the relative film thickness d/d_{dry} the values increase from 1.09 to 1.22. The characteristic time constant for this water incorporation is 110 s which is a little smaller than that of thick gold film. Thus, the thin gold film response also faster than the thick one, which is similar to the process of temperature increasing.

Unfortunately, due to the gap in the experimental data, it is unknown what happens to the thin gold film during the time between 520 s and 2040 s and so there is no way to compare the thick and the thin gold films during this time interval.

Looking into the changes such temperature jump had made to the gold layer surface, again AFM is used. Figure 5.4 compares the morphology of the samples after being switched back and dried. Very clearly, the gold surface morphology is altered by this switching process. The gold structure has coarsened to characteristic lateral structures of 200 nm (thin gold layer) and 230 nm (thick gold layer). Moreover, a crystalline appearing morphology is present and the initial spheres of gold have merged into ribbon-like structures.

In comparison between both gold layer thicknesses, the thinner gold layer sample reacts faster and shows very similar switching characteristics of the main nbc-PNIPAM film regarding the total shrinkage d/d_{dry}. As a consequence, such type of bilayer film is better suited for applications related to nano-switches.

5.5 Swelling Kinetics

Because the thin gold layer appears better suited for switching kinetics this bilayer sample is investigated in detail regarding its swelling kinetics and aging as well. For this purpose a fresh, dry, gold coated nbc-PNIPAM film with 0.4 nm nominal gold layer thickness is mounted into the custom-made vapor chamber in air, thermostated to 23 °C. The swelling and deswelling cycle protocol is detailed in the experimental section. The addition of D_2O marks the starting point of the swelling kinetics (time = 0). 7 cycles were performed and the deswollen sample is always reused in the subsequent cycle again.

In figure 5.10 the measured neutron reflectivity curves are displayed. These curves show that basically after each complete swelling and deswelling cycle the bilayer sample is unchanged. Small changes occur only in the nbc-PNIPAM layer (main layer). Whereas the initially freshly used film contains no deuterated water, within the first two cycles the amount of D_2O increases to 5 vol%. In the following cycles this value remains constant. As reported for cyclic treatment of PNIPAM based diblock copolymer films such behavior has two origins [WW09a]: Water can be caused to remain by formation of strong chemical bonds between D_2O and PNIPAM molecules (bound water). Alternatively, H-D exchange

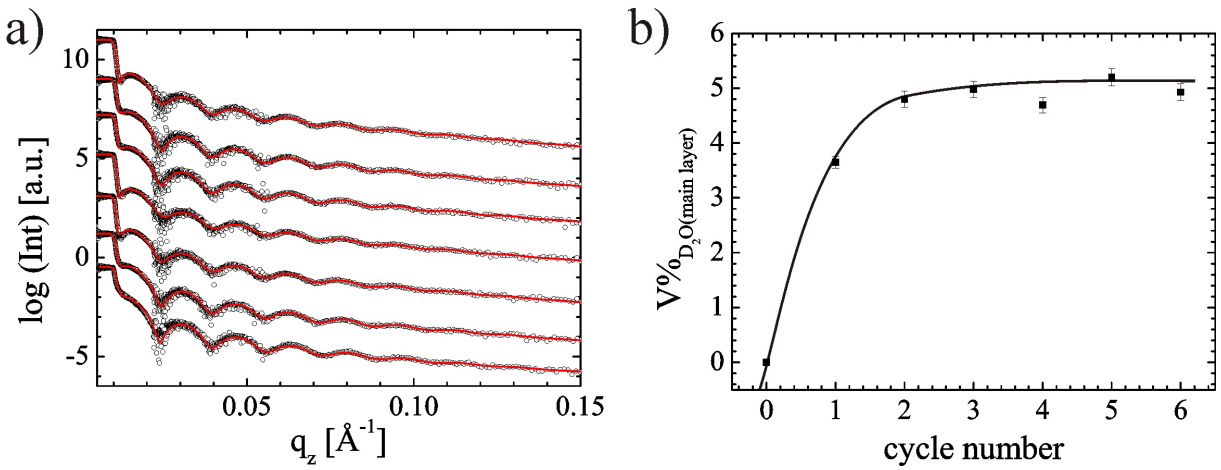

Figure 5.10: (a) Neutron reflectivity data (dots) shown together with model fits (lines) for the nbc-PNIPAM film coated with 0.4 nm nominal thick gold layer initially prepared (bottom curve) and measured after complete swelling-deswelling cycles (number of cycles increases from bottom to top). The curves are shifted for clarity. (b) Volume percentage of water in the main layer of the film as a function of cycle number.

occurring during water storage inside the film can give the impression of water that is not extractable. As compared to the diblock copolymer sample (investigated in reference [HS08]) no strong interface enrichment is found in the gold coated nbc-PNIPAM and the remaining amount is larger, perhaps due to the presence of the gold layer. 5 vol% of D_2O is found in the film after it is cycled to equilibrium (see figure 5.7b). Such an amount cannot totally result from the H-D exchange of the -CONH- moieties of the polymer, and thus some bound D_2O is present as well.

With grazing incidence small angle X-ray scattering (GISAXS) the cycled films are characterized concerning changes of the inner film structure. Figure 5.11 shows the vertical and horizontal cuts from the 2D GISAXS intensity. From the vertical cuts, it can be concluded that the perpendicular structure (correlated roughness, highlighted by the box in figure 5.10a) is installed in the first cycles and later damped with increasing cycle number. For large wavelengths within the limited experimental resolution, the substrate and the polymer-vacuum interface are correlated [MBP98b, MBP00]. So the long-ranged correlated nbc-PNIPAM film becomes better defined in the initial cycles and later independent in its surface structures from the substrate by slight roughening of the surface [MB99, MB01]. From the horizontal cuts no influence of the cycling on the inner lateral film structure is found. In good agreement with the pure nbc-PNPAM films of different thickness [WW08] the films investigated here show a weak peak in the intensity at

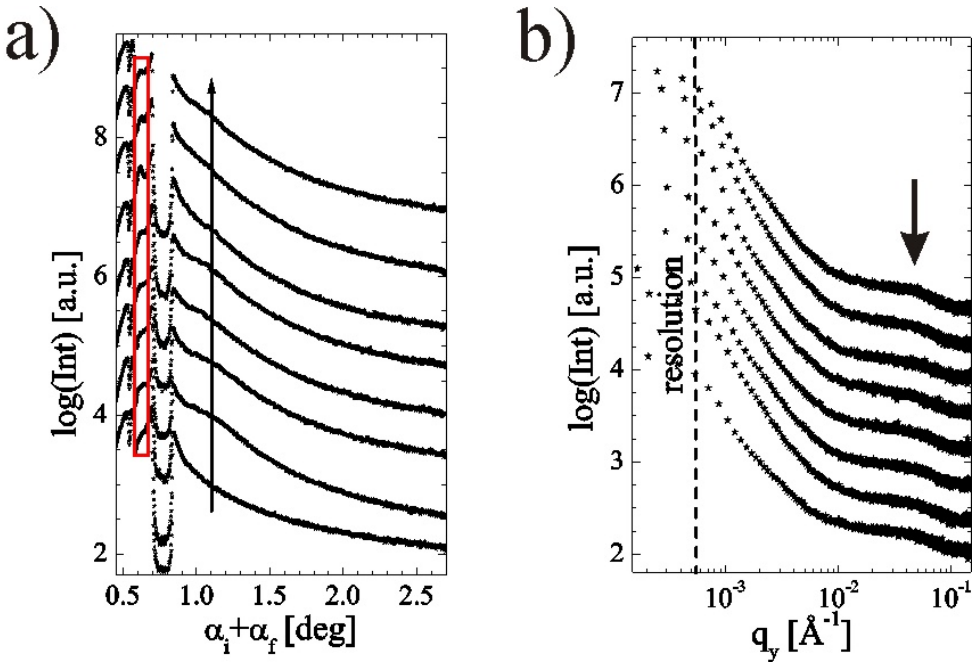

Figure 5.11: GISAXS data of nbc-PNIPAM films before swelling-deswelling cycle (bottom) and after seven swelling-deswelling cycles (subsequently shifted seven curves): (a) vertical cuts showing structures along the surface normal and (b) horizontal cuts (dots) showing in-plane structures.

large values of the scattering vector component q_y (marked with an arrow). Identical to micro-phase separated systems, the peak is a structure factor type information, showing that the thin nbc-PNIPAM films exhibit an internal structure. It resembles the distance between adjacent regions of hydrophobic *n*-butyltrithiocarbonate end groups in a PNIPAM matrix. The corresponding mean distance between domains of chain ends is 25 nm. Comparing this value with the micellar size detected in solution shows that the micelles are indeed bridged and entangled inside the film [WW08]. So GISAXS indicates no severe aging of the gold coated nbc-PNIPAM film which is important for applications.

During swelling and deswelling cycles in-situ GISAXS measurements are impossible due to radiation damage occurring at swollen nbc-PNIPAM films [WW09a]. As a consequence, in-situ neutron reflectivity and off-specular scattering are used again to investigate the time dependence of the cycling.

As detailed in the previous section, the integration of selected areas from the collected 2D neutron data is a strong tool to characterize the time dependent behavior. The same boxes are chosen as shown in figure 5.5. Therefore *Y1* refers to integration in a region of

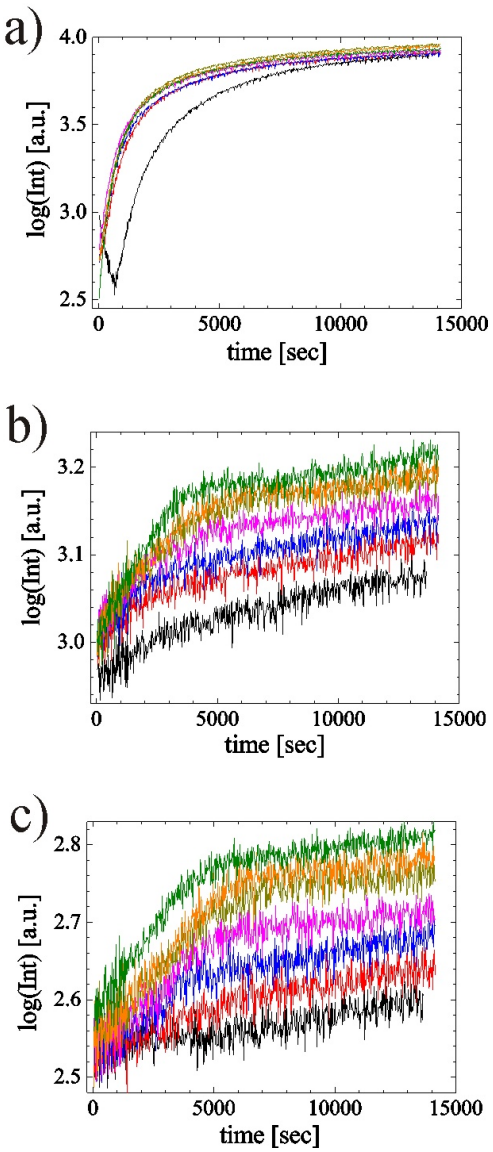

Figure 5.12: Integrated intensities of the 2D TOF neutron data with integration areas denoted (a) *M*, (b) *Y1* and (c) *Y2* showing the individual swelling behavior within the different cycles. From bottom to top the number of the cycle increases.

off-specular scattered intensities related to the Yoneda peak of deuterated material (see figure 5.12b) and *Y2* to protonated material (see figure 5.12c), respectively. For comparison the specularly reflected intensity (M) is integrated in a minimum of the reflectivity as well (see figure 5.12a).

Regarding the film thickness, despite the initial swelling, which behaves complex, in all swelling cycles the films swell by incorporation of water molecules. The initial swelling first requires a rearrangement of the molecules, which first causes even shrinkage before

the film swells. In contrast, the incorporation of D_2O results in an increase of the diffuse scattering. The off-specular intensities *Y1* and *Y2* increase with time due to the build-up of a lateral structure inside the nbc-PNIPAM film because D_2O selectively diffuses into parts of the film which are not occupied by the hydrophobic end-groups.

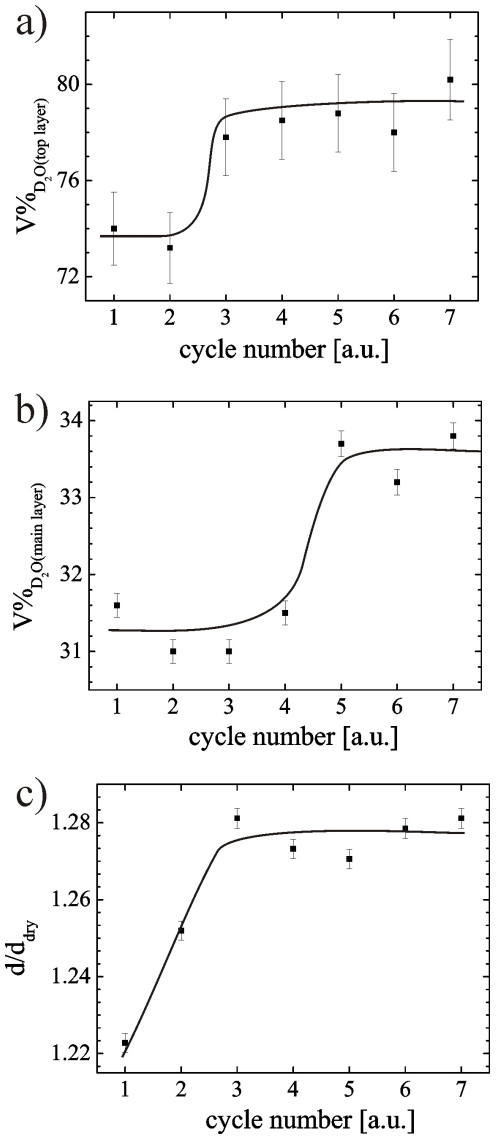

Figure 5.13: Maximum amount of water incorporated inside the (a) top part (gold and nbc-PNIPAM containing) and (b) main part (nbc-PNIPAM) at the end of each swelling cycle plotted as a function of the cycle number. (c) Cycle dependent change of the film thickness d normalized by the initial dry film thickness d_{dry}.

From a fit to the kinetic neutron reflectivity data the maximum amount of water is extracted which is incorporated inside the bilayer films and the degree of swelling (see figure

5.13). All together these data show that the initially prepared film improves after some cycles and is able to swell more and to incorporate more water. Thus again no aging is observed, which would reduce the film performance. After 5 cycles equilibrium is reached. The degree of swelling, as well as the amount of incorporated water are independent from the cycle number. In detail, the top part of the film, containing the gold, behaves different to the main part which is pure nbc-PNIPAM. In good agreement with the switching experiment, more water molecules are incorporated in the top part as compared to the main film, due to the interaction with the gold.

Regarding the extracted parameters, the cycled sample after 7 cycles is in good agreement with the starting condition of the temperature jump experiment. In saturated water vapor atmosphere the relative film thickness d/d_{dry} is 1.28, the nbc-PNIPAM film (main layer) water content is 34 vol% and the top layer contains nearly 80 vol% water (in figure 5.6d a smaller value is observed due to the fast reaction of the top layer to the temperature jump).

5.6 Conclusion

A simplified thin film sensor and nano-switch which consists of the active (sensor) layer and a metal top-layer in thin film geometry, are successfully prepared and characterized. nbc-PNIPAM is used with a gold layer on top which is deposited by sputter deposition. From the comparison of the two different gold layer thicknesses used in this investigation (nominal 0.4 nm and 5 nm), the thinner one turned out to be better suited for the use in switching due its faster response time. The structural characterization based on in-situ neutron scattering shows that at least 5 swelling and deswelling cycles of the bilayer films are necessary to achieve an equilibrium film structure regarding the increase of the film thickness caused by the swelling and the amount of water stored in the film. In the initial stages the films rearrange from the structure formed during the preparation. However, in the dry films this is not reflected by a marked rearrangement of the inner micro-phase separation-like demixing of PNIPAM and its end-groups, but caused by a change of the gold layer morphology. As the water molecules mainly have to pass this gold layer it is obvious that such rearrangement will influence the swelling performance. Nevertheless, this process is not giving rise to a severe aging of the nbc-PNIPAM film.

The observed switching behavior due to a temperature jump above the LCST is not just

a simple release of water molecules but a two step process. The water release and film shrinkage is followed by a relaxation of the molecules and a small secondary water uptake. Both processes are modeled within the swelling and deswelling model by Li and Tanaka [LY90]. Thus the incorporation of water molecules is not a simple diffusion process as observed previously for PNIPAM based block copolymer films.

With respect to applications however, one has to consider that the changes in film thickness are small, both in the switching and cycling. This is caused, on the one hand by the small value of the total nbc-PNIPAM film thickness used in this investigation, and on the other hand, by constraints added to the system due to the top gold layer. Pure nbc-PNIPAM films have shown a much stronger swelling if exposed to water vapor atmosphere [WW08]. Nevertheless, a thin gold layer is necessary for such applications to act as a contact material or as a capacitor. Based on the observations on block copolymer thin films with increased hydrophobic blocks which swell less if exposed to water vapor atmosphere [WW09a], the presented system appears quite optimized.

Chapter 6

PNIPAM Based Diblock and Triblock Thin Films

6.1 Introduction

In chapter 4 and 5, structures and kinetics of end-capped poly(*N*-isopropylacrylamide) (PNIPAM) thin films have been investigated in detail. It is known that the addition of hydrophobic chain ends to pure PNIPAM homopolymer films is a simple way to form internal cross-links to build up a gel. However, with an increasing hydrophobic block length, the swelling capability of thin films decreases [WW08]. Besides, slight changes in the chemical composition of PNIPAM have important consequences on the water/PNIPAM phase diagram. The LCST of PNIPAM can be raised or lowered via introduction of hydrophilic or hydrophobic comonomers, respectively [TLD75]. Moreover, the phase transition temperature depends not only on the level of hydrophobe incorporation and on its chemical structure but also on its position in the chain [KP01, CZ05]. Thus, although PNIPAM end-capped with a very short hydrophobic end group, *n*-butyltrithiocarbonate, turns out to be a good candidate for applications which can exhibit the strongest swelling, thereby maintaining the gel character [WW08], it is necessary and of interest to investigate PNIPAM based diblock and triblock copolymer with a longer hydrophobic group.

In most cases, polystyrene (PS) was chosen as the hydrophobic, glassy block, and diblock copolymers P(S-*b*-NIPAM) [NM04, HT04, ZW05, TK08], and occasionally also triblock copolymers P(S-*b*-NIPAM-*b*-S) were studied [LHH01, HS08, NA08]. Therefore, in the present work, a diblock copolymer P(S-*b*-NIPAM) and a triblock copolymer P(S-

b-NIPAM-*b*-S) are selected. Both copolymers have a similar volume fraction of the hydrophobic group (∼0.2). As a consequence, the influence of hydrophobic group length can be compared between them and an end-capped PNIPAM (denoted with nbc-PNIPAM) and the effects of the position of the hydrophobic group in the chain is studied.

6.2 Experimental Section

Materials. The diblock copolymer used is poly(styrene-*block*-*N*-isopropylacrylamide), denoted P(S-*b*-NIPAM), with a molecular weight of 24960 g mol^{-1}, and a volume fraction of PS in the copolymer of 0.20. The triblock copolymer used is poly(styrene-*block*-*N*-isopropylacrylamide-*block*-styrene), denoted P(S-*b*-NIPAM-*b*-S), with a molecular weight of 12300 g mol^{-1}, and a volume fraction of PS in the copolymer of 0.19.

Sample Preparation. Again, silicon with an oxide layer surface was used as the substrate material and cleaned following the base cleaning protocol as described in chapter 4. The initial dry films with different thicknesses were prepared by spin coating (2000 rpm, 30 s) from a 1,4-dioxane solution at room temperature onto the pre-cleaned Si substrates.

6.3 Structural Investigation

Microbeam grazing incidence small-angle X-ray scattering (μGISAXS) is well suited to investigate structures parallel to the surface, so-called lateral structures, and long-range correlations. In contrast to AFM which is limited to the sample surface, μGISAXS can probe structures also inside the film. Figure 6.1 shows the line cuts from the two-dimensional μGISAXS data measured for a representative set of P(S-*b*-NIPAM) films of different thicknesses.

In figure 6.1a the detector scans are shown. The specular peak is blocked by a beam stop to avoid damage of the sensitive detector. In addition to the Yoneda peaks, which are located at the critical angles of the investigated materials (Si, PS and PNIPAM), strong modulations in the intensity are detected. These strong modulations are caused by a partial phase coherence of X-ray waves diffusely scattered from different interfaces, which yields a concentration of intensity in narrow sheets in reciprocal space. The detector

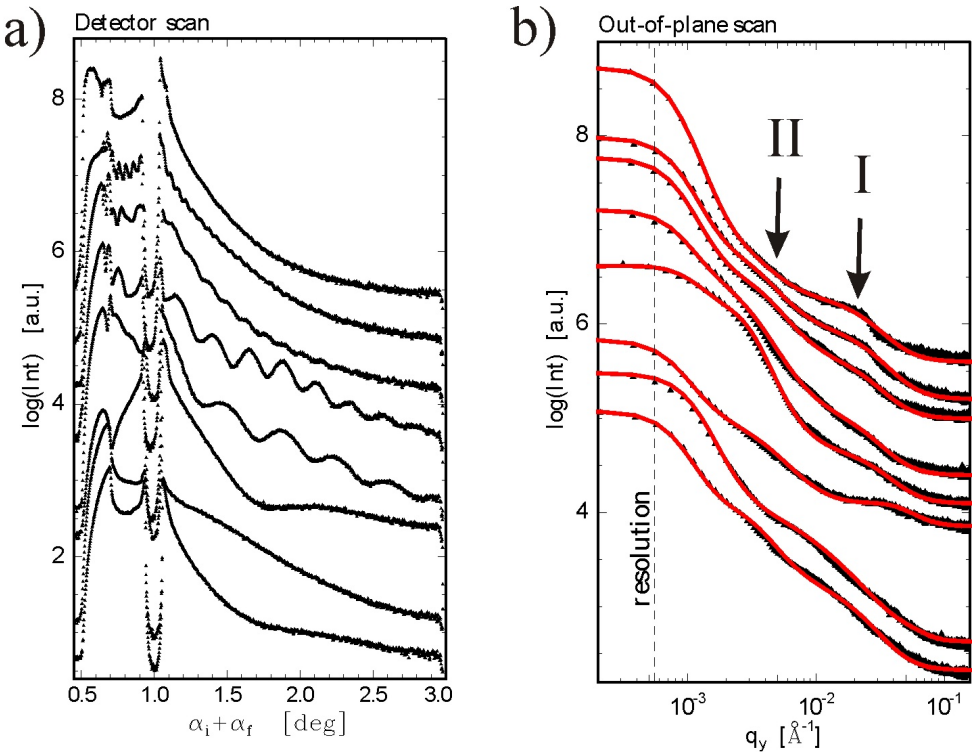

Figure 6.1: Line cuts from the μGISAXS 2d data for a representative selection of P(S-*b*-NIPAM) films of different film thicknesses (0.8, 1.7, 2.5, 6.6, 17.5, 29, 66, 122, and 220 nm from bottom to top). (a) Detector scans shown as a function of the detector angle $\alpha_i + \alpha_f$ and (b) out-of plane scans shown as a function of the q_y component of the scattering vector. The solid lines are fits to the data as described in the text. The resolution limit is indicated by the dashed line. From bottom to top the film thickness increases and the curves are shifted along the y-axis for clarity. The structure factors are marked by arrows.

scan cuts through these narrow intensity sheets give rise to a modulation of the intensity. The necessary condition for observing the partial phase coherence of diffusely scattered waves is a roughness correlation between the SiO_x surface and the P(S-*b*-NIPAM) surface. Analogous to a thin layer of snow on hills, the thin P(S-*b*-NIPAM) film replicates the SiO_x surface topography. Thus, a long-range correlation between both interfaces is installed and the thickness d of the P(S-*b*-NIPAM) film determines the distance between adjacent minima in the intensity modulation in the detector scan. This phenomena has also been found on nbc-PNIPAM thin films and is discussed in detail (see chapter 4). The long-range correlation is formed mainly due to the interaction at the interface between the substrate and the film, and the interface between the film and the air [WW08]. For the thick film (220 nm), the modulations become seriously damped because with increasing film thickness, the influence from both interfaces is reduced and the initially long-range correlated P(S-*b*-NIPAM) film becomes independent in its surface structures from the

substrate by slight roughening [WW08].

Figure 6.1b shows out-of plane scans cut from the two-dimensional μGISAXS data. None of the scattering curves exhibit a strong intensity peak such as one will expect for well-defined microphase-separated systems. Instead, one or two weak and broad intensity peaks at small q_y values are present, and the intensity peaks shift toward larger q_y values with increasing film thickness. The intensity peak is a structure factor type information, giving a nearest-neighbor distance (e.g., between spheres in a matrix, cylinders in a matrix, or adjacent lamellae in case of a triblock copolymer). For very thin films (film thickness below 1.7 nm), the rise in intensity is due to the presence of large-scale structures, which have a broad size distribution. Such large structures are formed due to dewetting because the film is very thin [BWF92]. Thus, pancake-like structures are formed instead of a homogenous layer. Such a behavior is very common for many types of polymer thin film systems like nbc-PNIPAM thin films (see chapter 4). With increasing film thicknesses, the intensity peaks rise up and shift toward larger q_y values, which hints an internal structure being installed in the films. To acquire detail information about internal structures, the out-of plane cuts are fitted with a simplified model. This model accounts for a structure factor due to the distance between neighboring domains of hydrophobic groups in the PNIPAM matrix (denoted structure factor I). Moreover, it includes a structure factor due to the presence of large heterogeneities (denoted structure factor II) and takes the experimental resolution into account. Both structure factors are distributed with a Gaussian function. The solid lines in figure 6.1b show the corresponding fits to the out-of plane scans. The resulting mean distance between domains of the hydrophobic group is 80 nm. The resulting distance corresponding to the structure factor II is 300 nm. In addition, the intensity peaks corresponding to structure factor I are more pronounced in thicker films than in thin films, while for the intensity peaks corresponding to structure factor II, the situation is opposite. Thus, the heterogeneities are more densely populated in thinner films, or in other words, thicker films are more perfect with respect to the inner structure.

For P(S-*b*-NIPAM-*b*-S) triblock thin films, the situation is different. Figure 6.2 shows the line cuts from the two-dimensional μGISAXS data measured for a representative set of P(S-*b*-NIPAM-*b*-S) films of different thicknesses. From the detector scans of figure 6.2a, strong modulations in the intensity are observed, even for very thick films. Thus, a long-range correlation between substrate and the film exists for P(S-*b*-NIPAM-*b*-S) triblock

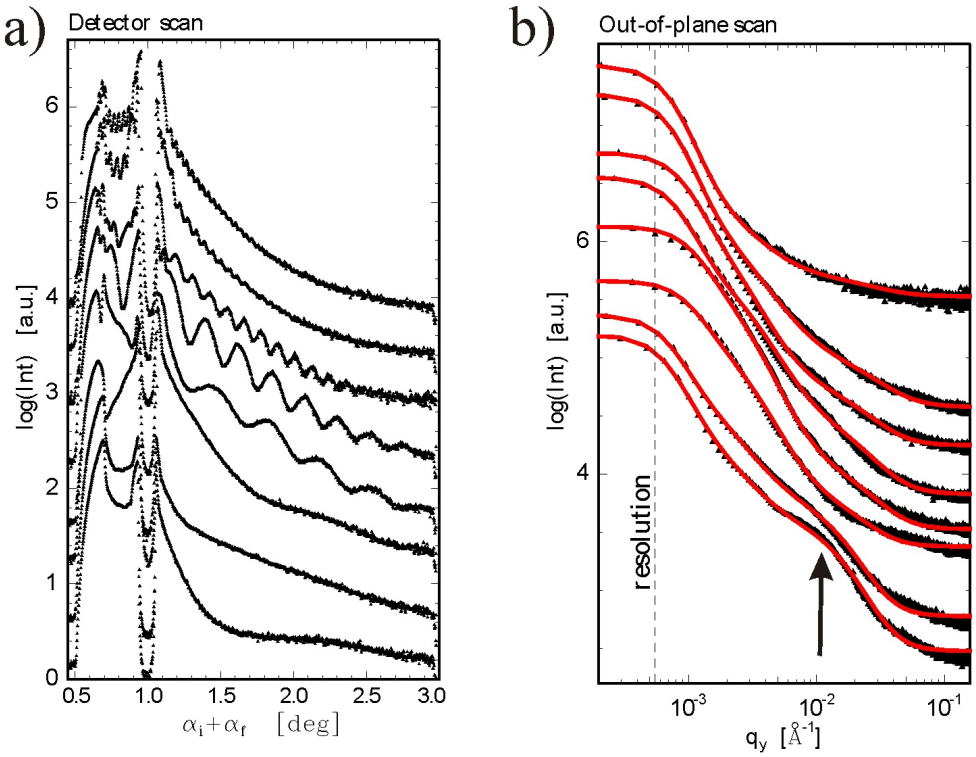

Figure 6.2: Line cuts from the μGISAXS 2d data for a representative selection of P(S-*b*-NIPAM-*b*-S) films of different film thicknesses (1.0, 1.8, 2.5, 7, 18, 31, 67, 125, and 230 nm from bottom to top). (a) Detector scans shown as a function of the detector angle $\alpha_i + \alpha_f$ and (b) out-of plane scans shown as a function of the q_y component of the scattering vector. The solid lines are fits to the data as described in the text. The resolution limit is indicated by the dashed line. From bottom to top the film thickness increases and the curves are shifted along the y-axis for clarity. The intensity peak corresponding to the structure factor is marked by an arrow.

thin films with a large thickness range, from 2 to 230 nm.

Figure 6.2b shows out-of plane scans cut from the two-dimensional μGISAXS data. None of the scattering curves exhibit a strong intensity peak. Actually, the intensity peaks of P(S-*b*-NIPAM-*b*-S) thin films are even much weaker than those of P(S-*b*-NIPAM) films. Thus, no obvious lateral structures due to microphase separation are installed in the films. Only for very thin films (thickness below 1.8 nm), very weak and broad intensity peaks can be found which are due to the presence of large-scale structures. Possible origins are contributions of dewetting. The resulting structure to structure distance corresponding to such intensity peaks is 100 nm.

In conclusion, compared to nbc-PNIPAM thin films, thin films by using of P(S-*b*-NIPAM)

diblock copolymer with a longer hydrophobic group show a better microphase separation, while for triblock system, there is no obvious improvement. This is interesting as nbc-PNIPAM can be considered as a extreme case of triblock systems. Thus, the microphase separation of PNIPAM based copolymer thin films in this work is more influenced by the position of the hydrophobic group in the chain than by the hydrophobic group length. However, none of them shows a well-defined microphase sparation, which is caused by the used solvent. In case of a more selective solvent, a more pronounced microphase separation is expected. Since the spin-coating process is very complicated and even in the case of simple homopolymers not fully understood, it is unknown why no well-defined microphase-separated structures can be formed. The diblock and the triblock films both show a long-range correlation between substrate and the film, which is similar to the case of nbc-PNIPAM. As the long-range correlation is mainly influenced by the interaction of the interfaces, this is expected because the substrates for the three different polymer films are the same and pre-cleaned in the same way, and the main part of three different polymer films is also the same - PNIPAM.

6.4 Swelling Experiments

To address the LCST behavior in thin films as a function of the degree of swelling, the films are exposed to saturated water vapor. The experimental set-up is similar to the one used in chapter 4. The thickness of dry films and of swollen films is measured as a function of temperature with optical interference. Starting at room temperature, each sample is allowed to equilibrate after each temperature increase by $\Delta T = 1$ °C for 30 min. Equilibration is concluded from the absence of any changes in the spectra of the optical interference measurements. The reported temperature-dependent changes are reversible. The resulting spectra are fitted including changes in the refractive index due to incorporation of water. The optical constants of P(S-*b*-NIPAM) and P(S-*b*-NIPAM-*b*-S) are taken as reference for dry films, respectively.

Exposed to saturated water vapor atmosphere, a clear response in terms of swelling of the films is observed at room temperature. Figure 6.3 shows a very strong film thickness dependence of the total swelling. For diblock P(S-*b*-NIPAM) films, thin films with a thickness of 30 nm exhibit a swelling by a factor of 3.4 as compared to the dry film (triangles in figure 6.3a) and a factor of 1.6 as compared to the collapsed film at 34 °C (circles in figure

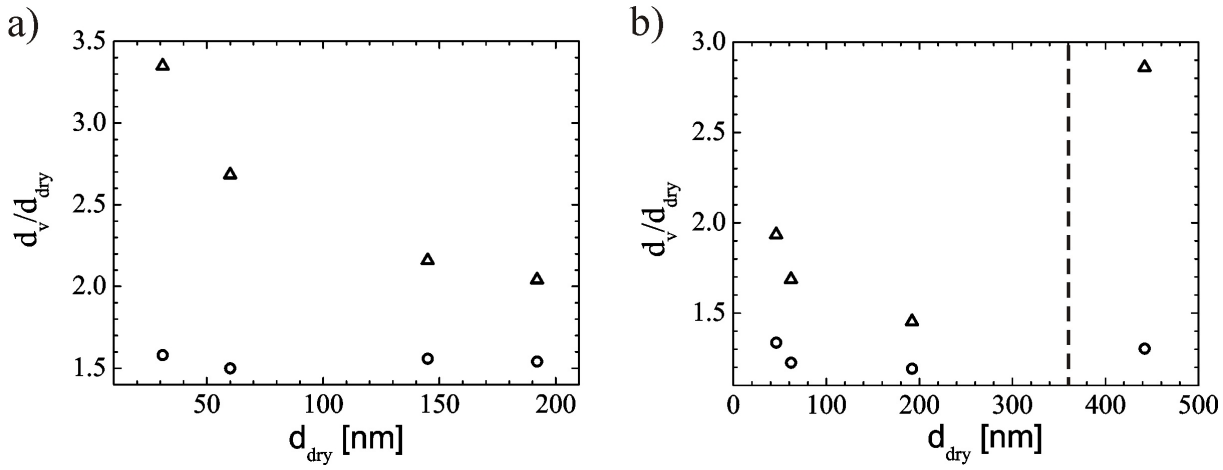

Figure 6.3: Thickness of P(S-*b*-NIPAM) films (a) and P(S-*b*-NIPAM-*b*-S) films (b) exposed to saturated water vapor d_v at 21.7 °C (triangles) and 34 °C (circles) normalized by the thickness of the dry films in air d_{dry}. Dashed line separates the thin films and the bulk-like film.

6.3a). With increasing film thickness the P(S-*b*-NIPAM) films undergo swelling with a decreasing factor. In case of the 190 nm thick film the swollen film thickness increases only by a factor of 2.1 as compared to the dry film. However, compared to nbc-PNIPAM thin films (see chapter 4), the decrease of the swelling factor of P(S-*b*-NIPAM) films with the increasing film thickness is much less. For nbc-PNIPAM films, the swelling factor of films with a thickness of 46 nm is 3.1, and in case of the 200 nm thick film the swelling factor is only 1.3.

It has been described in chapter 4 that one reason for the strong swelling observed in nbc-PNIPAM films might be the collapsed chain conformation, which is forced in the dry film due to the applied spin-coating technique. In combination with the hydrophilic substrate surface, which favors the PNIPAM segments as well as water, the swelling might be increased by a type of entropic spring change in the conformation of the micelles. With increasing film thickness this effect gets weaker because fewer nbc-PNIPAM molecules in the micelles are in a perturbed conformation. In the present case, the strong swelling of P(S-*b*-NIPAM) films still can be due to the collapsed chain conformation. However, due to a better microphase-separated structures installed and getting even better in thicker films, the swelling of diblock P(S-*b*-NIPAM) films is less influenced by the film thickness compared to that of nbc-PNBIPAM.

The triblock P(S-*b*-NIPAM-*b*-S) films (see figure 6.3b), with a thickness of 46 nm exhibit

a swelling by a factor of 1.95 as compared to the dry film and a factor of 1.35 as compared to the collapsed film at 34 °C. With increasing film thickness until 190 nm the triblock films also undergo swelling with a decreasing factor. In case of the 190 nm thick film the swollen film thickness increases only by a factor of 1.45 as compared to the dry film. Thus, compared to films of nbc-PNIPAM, films of P(S-*b*-NIPAM-*b*-S) with a longer hydrophobic group show a smaller swelling factor, especially for ultrathin films. However, in the case of very thick P(S-*b*-NIPAM-*b*-S) films, 442 nm for example, the swelling factor becomes much larger than the values of thinner films. Thick films with a thickness of 442 nm exhibit a swelling by a factor of 2.9 as compared to the dry film. As described in chapter 4, the decrease of the swelling factor with increasing film thickness is caused by the influence of substrate and the spin-coating process. For very thick films, both factors become very small and the behavior is more like the bulk material, while for bulk PNIPAM hydrogels a swelling factor of 8-10 (changes in volume of a factor of 10) have been reported [HS95], corresponding to a one-dimensional size increase of 2-3.

Figure 6.4 shows the measured LCST behavior. The temperature-dependent changes of the film thickness measured for P(S-*b*-NIPAM) films exposed to a saturated water vapor decrease with increasing film thickness (see figure 6.4a). In the derivative $\delta d/\delta T$ the transition temperature and the width of the transition are visible (see figure 6.4c). Within the experimental errors the transition temperature is at 28 °C for the thin films and seems to shift towards lower temperatures for the thickest films. However, the shift is not as strong as observed in nbc-PNIPAM (see chapter 4).

Figure 6.4b shows the temperature-dependent changes of the film thickness measured for P(S-*b*-NIPAM-*b*-S) films exposed to saturated water vapor decrease with increasing film thickness. Figure 6.4d shows the first derivative $\delta d/\delta T$. In figure 6.4e a focus on the first derivative $\delta d/\delta T$ of thin P(S-*b*-NIPAM-*b*-S) films with a thickness between 46 and 190 nm is shown. Within the experimental errors the transition temperature of the 46 nm film is at 26.5 °C and it shifts to 23.5 °C for the 190 nm film. It was observed that, for nbc-PNIPAM, the LCST of the 40 nm film is at 29 °C and it shifts to 27 °C for the 190 nm film. Thus, it can be conclude that with increasing hydrophobic group length, the LCST is decreasing. However, for very thick P(S-*b*-NIPAM-*b*-S) films, like the 442 nm film, the LCST shifts to a higher temperature, at 27 °C. In chapter 4, it has been described that the transition temperature is lower in thin films than in the bulk material. This might be the result from a confinement into a thin film or from the interaction with

the interfaces (substrate and water vapor). Thus, it is expected that with an increasing film thickness the LCST value should approach the bulk value because strong confinement typically would result in a lower transition temperature (see chapter 4). As a consequence,

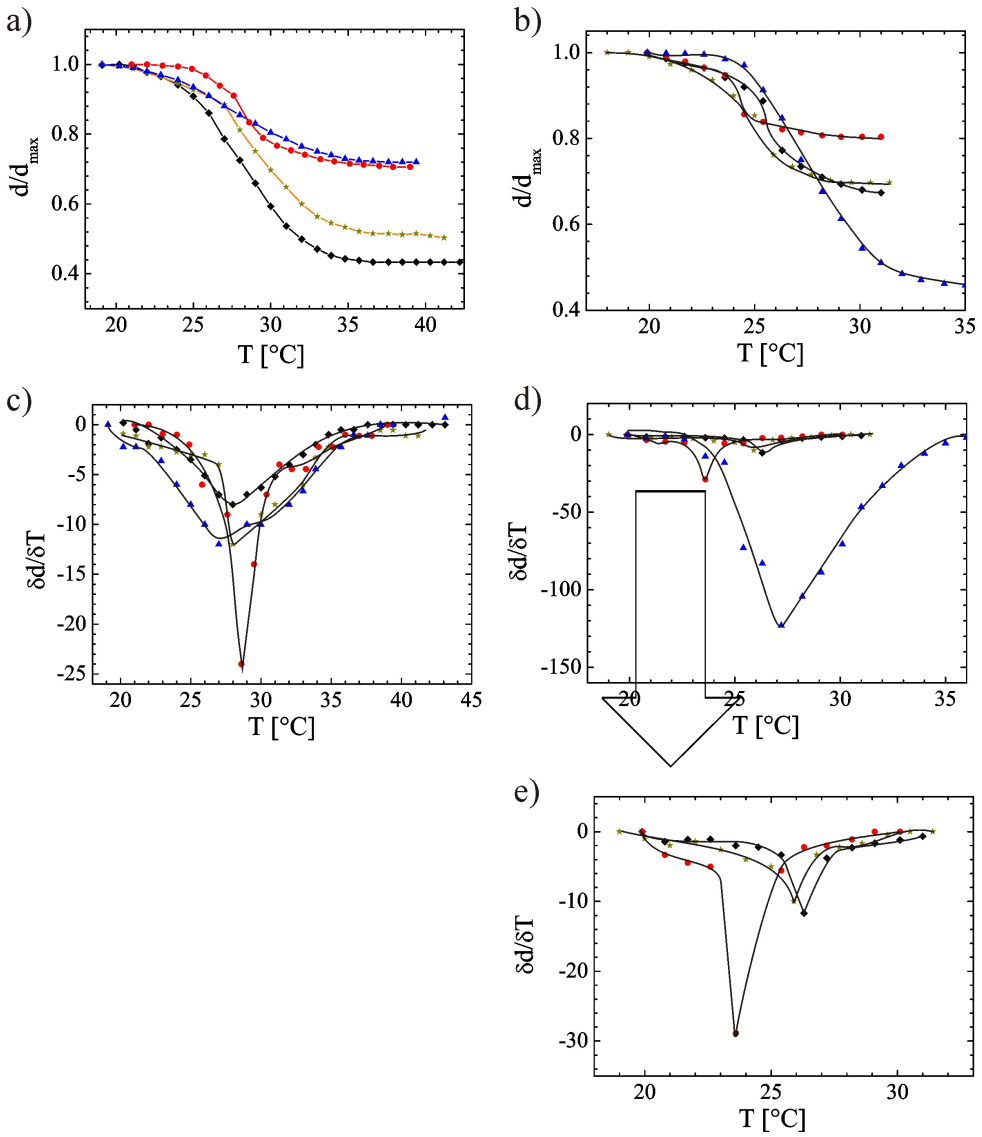

Figure 6.4: Temperature-dependent changes of the film thickness measured for P(S-*b*-NIPAM) films (a) and P(S-*b*-NIPAM-*b*-S) films (b) exposed to saturated water vapor. (c) and (d) are the first derivative $\delta d/\delta T$ for both films, respectively, indicating the transition temperature and the width of the transition. (e) is the focusing on the first derivative $\delta d/\delta T$ of thin P(S-*b*-NIPAM-*b*-S) films with thickness from 46 to 190 nm. For P(S-*b*-NIPAM) films, the swelling curves are measured for film thickness of 30 (rhombs), 62 (stars), 142 (circles), and 190 nm (triangles). For P(S-*b*-NIPAM-*b*-S) films, the swelling curves are measured for film thickness of 46 (rhombs), 66 (stars), 192 (circles), and 442 nm (triangles). The solid lines are guides to the eye.

it is more likely that the interaction with the interfaces affects the transition temperature.

In chapter 2, it is described that the phase transition temperature depends not only on the level of hydrophobe incorporation and its chemical structure but also on its position in the chain [KP01, CZ05]. This effect can be traced to differences in the structure of the micelles formed by the various hydrophobically modified (HM) PNIPAMs in cold water. Randomly modified HM-PNIPAMs adopt a loose micellar conformation in which the hydrophobic groups are partly exposed to water; the cloud point of their solutions is depressed significantly compared to that of PNIPAM solutions [KP01]. Thus, diblock P(S-*b*-NIPAM) films with a better ordered internal structure are expected to have a higher transition temperature compared to triblock P(S-*b*-NIPAM-*b*-S) films.

6.5 Conclusion

Thin diblock P(S-*b*-NIPAM) and triblock P(S-*b*-NIPAM-*b*-S) films are successfully prepared on SiO_x surfaces using spin coating. Both dry films exhibt a long-range correlation between interfaces. The diblock P(S-*b*-NIPAM) films show better microphase separated internal structures than the triblock P(S-*b*-NIPAM-*b*-S) films, which strongly influences the swelling and the LCST behavior of both films.

In the thin film geometry the thermosensitivity is still present for both investigated diblock and triblock films. Thus, omitting reactive groups, spin-coating results in physically cross-linked hydrogel films on solid supports. Compared to nbc-PNIPAM films, both films show a less swelling capability in a different way. The transition temperature is also slightly reduced compared to nbc-PNIPAM films. However, the prepared films still maintain the interesting features of PNIPAM revealed in the strength of the transition.

Thus, with respect to application, the presented system prepared with spin-coating appears to be interesting. The thickness can be tuned over a wide range (from 5 to 240 nm) and the thermal switching remains possible. Moreover, the transition temperature can be adjusted through the film thickness, hydrophobic group length and the position of the hydrophobic group in the chain. This will open novel possibilities in applications ranging from simple switches, solute separation, and drug delivery to tissue culture substrates and controlled adsorption of biopolymers.

Chapter 7

Water Storage in Diblock Thin Films

7.1 Introduction

Thin polymer films are used in various fields of application such as coatings to achieve protective, adhesive, dielectric, conducting, or resistive layers. Typically such layers are exposed to an environmental atmosphere, which contains a variety of small molecules. The most prominent example is air with its relative humidity defined by the thermodynamic parameters such as temperature and pressure. Depending on the type of small molecules, they can easily penetrate the polymer network and are incorporated inside the thin polymer film. The absorption of gases from the atmosphere such as carbon dioxide and water or exhaust fumes into polymers has non-negligible implications for the properties of the polymer materials. It can cause changes in thermal and mechanical properties.

Penetration of a small molecular species into an initially dry polymer film is driven by a chemical potential gradient. It is normally accompanied by swelling and plasticization of the polymer. Thus, the polymer film thickens and softens. The penetrating molecule may be a solvent or a nonsolvent of the particular polymer, depending on the thermodynamic properties of the polymer-molecule pair. A significant body of work has examined experimental and theoretical characteristics of swelling and dissolution of glassy polymer films by single organic solvent molecules [HCY87, GTP91, DCJ95, SDF02, TRL05, MBP06c, MBP07]. However, with respect to applications, the absorption-induced swelling of thin films can be problematic due to its related increase in film thickness, which can cause unwanted strain in a system.

In chapter 4, 5, and 6, it is shown that PNIPAM thin diblock or triblock copolymer films can incorporate water molecules from a surrounding water vapor atmosphere, with a significant swelling of the films. It is also known that with increasing hydrophobic block length, the swelling capability of thin films decreases [WW08]. Here, another kind of thin film, which allows for water storage without any increase in film thickness, is presented. Thus, these films will avoid problems related to strains which are caused by swelling. The basic key for the preparation of such thin films is the installation of a glassy network which has sufficient space to incorporate water molecules but cannot increase in size. This is achieved by a thin film preparation using an asymmetric diblock copolymer poly(styrene-block-*N*-isopropylacrylamide) (P(S-*b*-NIPAM)) with a long PS and short PNIPAM block in combination with a solvent which is more equal in interaction with the both blocks as compared to water. Such films allow a total water storage of 17.4% with a total film thickness increase of only 2.5%.

In most cases, polystyrene (PS) was chosen as the hydrophobic, glassy block, and diblock copolymers P(S-*b*-NIPAM) [NM04, HT04, ZW05, TK08], and occasionally also triblock copolymers P(S-*b*-NIPAM-*b*-PS) were studied [LHH01, HS08, NA08]. Whereas all these investigations on hydrogel systems focus on strong swelling of the thermoresponsive material, so far the non-swelling case was not focused on. Moreover, typically water is used as a solvent for the investigation of block copolymer solutions of copolymers containing PNIPAM and PS blocks and for thin film preparation (including dialysis from organic solvent into water). The direct use of organic solvents such as 1,4-dioxane is rare [WW08, WW09a, WW09b].

In the present work, the cyclic switching of water storage in thin block copolymer films containing PNIPAM and PS is probed. Films with a PNIPAM volume fraction of 0.276 prepared out of 1,4-dioxane show no swelling but absorption of water. During water storage a small reorganization of the initial microphase separation morphology of such films was reported recently [WW09b]. After the extraction of the stored water by applying vacuum, this changed microphase separation morphology is frozen-in, which implies that water storage causes an irreversible change of the initially installed morphology. With storage cycles it is probed that to what extent these morphological changes affect the water storage capability. With respect to applications of these films, such an investigation of the aging is of strong interest. The structural investigation of the cyclic water storage and removal is performed with atomic force microscopy, grazing incidence small-angle X-ray

scattering, and in-situ neutron reflectivity. In general, neutron scattering is a frequently used technique to probe the structure and structural changes in hydrogel systems and films [SR02, YH03, YH06, SS08]. With neutron reflectivity the density profile along the surface normal is accessed. In-situ measurements allow for monitoring changes in the composition during contact with a surrounding water vapor. The in-situ neutron data are accompanied by optical methods and FTIR spectroscopy.

This chapter has the following structure: The introduction is followed by an experimental section. The next sections show results and discussion on the cyclic switching of the P(S-*b*-NIPAM) film. The conclusion part ends the chapter.

7.2 Experimental Section

Materials. An asymmetric diblock copolymer of poly(styrene-*block*-*N*-isopropylacrylamide), denoted P(S-*b*-NIPAM), with a molecular weight of 23500 g mol^{-1} and a polydispersity of 1.05 was purchased from Polymer Source Inc. The volume fraction of PNIPAM in the copolymer is 27.6%.

Sample Preparation. Silicon with an oxide layer surface is used as the substrate material and cleaned with a base cleaning protocol as described in chapter 4. Because of this protocol, at the Si surface an oxide layer of 1 nm is present, which has a surface roughness below 0.5 nm. The initial dry P(S-*b*-NIPAM) films with different thicknesses were prepared with spin-coating (2000 rpm, 30 s) from a 1,4-dioxane solution at room temperature onto these pre-cleaned Si substrates.

Storage Cycle Protocol. The storage cycle protocol is similar to the swelling cycle protocol of nbc-PNIPAM thin films described in chapter 5. The initial dry P(S-*b*-NIPAM) film of the desired film thickness was mounted in a custom-made vapor chamber in air, thermostated to 23 °C, and investigated. To start the first storage cycle, the vapor chamber was evacuated, and the water reservoir of the vapor chamber was filled with D_2O to install a saturated D_2O atmosphere. The addition of D_2O marks the starting point of the water absorption kinetics (time = 0). After reaching equilibrium of water storage (240 min) the film is fully water storaged. The removal of D_2O was initiated by pumping the vapor chamber through a vacuum pump. Thus, water release from the thin film occurs,

and the P(S-*b*-NIPAM) film relaxes back in vacuum to a new dry state. This deswollen film was used in the next storage cycle as the initial dry film (see figure 7.1). To address aging effects of the water storage, the storage and removal cycles were repeated seven times. Samples were investigated in-situ during these cycles with neutron reflectivity and ex-situ after individual cycles with the other experimental techniques.

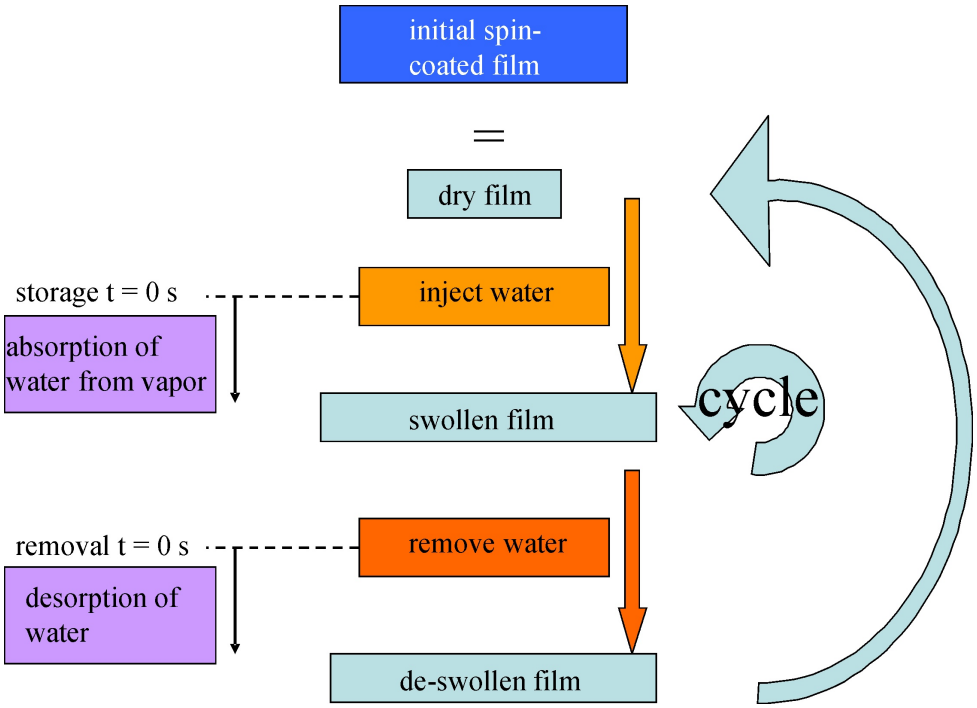

Figure 7.1: Schemic drawing of applied storage and removal cycle.

For the investigated range of P(S-*b*-NIPAM) film thicknesses no delamination was observed. However, very thick films exhibit delamination from the substrate in such cycles.

Neutron Reflectivity and Off-Specular Scattering. The theory and the set-up of this technique is described in detail in chapter 2 and 3, respectively. Kinetic changes due to the applied storage and removal cycles were probed by performing reflectivity scans every 30 s. The initial dry P(S-*b*-NIPAM) film used for cyclic switching, and the resulting deswollen P(S-*b*-NIPAM) film at the end of each cycle was additionally probed with an increased counting time of 3600 s. The probed q_z range between 0.01 and 0.85 nm^{-1} is selected to cover the critical edges of protonated (Si and P(S-*b*-NIPAM)) and deuterated (D_2O) substances. All reflectivity curves were fitted with the Motofit program [NA06] with appropriate error weighting and point-by-point resolution smearing. An automated

batch fit approach is taken, with all the data sets being analyzed in series. The scattering length densities of 2.07 $\times$ 10^{-6} Å^{-2} for Si, 3.47 $\times$ 10^{-6} Å^{-2} for Si oxide, 1.30 $\times$ 10^{-6} Å^{-2} for P(S-*b*-NIPAM), and 6.36 $\times$ 10^{-6} Å^{-2} for D_2O were fixed from initial fits and agree with literature values [ND01].

FTIR spectroscopy. The H-D exchange reaction between P(S-*b*-NIPAM) and D_2O was measured with FTIR spectroscopy using a JASCO FTIR-4100 spectrometer. The set-up and experimental process of this technique has been described in chapter 3.

7.3 Structure Investigation

a. Initially Spin-Coated Films. Using 1,4-dioxane solutions P(S-*b*-NIPAM) films of different thicknesses were prepared on Si with spin-coating. To obtain a large range of different film thickness, the concentration of the solutions used for spin-coating was varied from 0.1 to 30 mg/mL. The spin-coating parameters (spinning speed, acceleration, and spinning time) were kept fixed and films were prepared at room temperature. With optical microscopy the surfaces appear smooth and continuous. No large-scale heterogeneities are observed. Thus, the P(S-*b*-NIPAM) films behave with respect to surface structures very similar to films of end-capped PNIPAM prepared from dioxane solutions [WW08], whereas it was reported that very thick (bulklike) PNIPAM gel films (thicknesses on the order of 60 μm) were inhomogeneous on a micrometer scale [ZS96].

The X-ray reflectivity measurements at the initial spin-coated films confirm the film homogeneity observed with optical microscopy, except for an extremely thin film (thickness of 0.8 nm). Figure 7.2a shows the corresponding data for a selection of dry P(S-*b*-NIPAM) films. From the bottom to the top, the film thickness increases from 0.8 to 190 nm. All reflectivity curves, with the exception of the data from the thinnest film, exhibit well-pronounced fringes, which extend to large values of the scattering vector component q_z. So all the films with thicknesses larger than 0.8 nm are homogeneous films with a small surface roughness. For smaller film thicknesses, represented by the thinnest film (0.8 nm), the fringes in the reflectivity curve are strongly damped due to the imperfections of the block copolymer layer.

Although spin-coating is a widely used process, its theoretical description is complicated and even in the case of simple homopolymers not fully understood. Therefore, typi-

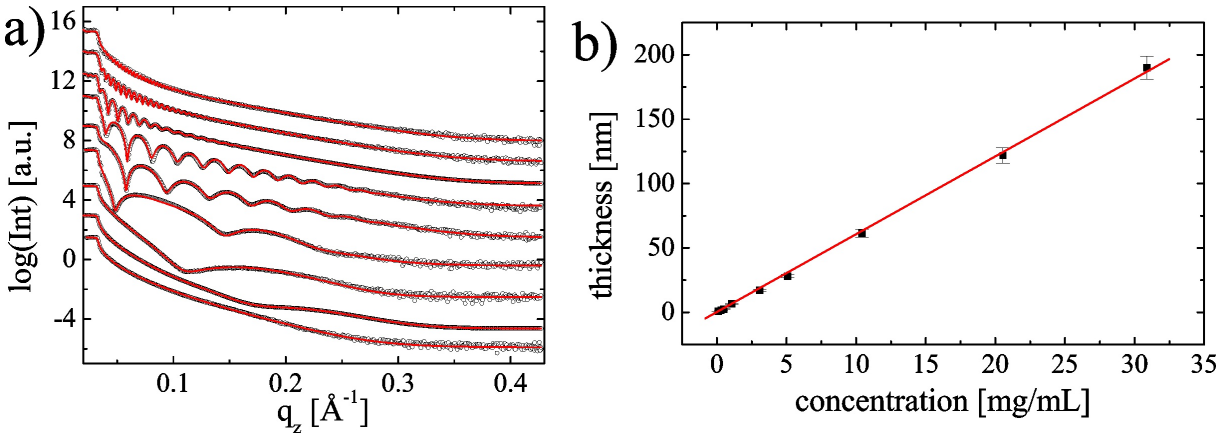

Figure 7.2: (a) X-ray reflectivity data (dots) shown together with model fits (lines) for the thickness regime covered in this investigation. With increasing thickness (0.8, 1.7, 2.5, 6.6, 17.1, 28.1, 61.4, 121.8, and 190 nm from bottom to top) the curves are shifted along the y-axis for presentation. (b) Film thickness plotted as a function of the P(S-*b*-NIPAM) concentration of the 1,4-dioxane solution used for spin-coating. The solid line is a linear fit.

cally in literature empirical relations are used to describe the dependence of the obtained film thickness on the spinning parameters or the concentration [LCJ88, SLL90, SDW97]. Figure 7.2b shows that the linear dependence of the resulting dry film thickness on the concentration used for spin-coating is valid for the investigated diblock copolymer P(S-*b*-NIPAM), if spin-coated from 1,4-dioxane solutions. From Figure 7.2b it is easily possible to prepare P(S-*b*-NIPAM) films of the desired thickness in a reproducible way. This saves material and allows for experiments with the film thickness as a control parameter.

To probe the surface structure of the P(S-*b*-NIPAM) films with high resolution, atomic force microscopy (AFM) is used. Figure 7.3a-d shows an example of topography data having a scan size of 1 μm $\times$ 1 μm to emphasize local surface structures for dry films with thicknesses of 1.7, 28.1, 121.8, and 204 nm. In this range of film thicknesses, all films have a surface structure on the nanometer scale, which is caused by a microphase-separation morphology of P(S-*b*-NIPAM). In contrast, for very thin films, such as for 0.8 nm film thickness, only large polymer islands (180-250 nm in diameter) are observed. The Si substrates are no more homogeneously covered, if the material present is insufficient to form a complete P(S-*b*-NIPAM) film. This incomplete surface coverage causes a large surface roughness (peak-to-valley amplitude equal to the film thickness), which explains the absence of fringes in the X-ray reflectivity data. During the spin-coating dewetting occurs which was observed in case of many other polymer-solvent pairs as well [MBP05].

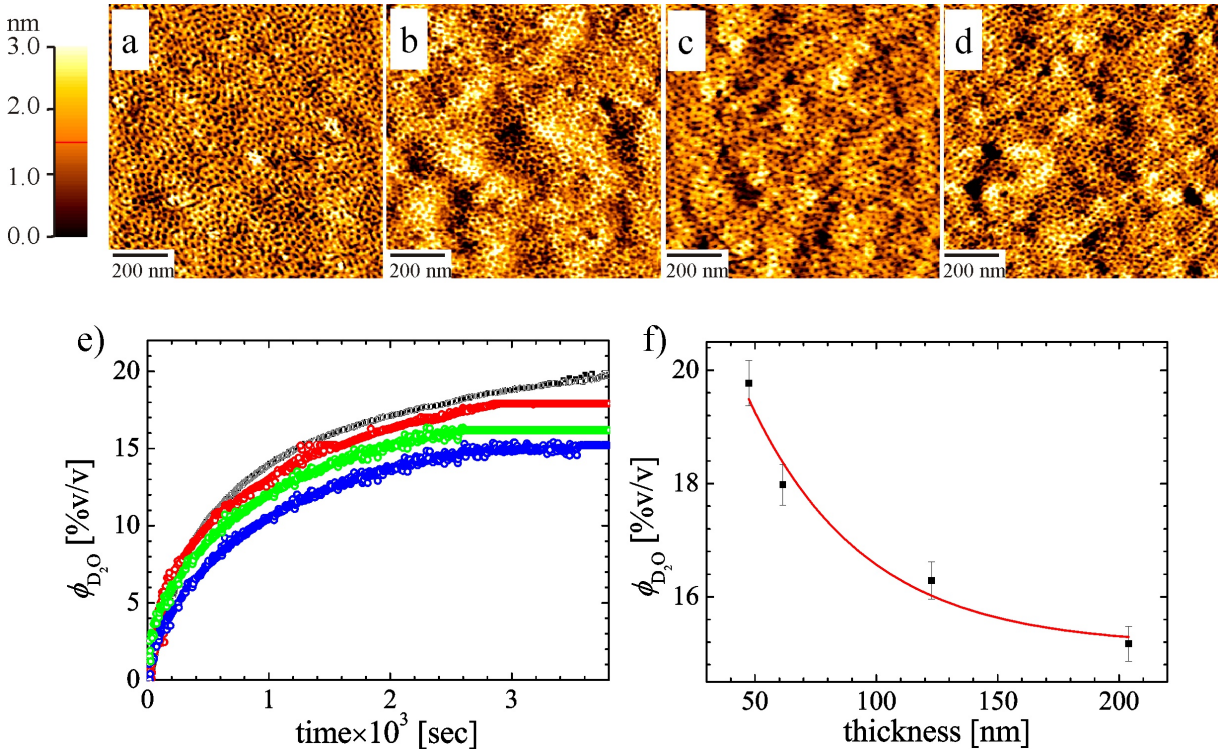

Figure 7.3: Topography AFM images of P(S-*b*-NIPAM) films with different thicknesses: a) 17.1 nm; b) 28.1 nm; c) 121.8 nm; d) 204 nm. The scan area is 1 μm × 1 μm for all AFM images. The structure height increases with the brightness of the structures in the images. The height scale bar range is 0 - 3 nm. e) Time-dependent changes of the water uptake for different thicknesses. From top to bottom the thickness decreases: 47 (black), 61.4 (red), 121.8 (green) and 204 nm (blue). f) Water uptake as function of film thickness.

However, in case of hydrogel films dewetting has not been investigated in detail so far [ADR08]. In contrast, alternative routes for patterning were applied, such as techniques based on lithography [RA04, ST06, BP07] or on the self-organization in thin soft films when they are confined by adhesive forces such as the van der Waals and electrostatic forces [GM06].

At higher concentrations, continuous films are formed, which exhibit a surface structure reflecting the microphase-separated structure of the diblock copolymer. With increasing film thickness, the surface structures coarsen laterally and become more oriented, whereas the height of the surface structures (peak-to-valley amplitude) decreases from 2 to 0.5 nm. Hence, a simple way to control the film thickness for water storage applications of the glassy thin P(S-*b*-NIPAM) films is at hand by varying the concentration of the P(S-*b*-NIPAM) solutions. With respect to applications requiring homogeneous films, the film

thickness range from 1.7 to 204 nm is accessible.

Whereas with X-ray reflectivity only the structure along the surface normal is detectable, and AFM is limited to the sample surface, microbeam grazing incidence small-angle X-ray scattering (μGISAXS) is well suited to investigate structures parallel to the surface, so-called lateral structures which are either inside or on top of the film and long-ranged correlations. Figure 7.4a and b show the line cuts from the two-dimensional μGISAXS data measured for a representative set of P(S-*b*-NIPAM) films of different thicknesses.

In figure 7.4a detector scans are shown. To focus on the modulation of the intensities along the vertical direction (at $q_y = 0$), starting near the Yoneda region, a zoom-in line cut of the 2d intensity is selected. The specular peak is blocked by a beam stop to avoid damage to the sensitive detector. In addition to the Yoneda peaks, which are located at the critical angles of the investigated materials (Si, PNIPAM and PS), strong modulations in the intensity are detected except for very thin films (below 1.7 nm) and very thick films (above 121.8 nm). These strong modulations are caused by a partial phase coherence of X-ray waves diffusely scattered from different interfaces, which yields a concentration of intensity in narrow sheets in reciprocal space. The detector scan cuts through these narrow intensity sheets giving rise to a modulation of the intensity. If the film is uncorrelated, all interfaces scatter independently and the diffuse intensities of all individual interfaces superpose. Thus, the necessary condition for observing the partial phase coherence of diffusely scattered waves is a roughness correlation between the SiO_x surface and the P(S-*b*-NIPAM) surface. Thus, a long-ranged correlation between both interfaces is installed and the thickness d of the P(S-*b*-NIPAM) film determines the distance between adjacent minima in the intensity modulation in the detector scan.

Because of the conformation of the polymer chains, not all lateral structure sizes of the roughness spectrum of the substrate can be replicated by a polymer film. This long-ranged correlation is formed mainly due to the interaction at interfaces, and the reason of the formation of such correlation is described in detail in chapter 4. Very thin films (below 1.7 nm), show a damped curve due to the imperfections of the hydrogel layer. Instead of a continuous layer, the SiO_x surface is covered with polymer patches. This incomplete surface coverage causes a large surface roughness. Because the influence of the substrate is decreasing with increasing film thickness, for very thick films (above 121.8 nm), the initially long-ranged correlated P(S-*b*-NIPAM) film becomes independent in its surface

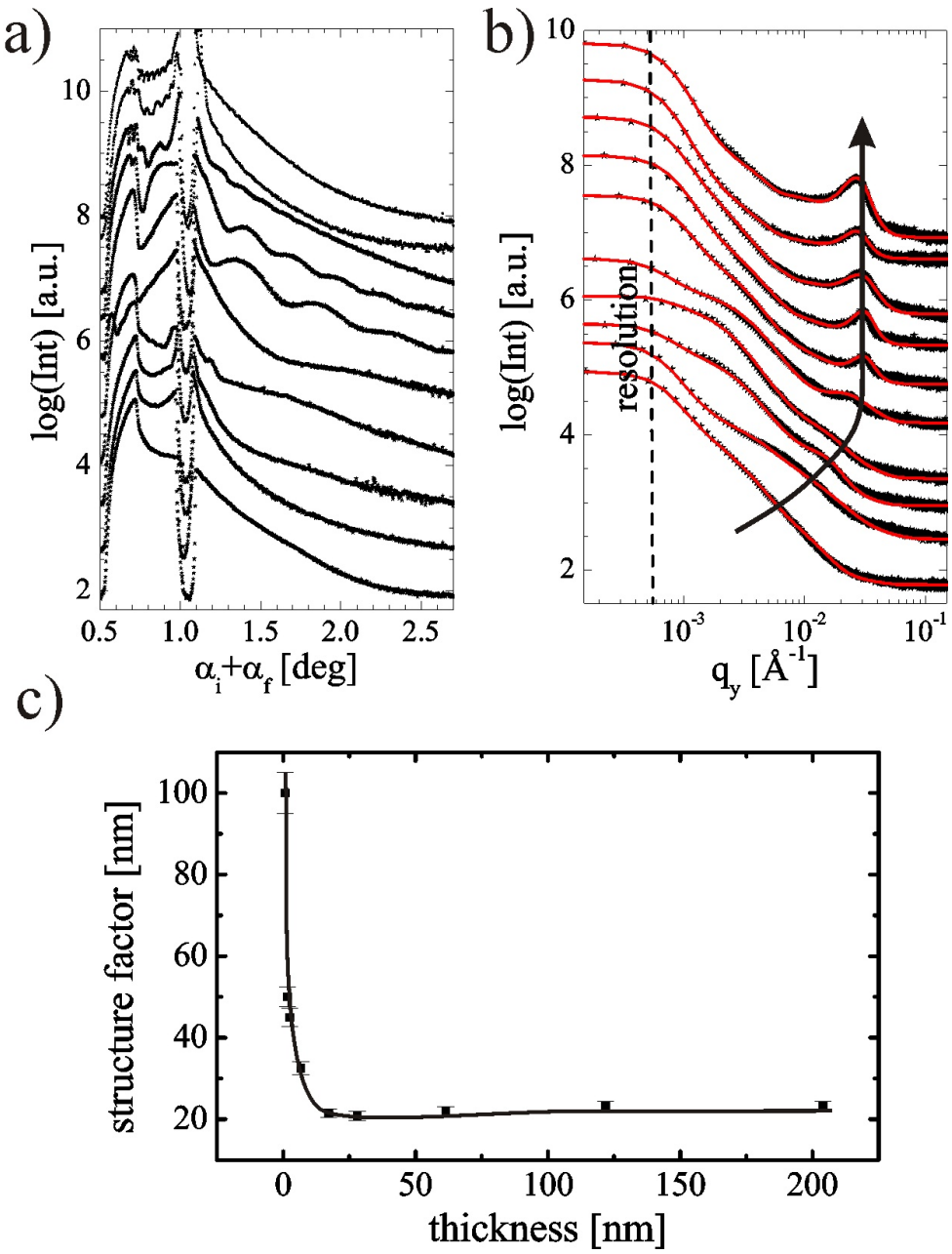

Figure 7.4: Line cuts from the μGISAXS 2d data for a representative selection of different film thicknesses (0.8, 1.7, 2.5, 6.6, 17.1, 28.1, 47, 61.4, 121.8, and 190 nm from bottom to top). (a) Detector scans shown as a function of the detector angle $\alpha_i + \alpha_f$ and (b) out-of plane scans shown as a function of the q_y component of the scattering vector. The solid lines are fits to the data as described in the text. The resolution limit is indicated by the dashed line. From bottom to top the film thickness increases and the curves are shifted along the y-axis for clarity. The structure factor peaks are marked by an arrow. (c) Structure factor shown as a funtion of the film thickness.

structures from the substrate by slight roughening. Thus, reflectivity curves of very thick films show very weak modulations.

P(S-*b*-NIPAM) films with thicknesses of 6 nm or larger are physically cross-linked hydrogels because during spin-coating with increasing concentration of the deposited P(S-*b*-NIPAM) solution on the solid support the bridging of micelles in addition to entanglement favors the gelation. Thus, an internal structure comparable to the microphase separation structure in diblock copolymers with hydrophobic blocks is expected. Figure 7.4b shows out-of plane scans cut from the two-dimensional μGISAXS data. Most of the scattering curves exhibit a strong intensity peak such as one will expect for microphase-separated systems. Instead, for thin films with thicknesses smaller than 6 nm, a weak and broad intensity peak at small q_y values is present, and the intensity rises toward larger q_y values. The rise in intensity is due to the presence of large-scale structures. The correponding structure factor as a function of film thickness is shown in figure 7.4c. The structure factor decreases from 100 to 20 nm with an increasing film thickness from 0.8 to 17.1 nm. For the films thicker than 17.1 nm, the structure factor is constant at 20 nm. Combined with the result from AFM and X-ray reflectivity, it can be concluded that when the film thickness is above 17.1 nm, a nicely ordered perpendicular cylinder structure with a structure factor of 20 nm is installed in P(S-*b*-NIPAM) films.

b. Comparison between Dry and Cycled Films. With optical interference measurements the time-dependent swelling of the P(S-*b*-NIPAM) films was examined as a function of film thickness. All homogeneous films show no increase in film thickness during water uptake. The incorporation of water causes only a change in the refractive index, which is used to determine the amount of water stored inside the film. The kinetics of water uptake are shown for four selected film thicknesses in figure 7.3e. Interestingly, with increasing film thickness the ability to include water into the film decreases (see figure 7.3f).

Out of the accessible film thickness range for the storage and removal cycles one fixed film thickness was selected to accommodate with the limited available neutron beamtime. A P(S-*b*-NIPAM) film thickness of 47 nm was selected, which is on the one hand not in the extreme of the accessible film thickness range and on the other hand marks a good candidate for applications. With neutron reflectivity, GISAXS, and AFM the initial dry P(S-*b*-NIPAM) film and the same film after each cycle are probed (see figure 7.1). Figure 7.5 shows the corresponding AFM data, giving information about changes in the film surface.

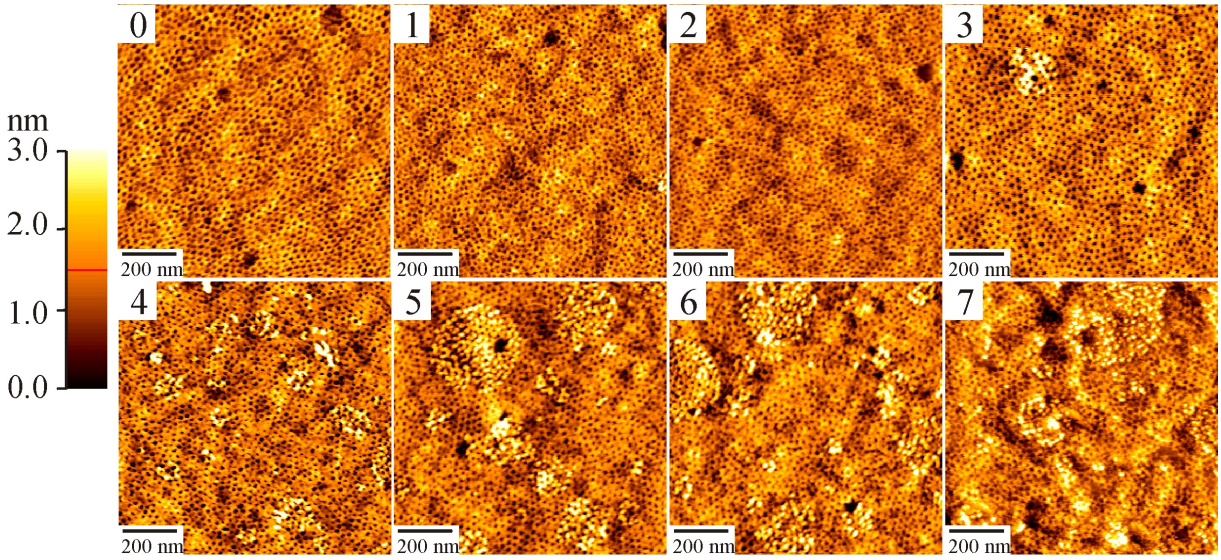

Figure 7.5: Topography AFM images of P(S-*b*-NIPAM) films before water storage (0) and after 7 water storage cycles (1 - 7), respectively. The scan area is 1 μm $\times$ 1 μm for all AFM images. The structure height increases with the brightness of the structures in the images. The height scale bar range is 0 to 3 nm.

The perpendicularly oriented cylindrical domains of PNIPAM in the PS matrix are quite distinct in all the images. The domain size is 20 nm in diameter. Upon increasing water storage cycles, the surface roughness of the P(S-*b*-NIPAM) film increases slightly, the cylindrical domains become more and more distorted, and some larger structures rise up on the film surface. Regarding the film surface the aging of the P(S-*b*-NIPAM) film starts significantly with the fourth cycle. However, the local microphase separation structure remains unchanged in size.

To get information about changes of the structure inside the P(S-*b*-NIPAM) film, neutron reflectivity is used. Figure 7.6 shows the corresponding data and the resulting scattering length density (SLD) profiles.

Whereas for X-rays the P(S-*b*-NIPAM) film appears mostly homogeneous along the surface normal due to the negligible contrast, due to the much larger contrast in neutron reflectivity an internal structure is resolved. The initially spin-coated, dry film has to be described as a bilayer. The bottom layer, namely the part of the polymer film which is directly in contact with the substrate (denoted interface part), has an SLD of 0.87 $\times$ 10^{-6} Å^{-2} and a thickness of 1.9 nm. Because the SLD of the pure PNIPAM bulk material from the literature is 0.869 $\times$ 10^{-6} Å^{-2} [DN01], it can be concluded that close to the

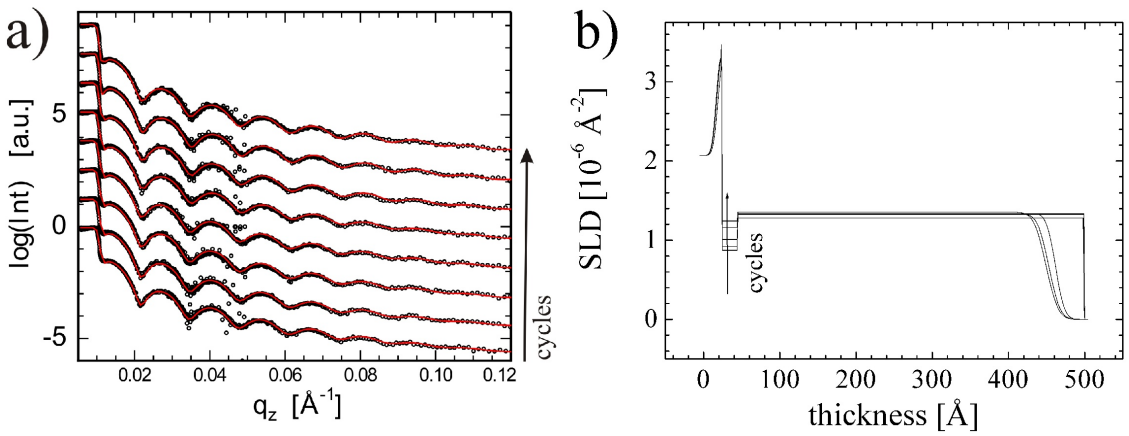

Figure 7.6: a) Neutron reflectivity data (dots) shown together with model fits (lines) for the 47 nm thick P(S-*b*-NIPAM) film initially prepared (bottom curve) and measured after complete storage and removal cycles (number of cycles increases from bottom to top). b) Resulting scattering length density (SLD) profiles show a bilayer structure on top of the Si substrate.

Si substrate a purely PNIPAM containing layer is present. In contrast, the top layer, namely the part of the polymer film which is in contact with air (denoted main part), has an SLD of 1.30×10^{-6} Å^{-2}. This top layer has a thickness of 45.5 nm and an average roughness of 0.5 nm. Therefore, the main part of the film consists of P(S-*b*-NIPAM). The interface enrichment of PNIPAM can be explained by the hydrophilicity introduced by the chemical treatment of the substrate used for cleaning of the Si [WW09b]. The substrate has a hydrophilic oxide layer with a water contact angle of 0° (water can spread on the surface) [MBP06b]. This hydrophilic oxide layer has a very strong attraction to the PNIPAM segments, and a high volume fraction of PNIPAM segments is located at the interface with the substrate.

After each storage and removal cycle, the neutron reflectivity data are only slightly changed. Thus each storage and removal of water does not have a dramatic influence on the P(S-*b*-NIPAM) film. However, a careful inspection of the resulting SLD profiles (see figure 7.6b) shows slight changes. Fitting with a bi-layer model is still necessary, but the SLD of both layers changes with cycle number and the surface roughness increases in good agreement with the AFM data. In contrast, the thicknesses are not affected, which gives a first hint that the investigated P(S-*b*-NIPAM) film is well suited for cyclic storage applications and aging does not destroy the film.

With increasing cycle number the SLD values increase, which can only be explained by the irreversible incorporation of D_2O used in the investigation of the cyclic switching or by an H-D exchange reaction happening during the water storage.

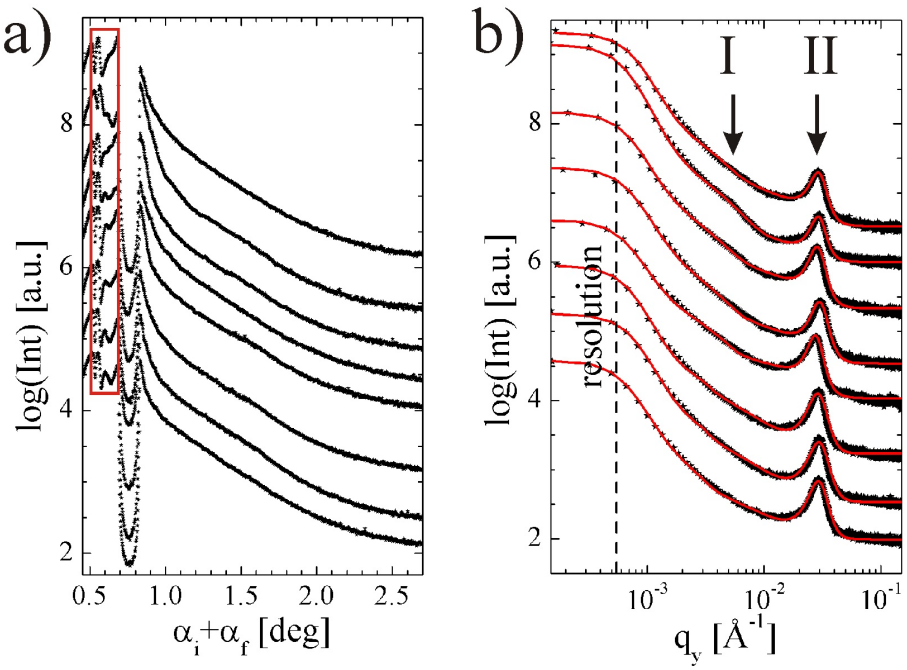

Figure 7.7: GISAXS data of P(S-*b*-NIPAM) films before water storage (bottom curve) and after 7 water storage cycles (subsequently shifted 7 curves), respectively. a) Vertical cuts showing structures along the surface normal and b) horizontal cuts (dots) displayed together with model fits (lines) showing in-plane structures.

Simultaneously with the neutron reflectivity the off-specular neutron scattering was measured at D17 as well. This off-specular scattering showed an increase in intensity with increasing number of swelling cycles due to a build-up of an internal disorder. However, detailed modelling of such off-specular neutron data is rather complicated and only information about large scale structures is obtained. Because grazing incidence small angle neutron scattering (GISANS) is strongly flux limited, GISAXS was used to obtain information about lateral structures inside the P(S-*b*-NIPAM) film on the scale of the micro-phase separation structure. In GISAXS the contrast is less favorable as compared with GISANS, but as visible in figure 7.7 the inner film structure is well resolved.

Figure 7.7 shows the vertical and horizontal cuts from the 2D GISAXS intensity. From the vertical cuts, it can be found that the perpendicular structure (correlated roughness, highlighted by the box in figure 7.7a) is damped with increasing cycle number. So the initially long-ranged correlated P(S-*b*-NIPAM) film becomes independent in its surface structures from the substrate by slight roughening.

In the horizontal cuts one well pronounced peak (denoted with II in figure 7.7b) is present from the beginning and a second broad and shoulder-like peak (denoted with I in figure 7.7b) is building-up in the last cycles. The intense peak is caused by the micro-phase separation structure and from a fit to the data a structural length of 20 nm can be obtained. This value is in good agreement with the AFM data and represents the distance between adjacent PNIPAM cylinders in the PS matrix. During cycling the micro-phase separation structure is not changed (neither swollen nor shrunk), which is a good argument to exclude residual solvent being present inside the P(S-*b*-NIPAM) film after a finished storage and removal cycle. Only the peak intensity is slightly decreasing with increasing cycle number showing a slight disordering of the PNIPAM cylinders inside the PS matrix.

During the cycling of the film a second and larger structure is growing causing the shoulder-like peak. This larger structure is domains on the size of 150 nm which are seen to some extend with AFM on the film surface as well. Thus the perturbance of the structure yields domains inside the film and at the film surface which cause the main aging of the P(S-*b*-NIPAM) film.

7.4 Water Storage and Removal Cycles

For a deeper understanding of the aging the water storage and removal is probed with in-situ neutron reflectivity and off-specular scattering. In-situ GISAXS measurements are impossible for this investigation due to radiation damage occurring at swollen P(S-*b*-NIPAM) films. Anyhow, the contrast necessary for determining the water content in thin P(S-*b*-NIPAM) films is gained from the use of deuterated water (D_2O) in combination with the protonated polymer in a neutron scattering experiment. In a kinetic experiment the initially prepared dry glassy film is exposed cyclic to water vapor (see figure 7.1) and with in-situ neutron scattering the changes of the film due to storage of water are monitored. In figure 7.8a, a representative 2D detector pattern of scattered intensity

(displayed as a function of wavelength λ and the exit angle α_f) is presented. The red boxes in figure 7.8a mark selected regions in the intensity, which are used for analysis: the specular reflectivity region (M) and the off-specular reflectivity regions (Yoneda peaks of deuterated material *Y1* and of protonated material *Y2*). Because off-specular scattered intensities are significantly smaller than the specular ones, a detailed analysis of intensity as a function of lateral scattering vector component q_x is impossible for the kinetic data. To maintain the very high time resolution of the scattering experiment and account for the kinetic changes of the films due to water storage, integration is performed in q-space rather than in the time domain [MBP06c, MBP07]. The necessary improvement of statistics is achieved by an integration of off-specular intensities using the boxes detailed above [MBP06c]. After normalization by the neutron beam monitor the specular intensity M and off-specular intensities *Y1* and *Y2* result [MBP07].

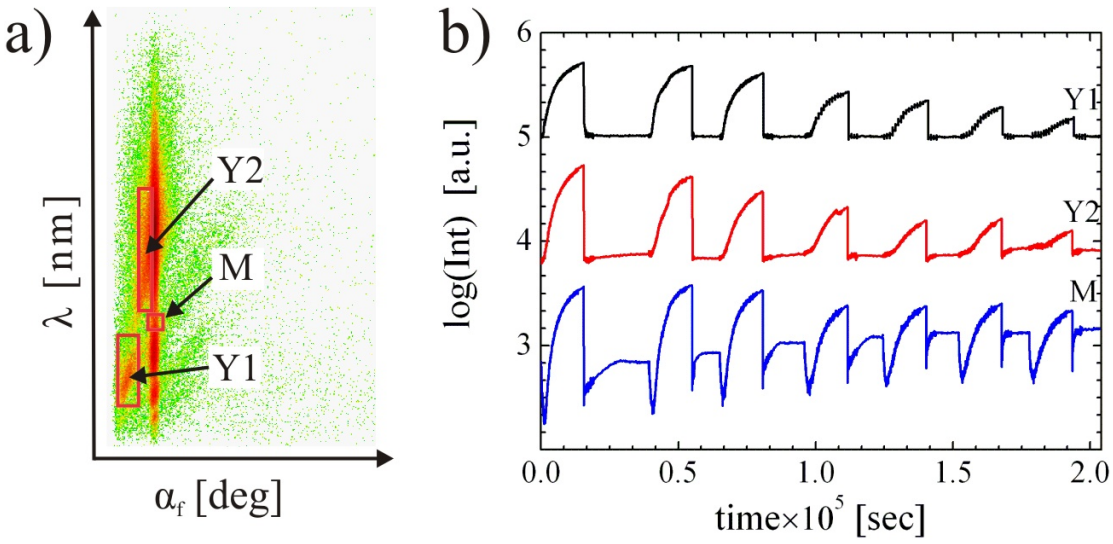

Figure 7.8: (a) Representative 2d detector pattern of scattered intensity displayed in the wavelength λ vs exit angle α_f presentation. The red boxes mark the area integrated for the analysis of diffuse scattering. (b) Intensities integrated over the areas *Y1*, *Y2*, and M (as explained in the text) shown on a logarithmic axis as a function of time for seven storage and removal cycles. The curves are shifted along the y-axis for presentation.

Figure 7.8b shows the time evolution of the specular reflectivity (M) and the off-specular reflectivities (*Y1*, *Y2*) for the seven repetitive cycles of water storage and removal. Because of the incorporation of D_2O, the scattering length density (SLD) of the film increases, resulting in the increase of the reflected intensity and shift of the position of the

total reflection edge toward a smaller λ value. Accordingly, the intensity in the region *M* increases with absorption of D_2O. The off-specular intensities *Y1* and *Y2* increase with time due to the buildup of a lateral structure inside the glassy block copolymer film because D_2O selectively diffuses into parts of the film. After the vapor is extracted, both of the specular and the off-specular intensities decrease to the initial state of the water storage immediately and reach stability after 2.5 h. However, with increasing cycle number the actual intensity values change, and only the overall shape stays unchanged. As expected in terms of an aging process, the amplitudes decrease from cycle to cycle.

A more detailed analysis of the time evolution of water storage in the glassy hydrogel film is achieved by fitting the individual neutron reflectivity curves (see figure 7.9). From these fits the total P(S-*b*-NIPAM) film thickness and water penetration (%v/v) are determined.

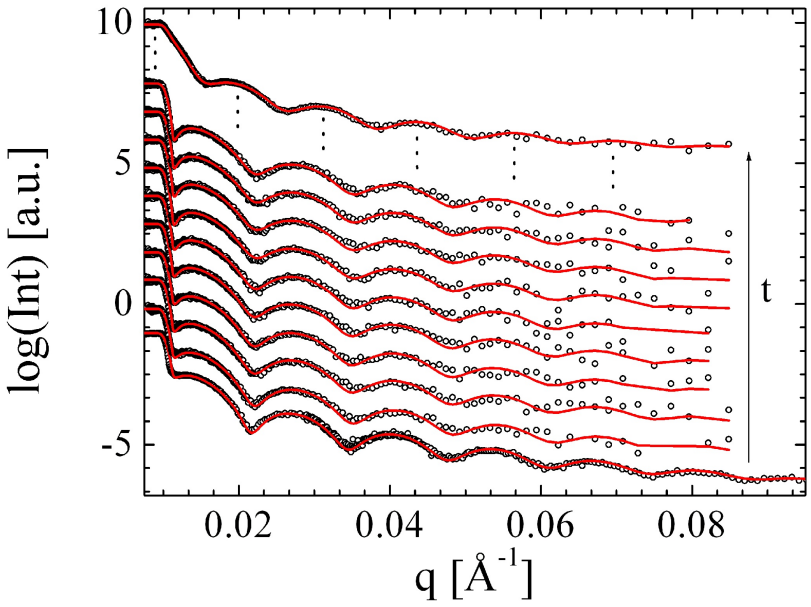

Figure 7.9: Neutron reflectivity data (open circles) displayed together with best model fits (lines) corresponding to the swelling in D_2O atmosphere. Each dataset is offset vertically by fixed log units. For reasons of clarity only a subset of the data showing the beginning of swelling is displayed, although all fits were of similar quality. The initial dry film (bottom curve) and the final swollen film (top curve) are shown for comparison.

The injection of D_2O marks the start of the water-absorbing process for each cycle. In the first cycle, from the beginning of the D_2O penetration until the saturation is reached, the

total thickness of the film only increased by 1.2 nm, with the thickness of the interface part of the film (bottom layer) increasing by 0.25 nm. So in total, the glassy hydrogel film increases its thickness only by 2.5%, which is the key point for applications. In detail, the interface part (bottom layer) swells by 10.8% in height which is much more than the main part (top layer), which swells only 2.2% in height. It indicates that the high PS volume fraction seriously reduces the swelling capability of the P(S-*b*-NIPAM) film as the bottom layer mainly consists of PNIPAM. As the solid substrate is not deformable and thus the swelling can only happen in the direction normal to the surface, it can be concluded that the volume of the whole P(S-b-NIPAM) film only increased by 2.5% [WW09a].

From the changes of the SLD values, the D_2O volume fraction ϕ_{D_2O} of the film is calculated using

$$\phi_{D_2O} = \frac{n - n_1}{n_2 - n_1} \tag{7.1}$$

where n denotes the in-situ probed SLD of the film, n_1 the initial SLD of the dry film, and n_2 the SLD of D2O. In figure 7.10a and b, the time evolutions of the D_2O volume fraction ϕ_{D_2O} of the top layer and the bottom layer are presented.

The water absorption of the main part of the film, given by the top layer, can be divided in two different regimes. They are denoted by stage I and II (see figure 7.11). In the first regime (stage I, 0-1.22 $\times$ 10^3 s), the water storage rate first increases rapidly and then reaches a plateau. D_2O vapor molecules enter into the porous structure of the block copolymer film and diffuse into all accessible volume of the film. During this mass uptake the initial film structure stays unchanged as proven by the off-specular scattering shown in figure 7.8b because the integrated values of the off-specular intensities *Y1* and *Y2* show nearly no increase, meaning that D_2O has not yet selectively diffused into the PNIPAM domains in this stage. As a consequence, the D_2O volume fraction ϕ_{D_2O} of the top layer is increased to 5% irrespective of the cycle number. Obviously, the accessible porous structure is not affected by the cyclic switching of the P(S-*b*-NIPAM) film. In the second regime (stage II, 1.22 $\times$ 10^3 s-end) the coiled PNIPAM chains start to swell and attract selectively D_2O molecules because PNIPAM is soluble in D_2O, which causes a strong attractive interaction between them, whereas the net interaction between the polymer segments of the copolymer is repulsive. This causes a strong increase of the integrated off-specular intensities *Y1* and *Y2* (see figure 7.8b). An internal contrast is built up due to enrichment of D_2O in selected domains and a reorganization of the initial microphase

separation morphology. Because PS has a strong repulsive interaction with D_2O and PNIPAM, the PNIPAM chains initially can only swell to the free volume space between the PS and PNIPAM domains, which is formed due to the phase separation between PS and PNIPAM, until maximum water storage is reached. With increasing cycle number this maximum value decreases.

The water absorption of the very thin interface part of the P(S-*b*-NIPAM) film, which consists of pure PNIPAM, behaves differently from the majority of the film (see figure 7.10b). Only a single regime is discovered in the increase in the absorbed water from the increase in SLD. Similar to the second regime probed for the main part of the film, the ability to incorporate water decreases with increasing cycle number. However, the effect is not as strong as for the main part of the film.

The swelling kinetics of a spherical gel was formulated by Tanaka and Fillmore on the basis of a cooperative diffusion theory [TT90], wherein the shear modulus was considered to be negligible in comparison with the osmotic compressive modulus. By including a non-negligible shear modulus, Peters and Candau [PA88] developed a general model to characterize the swelling kinetics of spherical, cylindrical, and disklike polymer gels. Later, Li and Tanaka [LY90] proposed a two-process mechanism after realizing that neither gel swelling nor shrinking can be considered to be a pure diffusion process.

They predicted that the shear modulus (μ) is related to the net osmotic modulus (M_{os}) and the osmotic bulk modulus (K_{bulk}) by [66]

$$R = \frac{\mu}{M_{os}} = \frac{\mu}{K + \frac{4}{3}\mu} \tag{7.2}$$

According to Li and Tanaka, the swelling or shrinking follows a first-order kinetics (see chapter 2), i.e.

$$\ln\left(\frac{\phi_{D_2O}(\infty) - \phi_{D_2O}}{\phi_{D_2O}(\infty)}\right) = \ln B_1 - t/\tau_1 \tag{7.3}$$

where B_1 is related to R by

$$B_1 = \frac{2(3-4R)}{\alpha_1^2 - (4R-1)(3-4R)} \tag{7.4}$$

and τ_1 is related to the collective diffusion coefficient D_c by

$$D_c = \frac{3Z_\infty^2}{\tau_1 \alpha_1^2} \tag{7.5}$$

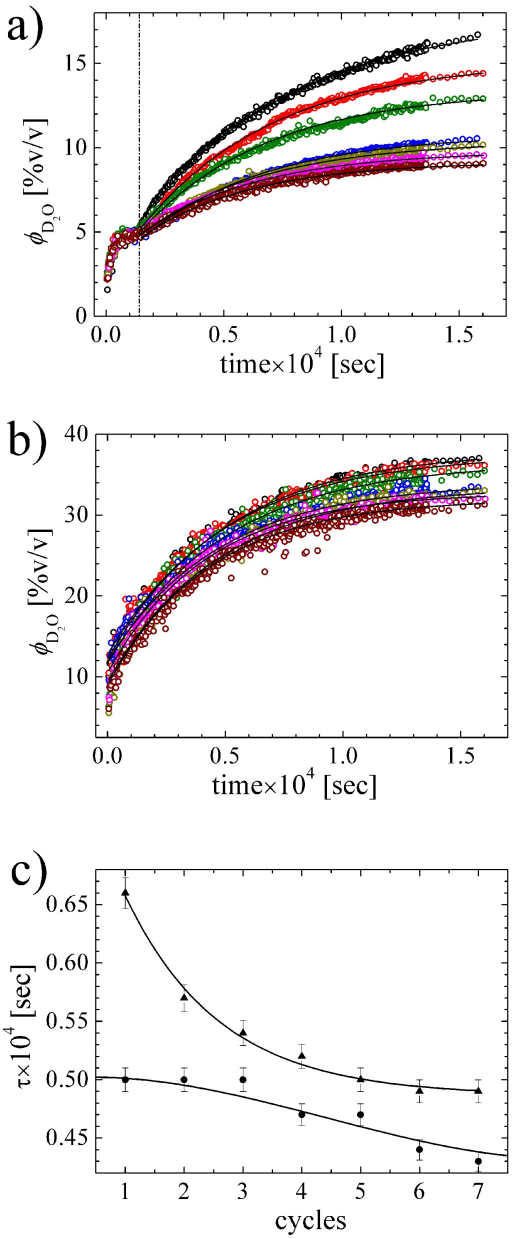

Figure 7.10: Water absorption inside the P(S-*b*-NIPAM) film as a function of time for seven storage cycles: (a) for the main part of the film (top layer) and (b) for the interface part of the film (bottom layer). From top to bottom: black, red, green, blue, dark yellow, magenta, and dark red wine circles represent cycle number 1 to 7, respectively. Lines in panels (a) and (b) are fits of eq. 7.1. (c) Time constants τ determined for the storage kinetics of each individual cycle for the main (circle) and interface (triangle) part of the film.

with α_1 being a function of R, i.e.

$$R = \frac{1}{4}\left[1 + \frac{\alpha_1 J_0(\alpha_1)}{J_1(\alpha_1)}\right] \tag{7.6}$$

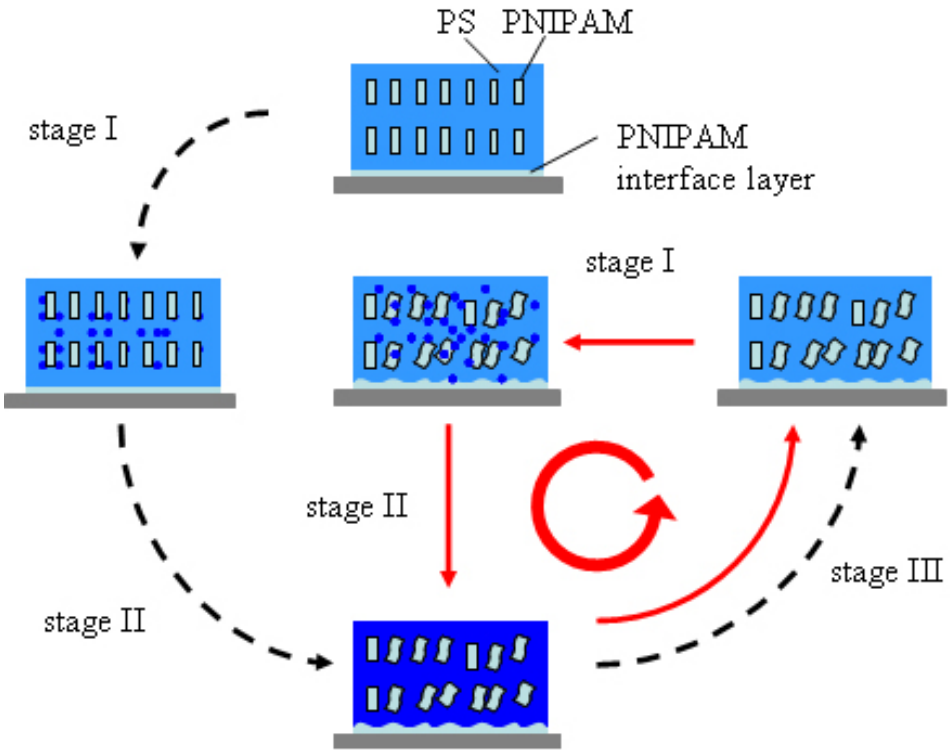

Figure 7.11: Structural evolution during the applied storage and removal cycles. The initial cycle is indicated by the dashed arrows and the all subsequent cycles with the solid arrows. Dark blue dots represent water. The changes are exaggerated.

and Z_∞ being the disk thickness in the final swelling equilibrium state, where J_0 and J_1 are the zeroth- and first-order Bessel functions. The detail of this model can be found in chapter 2 and the reference LY90. In case of a thin film Z_∞ is replaced by the part of the thickness of the film which is occupied by water. The t-dependence of $[(\phi_{D_2O}(\infty) - \phi_{D_2O})/(\phi_{D_2O}(\infty))]$ can lead first to B_1 and τ_1 and then to R and D_c on the basis of eq. 7.3-7.6.

Figure 7.10a shows the water uptake of the main part of the film versus time. At $t \rightarrow \infty$ the maximum water uptake $\phi_{D_2O}(\infty)$ is reached. On the basis of eq. 7.3, B_1 and τ_1 were determined by fitting. As visible in Figure 7.10a, the main part of the swelling of the thin P(S-*b*-NIPAM) film can be described by the first-order kinetics (eq. 7.3). Table 7.1 summarizes the values of $\phi_{D_2O}(\infty)$, τ_1, B_1, R, and D_c of the main part of the film.

In case of a thin gelatine gel film, the value of R is about 0.67 [ZS96, WC94] and for macroscopic sized gels [LY90, ZM93] the value of R is in a range from 0.3 to 0.4, which

Table 7.1: values of $\phi_{D_2O}(\infty)$, τ_1, B_1, R, and D_c of the main part of the P(S-*b*-NIPAM) film

cycle No.	$\phi_{D_2O}(\infty)$	$\tau_1/10^4$ s	B_1	R	$D_c/10^{-15}$ cm^2/s
1	17.8±0.2	0.66±0.02	0.85±0.02	0.55±0.02	4.59±0.03
2	15.2±0.2	0.57±0.02	0.85±0.02	0.55±0.01	5.09±0.03
3	13.2±0.2	0.54±0.02	0.82±0.03	0.53±0.02	4.71±0.02
4	10.8±0.1	0.52±0.02	0.77±0.02	0.44±0.02	3.52±0.03
5	10.4±0.1	0.52±0.02	0.71±0.02	0.34±0.02	2.79±0.04
6	9.8±0.1	0.49±0.02	0.68±0.02	0.29±0.01	2.68±0.04
7	9.2±0.1	0.49±0.02	0.68±0.02	0.29±0.01	2.65±0.04

are comparable to the values obtained here. According to the definition of R, the decrease of R during cycling means K_{bulk} increases faster than μ. The value of B_1 is 0.71 for very thick disk-like gels (1.33 mm in thickness) [LY90] and 0.87-0.95 for thick films (60 μm in thickness) [ZS96]. τ_1 is 1.3 $\times$ 10^4 s for the disk-like gels [LY90] and 0.05-0.16 $\times$ 10^4 s for thin films [ZS96]. Again, determined values in the present work cover this range and are decreasing with cycle number. In the final cycles this decrease stops, which demonstrates that the aging is not continuing. Only the values of D_c, which is related to the final thickness of the film Z_∞, is much smaller (6-9 factor) than those of the literature [TRL05, ZS96], because film thickness in the present work is in the nanometer scale.

Figure 7.10b shows the water uptake of the interface part of the film (bottom layer) versus time. Table 7.2 summarizes the values of $\phi_{D_2O}(\infty)$, τ_1, B_1, R, and D_c resulting from the model described above.

As table 7.2 shows, the values of τ_1 have only a slight decrease and the values of B_1 and R are nearly constant. The values of B_1 and R of the interface layer are nearly the same as those of the main layer during the last cycles. For comparison the resulting relaxation times of both parts are shown in figure 7.10c.

Regarding relaxation times, it is worth noting that pure, thick PNIPAM homopolymer

Table 7.2: values of $\phi_{D_2O}(\infty)$, τ_1, B_1, R, and D_c of the interface part of the P(S-*b*-NIPAM) film

cycle No.	$\phi_{D_2O}(\infty)$	$\tau_1/10^4$ s	B_1	R	$D_c/10^{-15}$ cm^2/s
1	38.0±0.4	0.50±0.02	0.68±0.01	0.29±0.01	7.23±0.02
2	37.5±0.4	0.50±0.02	0.66±0.01	0.29±0.01	6.98±0.02
3	36.5±0.4	0.50±0.02	0.68±0.02	0.29±0.01	7.07±0.02
4	34.0±0.4	0.47±0.02	0.68±0.02	0.29±0.01	7.25±0.02
5	33.5±0.4	0.47±0.02	0.72±0.02	0.34±0.01	7.98±0.02
6	32.8±0.3	0.44±0.02	0.68±0.02	0.29±0.01	7.61±0.02
7	32.0±0.3	0.43±0.02	0.72±0.02	0.34±0.01	8.53±0.03

gel films follow the same behavior but with a strong thickness increase [ZS96]. The relaxation times of pure PNIPAM gel film were 530 s at 21 °C and 810 s at 25 °C. For the investigated P(S-*b*-NIPAM) film the relaxation times of the main part of the film are larger than the ones of the interface part. For the main part of the initially prepared film, $t = 626$ s is determined at 23 °C, which compares well with the observations by Zhou and Wu [ZS96]. Thus, diffusion in the second regime is driven by the PNIPAM domains. However, in contrast to PNIPAM gel films, in the investigated P(S-*b*-NIPAM) film the volume fraction of the PS domain takes a dominant role (72.4%), and thus the total swelling is seriously restricted.

In summary, the mechanism of water storage and water removal in cyclic switching of the P(S-*b*-NIPAM) film is described in figure 7.11. In a first stage (stage I), the water molecules diffuse into all accessible volume of the whole P(S-*b*-NIPAM) film. Next, in a second stage (stage II), the PNIPAM chains are in contact with the water molecules and swell but are restricted by the PS domains, which causes a slight reorganization of the initial micro-phase separation morphology (overemphasized for clarity in figure 7.11). Third (stage III), after extraction of the water by applying vacuum, the PNIPAM cannot relax back totally because of the restriction by the PS domains and deformations remain. The resulting structure serves as the input for the next swelling, again starting with the

stage I process, but water molecules enter in a modified P(S-*b*-NIPAM) film. After several repeated cycles, the PNIPAM structures equilibrate in a different and, with respect to the water storage capacity, less favorable morphology.

7.5 Aging During Cyclic Switching

The aging of the P(S-*b*-NIPAM) film in terms of the water storage capacity is visualized by the maximum water absorption of the P(S-*b*-NIPAM) film at the end of each water storage cycle shown in figure 7.12. In fact, in the first four cycles for the entire film the aging is stronger, than in the subsequent three cycles. During the first four cycles, for the main part of the film the maximum storage capacity decreases from 17.8 to 10.8%. However from the fourth cycle to the seventh cycle, it only decreases slightly (from 10.8% to 9.2%), which shows that the film gradually reaches the equilibrium state of aging. With respect to application such a behavior is advantageous. The film can be reused for water storage and aging slows down.

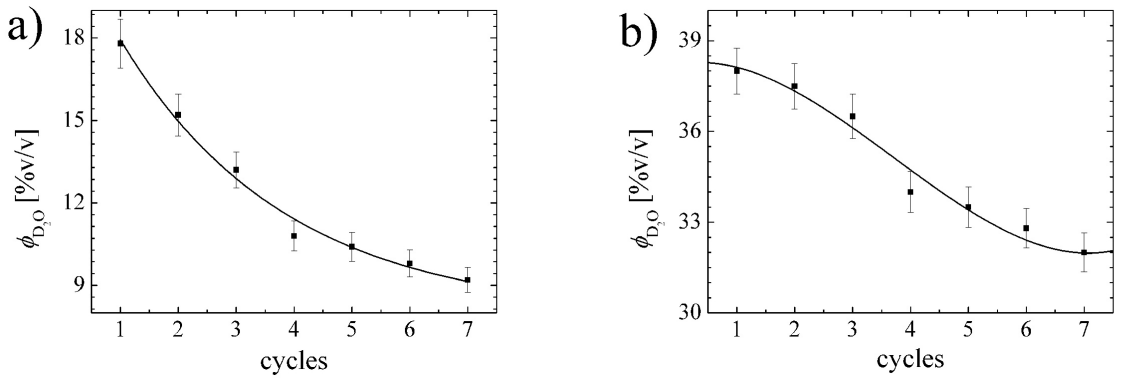

Figure 7.12: Maximum water absorption of the P(S-*b*-NIPAM) film at the end of each water storage cycle plotted as a function of the cycle number: a) for the main part of the film and b) for the interface part of the film.

In contrast to the behavior of the main part of the film, the interface part (pure PNIPAM) has a stronger ability of water storage. It absorbs 38% water at the end of the first water storage cycle. Moreover, as compared to the main part it shows lower reduction in the water storage ability with increasing cycle number. In the interface part of the film, consisting of pure PNIPAM, the decrease of the stored water volume fraction is from

initially 38 to 32% after 7 cycles. The difference between the main part and the interface part of the film in terms of aging indicates that the main reason of such decrease is due to a structural reorganization of the micro-phase separated structure, whereas the pure PNIPAM part undergoes more reversible changes.

The initial structure of the P(S-*b*-NIPAM) film results from its preparation out of 1,4-dioxane solution. Because dioxane is much less selective for both blocks of the diblock copolymer than water, the structure is different from the one which would have been observed from an aqueous solution. After being in contact with water vapor, caused by the absorption of water from the vapor, the glassy and water-insoluble PS blocks confine the swelling of the water soluble PNIPAM blocks. The morphology starts to slightly re-arrange within the spatial confinement introduced by the glassy PS matrix which causes the deformation and slight destruction of the initially formed PNIPAM structures (see figure 7.11). GISAXS and AFM reveal that this change is due to a domain formation whereas the local micro-phase separation structure (cylinders of PNIPAM in a matrix of PS) is unaffected. After several cycles, the water incorporation ability of PNIPAM blocks is reduced but finally reaches an equilibrium state, which is again important for applications which require cyclic water storage.

7.6 H-D Exchange Reaction

From the neutron reflectivity data measured before each storage cycle and after water removal, slight modifications of the P(S-*b*-NIPAM) film were observed (see figure 7.6). These changes cannot be explained by the rearrangement of the P(S-*b*-NIPAM) film. Any rearrangement of the PS and PNIPAM domains, both being fully protonated, cannot explain an increase in SLD. Deuterated material (D_2O) needs to be involved to explain such increase of the SLD. From the measured increase in SLD the amount of remaining water in the P(S-*b*-NIPAM) film is determined (see figure 7.13). The main and interface part of the film behave differently. After one cycle, in the main part of the film $\sim$1%v/v water remains. Within the error bar this values stays unchanged for the subsequent six cycles. In contrast, in the interface part of the film, the amount of remaining water increases during the first six cycles and reaches an equilibrium value of 7%v/v significantly later. Such a difference can be caused either by the composition of the different parts (main versus interface - P(S-*b*-NIPAM) versus PNIPAM) or by the interaction with the

Si substrate.

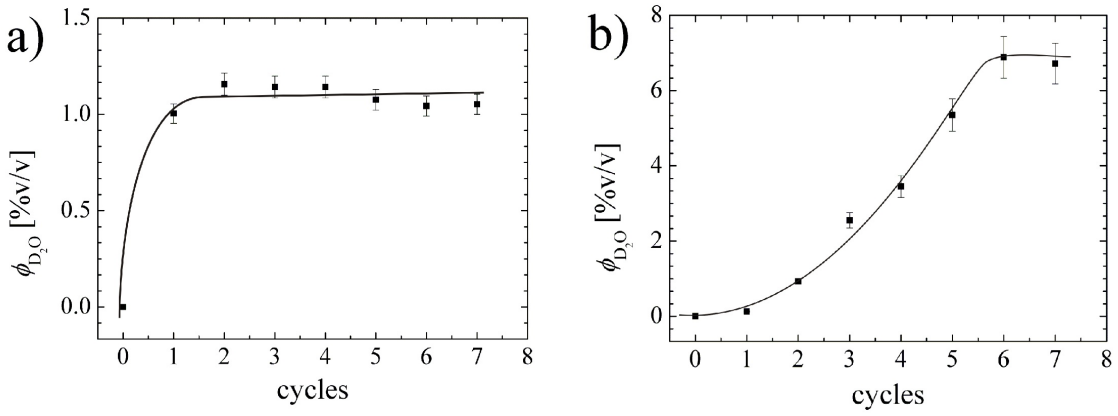

Figure 7.13: The remaining water in the P(S-*b*-NIPAM) film at the end of each removal of the water vapor plotted as a function of the storage and removal cycle: a) for the main part of the film and b) for the interface part of the film.

The remaining water can be caused by formation of strong chemical bonds between D_2O and PNIPAM molecules (bound water). Alternatively, H-D exchange occurring during water storage inside the film can give the impression of not extractable water. To get independent information, FTIR was used on the P(S-*b*-NIPAM) film before and after exposure to the vapor of H_2O and D_2O for 30 min at 23 °C. The results are shown in figure 7.14. For the dry P(S-*b*-NIPAM) film, two bands due to NH_2 groups were observed at 3300 and 1550 cm^{-1}, which result from N-H stretching. Besides these bands, the absorption bands in the range of 2800 - 3000 and 1650 cm^{-1}, assigned to C-H stretching, and the characteristic peak of the C=O, are observed respectively. After the dry film exposure to H_2O vapor for 30 min and drying in air for 15 min, there was no change except that the 3300 cm^{-1} band is damped and broadened.

However, when the dry P(S-*b*-NIPAM) film was exposed to the D_2O vapor for 30 min, and then dried in air for 15 min, the bands corresponding to NH_2 disappeared, and two bands appeared at 2411 and 2343 cm^{-1}. These bands are attributed to asymmetric and symmetric N-D stretching. It can be concluded that the exchange reaction between NH_2 and D_2O occurred during the water storage. The exchange probably proceeds via anionic intermediates. This indicates that the basic strength of the -NH_2 group of P(S-*b*-NIPAM) is stronger than the pKa value of D_2O. Consequently, H-D exchange has to be considered and is the origin of the apparently remaining water. Thus, the FTIR result is in good

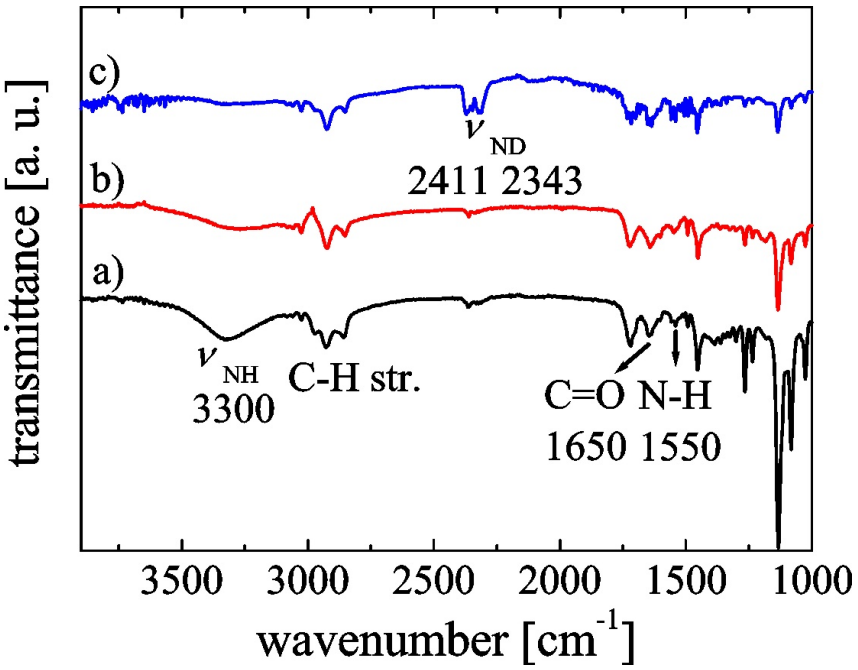

Figure 7.14: IR spectra of P(S-*b*-NIPAM) film: a) as prepared, b) after exposure to H_2O at 296 K for 30 min followed by drying in air at 296 K for 15 min and c) after exposure to D_2O at 296 K for 30 min followed by drying in air at 296 K for 15 min.

agreement with the GISAXS observation and residual solvent being deposited during cycling can be excluded.

7.7 Conclusion

Using P(S-*b*-NIPAM) with a long PS and a short PNIPAM block in combination with a solvent, which is more equal in interaction with the both blocks than water, results in thin films, which allow for water storage without swelling. The installed glassy matrix suppresses the swelling inherent for hydrogel films (e.g. PNIPAM films) and gives the necessary stability to enable repeated water storage. Although the internal rearrangement of the structure installed out of 1,4-dioxane during storage cycles decreases the amazingly high capability of incorporating close to 17% water in total without swelling, aging of the films is limited. Aging stops after several storage cycles, and a reduced water storage capacity remains. The mechanisms of the water storage and water removal do not depend on the cycle number (see figure 7.11). With the investigated glassy films, a new material is at hand which allows repeated storage of water at fixed volume or fixed film thickness

conditions. Thus this material will avoid problems related to swelling induced strain. It can be used for coatings reducing humidity in nano-applications, which might suffer from changes in the water content of the surrounding atmosphere.

Chapter 8

Microflow on PNIPAM Based Diblock Thin Films

8.1 Introduction

Microfluidic devices which manipulate microquantities of liquid solutions allow substantial improvement of the efficiency of chemical processes. The studies of fluid flow in confined geometries are essential for many applications as microanalytics or high throughput devices and reactors [DE97, WBH99, IRF01]. On the other hand, PNIPAM based copolymer thin films have been investigated as a prominent candidate for advanced applications such as thermoresponsive surfaces, miniaturized sensor systems and nano-switches [TPA06, GM07, GM08, KD09]. Whereas thermoresponsive surfaces make use of a change in the wetting properties, triggered by a change in temperature, miniaturized sensor systems and nano-switches are based on the change in hydrogel film thickness, because the surface area is fixed [WW08]. Therefore, the combination of PNIPAM based copolymer thin films and the microfluidic devices will open new applications like miniaturized sensor systems and nano-switches in flow.

Moreover, a simplified thin film sensor and nano-switch will consist of the active (sensor) layer and a metal top-layer. The active layer contains PNIPAM. The metal top-layer can be coated on polymer thin films by many ways, such as evaporation and sputtering [HA03, KG09]. However, by evaporation or sputtering, due to the high kinetic energy of incoming metal atoms, it is possible to change the morphology of the film and introduce unexpected chemical and physical reactions on the film surface, which could have non-

negligible implications for the properties of the polymer materials. The use of microfluidic devices offers another way for metal coating on polymer films, which might not introduce any strong chemical or physical reaction to the film surface. Thus, polymer thin films can maintain their original properties, which is very important in the view of many applications.

Up to now, mostly microscopy based experimental techniques have been employed to investigate the behavior of fluids in channels and confined near surfaces. Although crucial, these techniques should be complemented with others to cover a larger range of characteristic lengths. Moreover, complementary methods should be sensitive to composition fluctuations and provide a direct statistically relevant information via a representative sampling. All these features are clearly within reach of scattering techniques. In fact, grazing incident small angle X-ray scattering (GISAXS) can provide information about object shapes, sizes, and characteristic correlation lengths between objects [MBP97] with a high spatial resolution. Due to the peculiar geometry of the experiment, it offers a dramatic enhancement of the signal coming from the probed interface, without significantly sensing the overlaying bulk of solution (which is accessible via more conventional x-ray scattering) [NJA01].

8.2 Experimental Section

Materials. An asymmetric diblock copolymer of poly(styrene-*block*-*N*-isopropylacrylamide), denoted P(S-*b*-NIPAM), with a molecular weight of 23500 g mol^{-1} and a polydispersity of 1.05 was purchased from Polymer Source Inc. The volume fraction of PNIPAM in the copolymer is 27.6%. The initial dry P(S-*b*-NIPAM) films with different thicknesses were prepared by spin-coating (2000 rpm, 30 s) from a 1,4-dioxane solution at room temperature onto pre-cleaned glass substrates. The cleaning protocol is described in chapter 4. A water based gold nanoparticle suspension (nominal mean particle size of 20 nm and concentration of 7 $\times$ 10^{11} particles/mL from G. Kisker GmbH, Germany) was used for metal coating.

Experimental Set-up. Figure 8.1 shows the design layout of the fluidic cell. The detail of the design of fluidic cell can be found elsewhere [MJF08]. Basically, the main idea is to create a complete channel system with the input and output connectors. The top window

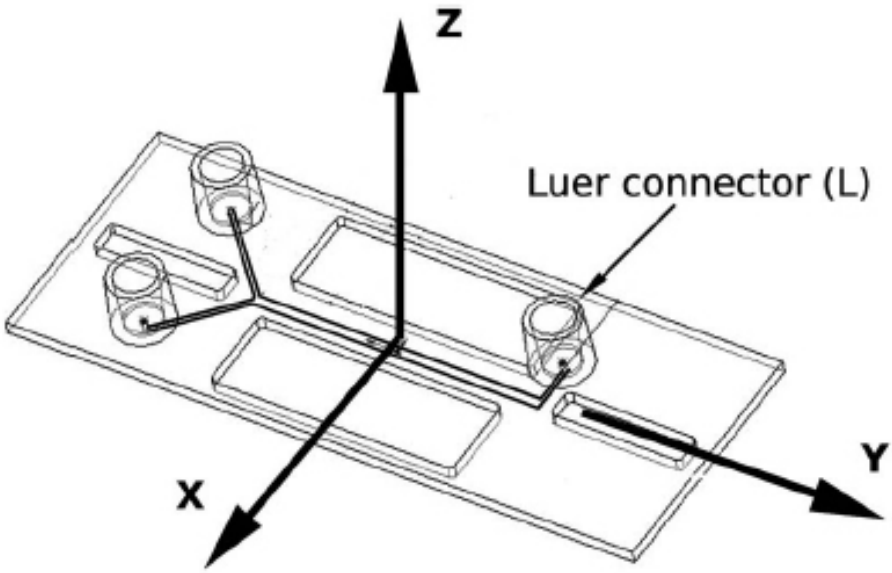

Figure 8.1: Design layout of the fluidic cell taken from reference [MJF08]. The asymmetric design with two inlets and one outlet (or vice versa) enables mixing of fluids. Included is a realspace coordinate system.

of the cell was kept thin and transparent to visible light in order to allow for optical characterization. The material of the cell body is a commercially available cyclic olefin based copolymer resistant to polar organic solvents and water. This material can be easily machined and thermally bonded to itself. It has a relatively low absorption in the X-ray range. Moreover it is transparent to visible light which enables optical characterization of the flow via microscopy. In order to keep absorption low, a wall thickness of 0.5 mm is determined as an optimum value. The channel width is chosen to be 1 mm, which provides a reasonable trade-off in terms of transmission and the beam´s footprint. The footprint length for the set-up is 7.45 mm under the experimental conditions used, and the small channel size makes it easy to align the cell in the beam.

GISAXS experiments were performed at beamline BW4 at HASYLAB (DESY) in Hamburg. The wavelength is 0.138 nm and the incident angle is 0.5°. Figure 8.2 shows the GISAXS geometry. The whole channel is brought in contact with the surface of a variable flat object (e.g., a glass surface coated with a PNIPAM film). The complete assembly (top surface with channel system and substrate) is then attached onto the X-ray goniometer via a rigid metal clamp. In order to prevent contamination of the investigated substrate surface via diffusion of adhesive, no glue is used to seal the channel. The incident beam

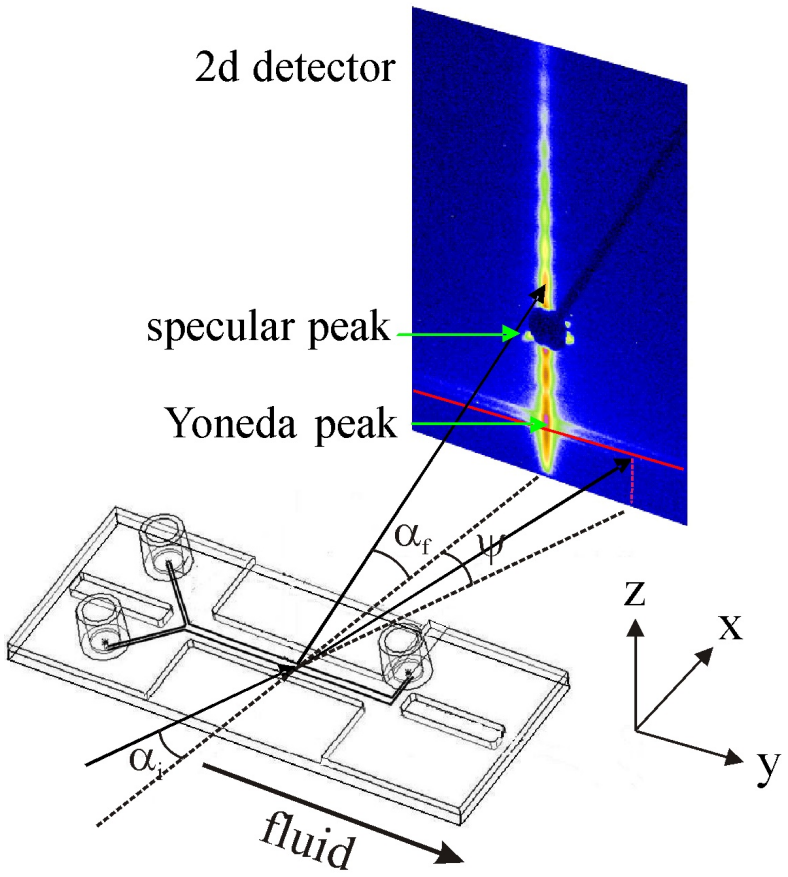

Figure 8.2: Sketch of the GISAXS geometry.

is focused on the center of the channel of the cell. The whole experiment was performed at room temperature. The addition of water or gold suspension marks the starting point of the kinetics (time = 0). The counting times for the kinetic measurement are 600 s for the water fluid and 80 s for the water based gold suspension in order to achieve the best time resolution and spatial resolution simutanously. The counting time for the static measurements ex-situ is 3600 s.

Injection of the water or the water based gold suspension was performed using a syringe pump (model PHD 2000 infuse/withdraw from Harvard Apparatus). The syringes were connected to the cell via 1.8 mm inner diameter silicone tubes and Luer adapters.

8.3 Injection of Water

In order to identify the characteristic features introduced by each component of the setup, the diffuse scattering was measured in GISAXS configuration for the bare substrate (glass), the bare substrate plus a cell and the thin film on the substrate plus a cell. In this case, the film thickness is 160 nm. Figure 8.3a shows the detector scan from the two-dimensional GISAXS data. At small exit angles ($\alpha_i + \alpha_f$ ~0.55-0.75°), the Yoneda peaks of the different materials are observed. The bare glass substrate shows a well defined, relatively sharp peak, as expected for bare glass. The bare substrate plus a cell shows a multipeak located at smaller exit angles. This observation is expected because the critical angle of glass is larger than that of polyolefins due to the larger electron density of glass. The thin film on the substrate plus a cell shows a peak at 0.685°, which corresponds to the Yoneda peak of P(S-*b*-NIPAM). Because the electron densities of PS and PNIPAM are similar, there is only one peak present instead of two. Besides of the Yoneda peaks of the polymer and the glass, there is no additional strong feature observed in the diffuse scattering region of the thin film on the substrate plus a cell. As a consequence, the designed fluidic cell is well suited for GISAXS experiments and will not dominate the observed diffuse scattering.

Figure 8.3b shows the out of plane scan from the two-dimensional GISAXS data. For the out of plane cut of the bare glass substrate, there are no obvious intensity peaks. The whole curve is smooth and has a Gaussian shape. This is expected as no internal structures are installed on the bare glass substrate. For the out of plane cut of the bare glass substrate plus a cell, a very weak and broad intensity peak (denoted as structure factor II) arises up at a small q_y value, which hints a large distance between two neighboring structures. This intensity peak is introduced by the cell. In the case of the out of plane cut of the thin film on the substrate plus a cell, a stronger intensity peak at a larger q_y value is present and corresponds to a structure factor of 20 nm (denoted as structure factor I). This value is the same as obtained for this polymer thin film measured before but without the cell (see chapter 7). It is corresponding to the structure-structure distance of the microphase separated cylinder structure installed in the film. Besides this intensity peak, no additional strong feature was observed. Thus, again, the designed fluidic cell is well suited for GISAXS experiments avoiding much interference.

Once it was established that the cell itself introduces very little additional contribution to

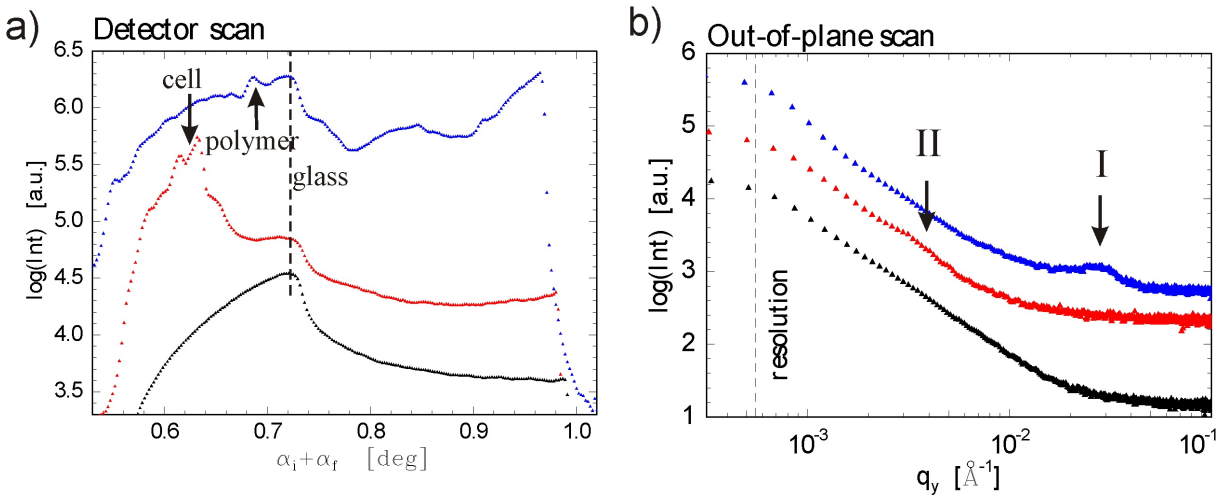

Figure 8.3: Detector scan cuts (a) shown as a function of the detector angle $\alpha_i + \alpha_f$ and out of plane scan cuts (b) shown as a function of the q_y component of the scattering vector from the 2D GISAXS pattern. The cuts of the bare glass substrate, the bare substrate plus a cell and the thin film on the substrate plus a cell are shifted from bottom to top. The Yoneda peak corresponding to the glass is marked by a dash line. The Yoneda peaks corresponding to cell materials and P(S-*b*-NIPAM) are marked by arrows. The intensity peaks corresponding to P(S-*b*-NIPAM) (I) and glass (II) are marked by arrows in the out of plane scan.

the diffuse scattering, pure water was injected into the channel. During this experiment, the flow rate was kept at a value of 0.02 mL/min. It was shown in previous measurements that the same polymer film doesn´t swell in contact with water vapor (see chapter 7), so it is of special interest to explore whether such a film can swell in water fluid or not. Figure 8.4a shows a selected series of the detector scan from the two-dimensional GISAXS data focusing on the region between the Yoneda peak and the beamstop. The time interval between two neighboring curves is 10 min. It is observed that at the beginning of the injection (time = 0), there are only 3 intensity peaks in this region as marked by arrows. With increasing time, more peaks arise up. At the time = 190 min, there are 5 peaks shown in this region. It is discussed in chapter 2 and 4 that, these modulations are caused by a partial phase coherence of X-ray waves diffusely scattered from different interfaces. The necessary condition for the partial phase coherence of diffusely scattered waves is a roughness correlation between the SiO_x surface and the polymer surface. Thus, a long-range correlation between both interfaces is installed and the thickness of the polymer film determines the distance between adjacent minima in the intensity modulation in the detector scan

$$\Delta q_z = \frac{2\pi}{d} \tag{8.1}$$

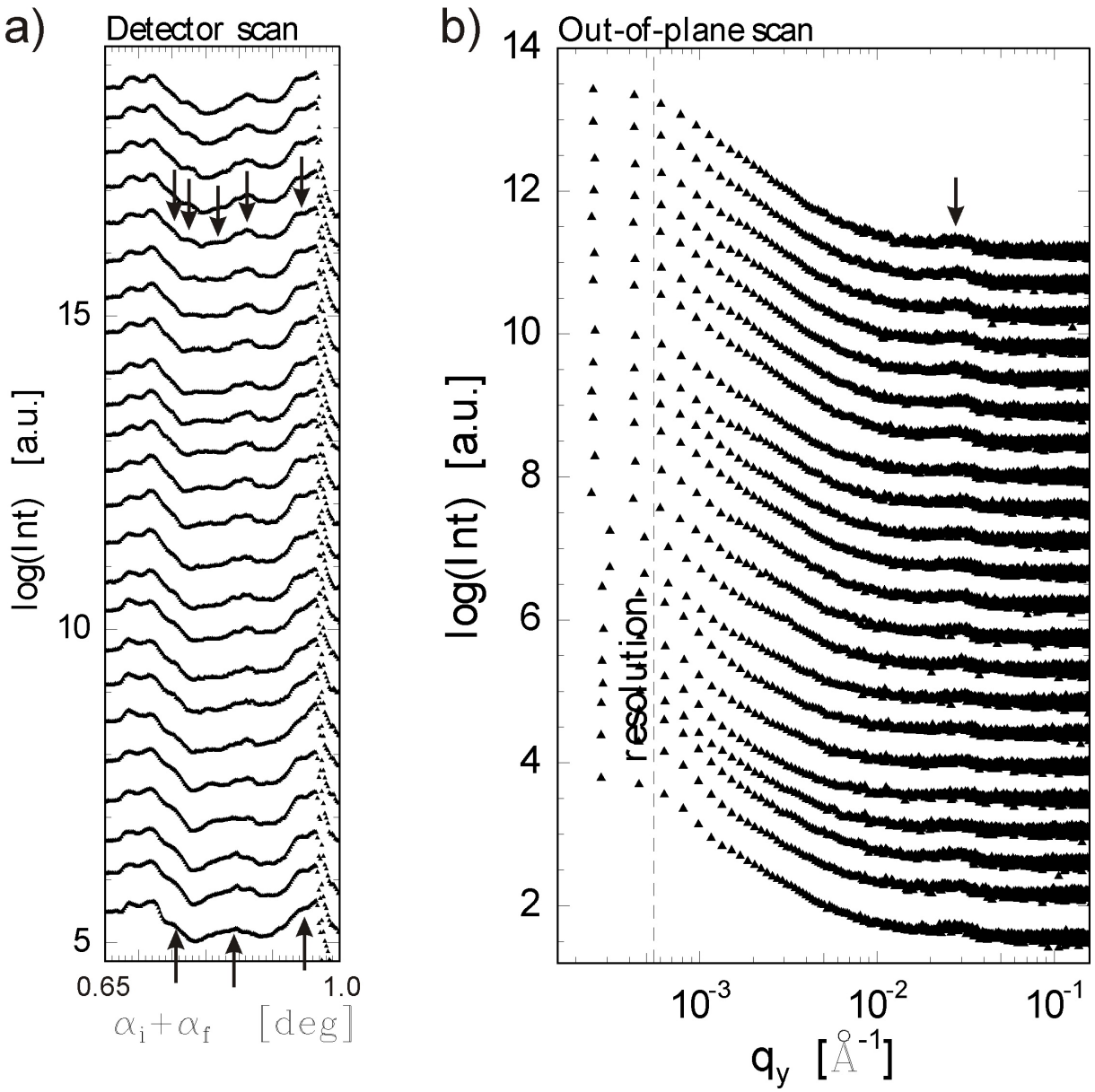

Figure 8.4: Detector scan cuts (a) shown as a function of the detector angle $\alpha_i + \alpha_f$ and out of plane scan cuts (b) shown as a function of the q_y component of the scattering vector from the 2D GISAXS pattern. These cuts are corresponding to the GISAXS pattern of the swelling kinetics of a 160 nm P(S-*b*-NIPAM) thin film with a time scale from 0 to 250 min (shifted from bottom to top). The intensity peaks are marked by arrows.

Such a film thickness can be named as correlated thickness. Thus, by eq. 8.1, the time evolution of the correlated film thickness is obtained (see figure 8.5a). The injection of water marks the start of the experiment. The swelling of the film can be divided in three different regimes. They are denoted by stage I, II and III (see figure 8.5a). In the first regime (stage I, 0-2.0 $\times$ 10^3 s), the film thickness has a slight decrease. This decrease

could be due to the reorganization of the film surface morphology caused by the presence of water. At this stage, water has not yet diffused into the film. In the second regime (stage II, 2.0-7.2 $\times$ 10^3 s) the coiled PNIPAM chains start to swell and selectively attract water molecules because PNIPAM is soluble in water (see chapter 7). This causes a strong increase of the film thickness from 150 to 310 nm. In the third regime (stage III, 7.2 $\times$ 10^3 s-end) the polymer film finally reaches an equilibrium state. Another important parameter related to the film morphology is the long-range correlation between the film and the substrate. This parameter can not be obtained directly from the GISAXS data. An indirect way to show the changes of long-range correlation is to measure the intensity amplitude of the modulations in the detector scan (see figure 8.6).

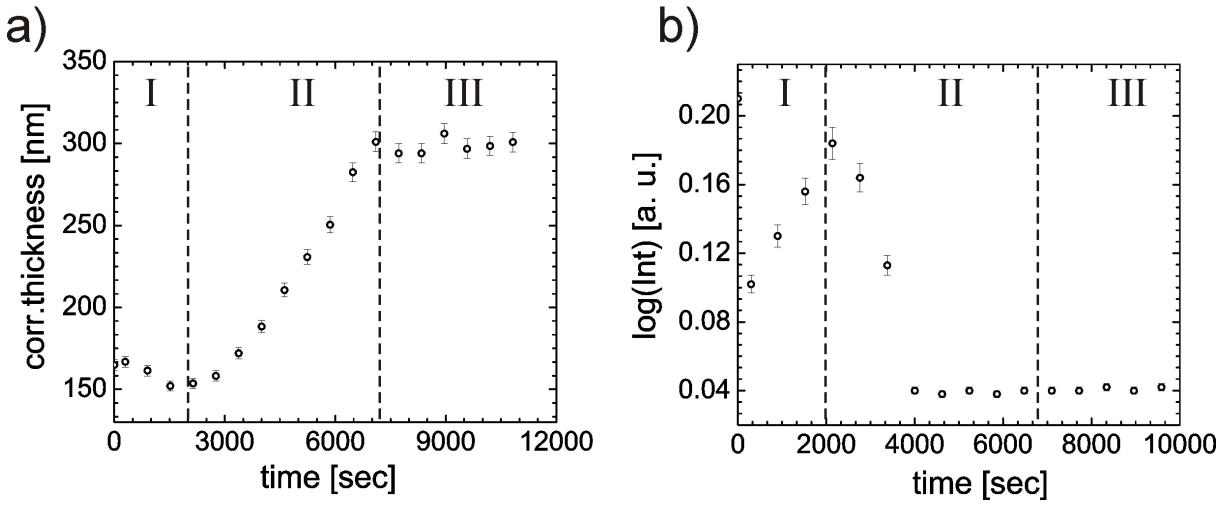

Figure 8.5: The time evolution of the film thickness (a) and the intensity amplitude of the modulations (b) in the detector scan. The sample is a 160 nm P(S-*b*-NIPAM) thin film with a pure water fluid.

Figure 8.5b shows the time evolution of the intensity amplitude of the modulations in the detector scan. Regarding the three different regimes taken from the change in film roughness, the behavior is more complex. In the first regime (stage I), the intensity amplitude has a strong increase, which gives a hint that the film surface has a stronger long-range correlation to the substrate than in the case of the dry film. This means that in the first regime, the coiled PNIPAM chains start to rearrange and the film surface becomes more rough but is still correlated to the substrate as shown in figure 8.7. In the second regime (stage II), the intensity amplitude decreases rapidly which hints the weakening of the long-range correlation. Thus, in the second regime, due to further swelling and the big increase in film thickness, the film surface becomes slightly independent on the substrate. However the long-range correlation doesn´t disappear as the intensity amplitude doesn´t

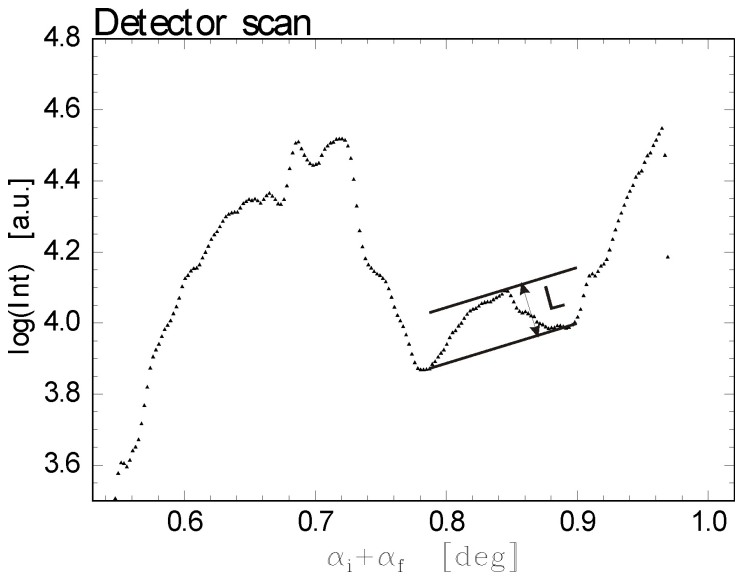

Figure 8.6: Detector scan cuts shown as a function of the detector angle $\alpha_i + \alpha_f$ from the 2D GISAXS pattern of the initial 160 nm P(S-*b*-NIPAM) film. The intensity amplitude of the modulation is marked by "L".

decrease to zero. In the third regime (stage III), the intensity amplitude stays constant which means that the long-range correlation also becomes constant. In figure 8.7, these three regimes are sketched.

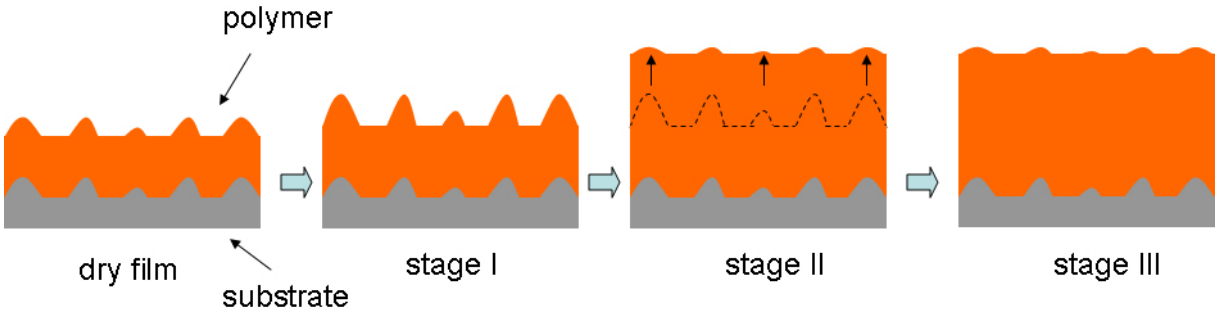

Figure 8.7: Sketch of three different regimes corresponding to the time evolution of the intensity amplitude of the modulation in the detector scan. The sample is a 160 nm P(S-*b*-NIPAM) thin film with a pure water fluid.

Figure 8.8 shows the AFM topograph images of the initial dry film and the film after the fluidic experiment. The initial dry film shows a well-defined microphase separated cylinder structure perpendicular to the film surface (see chapter 7). After the fluidic experiment, the surface structure is distored and orientated to the direction of the flow. Thus, the water flow changes the surface topograph of the film during the fluidic experiment. However,

from the out of plane scan of the 2D GISAXS pattern (see figure 8.5b), it can be found that the structure factor (marked by an arrow) keeps constant during the experiment. Thus, the internal structure of the film is not influenced by the flow, which is a big adventage for appliations as the most film properties related to the internal structures can remain.

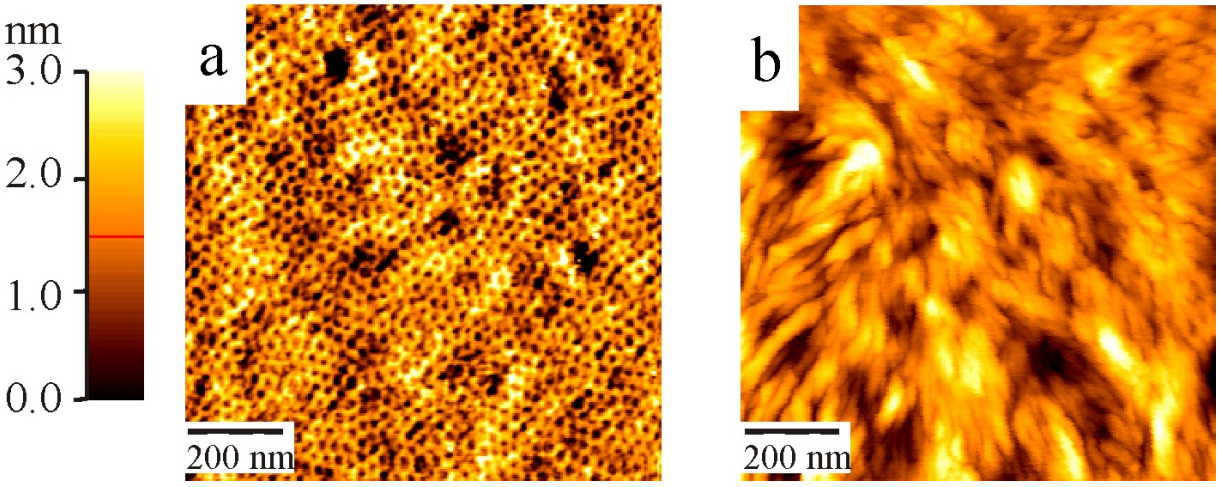

Figure 8.8: Topography AFM images of the 160 nm P(S-*b*-NIPAM) film before (a) and after (b) the fluidic experiment. The scan size is 1 μm $\times$ 1 μm. The structure height increases with the brightness of the structures in the images. The height scale bar range is 0 to 3 nm.

8.4 Injection of Gold Suspension

a. Flow Rate 0.02 mL/min. To test the metal top-layer deposition by the microfluidic device, a water based gold nanoparticle suspension was injected into the channel. A P(S-*b*-NIPAM) film with a thickness of 122 nm was used as a template. The flow rate was set to 0.02 mL/min. Figure 8.9a shows a selected series of detector scan from the two-dimensional GISAXS data focusing on the region between the Yoneda peak and the beamstop. The injection of the gold suspension marks the start of the experiment. The time interval between two neighboring curves is 200 s. Three different regimes are presented. In the first regime (stage I, 0-1.6 $\times$ 10^3 s), the average distance between two neighboring modulations on the detector scan has only a slight decrease which hints that the film thickness has a slight increase. Moreover, the amplitude of intensity peaks first shows a quick increase, and then damps rapidly with increasing time, which means that the long-range correlation between interfaces first is enhanced, and then weakens. This is probably because the film surface becomes slightly independent on the substrate by

swelling (see the previous section). With increasing time, the Yoneda peak of polymer stays constant in this regime. No additional Yoneda peaks are found. Thus, in this time interval, no gold is deposited onto the film surface. In the second regime (stage II, 1.6-4.0 $\times$ 10^3 s), the Yoneda peak is shifted to a larger exit angle, which is located between the Yoneda peak of the polymer and the Yoneda peak of the gold. This happens only when a nanocomposite is formed, which is composed of both the gold and the polymer. Thus, gold nanoparticles are deposited onto the film surface and form a nanocomposite with the polymer in this regime. Moreover, more modulations rise up on the detector scan, which means the film swells. In the third regime (stage III, 4.0 $\times$ 10^3 s-end), two different Yoneda peaks can be clearly distinguished. They are corresponding to the Yoneda peak of gold and the Yoneda peak of gold-polymer composite, respectively. Thus, in this regime, due to further gold nanoparticle deposition, besides gold-polymer composite, pure gold clusters start to form.

In the out-of-plane scan from the two-dimensional GISAXS data (see figure 8.9b), also there three regimes are distinguished. These cuts are made at the critical angle of gold to address the struture formed by gold nanoparticles. In the first regime, no obvious intensity peaks are shown as gold particles have not yet deposited on the film surface. In the second regime, intensity peaks rise up at small q_y values which coreponds to a large struture to structure distance. These intensity peaks are correponding to a structure factor of 600 nm, which are the structure-structure distance of the gold-polymer composites. In the third regime, intensity peaks rise up at even smaller q_y values which are close to the resolution limit. In this regime, a homogenous layer of gold starts to form. Thus, a very large structure size is expected [KG09].

The detaill analysis of the time evolution of the correlated film thickness can be obtained using eq. 8.1. In figure 8.10a, the time evolution of the correlated film thickness can also be divided into three regimes correspondingly. In the first regime (stage I, 0-1.6 $\times$ 10^3 s), the film thickness has only a slight increase. In the second regime (stage II, 1.6-4.0 $\times$ 10^3 s), the film starts to swell and has a sharp increase in thickness until it reaches a plateau. Afterwards, the film has a slight deswelling until it reaches a new equilibrium state which is the third stage. In figure 8.10b, the time evolution of the intensity amplitude of the modulations in the detector scan is shown. Different from the case of pure water fluide, the intensity amplitude damps quickly after a very short increase. Thus, due to gold deposition and film swelling, the long-range correlation between interfaces is difficult

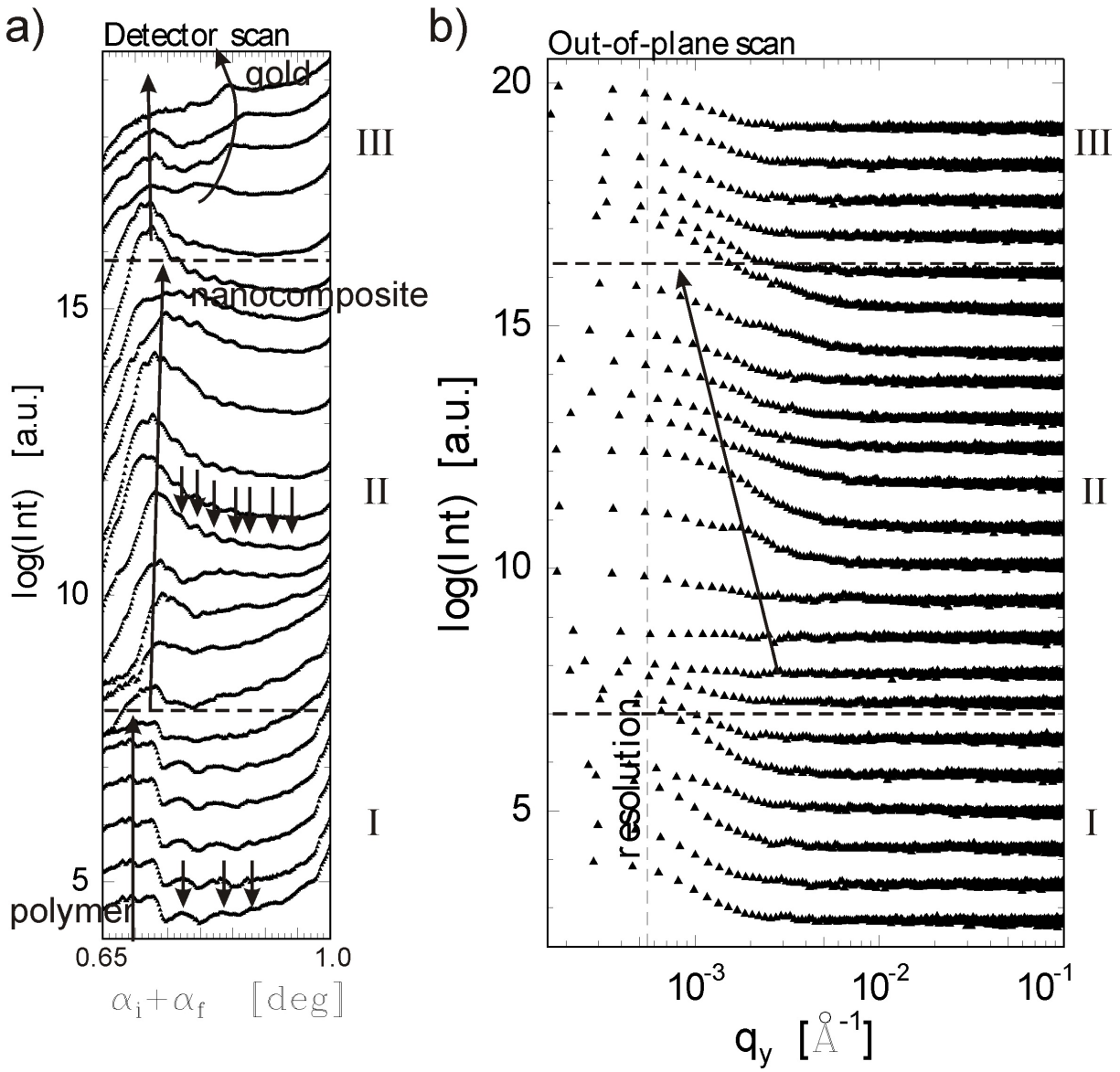

Figure 8.9: Detector scan cuts (a) shown as a function of the detector angle $\alpha_i + \alpha_f$ and out of plane scan cuts (b) shown as a function of the q_y component of the scattering vector from the 2D GISAXS pattern. The cuts are corresponding to the GISAXS pattern of the kinetics of a 122 nm P(S-*b*-NIPAM) thin film with a water based gold nanoparticle suspension. The time scale is from 0 to 460 min from bottom to top. The flow rate was set to 0.02 mL/min. The intensity peak positions are marked by arrows.

to keep. However certain long-range correlation still remains as the value of the intensity amplitude does not decrease to zero.

Figure 8.11 describes the three different stages mentioned above. In the first stage, only the film thickness has a slight increase due to swelling. No gold is deposited on the

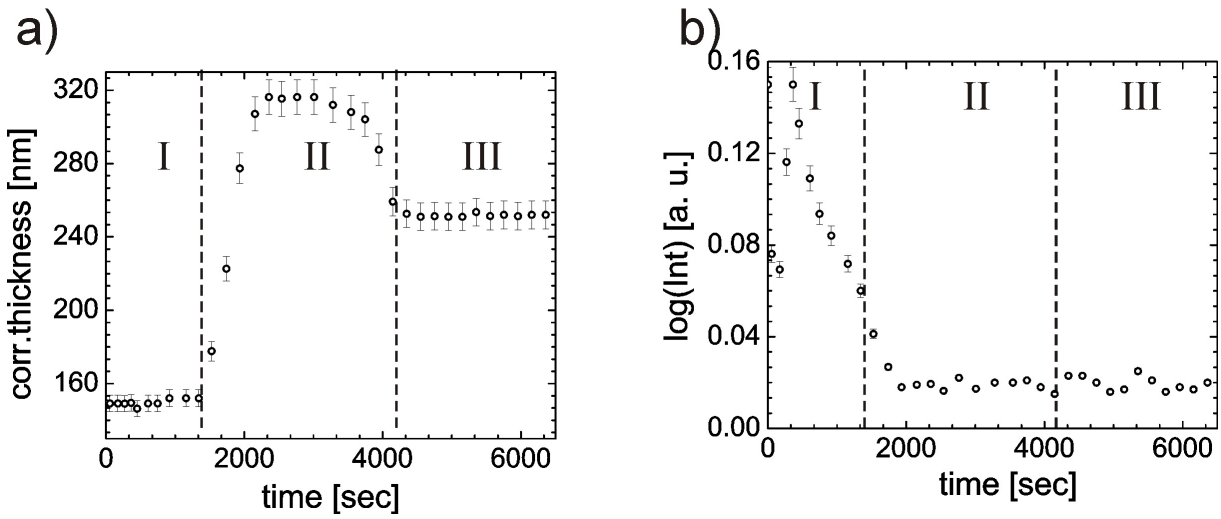

Figure 8.10: The time evolution of the film thickness (a) and the intensity amplitude of the modulation in the detector scan (b). The sample is a 122 nm P(S-*b*-NIPAM) thin film with a water based gold suspension. The flow rate is 0.02 mL/min.

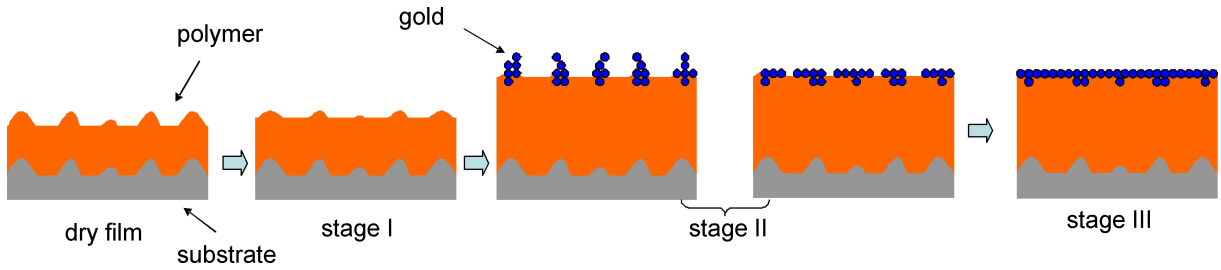

Figure 8.11: Sketch of three different regimes of the film. The sample is a 122 nm P(S-*b*-NIPAM) thin film with a water based gold suspension.

film. In stage II, gold nanoparticles form composite with the polymer. Moreover, based on these composites, gold nanoparticles form a hill-like structure. However, with further gold deposition, such a hill-like structure is wiped-out and a homogenous gold layer starts to form. Thus, the film thickness has a strong increase at the beginning of this stage due to the swelling and the gold deposition. Later, due to the disappearance of the gold clusters, the film thickness has a slight decrease. Finally, in stage III, further gold deposition forms a more homogenous gold layer but the film thickness keeps constant.

Although the mechanism of gold deposition on polymer thin film by microfluid is still unclear, G. Kaune et al. [KG09] found that by sputtering, when a gold atom impinges on the polymer surface, it is adsorbed and diffuses laterally along the surface. The chemical bond to the polymer chains is weak and the adatom can desorb again easily. However, once stable nuclei have formed, diffusing adatoms can be captured and the nuclei grow

in size to small clusters. To minimize the interface with the polymer, the clusters adapt a spherical or ellipsoidal shape. Once the critical cluster density is reached, a distinctive lateral growth starts by adsorption of diffusing adatoms, and the surface coverage increases rapidly. In the present work, stage I can be considered as the gold particles diffusing laterally along the surface but not adsorbed on the surface. In stage II, stable nuclei as nanocomposites have formed, diffusing adatoms can be captured, the nuclei grow in vertical direction. However, such structure is not stable and with further gold deposition, it will collapse. Thus, in stage III, a distinctive lateral growth starts by adsorption of diffusing adatoms and a homogenous gold layer starts to form.

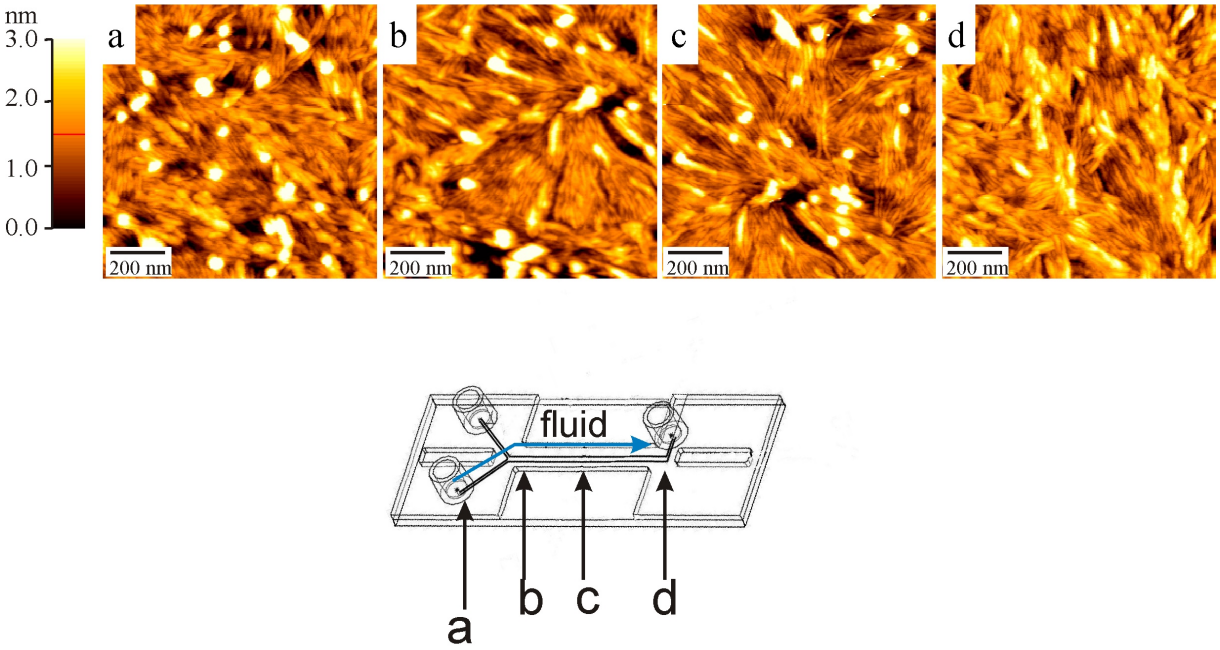

Figure 8.12: Topography AFM images of the 122 nm P(S-*b*-NIPAM) film surface taken at different positions along the channel (a-d as marked on the sketch of the cell). The scan size is 1 μm $\times$ 1 μm. The structure height increases with the brightness of the structures in the images. The height scale bar range is 0 to 3 nm. The direction of the fluid is marked by the blue arrow.

Figure 8.12 shows the topography images of the film surface taken at different positions along the channel. Similar to the case of sputtering [KG09], the gold clusters adopt a spherical or ellipsoidal shape to minimize the interface with the polymer. The average structure size of the gold cluters is 130 nm. As the nominal mean particle size is 20 nm, each cluster is corresponding to 6-7 particles. From the beginning to the exit of the channel (as marked by the blue arrow), the cluster density of gold nanoparticles on the film

shows a decreasing gradient. It was also reported that thickness uniformity of metal layer can be greatly improved when the direction of the flow is alternated periodically [GED04]. The reason for the surface density gradient is that the gold nanoparticles deposit fast and the flow rate is slow. Thus, gold nanopartices deposit much more at the beginning of the channel than at the end of the channel.

b. Flow Rate 0.01 mL/min. To test the influence of the flow rate to the swelling and gold deposition of the film, an identical sample with a different flow rate (0.01 mL/min) of gold suspension was investigated. Figure 8.13a shows the corresponding detector scan. In the detector scan, it is observed that with increasing time, the modulations on the detector scan shift to larger exit angles. The shift of modulations is due to the change of the film surface moprphology. However, the film thickness shows no change during the experiment as the distance between two neighboring modulations keeps constant. Also the Yoneda position of polymer does not change. No Yoneda peak of gold is found. Thus, gold particles do not deposite on the film surface with such a slow flow rate. In the out-of-plane scan (see figure 8.13b), there is no intensity peak rising up with increasing time, which also hints that the gold particles do not deposit on the film surface.

The explanation for this is that because of the slow flow rate, most gold particles are deposited at the beginning of the channel. Few gold particles are brought to the center or even the end part of the channel by the water flow. As the X-ray is always focused on the center of the channel, no signal of gold can be found. This explanation is proved by the AFM topography images of the film surface taken at different positions along the channel (see figure 8.14). As shown in figure 8.14, at the beginnng of the channel (position a), many gold particles are deposited on the film surface, the average structure size is 122 nm, which is comparable to the case of the sample with a faster flow rate (0.02 mL/min). However, at position b as marked in figure 8.14, the surface density of gold particles is seriously reduced, whereas at position c, the center of the channel and also the position where X-ray is focused, no trace of gold is found.

Figure 8.15a shows the time evolution of the film thickness. The thickness of the film is constant within the error bar. In figure 8.15b, the time evolution of the intensity amplitude of the modulations is shown. The intensity amplitude first increases and then decreases, which hints that the long-range correlation between the film surface and the substrate is enhanced first and then weakens. Such change can be due to the water se-

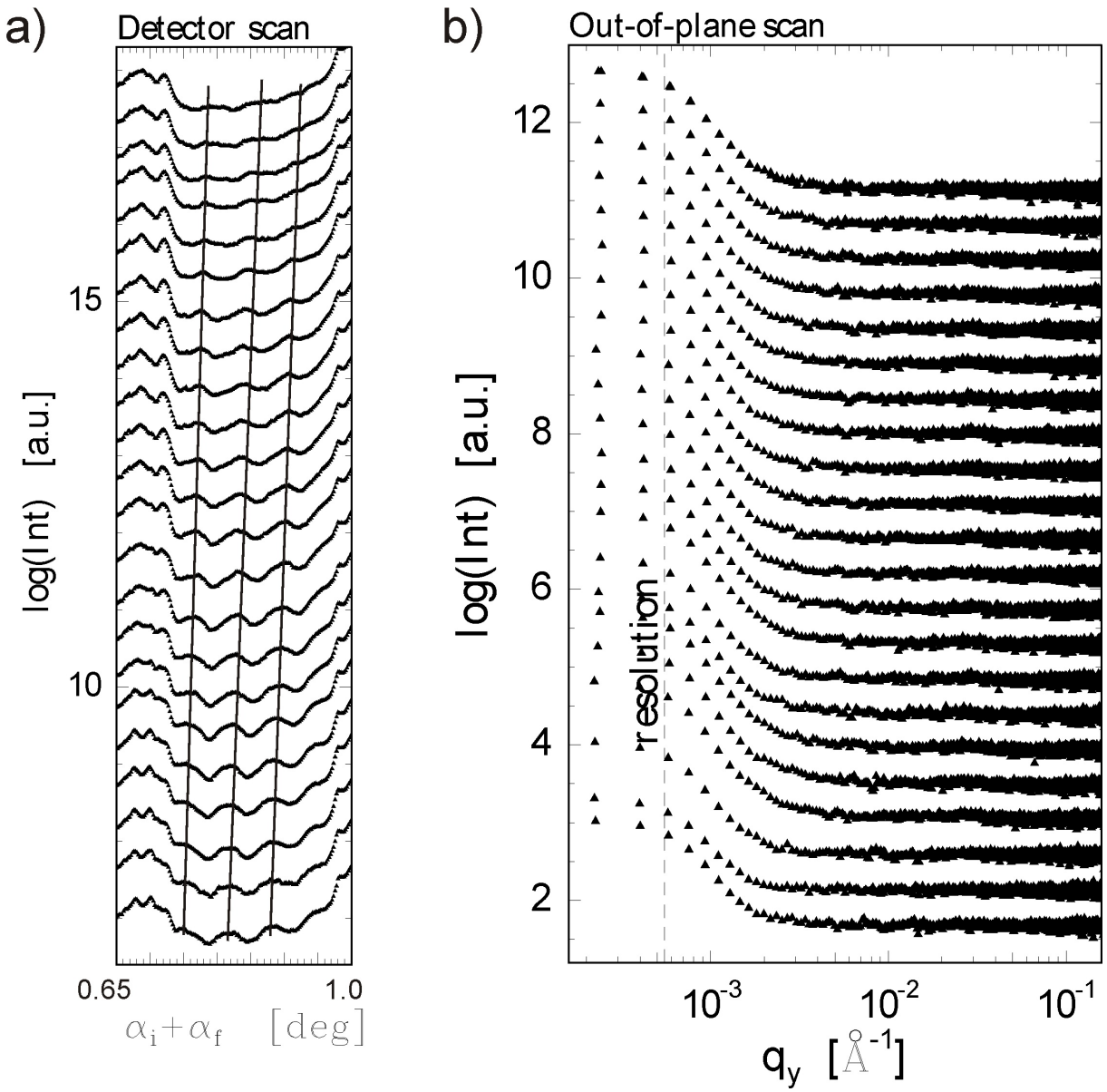

Figure 8.13: Detector scan cuts (a) shown as a function of the detector angle $\alpha_i + \alpha_f$ and out-of-plane scan cuts (b) shown as a function of the q_y component of the scattering vector from the 2D GISAXS pattern. The cuts correspond to the GISAXS pattern of a 122 nm P(S-*b*-NIPAM) thin film with a water based gold nanoparticle suspension. The flow rate is 0.01 mL/min. The time scale is from 0 to 460 min from bottom to top. The intensity peak positions are marked by straight lines.

lectively diffuse into the PNIPAM chains, which causes the distortion and reorganization of the internal morphology (see chapter 7). However, due to the limitation of the glassy block (PS) and a small flow rate, the film thickness does not increase, which is in contrast to the behavior observed in pure water at higher flow rate.

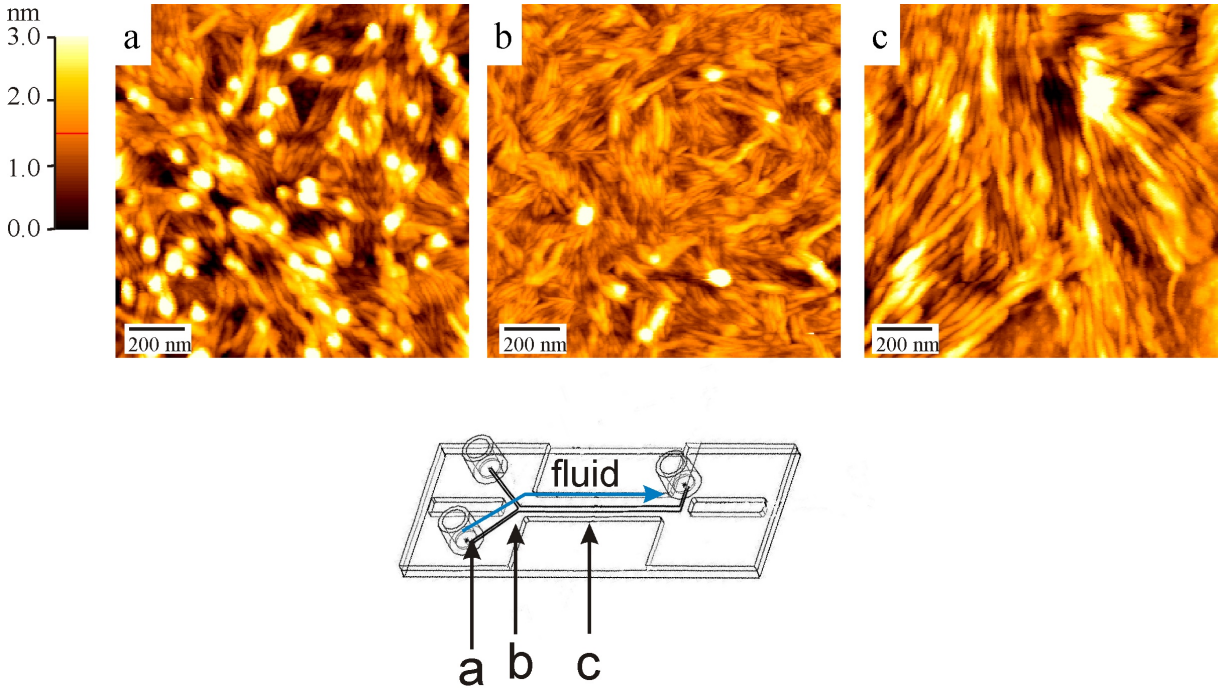

Figure 8.14: Topography AFM images of the 122 nm P(S-*b*-NIPAM) film surface taken at different positions along the channel (a-c as marked on the sketch of the cell). The scan size is 1 μm $\times$ 1 μm. The structure height increases with the brightness of the structures in the images. The height scale bar range is 0 to 3 nm. The direction of the fluid is marked by the blue arrow.

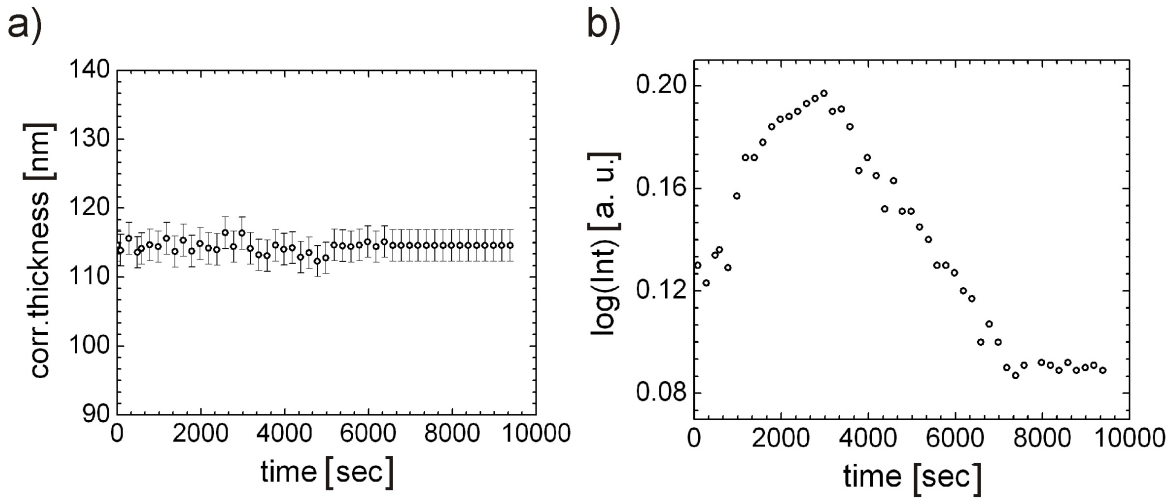

Figure 8.15: The time evolution of the film thickness (a) and the intensity amplitude of the modulations in the detector scan (b). The sample is a 122 nm P(S-*b*-NIPAM) thin film with a water based gold suspension. The flow rate is 0.01 mL/min.

Thus, by conclusion, both the swelling and the gold deposition of the P(S-*b*-NIPAM) film is strongly influenced by the flow rate.

8.5 Conclusion

In the present work, an optimized fluidic set-up for hydrogel thin film swelling and gold deposition is demonstrated. This set-up allows the P(S-*b*-NIPAM) film which cannot swell in water vapor to swell in flowing water. The morphology of the film surface is changed by the presence of the flowing liguid. However, the internal structure of the film remains unchanged, which is a big adventage in applications of nanosensors and switches. The gold deposition on the P(S-*b*-NIPAM) film by using a water based gold nanoparticle suspension is successful. The surface density of gold clusters and the swelling properties of the film is strongly dependent on the flow rate.

Chapter 9

Structure near the Volume-phase Transition

9.1 Introduction

A PNIPAM based gel in water undergoes a volume-phase transition at its transition temperature. This is due to the hydrophobic interaction between NIPAM and water molecules. The critical phenomena of this volume-phase transition were studied by calorimetry [LY90], dynamic light scattering (DLS) [SE88], and friction measurements [TM91]. The divergence of the correlation length in gels were studied by Tanaka et al. for acrylamide gels [TT73] and by Sato et al. [SE88] for NIPAM gels. However, since a DLS method was employed in these studies, the understanding of the spatial fluctuations of concentration were limited to the characteristic length scale of the wavelength of light. Later, Geissler et al. studied the crosslinking density dependence of the gel inhomogeneity and osmotic modulus for several kinds of gels, e.g., gels made of poly(acrylamide) [HAM85, MS89], poly(dimethylsiloxane) [MS91], poly(vinyl acetate) [HF91], by combining small-angle neutron scattering (SANS) with osmotic deswelling measurements. SANS is a relevant technique for investigations of such a spatial inhomogeneity in the length scale from a few tens of angstroms to a thousand of angstroms [HAM85]. Geissler et al. proposed a scattered intensity function for the gel was well described with a combination of Gauss and Lorentz-type functions, i.e.,

$$I(q) = I_G(0)\exp(-\Xi^2 q^2) + [I_L(0)/(1+\xi^2 q^2)] \tag{9.1}$$

$I_G(0)$ and $I_L(0)$ are the intensities at $q = 0$ for the contributions of Gaussian and Lorentzian functions, respectively. The Gaussian part results from solidlike inhomogene-

ity, having a characteristic size of Ξ, which is due to the introduction of crosslinks into the system. The Lorentzian part is originated from the liquid nature of the local concentration fluctuations of the gel characterized with a correlation length ξ. Ξ decreases systematically with polymer volume fraction, ϕ, indicating the nature of Ξ being the solidlike inhomogeneity. On the other hand, the intensity function for solutions was well fitted with the so-called Ornstein-Zemike (OZ) equation (a Lorentzian function), i.e.,

$$I(q) = \frac{I_L(0)}{1 + \xi^2 q^2} \tag{9.2}$$

It was found that both ξ and $I_L(0)$ diverged at the spinodal temperature, T_s [SM92].

Despite many studies of PNIPAM based gels or solutions, the knowledge on thin PNIPAM films is still limited. In the case of triblock copolymers with two polystyrene (PS) blocks sandwiching a central PNIPAM block all well-known microphase separation structures were reported [NA07]. Swelling of the middle block leads to physically cross-linked gels, where the end-block domains form the physical cross-links. Thus, a PNIPAM based triblock thin film is a prominent candidate for a thermoresponsive hydrogel. Compared to SANS, grazing incidence small-angle neutron scattering (GISANS) is better suited to investigate structures of thin films. It can probe structures parallel to the surface, so-called lateral structures and long-ranged correlations. Therefore, it is of great interest to explore the details of hydrogel thin film structure near the volume-phase transition by using the GISANS technique.

9.2 Experimental Section

Materials. The triblock copolymer used is poly(styrene-*block*-*N*-isopropylacrylamide-*block*-styrene), denoted P(S-*b*-NIPAM-*b*-S), with a molecular weight of 32300 g mol^{-1}, and a volume fraction of PS in the copolymer of 0.07. D_2O (99.95%) was purchased from Deutero GmbH.

Sample Preparation. A silicon block ($L \times W \times H = 8 \times 5 \times 1.5\ cm^3$) with an oxide layer surface was used as the substrate material and cleaned following the base cleaning protocol as described in chapter 4. The initial dry films with a thickness of 442 nm were prepared by spin coating (2000 rpm, 30 s) from a 1,4-dioxane solution at room tempera-

ture onto the pre-cleaned Si substrates.

GISANS scattering. GISANS experiments were performed in the beamline D16 of ILL, France. The set-up is similar to that of GISAXS as described in chapter 2. A neutron flux having the average wavelength of 4.67 Å was used as the incident beam. The incident angle is 0.7°. The scattered neutrons were counted with a two dimensional detector of 128 pixel × 128 pixel (260 mm × 260 mm sensitive area, 2 mm × 2 mm pixel size) placed 1.0 m apart from the sample position. The sample was sealed in a brass cell and the temperature of the cell was controlled by a thermobath. The temperature was controlled with the precision of ±0.1 °C. D_2O was injected into the cell by a syringe. Thus, the film swells in water. According to the results obtained by an optical interferometer, the sample was held at the given temperature at least 20 min before data collection. GISANS intensity curves were observed at nine temperatures (12, 15, 16, 17, 18, 19, 20, 29, 31°C). The two dimensional data were corrected for fast neutrons, detector inhomogeneity, and transmission and then were radially averaged. Thus obtained one dimensional data were rescaled to the absolute intensity scale.

9.3 Structure Investigation

The phase transition temperature of the P(S-*b*-NIPAM-*b*-S) thin film was measured by optical interferometry. As shown in figure 9.1, the thin film in water undergoes a sharp and discontinous volume phase transition at $T_c = 28.8$°C. This transition temperature is a little lower than that of PNIPAM homopolymer (∼30°) because of the introduction of the hydrophobic group [WW08, TLD75].

Figure 9.2 shows log-log (a) and Ornstein-Zernike plots ($I^{-1}(q)$ vs q^2 plot) (b) of GISANS intensity curves from the P(S-*b*-NIPAM-*b*-S) sample at different temperatures. Figure 9.2b shows that the hydrogel thin film can be predicted with eq. 9.2. All of the curves have a nonzero intercept, $1/I(0)$, and linearly increases with q^2 as indicated with a straight line. However, the fits are best at small q region. At large q region, the curves have a systematic deviation from the fits.

Figure 9.3 shows the same log-log plots from the P(S-*b*-NIPAM-*b*-S) sample but is focused on small q region. It is observed that the scattered intensity increases at small q region

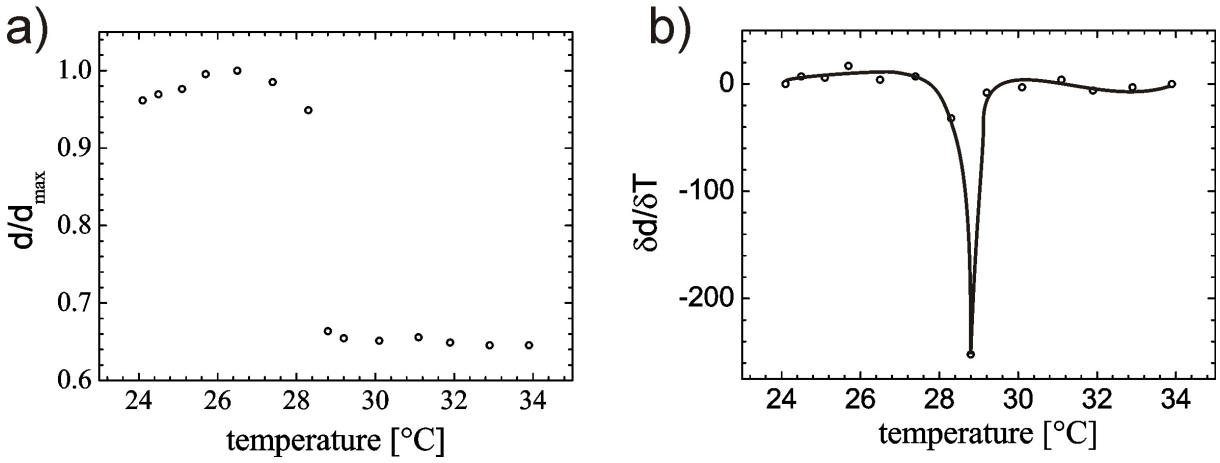

Figure 9.1: (a) Temperature-dependent changes of the film thickness measured for the P(S-*b*-NIPAM-*b*-S) film exposed to saturated water vapor. (b) first derivative indicating the transition temperature and the width of the transition.

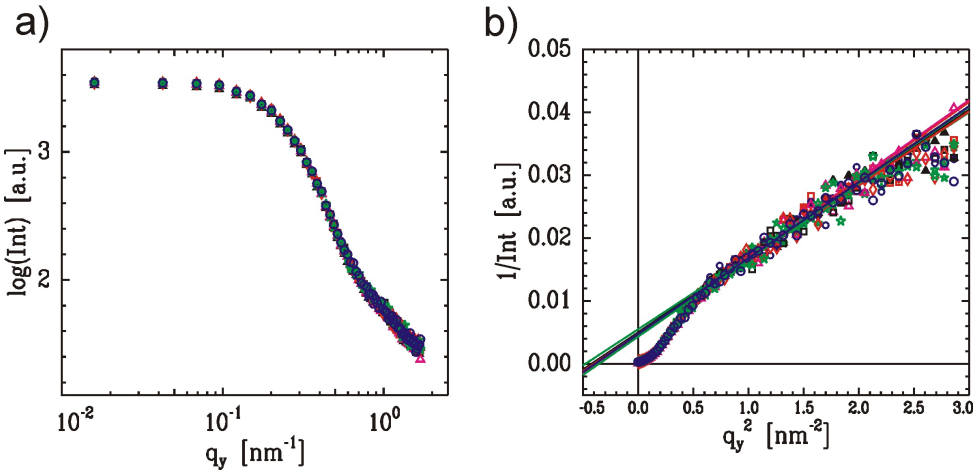

Figure 9.2: GISANS scattered intensity profiles for P(S-*b*-NIPAM-*b*-S) film at different temperatures: (a) log-log and (b) Ornstein-Zernike plots ($I^{-1}(q)$ vs q^2 plot). The curves represent 9 temperatures: 12°C (black triangle), 15°C (green star), 16°C (red square), 17°C (big blue circle), 18°C (red rhomb), 19°C (black square), 20°C (red triangle), 29°C (magenta triangle), 31°C (small blue circle). The straight line in (b) indicates the fit with eq. 9.2.

with increasing temperature. As discussed above, a two-parameter curve fitting with eq. 9.2 was performed by varying $I_L(0)$ and ξ as fitting parameters. However, the fits do not agree well with the neutron scattering data at large q region. Such deviation is due to that the eq. 9.2 is proposed for polymer solutions instead of disk-like gels. Crosslinks are not considered into the equation. The exact solution for the scattering function from gels has not been proposed yet because of complexity and variety of crosslink formation. However, several scattering functions are proposed. Hechet et al. [HAM85] tried to

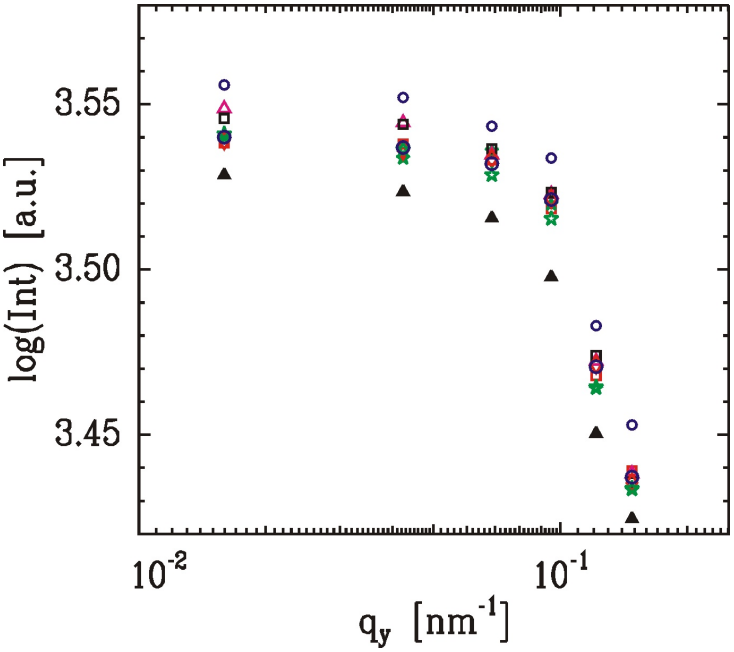

Figure 9.3: GISANS scattered intensity profiles for P(S-*b*-NIPAM-*b*-S) film at different temperatures in log-log format and focused on small q region. The curves represent 9 temperatures: 12°C (black triangle), 15°C (green star), 16°C (red square), 17°C (big blue circle), 18°C (red rhomb), 19°C (black square), 20°C (red triangle), 29°C (magenta triangle), 31°C (small blue circle).

separate the scattered intensity function into two contributions, i.e., solution-like and solid-like concentration fluctuations. The solution-like concentration fluctuations were assumed to be the same to the corresponding polymer solution. Horkay et al. [MS91, HF91] assumed that the solidlike concentration fluctuations had the form of $\exp(-q^2\Xi^2)$ and proposed a scattering function - eq. 9.1 for chemically crosslinked gels. Based on this equation, Martin Medebach proposed a experimental fuction which can perfectly fit the D16 data

$$I(q) - I_0 = \frac{A}{w\sqrt{\pi/2}} \exp(-2(\frac{q - x_c}{w})^2) + \frac{I_L(0)}{1 + \xi^2 q^2} \tag{9.3}$$

where I_0 is a constant, A is the amplitude, w is the width of the peak, x_c is a shift in x-direction. Similar to eq. 9.1, the former part is a Gaussian function and the second part is the Ornstein-Zemike equation. For fitting, I_0 is set to 12.2±3.5, A is set to 1650±30, w is set to 0.385±0.002, and x_c is set to 0.0142±0.0052. The fitting region is from -1.6 to 1.6 nm^{-1}. Figure 9.4 shows the result of curve fitting at 12, 20, 29 and 31°.

Figure 9.5 shows ξ (a) and $I_L(0)$ as a function of temperatures, respectively. ξ is in the order of a few tens of angstrom and has a big increase near 29°. $I_L(0)$ also shows a similar behavior. Theoretically one expects both the correlation length, ξ and the susceptibility

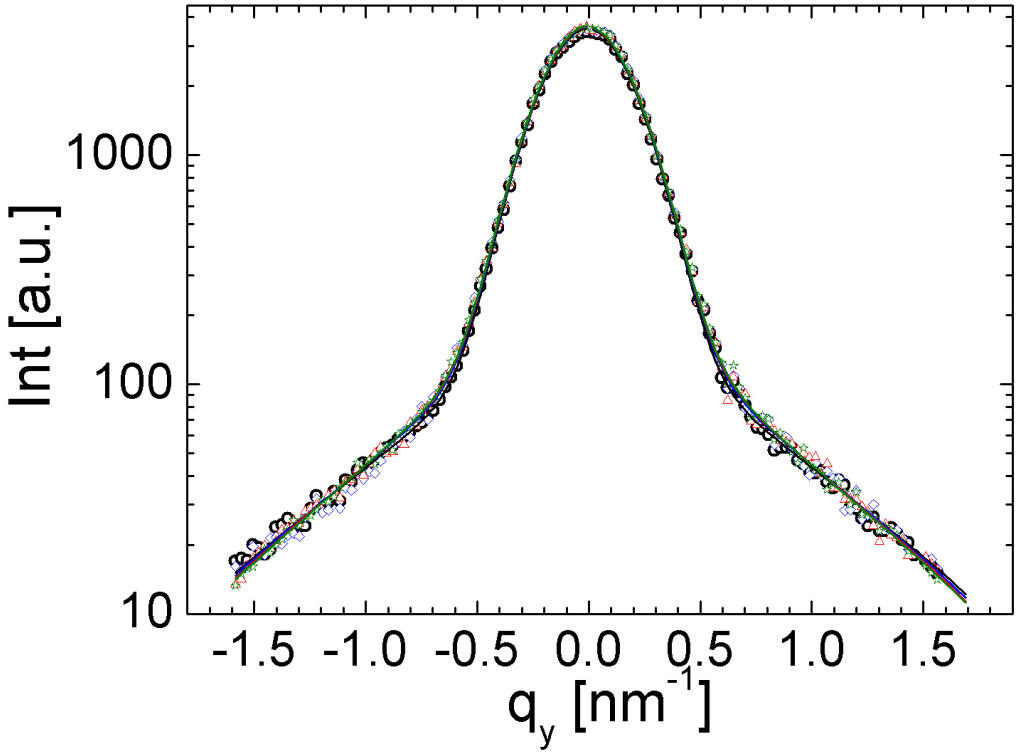

Figure 9.4: Temperature dependence of GISANS scattered intensity profile. The curves represent 4 temperatures: 12°C (black cricle), 20°C (blue rhomb), 29°C (red triangle), 31°C (olive star). The solid lines are the correponding fitting.

(proportional to $I_L(0)$) diverge at the spinodal temperature [SG97]. Thus, the spinodal temperature, T_s, obtained from the GISANS data, is in good accordance with the tansition temperature measured by optical interferometry.

9.4 Conclusion

The small-length scale structure of P(S-*b*-NIPAM-*b*-S) thin film near the volume-phase transition is probed by using GISANS technique. The scattered intensity function was described with Ornstein-Zemike (OZ) equation (a Lorentzian function) and an experimental equation based on eq. 9.1. Compared to Ornstein-Zemike (OZ) equation, the experimental equation which takes the crosslinks into consideration can better fit the GISANS data. The correlation length, ξ and $I_L(0)$ both have a big increase at the spinodal temperature, which is in good accordance with the transition temperature measured

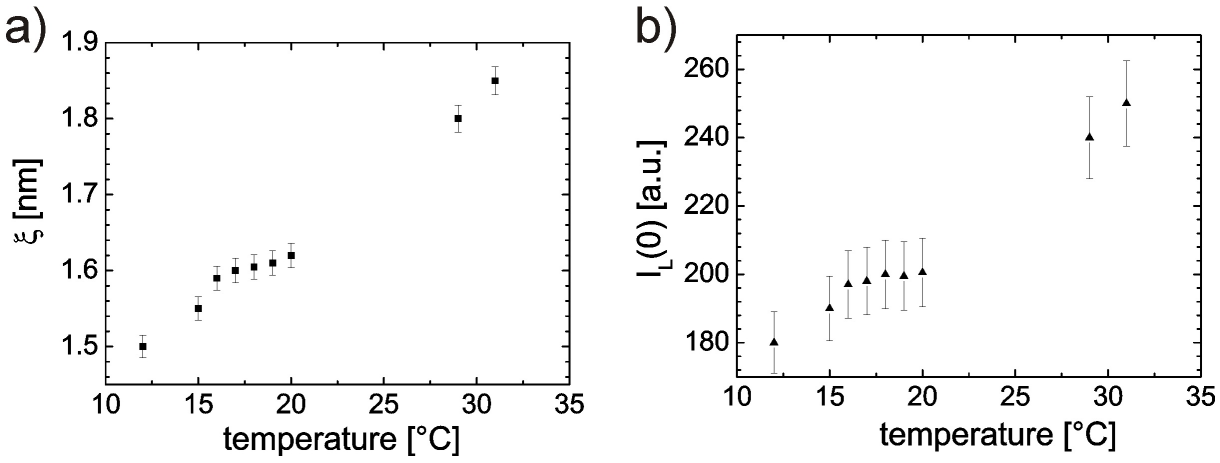

Figure 9.5: Plots of ξ (a) and $I_L(0)$ as a function of temperatures, respectively.

by optical interferometry.

Chapter 10

Summary

In this thesis, the focus is on the investigation of the structure and kinetics of PNIPAM based copolymer thin films. The hydrophobic group plays the key role for the swelling and switching process: It forms physical cross-links during swelling. An internal structure is installed in thin films due to the microphase separation of the hydrophilic and hydrophobic segments. The swelling capability and the LCST of thin films can be changed by introduction of hydrophobic comonomers. Moreover, not only the level of hydrophobe incorporation but also the position of hydrophobic comonomers in the chain can influence the LCST and swelling capability. In detail, the microphase separated structure installed in thin films is changed from sphere-like to cylinder-like structures dependent on the level of hydrophobe incorporation. The diblock shows a better microphase separated structure compared to the triblock with the same level of hydrophobe incorporation. As a consequence, the swelling capability and the LCST of thin films of the diblock are less affected by the film thickness than those of the triblock. Thin films of PNIPAM based copolymer with shortest hydrophobic end groups show the strongest swelling and highest LCST. With increasing hydrophobic group length, the swelling factor is decreasing and the LCST shifts to a lower temperature. It was observed that with a PS volume fraction of 72.6%, the swelling factor is only 1.03 and no phase transition behavior is found.

Besides of hydrophobic comonomers, film thickness is another important parameter which effects the swellling and switching process. Since the thin film is a confined system, it is influenced by the interactions from both interfaces: the interface between the air/water vapor and the film, and the interface between the substrate and the film. Due to the pre-hydrophilic cleaning of the substrate, the attraction of the NIPAM segments to the substrate surfaces is very strong, and a high volume fraction of NIPAM segments in the

surface layer forms. Thus, the interaction of the substrate surface is more favorable for the NIPAM segments. In contrast, the second interface, namely the polymer film surface, is in contact with air/water vapor. This interface is much less hydrophilic and favor the interaction with the hydrophobic group. As a consequence, by spin-coating, a collapsed chain conformation perpendicular to the substrate surface is formed, which causes a strong swelling compared to the bulk material. However, with increasing film thickness this effect gets weaker because fewer polymer molecules are in a perturbed conformation. Therefore, the selling factor is decreasing with increasing film thickness. However, for thick films (above 400 nm), the swelling factor approaches the value of bulk material as the confinement is weak in this case.

The swelling and switching kinetics of thin films of two different PNIPAM based copolymers is probed by in-situ neutron reflectometry. One of them is the nbc-PNIPAM which shows the strongest swelling and sharpest transition in all the investigated polymers. The other is the diblock P(S-*b*-NIPAM) with a PS volume fraction of 72.4%, which shows no swelling in thickness and no transition in contact with water vapor but can incorporate a large amount of water by a maximum volume percentage of 17%. The neutron scattering data of both of them can be fitted by the swelling and deswelling model proposed by Li and Tanaka [LY90]. Thus, the swelling and deswelling of these thin films is a two-process mechanism and neither swelling nor shrinking can be considered to be a pure diffusion process as observed previously for PNIPAM based block copolymer films.

Moreover, with respect to applications, a simplified thin film sensor and nano-switch which consists of the active (sensor) layer and a gold top-layer in thin film geometry, are successfully prepared and characterized. The thermosensitivity is still present for such systems. The thickness and structures of the gold layer have a strong impact on the swelling and switching behavior of thin films.

The combination of microfluidic devices and hydrogel thin films is successful. Films which can not swell in water vapor can swell in water fluid with a certain flow rate. The gold deposition on top of thin films by microfluid is also successful, which offers another way for gold deposition on hydrogel thin films besides of the commonly used methodes: sputtering and evaporation.

A small length scale structure of thick hydrogel films (442 nm) appoarching the tran-

sition temperature is sucessfully probed by GISANS. The increase of correlation length with increasing temperature agrees well with a experimental function modified from the Geissler's equation [HAM85]. Thus, the phase transition of thick films is similar to that of previously observed PNIPAM based block copolymer films [SM92].

Bibliography

[AK00] Akiyoshi, K.; Kang, E.−C.; Kurumada, S.; Sunamoto, J.; Principi, T.; Winnik, F.M. *Macromolecules* 33, 3244 (2000).

[ADR08] Alves de Rezende, C.; Lee, L.-T.; Galembeck, F. *Langmuir* 24, 7346 (2008).

[AR02] Akashi, R.; Tsutsui, H.; Komura, R. *Adv. Mater.* 14, 1808 (2002).

[AJ09] Adelsberger, J. *presentation in "Intelligent Hydrogel" workshop*, Deutsche Forschungsgemeinschaft (DFG), Dortmund (2009)

[ASA00] Asher, S.A.; Weismann, J.M.; Sunkara, H.B. *US Patent* 6165389 (2000).

[ASH89] Anastasiadis, S.H.; Russell, T.P.; Satija, S.K.; Majkrzak, C.F. *Phys. Rev. Lett.* 62, 1852 (1989).

[AV] Aseyev, V.; Tenhu, H.; Winnik, F.M. In *Self-Organization of Amphiphilic Copolymers in Aqueous Media*; Khokhlov, A.R., Ed.; Springer-Verlag GmbH: Heidelberg, Germany, in press.

[BC97] Braun, C. *Parratt32* (1997-99) or *The Reflectivity Tool* version 1.5.2 (HMI Berlin).

[BCS96] Brazel, C.S.; Peppas, N.A. *Polym. Mater. Sci. Eng.* 74, 370 (1996).

[BP07] Bhatnagar, P.; Strickland, A.D.; Kim, I.; Malliaras, G.G.; Batt, C.A. *Appl. Phys. Lett.* 90, 144107 (2007).

[BT00] Brückel, T.; Heger, G; Richter, D. *Neutron Scattering* vol. 5, Forschungszentrum Jülich GmbH (2000).

[CJE97] Chung, J.E.; Yokoyama, M.; Suzuki, K.; Aoyagi, T.; Sakurai, Y.; Okano, T. *Colloids Surf. B* 9, 37 (1997).

[CME00] Callow, M.E.; Callow, J.A.; Ista, L.K.; Coleman, S.E.; Nolasco, A.C.; Lopez, G.P. *Appl. Environ. Microbiol.* 66, 3249 (2000).

[CS08] Couet, S.; Diederich, T.; Schlage, K.; Röhlsberger, R. *Rev. Sci. Instrum.* 79, 093908 (2008).

[CX05] Cheng, X.; Canavan, H.E.; Stein, M.J.; Hull, J.R.; Kweskin, S.J.; Wagner, M.S.; Somorjai, G.A.; Castner, D.G.; Ratner, B.D. *Langmuir* 21, 7833 (2005).

[CZ05] Cao, Z.; Liu, W.; Gao, P.; Yao, K.; Li, H.; Wang, G. *Polymer* 46, 5268 (2005).

[DCJ95] Durning, C.J.; Hassan, M.M.; Tong, H.M.; Lee, K.W. *Macromolecules* 28, 4234 (1995).

[DD91] DeRossi, D.; Kajiwara, K.; Osada, Y.; Yamauchi, A. *Polymer Gels. Fundamentals and Biomedical Applications* Plenum Press: New York (1991).

[DD99] Dhara, D.; Nisha, C.K.; Chatterji, P.R. *J. Macromol. Sci., Pure Appl. Chem.* A36, 197−210 (1999).

[DE97] Delamarche, E; Bernard, H; Schmid, H; Michel, B; Biebuyck, H *Science* 276, 779 (1997).

[DJ92] Daillant, J.; Belorgey, O.J. *Chem. Phys.* 97, 5824 (1992).

[DJ99] Daillant, J.; Gibaud, A. *X-ray and Neutron reflectivity: Principles and Applications*, Lecture Notes in Physics, vol. 58, Springer-Verlag, Berlin (1999).

[DJL03] Drury, J.L.; Mooney, D.J. *Biomaterials* 24, 4337−4351 (2003).

[FH91] Feil, H.; Bae, Y.H.; Jan, F.; Kim, S.W. *J. Membr. Sci.* 64, 283 (1993).

[FMJ00] Fasolka, M.J.; Banerjee, P.; Mayes, A.M.; Pickett, G.; Balazs, A.C. *Macromolecules* 33, 5702 (2000).

[FS89] Fujishige, S.; Kubota, K.; Ando, I. *J. Phys. Chem.* 93, 3311 (1989).

[FS06] Furyk, S.; Zhang, Y.; Ortiz-Acosta, D.; Cremer, P.S.; Bergbreiter, D.E. *J. Polym. Sci., Part A: Polym. Chem.* 44, 1492 (2006).

[GAY93] Grosberg, A. Y.; Kuznetsov, D.V. *Macromolecules* 26, 4249 (1993).

[GD02] Gan, D.; Lyon, L.A. *Macromolecules* 35, 9634 (2002).

[GED04] Goluch, E.D.; Shaikh, K.A.; Ryu, K.; Chen, J.; Engel, J.; Liu, C. *Appl. Phys. Lett.* 85, 16 (2004)

[GP02] Gupta, P.; Vermani, K.; Garg, S. *Drugs DiscoV. Today* 7, 569 (2002).

[GM06] Gonuguntla, M.; Sharma, A.; Subramanian, S.A. *Macromolecules* 39, 3365 (2006).

[GM07] Guenther, M.; Kuckling, D.; Corten, C.; Gerlach, G.; Sorber, J.; Suchaneck, G.; Arndt, K.-F. *Sensors and Actuators B-Chem.* 126, 97 (2007).

[GM08] Guenther, M.; Gerlach, G.; Corten, C.; Kuckling, D.; Sorber, J.; Arndt, K. -F. *Sensors and Actuators B-Chem.* 132, 471 (2008).

[GTP91] Gall, T.P.; Kramer, E. *J. Polymer* 32, 265 (1991).

[HA03] Heilmann, A. *Polymer Films with Embedded Metal Nanocomposites* Springer-Verlag, Berlin Heidelberg (2003).

[HAS02] Hoffman, A.S. *Adv. Drug Deliv. Rev.* 54, 3 (2002).

[HAM85] Hecht, A.M.; Duplessix, R.; Geissler, E. *Macromolecules* 18, 2167 (1985).

[HCY87] Hui, C.Y.; Wu, K.C.; Lasky, R.C.; Kramer, E.J. *J. Appl. Phys.* 61, 5129 (1987).

[HDL03] Huber, D.L.; Manginell, R.P.; Samara, M.A.; Kim, B.I.; Bunker, B.C. *Science* 301, 352 (2003).

[HE02] Hecht, E. *Optics* 4th ed. Addison Wesley (2002).

[HF91] Horkay, F; Hecht, A.M.; Mallam, S.; Geissler, E.; Renie, A.R. *Macromolecules* 24, 2896 (1991)

[HHP00] Huinnk, H.P.; Brokken-Zijp, J.C.M.; van Dijk, M.A and Sevink, G.C.A. *J. Chem. Phys.* 112 (5), 2452 (2000).

[HI04] Hirata, I.; Okazaki, M.; Iwata, H. Polymer 45, 5569 (2004).

[HM68] Heskins, M.; Guillet, J.E. *J. Macromol. Sci.* A2, 1441 (1968).

[HS95] Hirotsu, S.; Yamamoto, I.; Matsuo, A.; Okajim, T.; Furukawa, H.; Yamamoto, T. *J. Phys. Soc. Jpn.* 64, 2898 (1995).

[HS08] Hietala, S.; Nuopponen, M.; Kalliomaki, K.; Tenhu, H. *Macromolecules* 41, 2627 (2008).

[HT04] Hellweg, T.; Dewhurst, C.D.; Eimer, W.; Kratz, K. *Langmuir* 20, 4330 (2004).

[HY84] Hirokawa. Y.; Tanaka, T. *J. Chem. Phys.* 81, 6379 (1984).

[HV94] Holy, V.; Baumbach, T. *Phys. ReV. B* 49, 10668 (1994).

[IH91] Iwata, H.; Oodate, M.; Uyama, Y.; Amemiya, H.; Ikada, Y. *J. Membr. Sci.* 55, 119 (1991).

[IJN92] Israelachvili, J.N. *Intermolecular Surface Forces*; 2nd ed. Academic Press: London (1992).

[IRF01] Ismagilov, R.F.; Ng, J.M.K.;Kenis, P.J.A.; Whitesides, G.M. *Anal. Chem.* 73, 5207 (2001).

[LCJ88] Lawrence, C.J. *Phys. Fluids* 31, 2786 (1988).

[LHH08] Lin, H.-H.; Cheng, Y.-L. *Macromolecules* 34, 3710 (2001).

[LL00] Liang, L.; Rieke, P.C.; Liu, J.; Fryxell, G.E.; Young, J.S.; Engelhard, M.H.; Alford, K.L. *Langmuir* 16, 8016 (2000).

[LLD86] Landau, L.D.; Lifshitz, E.M. *Theory of Elasticity* Pergamon, Oxford (1986).

[LM01] Lanz, M.; Lehmann, E.; Imhof, R.; Exnar, I.; Novak, P. *J. Power Sourc.* 101, 177 (2001).

[LP99] Lenz, P. *Adv. Mater.* 11, 1531 (1999).

[LY90] Li, Y.; Tanaka, T. *J. Chem. Phys.* 92, 1365 (1990).

[LZ00] Liu, Z.; Calvert, P. *AdV. Mater.* 12, 288 (2000).

[JDM02] Jones, D.M.; Smith, J.R.; Huck, W.T.S.; Alexander, C. *Adv. Mater.* 14, 1130 (2002).

[KA02] Kikuchi, A.; Okano, T. *Adv. Drug Deliv. Rev.* 54, 53 (2002).

[KA04] Kikuchi, A.; Okano, T. *Macromol. Symp.* 205, 217 (2004).

[KD07] Kessler, D.; Theato, P. *Macromol. Symp.* 249, 424 (2007).

[KD09] Kuckling, D. *Colloid. Polym. Sci.* 287, 881 (2009).

[KDE99] Kataoka, D. E.; Troian, S. M. Nature (London) 402, 794 (1999).

[KG09] Kaune, G.; Ruderer, M.A.; Metwalli E.; Wang, W.; Couet, S.; Schlage, K.; Röhlsberger, R.; Roth, S.V.; Müller-Buschbaum, P. *ACS Appl. Mater. Interfaces* 1, 353 (2009).

[KH-C01] Kim, H.-C. and Russell, T. P. *J. Pol. Sci.: B: Poly Phys.* 39, 663 (2001).

[KJ99] Kraus, J.; Müller-Buschbaum, P.; Stamm, M.; Bucknall, D. *J. Polym. Sci., Phys.* 37, 2862 (1999).

[KK90] Kubota, K.; Fujishige, S.; Ando, I. *J. Phys. Chem.* 94, 5154 (1990).

[KM08] Karg, M.; Pastoriza-Santos, I.; Rodriguez-Gonzalez, B.; von Klitzing, R.; Wellert, S.; Hellweg, T. *Langmuir* 24, 6300 (2008).

[KP01] Kujawa, P.; Winnik, F.M. *Macromolecules* 34, 4130 (2001).

[KP06] Kujawa, P.; Segui, F.; Shaban, S.; Diab, C.; Okada, Y.; Tanaka, F.; Winnik, F.M. *Macromolecules* 39, 341 (2006).

[KR04] Kanazawa, R.; Yoshida, T.; Gotoh, T.; Sakohara, S. *J. Chem. Eng. Jpn.* 37, 59 (2004).

[KR81] Kjellander, R.; Florin, E. *J. Chem. SOC., Faraday Trans. 1* 77, 2053 (1981).

[KSW92] Kim, S. W.; Bae, Y.H.; Okano, T. *Pharm. Res.* 9, 283 (1992).

[KT08] Koga, T.; Tanaka, F.; Motokawa, R.; Koizumi, S.; Winnik, F. M. *Macromolecules* 41(23), 9413 (2008).

[KY98] Kaneko, Y.; Nakamura, S.; Sakai, K.; Aoyagi, T.; Kikuchi, A.; Sakurai, Y.; Okano, T. *Macromolecules* 31, 6099 (1998).

[MA90] Matsuyama, A.; Tanaka, F. *Phys. Rev. Lett.* 65, 341 (1990).

[MA91] Matsuyama, A.; Tanaka, F. *J. Chem. Phys.* 94, 781 (1991).

[MA92] Menelle, A.; Russell, T.P.; Anastasiadis, S.H.; Satija, S.K.; Majkrzak, C.F. *Phys. Rev. Lett.* 68, 67 (1992).

[MB99] Mahltig, B.; Walter, H.; Harrats, C.; Müller-Buschbaum, P.; Jerome, R.; Stamm, M. *Phys. Chem. Chem. Phys.* 1, 3853 (1999).

[MB01] Mahltig, B.; Müller-Buschbaum, P.; Wolkenhauer, M.; Wunnicke, O.; Wiegand, S.; Gohy, J.F.; Jerome, R.; Stamm, M. *J. Colloid Interface Sci.* 242, 36 (2001).

[MBP97] Müller-Buschbaum, P.; Vanhoorne, P.; Scheumann, V.; Stamm, M. *Europhys. Lett.* 40, 655 (1997).

[MBP98a] Müller-Buschbaum, P.; Stamm, M. *Physica B* 248, 229 (1998).

[MBP98b] Müller-Buschbaum, P.; Stamm, M. *Macromolecules* 31, 3686 (1998).

[MBP98c] Müller-Buschbaum, P.; Gutmann, J.S.; Lorenz, C.; Schmitt, T.; Stamm, M. *Macromolecules* 31, 9265 (1998).

[MBP99] Müller-Buschbaum, P.; Gutmann, J.S.; Stamm, M.J. *Macromol. Sci.-Phys. B* 38 (5 & 6), 577 (1999).

[MBP00] Müller-Buschbaum, P.; Gutmann, J.S.; Kraus, J.; Walter, H.; Stamm, M. *Macromolecules* 33, 569 (2000).

[MBP01] Müller-Buschbaum, P.; Gutmann, J.S.; Lorenz-Haas, C.; Mahltig, B.; Stamm, M.; Petry, W. *Macromolecules* 34, 7463 (2001).

[MBP02] Müller-Buschbaum, P.; Gutmann, J.S.; Lorenz-Haas, C.; Wunnicke, O.; Stamm, M.; Petry, W. *Macromolecules* 35, 2017 (2002).

[MBP03a] Müller-Buschbaum, P. *Anal. Bioanal. Chem.* 376, 3 (2003).

[MBP03b] Müller-Buschbaum, P. *Eur. Phys. J. E* 12, 443 (2003).

[MBP05] Müller-Buschbaum, P.; Bauer, E.; Wunnicke, O. and Stamm, M. *J. Phys.: Condens. Matter* 17, 363 (2005).

[MBP06a] Müller-Buschbaum, P.; Bauer, E.; Pfister, S.; Roth, S.V.; Burghammer, M.; Riekel, C.; David, C.; Thiele, U. *Europhys. Lett.* 73, 35 (2006).

[MBP06b] Müller-Buschbaum, P.; Maurer, E.; Bauer, E.; Cubitt, R. *Langmuir* 22, 9295 (2006).

[MBP06c] Müller-Buschbaum, P.; Bauer, E.; Maurer, E.; Cubitt, R. *Physica B* 703, 385 (2006).

[MBP07] Müller-Buschbaum, P.; Bauer, E.; Maurer, E.; Nelson, A; Cubitt, R. *Phys. Status Solidi (RRL)* 1, 68 (2007).

[MBP07b] Müller-Buschbaum, P. Lecture notes for Polymerphysik I (2007).

[MC02] Mangeney, C.; Ferrage, F.; Jullien, L.; Ouari, O.; Rekai, E.D.; Laschewsky, A.; Vikholm, I.; Sadowski, J.W. *J. Am. Chem. Soc.* 124, 5811 (2002).

[MGN53] Malcolm, G.N.; Rowlinson, J.S. *Trans. Faraday Soc.* 53, 921 (1953).

[MMJ95] Murray, M.J.; Snowden, M.J. *Adv. Col. Interface Sci.* 54, 73 (1995).

[MS89] Mallan, S.; Horkay, F.; Hecht, A.M.; Geissler, E. *Macromolecules* 22, 3356 (1989).

[MS91] Mallam, S.; Horkay, F.; Hecht, A.M.; Renie, A.R.; Geissler, E. *Macromolecules* 24, 543 (1991).

[MS02] Morita, S.; Wiesendanger, R.; Meyer, E. *Noncontact Atomic Force Mi-croscopy* Springer-Verlag Berlin Heidelberg (2002).

[MS07] Mias, S.; Sudor, J.; Camon, H. *Microsyst Technol.* Web alert (2007).

[MT02] Miyata, T.; Uragami, T.; Nakamae, K. *Adv. Drug DeliVery ReV.* 54, 79 (2002).

[MTL97] Morkved, T.L.; Jaeger, H.M. *Eurphys. Lett.* 40 (6), 643 (1997).

[MTT00] McMahon, T.T.; Zadnik, K. *Cornea* 19, 730 (2000).

[MZ09] Meng, Z.; Hendrickson, G. R., Lyon. L. A. *Macromolecules* 42, 7664 (2009).

[NA06] Nelson, A.J. *Appl. Crystallogr.* 39, 273 (2006).

[NA07] Nykänen, A.; Nuopponen, M.; Laukkanen, A.; Hirvonen, S.-P.; Rytela, M.; Turunen, O.; Tenhu, H.; Mezzenga, R.; Ikkala, O.; Ruokolainen, J. *Macromolecules* 40, 5827 (2007).

[NA08] Nykänen, A.; Nuopponen, M.; Hiekkataipale, P.; Hirvonen, S.-P.; Soininen, A.; Tenhu, H.; Ikkala, O.; Mezzenga, R.; Ruokolainen, J. *Macromolecules* 41, 3243 (2008).

[ND01] Dingenouts, N.; Seelenmeyer, S.; Deike, I.; Rosenfeldt, S.; Ballauff, M.; Lindner, P.; Narayanan, T. *Phys. Chem. Chem. Phys.* 3, 1169 (2001).

[NM04] Nuopponen, M.; Ojala, J.; Tenhu, H. *Polymer* 45, 3643 (2004).

[NJA01] Nielsen, J.A.; Morrow, D. Mc. *Elements of Modern X-Ray Physics* Wiley, New York (2001).

[OA04] Opdahl, A.; Koffas, T.S.; Amitay-Sadovsky, E.; Kim, J.; Somorjai, G.A. *J. Phys.-Condes. Matter* 16, R659 (2004).

[OAA97] Obaidat, A.A.; Park, K. *Biomaterials* 18, 801 (1997).

[OT98] Otsu, T.; Matsumoto, A. *Adv. Polym. Sci.* 136, 75 (1998).

[OY87] Osada, Y.; Kishi, R.; Hasebe, M. *J. Polym. Sci., Part C: Polym. Lett.* 25, 481 (1987).

[OY05] Okada, Y.; Tanaka, F. *Macromolecules* 38, 4465 (2005).

[OY93] Osada, Y.; Ross-Murphy, S.B. *Sci. Am.* 259, 42 (1993).

[QY01] Qiu, Y.; Park, K. *Adv. Drug Deliv. Rev.* 53, 321 (2001).

[PA88] Peters, A.; Candau, S.J. *Macromolecules* 21, 2278 (1988).

[PLG54] Parratt, L.G. *Phys. Rev. B* 95, 359 (1954).

[PM06] Prevot, M.; Dejugnat, C.; Möhwald, H.; Sukhorukov, G.B. *ChemPhysChem* 7, 2497 (2006).

[PR00] Pelton, R. *Adv. Col. Interface Sci* 85, 1 (2000).

[PYS98] Park, Y.S.; Ito, Y.; Imanishi, Y. *Langmuir* 14, 910 (1998).

[RA06] Richter, A.; Howitz, S.; Kuckling, D.; Arndt, K.F. *Sens. Actuators B* 99, 451 (2004).

[RG92] Reiter, G. *Phys. Rev. Lett.* 68, 1 (1992).

[RKVR88] Rao, K.V.R.; Devi, K.P. *Int. J. Pharm.* 48, 1 (1988).

[RSV06] Roth, S.V.; Döhrmann, R.; Dommach, M.; Kuhlmann, M.; Kröger, I.; Gehrke, R.; Walter, H.; Schroer, C.; Lengeler, B.; Müller-Buschbaum, P. *Rev. Sci. Instrum.* 77, 085106 (2006).

[RS09] Rols, S.; Orecchini, A.; Meulien, O. Institut Laue-Langevin, *http://www.ill.eu/instruments-support/instruments-groups/instruments/in4/* (2009).

[SDF02] Stamatialis, D.F.; Sanopoulou, M.; Raptis, I. *J. Appl. Polym. Sci.* 83, 2823 (2002).

[SDI03] Svergun, D.I.; Koch. M.H.J. *Rep. Progr. Phys.* 66, 1735 (2003).

[SE88] Sato, E; Tanaka, T *J. Chem. Phys.* 89, 1695 (1988).

[SDW97] Schubert, S.W. *Pol. Bul.* 38, 177 (1997).

[SG97] Strobl, G. *The Physics of Polymers* 2nd ed. Springer-Verlag Berlin Heidelberg (1997).

[SHG92] Schild, H.G. *Prog. Polym. Sci.* 17, 163 (1992).

[SLL90] Spangler, L.L.; Torkelson, M.; Royal, J.S. *Polym. Eng. Sci.* 30, 644 (1990).

[SMJ03] Serpe, M.J.; Jones, C.D.; Lyon, L.A. *Langmuir* 19, 8759 (2003).

[SMJ04] Serpe, M.J.; Lyon, L.A. *Chem. Mater.* 16, 4373 (2004).

[SPS95] Stayton, P.S.; Shimoboji, T.; Long, C.; Chilkoti, A.; Chen, G.; Harris, J.M.; Hoffman, A.S. *Nature (London)* 378, 472 (1995).

[SR02] Steitz, R.; Leiner, V.; Tauer, K.; Khrenov, V.; v. Klitzing, R. *Appl. Phys. A* 74, S519 (2002).

[SS76] Saeki, S.; Kuwahara, N.; Nakata, M.; Kaneko, M. *Polymer* 17, 685 (1976).

[SS96] Shinohara, S.; Tajima, N.; Yanagisawa, K. *J. Intell. Mater. Syst. Struct.* 7, 254 (1996).

[SS08] Schmidt, S.; Motschmann, H.; Hellweg, T.; von Klitzing, R. *Polymer* 49, 749 (2008).

[ST95] Salditt, T.; Metzer, T.H.; Peisel, J.; Reinker, B.; Moske, M.; Samwer, K. *Europhys. Lett* 32, 331 (1995).

[ST96] Salditt, T.; Lott, D.; Metzer, T.H.; Peisl, *J. Phys. Rev. B* 54, 5860 (1996).

[ST06] Schmidt, T.; Mönch, J.I.; Arndt, K.F. *Macromol. Mater. Eng.* 291, 755 (2006).

[TEI94] Tiktopulo, E.I.; Bychkova, V.E.; Ricka, J.; Ptitsyn, O.B. *Macromolecules* 27, 2879 (1994).

[TLD75] Taylor, L.D.; Cerankowski, L.D. *J. Polym. Sci., Polym. Chem. Ed.* 13, 2551 (1975).

[TK96] Tasaki, K. *J. Am. Chem. Soc.* 118, 8459 (1996).

[TK08] Troll, K.; Kulkarni, A.; Wang, W.; Darko, C.; Bivigou Koumba, A.M.; Laschewsky, A.; Müller-Buschbaum, P.; Papadakis C.M. *Colloid Polym. Sci.* 286, 1079 (2008).

[TKC93] Tam, K.C.; Wu, X.Y.; Pelton, R.H. *J. Polym. Sci., Polym. Chem. Ed.* 31, 963 (1993).

[TM91] Tokita, M; Tanaka, T *Science* 253, 1121 (1991).

[TM99] Tolan, M. *X-ray Scattering from Soft-Matter Thin Films* Springer-Verlag Berlin Heidelberg (1999).

[TPA06] Tamirisa, P.A.; Hess, D.H. *Macromolecules* 39, 7092 (2006).

[TRL05] Thompson, R.L.; McDonald, M.T.; Lenthall, J.T.; Hutchings, L.R. *Macromolecules* 38, 4339 (2005).

[TS05] Tsuji, S.; Kawaguchi, H. Langmuir 21, 8439 (2005).

[TT73] Tanaka, T.; Hocker, L.; Benedek, G. *J. Chem. Phys.* 59, 5151 (1973).

[TT78] Tanaka, T. *Phys. ReV. Lett.* 40, 820 (1978).

[TT79] Tanaka, T.; Fillmore, D. *J. Chem. Phys.* 70, 1214 (1979).

[TT82] Tanaka, T.; Nishio, I.; Sun, S.T.; Ueno-Nishio, S. *Science* 218, 67 (1982).

[TT85] Tanaka, T.; Sato, E.; Hirokawa, Y.; Hirotsu, S.; Peetermans, J. *Phys. Rev. Lett.* 55, 2455 (1985).

[TT90] Tanaka, T.; Fillmore, D. *J. Chem. Phys.* 92, 1365 (1990).

[VBC99] von Bechtolsheim, C.; Zaporojtchenko, V.; Faupel, F. *Appl. Surf. Sci.* 151, 119 (1999).

[WBH99] Weigl, B.H.; Yager, P. *Science* 283, 346 (1999).

[WC94] Wu, C.; Yan, C.-Y. *Macromolecules* 27, 4516 (1994).

[WC95] Wu, C.; Zhou, S. *Macromolecules* 28, 5388 (1995).

[WC97] Wu, C.; Zhou, S. *J. Macromol. Sci. Phys.* B36, 345 (1997).

[WC98a] Wu, C.; Wang, X. *Phys. Rev. Lett.* 80, 4092 (1998).

[WC98b] Wu, C. *Polymer* 39, 4609 (1998).

[WFM90] Winnik, F.M. *Macromolecules* 23, 233 (1990).

[WFM92] Winnik, F.M.; Davidson, A.R.; Hamer, G.K.; Kitano, H. *Macromolecules* 25, 1876 (1992).

[WH99] Walter, H.; Harrats, C.; Müller-Buschbaum, P.; Jérome, R.; Stamm, M. *Langmuir* 15, 1260 (1999).

[WW08] Wang, W.; Troll, K.; Kaune, G.; Metwalli, E.; Ruderer, M.; Skrabania, K.; Laschewsky, A.; Roth, S.V.; Papadakis, C.M.; Müller-Buschbaum, P. *Macromolecules* 41, 3209 (2008).

[WW09a] Wang, W.; Metwalli, E.; Perlich, J.; Papadakis, C.M.; Cubitt, R.; Müller-Buschbaum, P. *Macromolecules* 42, 9041 (2009).

[WW09b] Wang, W.; Metwalli, E.; Perlich, J.; Troll, K.; Papadakis, C.M.; Cubitt, R.; Müller-Buschbaum, P. *Macromol. Rapid Commun.* 30, 114 (2009).

[XY01] Xia, Y.; Qin, D.; Yin, Y.D. *Curr. Opin. Colloid Interface Sci.* 6, 54 (2001).

[YH03] Yim, H.; Kent, M.S.; Huber, D.L.; Satija, S.; Majewski, J.; Smith, G.S. *Macromolecules* 36, 5244 (2003).

[YH06] Yim, H.; Kent, M.S.; Mendez, S.; Lopez, G.P.; Satija, S.; Seo, Y. *Macromolecules* 39, 3420 (2006).

[YL03] Ying, L.; Kang, E.T.; Neoh, K.G.; Kato, K.; Iwata, H. *Macromol. Mater. Eng.* 288, 11 (2003).

[YQ95] Yan, Q.; Hoffman, A.S. *Polymer* 36, 887 (1995).

[YY63] Yoneda, Y. *Phys. Rev.* 131, 2010 (1963).

[YY06] Yan, Y.; Zhou, X.; Ji, J.; Yan, L.; Zhang, G. *J. Phys. Chem. B* 110, 21055 (2006).

[YYZ07] You, Y.-Z.; Zhou, Q.-H.; Manickam, D.S.; Wan, L.; Mao, G.-Z.; Oupicky, D. *Macromolecules* 40, 8617 (2007).

[ZS96] Zhou, S.; Wu, C. *Macromolecules* 29, 4998 (1996).

[ZW93] Zrinyi, M.; Rosta, J.; Horkay, F. *Macromolecules* 26, 3097 (1993).

[ZW05] Zhang, W.; Zhou, X.; Li, H.; Fang, Y.; Zhang, G. *Macromolecules* 38, 909 (2005).

List of Publications

Publications Related to the Dissertation

Wang, W.; Troll, K.; Kaune, G.; Metwalli, E.; Ruderer, M.; Skrabania, K.; Laschewsky, A.; Roth, S. V.; Papadakis, C. M.; Müller-Buschbaum, P. Thin films of poly(*N*-isopropylacrylamide) end-capped with *n*-butyltrithiocarbonate. *Macromolecules* 41, 3209 (2008).

Wang, W.; Metwalli, E.; Perlich, J.; Papadakis, C.M.; Cubitt, R.; Müller-Buschbaum, P. Cyclic switching of water storage in thin block copolymer films containing poly(*N*-isopropylacrylamide). *Macromolecules* 42, 9041 (2009).

Wang, W.; Metwalli, E.; Perlich, J.; Troll, K.; Papadakis, C.M.; Cubitt, R.; Müller-Buschbaum, P. Water storage in thin films maintaining the total film thickness as probed with in-situ neutron reflectivity. *Macromol. Rapid Commun.* 30, 114 (2009).

Wang, W.; Kaune, G.; Perlich, J.; Papadakis, C.M.; Bivigou Koumba, A.M.; Laschewsky, A.; Cubitt, R.; Schlage, K.; Röhlsberger, R; Roth, S.V.; Müller-Buschbaum, P. Swelling and switching kinetics of gold coated end-capped poly(N-isopropylacrylamide) thin films. accepted by *Macromolecules* (2010).

Troll, K.; Kulkarni, A.; Wang, W.; Darko, C.; Bivigou Koumba, A.M.; Laschewsky, A.; Müller-Buschbaum, P.; Papadakis C.M. The collapse transition of poly(styrene-*b*-(*N*-isopropylacrylamide) diblock copolymers in aqueous solution and in thin films. *Colloid Polym. Sci.* 286, 1079 (2008).

Kaune, G.; Ruderer, M. A.; Metwalli E.; Wang, W.; Couet, S.; Schlage, K.; Röhlsberger, R.; Roth, S. V.; Müller-Buschbaum, P. In-situ GISAXS study of gold film growth on conducting polymer films. *ACS Appl. Mater. Interfaces* 1, 353 (2009).

Adelsberger, J.; Kulkarni, A.; Jain, A.; Wang, W.; Bivigou-Koumba, A.; Busch, P.; Pipich, V.; Holderer, O.; Hellweg, T.; Laschewsky, A.; Müller-Buschbaum, P.; Papadakis, C.M. Thermo-responsive PS-*b*-PNIPAM-*b*-PS micelles: Aggregation behavior, segmental dynamics and thermal response. accepted by *Macromolecules* (2010).

Other Publications

Ruderer, M.A.;Metwalli, E.; Wang, W.; Kaune, G.; Roth, S.V.; Müller-Buschbaum, P. Thin Films of Photoactive Polymer Blends. *Chem.Phys.Chem.* 10, 664 (2009).

Metwalli, E.; Moulin, J.-F.; Perlich, J.; Wang, W.; Dietert, A.; Roth, S.V.; Müller-Buschbaum, P. Polymer template-assisted growth of gold nanowires using a novel flow-stream technique. *Langmuir* 25, 11815 (2009).

Perlich, J.; Memesa, M.; Diethert, A.; Metwalli, E.; Wang, W.; Roth, S.V.; Timmann, A.; Gutmann, J.S.; Müller-Buschbaum, P. Preservation of the Morphology of a Self-Encapsulated Thin Titania Film in a Functional Multilayer Stack: An X-Ray Scattering Study. *Chem. Phys. Chem.* 10, 799 (2009).

Perlich, J.; Memesa, M.; Diethert, A.; Metwalli, E.; Wang, W.; Roth, S.V.; Timmann, A.; Gutmann, J.S.; Müller-Buschbaum, P. Layer-by-layer fabrication of hierarchical structures in sol-gel templated thin titania films. *phys.stat.sol. (RRL)* 3, 118 (2009).

Abul Kashem, M.M.; Perlich, J.; Diethert, A.; Wang, W.; Memesa, M.; Gutmann, J.S.; Majkova, E.; Capek, I.; Roth, S.V.; Petry, W.; Müller-Buschbaum, P. Array of magnetic nanoparticles via particle co-operated self-assembly in block copolymer thin film. *Macromolecules* 42, 6202 (2009).

Kaune, G; Wang, W; Metwalli, E; Ruderer, M; Roßner, R; Roth, S.V.; Müller-Buschbaum, P. Layered TiO2:PVK nano-composite thin films for photovoltaic applications. *Euro. Phys. J. E* 26, 73 (2008).

Metwalli, E.; Couet, S.; Schlag, K.; Röhlsberger, R.; Körstgens, V.; Ruderer, M.; Wang, W.; Kaune, G.; Roth, S.V.; Müller-Buschbaum, P. In situ GISAXS investigation of gold sput-

tering onto a polymer template; *Langmuir* 24, 4265-4272 (2008)

Talks

Wang, W.; Troll, K.; Kaune, G.; Metwalli, E.; Ruderer, M.; Skrabania, K.; Laschewsky, A.; Roth, S.V.; Papadakis, C.M.; Müller-Buschbaum, P. Temperature dependent swelling and switching kinetics of gold coated end-capped PNIPAM thin films. DPG Frühjahrstagung, Dresden, 27 March 2009.

Wang, W.; Müller-Buschbaum, P. Structure and kinetic of thin stimuli-responsive hydrogel films based on amphiphilic diblock copolymers, DPG SPP 1259 "INTELLIGENTE HYDROGELE" Kolloquium, Dortmund, 21 September 2009.

Wang, W. Swelling of thin PNIPAM films as probed with neutron reflectivity DPG Hydrogel-Workshop, Karlsruhe, April 2009.

Wang, W.; Müller-Buschbaum, P.; Troll, K.; Kulkarni, A.; Papadakis, C.M.; Bivigou Koumba, A.M.; Laschewsky, A. Temperature dependent swelling behavior of PNIPAM based block copolymer thin films. Frühjahrstagung der Deutschen Phsikalischen Gesellscha-ft, Berlin, 25 Feb 2008.

Wang, W.; Perlich, J.; Kaune, G.; Bivigou Koumba, A.M.; Laschewsky, A.; Papadakis, C.M.; Robert, C.; Müller-Buschbaum, P. Temperature dependent swelling and switching kinetics of gold coated end-capped PNIPAM thin films. FRM-II Workshop on Neutron Scattering Burg Rothenfels, 23 July 2007.

Posters

Wang, W.; Troll, K.; Kaune, G.; Metwalli, E.; Ruderer, M.; Skrabania, K.; Laschewsky, A.; Roth, S.V.; Papadakis, C.M.; Müller-Buschbaum, P. Thin films of poly(*N*-isopropylacrylamide) end-capped with *n*-butyltrithiocarbonate. HASYLAB Usermeeting, Hamburg, 24 Jan 2008.

Wang, W.; Moulin, J.-F.; Perlich, J.; Abul Kashum, M.M.; Roth, S.V.; Laschewsky, A.; Papadakis, C.M.; Müller-Buschbaum, P. Response of thin hydrogel films to water flow

investigated with in-situ grazing incidence small-angle X-ray scattering. The 10th International Conference on Surface X-ray and Neutron Scattering, Paris, 2 July 2008.

Acknowledgement

First I would like to thank Prof. Dr. Peter Müller-Buschbaum for offering me the possibility to finish this thesis under his supervision, for his continuous support during the complete thesis time as well as for introducing me into this very interesting project. His scientific leadership, insight, encouragement, advice, inspiration and overall backing led me to reach my goal successfully. I am grateful for his detail discussion on technical and scientific issues during all critical beamtimes and later on data analysis.

I am grateful to Prof. Dr. Christine M. Papadakis, Kordelia Troll, and Amit Kulkarni who give me very useful suggestions and help me during my experiments.

I would like to acknowledge Prof. Dr. André Laschewsky, Katja Skrabania, and Achille M. Bivigou Koumba who synthesize the polymers used in this thesis.

I would like to thank Prof. Winfried Petry for giving me the chance to work on my thesis in his chair.

For the neutron reflectivity experiments at ILL, France, I would like to express my thanks to Dr. Ezzeldin Metwalli Ali, Jan Perlich, Gunar Kaune and Dr. Robert Cubitt from ILL who help me on the measurements there, and discuss with me on the data analysis.

I thank Dr. Deme Bruno at ILL for his support during the GISANS experiment.

I am grateful to Jean-Francois Moulin, Matthias Ruderer, Alexander Diethert, and Mottakin M. Abul Kashem from my office colleagues and Dr. Stephan V. Roth from HASYLAB, DESY for great help during the beamtimes for GISAXS experiment. Without their co-operation this investigation could not be accomplished.

I am grateful to Dr. Kai Schlage, Dr. Sebastian Couet and Prof. Dr. Ralf Röhlsberger from HASYLAB, DESY, Hamburg for the gold sputtering.

Special thanks go to Dr. Volker Körstgens for his constant help in writing the thesis.

I would like to send my acknowledgement to Mrs. Barbara Russ and Prof. Dr. Peter Böni of E21, Physics department, TU-Müunchen for X-ray reflectivity measurements.

I would like to express my thanks to other E13 colleagues Robert Meier, Dr. Johannes Wiedersich, Zhengyu Di, and Qi Zhong for discussions, and help during the daily work. I also thank all the other members, for their help and providing a nice working atmosphere.

The financial support from Deutsche Forschungsgemeinschaft (DFG) SPP 1259 (Mul1487/8) is gratefully acknowledged.

Finally I would like to thank my family for continuously supporting my scientific work abroad.